SAPIENZA
UNIVERSITÀ DI ROMA

Statistical/Climatic models to predict and project extreme precipitation events dominated by large-scale atmospheric circulation over the central-eastern China

Faculty of Civil and Industrial Engineering
Department of Civil, Building and Environmental Engineering
PhD in Environmental and Hydraulic Engineering

Qin Jiang
ID number 1979321

Supervisor
Francesco Cioffi

Co-Supervisor
Jun Wang

A.A. 2022-2023

Abstract

Global warming has posed non-negligible effects on regional extreme precipitation changes and increased the uncertainties when meteorologists predict such extremes. More importantly, floods, landslides, and waterlogging caused by extreme precipitation have had catastrophic societal impacts and led to steep economic damages across the world, in particular over central-eastern China (CEC), where heavy precipitation due to the Meiyu-front and typhoon activities often causes flood disaster. There is mounting evidence that the anomaly atmospheric circulation systems and water vapor transport have a dominant role in triggering and maintaining the processes of regional extreme precipitation. Both understanding and accurately predicting extreme precipitation events based on these anomalous signals are hot issues in the field of hydrological research.

In this thesis, the self-organizing map (SOM) and event synchronization were used to cluster the large-scale atmospheric circulation reflected by geopotential height at 500 hPa and to quantify the level of synchronization between the identified circulation patterns with extreme precipitation over CEC. With the understanding of which patterns were associated with extreme precipitation events, and corresponding water vapor transport fields, a hybrid deep learning model of multilayer perceptron and convolutional neural networks (MLP-CNN) was proposed to achieve the binary predictions of extreme precipitation. The inputs to MLP-CNN were the anomalous fields of GP at 500 hPa and vertically integrated water vapor transport (IVT). Compared with the original MLP, CNN, and two other machine learning models (random forest and support vector machine), MLP-CNN showed the best performance. Additionally, since the coarse spatial resolution of global circulation models and its large biases in extremes precipitation estimations, a new precipitation downscaling framework that combination of ensemble-learning and nonhomogeneous hidden Markov model (Ensemble-NHMM) was developed, to improve the reliabilities of GCMs in historical simulations and future projection. The performances of downscaled precipitation from reanalysis and GCM datasets were validated against the gauge observations and also compared with the results of traditional NHMM. Finally, the Ensemble-NHMM downscaling model was applied to future scenario data of GCM. On the projections of change trends in precipitation over CEC in the early-, medium- and late- 21st centuries under different emission scenarios, the possible causes were discussed in term of both thermodynamic and dynamic factors. Main results are enumerated as follows.

(1) The large-scale atmospheric circulation patterns and associated water vapor transport fields synchronized with extreme precipitation events over CEC were quantitatively identified, as well as the contribution of circulation pattern changes to extreme precipitation changes and their teleconnection with the interdecadal modes of the ocean. Firstly, based on the nonparametric Pettitt test, it was found that 23% of rain gauges had significant abrupt changes in the annual extreme precipitation from 1960 to 2015. The average change point in the annual extreme precipitation frequency and amount occurred near 1989. Complex network analysis showed that the rain gauges highly synchronized on extreme precipitation events can be clustered into four clusters based on modularity information. Secondly, the dominant circulation patterns over CEC were robustly identified based on the SOM. From the period 1960–1989 to 1990–2015, the categories of identified circulation patterns generally remain almost unchanged. Among these, the circulation patterns characterized by obvious positive anomalies of 500 hPa geopotential height over the Eastern Eurasia continent and negative values over the surrounding oceans are highly synchronized with extreme precipitation events. An obvious water vapor channel originating from the northern Indian Ocean driven by the southwesterly airflow was observed for the representative circulation patterns (synchronized with extreme precipitation). Finally, the circulation pattern changes produced an increase in extreme precipitation frequency from 1960–1989 to 1990–2015. Empirical mode decomposition of the annual frequency variation signals in the representative circulation pattern showed that the 2–4 yr oscillation in the annual frequency was closely related to the phase of El Niño and Southern Oscillation (ENSO); while the 20–25 yr and 42–50 yr periodic oscillations were responses to the Pacific Decadal Oscillation and the Atlantic Multidecadal Oscillation.

(2) A regional extreme precipitation prediction model was constructed. Two deep learning models-MLP and CNN were linearly stacked and used two atmospheric variables associated with extreme precipitation, that is, geopotential height at 500 hPa and IVT. The hybrid model can learn both the local-scale information with MLP and large-scale circulation information with CNN. Validation results showed that the MLP-CNN model can predict extreme or non-extreme precipitation days with an overall accuracy of 86%. The MLP-CNN also showed excellent seasonal transferability with an 81% accuracy on the testing set from different seasons of the training set. MLP-CNN significantly outperformed over other machine learning models, including MLP, CNN, random forest, and support

vector machine. Additionally, the MLP-CNN can be used to produce precursor signals by 1 to 2 days, though the accuracy drops quickly as the number of precursor days increases.

(3) The GCM seriously underestimated extreme precipitation over CEC but showed convincing results for reproducing large-scale atmospheric circulation patterns. The accuracies of 10 GCMs in extreme precipitation and large-scale atmospheric circulation simulations were evaluated. First, five indices were selected to measure the characteristics of extreme precipitation and the performances of GCMs were compared to the gauge-based daily precipitation analysis dataset over the Chinese mainland. The results showed that except for FGOALS-g3, most GCMs can reproduce the spatial distribution characteristics of the average precipitation from 1960 to 2015. However, all GCMs failed to accurately estimate the extreme precipitation with large underestimation (relative bias exceeds 85%). In addition, using the circulation patterns identified by the fifth-generation reanalysis data (ERA5) as benchmarks, GCMs can reproduce most CP types for the periods 1960–1989 and 1990–2015. In terms of the spatial similarity of the identified CPs, MPI-ESM1-2-HR was superior.

(4) To improve the reliabilities of precipitation simulations and future projections from GCMs, a new statistical downscaling framework was proposed. This framework comprises two models, ensemble learning and NHMM. First, the extreme gradient boosting (XGBoost) and random forest (RF) were selected as the basic- and meta- classifiers for constructing the ensemble learning model. Based on the top 50 principal components of GP at 500 hPa and IVT, this model was trained to predict the occurrence probabilities for the different levels of daily precipitation (no rain, very light, light, moderate, and heavy precipitation) aggregated by multi-sites. Confusion matrix results showed that the ensemble learning model had sufficient accuracy (>88%) in classifying no rain or rain days and (>83%) predicting moderate precipitation events. Subsequently, precipitation downscaling was done using the probability sequences of daily precipitation as large-scale predictors to NHMM. Statistical metrics showed that the Ensemble-NHMM downscaled results matched best to the gauge observations in precipitation variabilities and extreme precipitation simulations, compared with the result from the one that directly used circulation variables as predictors. Finally, the downscaling model also performed well in the historical simulations of MPI-ESM1-2-HR, which reproduced the change trends of annual precipitation and the means of total extreme precipitation index.

(5) Three climate scenarios with different Shared Socioeconomic Pathways and Representative Concentration Pathways (SSPs) were selected to project the future precipitation change trends. The Ensemble-NHMM downscaling model was applied to the scenario data from MPI-ESM1-2-HR. Projection results showed that the CEC would receive more precipitation in the future by ~30% through the 2075–2100 period. Compared to the recent 26-year epoch (1990–2015), the frequency and magnitude of extreme precipitation would increase by 21.9–48.1% and 12.3–38.3% respectively under the worst emission scenario (SSP585). In particular, the south CEC region is projected to receive more extreme precipitation than the north. Investigations of thermodynamic and dynamic factors showed that climate warming would increase the probability of stronger water vapor convergence over CEC. More wet weather states due to the enhanced water vapor transport, as well as the increased favoring large-scale atmospheric circulation and the strengthen pressure gradient would be the factors for the increased precipitation.

Keywords: Extreme precipitation, circulation pattern, climate change, precipitation downscaling, scenario projections

Content

Abstract ..... **I**

CHAPTER-1. Introduction **1**

1. Research background 1

2. Literature reviews 3

2.1 Changes in extreme precipitation and possible causes 3

2.1.1 Thermodynamic factor 4

2.1.2 Dynamic factor 4

2.2 Objective classifications of large-scale atmospheric circulation 6

2.2.1 Dimensionality reduction 6

2.2.2 Clustering 7

2.2.3 Fuzzy-rule based 7

2.2.4 Neural network 8

2.3 Predicting extreme precipitation events dominated by large-scale circulation 8

2.3.1 Regression model 9

2.3.2 Conditional probability model 9

2.3.3 Analog analysis 10

2.3.4 Deep learning model 10

2.4 Statistical downscaling and future projections of precipitation and its extremes 11

2.4.1 Statistical downscaling for GCMs 11

2.4.2 Projections of extreme precipitation 16

3. Literature comments 19

3.1 Issue 1: study on the links between the large-scale atmospheric circulation and extreme precipitation over central-eastern China 19

3.2 Issue 2: performances of the regional extreme precipitation prediction models 20

3.3 Issue 3: the reliability of GCMs and future projections of extreme precipitation 21

4. Objectives and structure of the thesis 22

4.1 Key scientific questions and research objectives 22

4.2 Structure of thesis 25

CHAPTER-2. Linking extreme precipitation events with large-scale atmospheric circulation over central-eastern China 26

Summary 26

1. Study area 26

2. Datasets 28

3. Methods 28

3.1 Pettitt test 29

3.2 Self-organizing map 30

3.3 Event synchronization 32

3.4 Rain gauges clustering by modularity 32

3.5 Local logistics regression 33

3.6 Quantitative partitioning technique 33

4. Results 34

4.1 Identified circulation patterns by SOM 34

4.2 Synchronized circulation patterns with extreme precipitation 38

4.3 Contribution analysis of extreme precipitation changes 43

5. Discussion-The potential mechanism for large-scale circulation patterns change 44

6. Conclusions 49

CHAPTER-3. Predictability of large-scale atmospheric circulation to extreme precipitation occurrences based on hybrid deep learning model 51

Summary 51

1. Motivations 51

2. Datasets 52

3. Methodology 53

3.1 Data preprocessing 53

3.2 Multilayer perceptron neural network 55

3.3 Convolutional neural networks 55

3.4 Hybrid model of MLP and CNN 57

3.5 Evaluation metrics 58

4. Results 59

4.1 Analysis of extreme precipitation events and related circulation features 59
4.2 Performance of MLP-CNN in predicting extreme precipitation 61
4.3 Comparison with other deep and machine learning models 63
5. Discussion-Performances of MLP-CNN in the ahead predictions for extreme precipitation 66
6. Case study-Performances of MLP-CNN in July 2021 extreme rainstorm in Henan province, China 67
7. Conclusions 68
CHAPTER-4. Performance of global circulation models in simulating extreme precipitation and large-scale atmospheric circulation 70
Summary 70
1. Motivations 70
2. Datasets 71
2.1 Gauge-based data 71
2.2 ERA5 71
2.3 GCMs 71
3. Methods 73
3.1 Extreme precipitation indices 73
3.2 Clustering of circulation patterns 74
3.3 Evaluation metrics 74
4. Results 75
4.1 Evaluation of extreme precipitation simulations 75
4.1.1 General analysis of annual precipitation 75
4.1.2 Error metrics 76
4.2 Evaluation of circulation patterns simulation 77
4.2.1 Geopotential height at 500 hPa 77
4.2.2 Identified circulation patterns of GCMs 78
5 Conclusions 86
CHAPTER-5. Precipitation downscaling and future projections using large-scale atmospheric circulation features 87
Summary 87

1. Motivations 87
2. Datasets 89
3. Methodology 90
3.1 Data preprocessing 90
3.2 Ensemble learning model 92
3.2.1 Extreme Gradient Boosting 92
3.2.2 Random Forest 93
3.2.3 Implementing ensemble learning with XGBoost and RF models 93
3.2.4 Parameters tuning and model validation 95
3.3 Nonhomogeneous hidden Markov model 96
3.4 Evaluation indicators 97
4. Results 97
4.1 Ensemble learning model performance in daily precipitation classification 97
4.2 Comparison of Ensemble-NHMM and NHMM 100
4.2.1 Precipitation variabilities 100
4.2.2 Extreme precipitation 105
4.3 Future precipitation projection under different climate change scenarios 106
4.3.1 Analysis of the historical period 107
4.3.2 Future precipitation projection 113
5. Discussion-Possible impacts of climate change on future precipitation changes 118
5.1 Future projections of water vapor transport 118
5.2 Future projections of weather states and circulation patterns 122
6. Conclusions 127
CHAPTER-6. Extended summary and prospect **129**
1. Main conclusions 129
2. Revisiting the research questions and future work 131
Appendix **133**
References **142**
ACKNOWLEDGEMENTS **165**

CHAPTER-1. Introduction

1. Research background

Thought-provoking conclusions, such as "*Human influence has warmed the climate ... is unprecedented,*" have been highlighted in the latest Intergovernmental Panel on Climate Change (IPCC) report (IPCC, 2021). This report illustrates the key findings of the changing climate and human roles, and possible futures, which show that global surface temperature in the last decade was nearly 1.09℃ warmer relative to pre-industrial conditions and its very likely to increase 1.0–5.7℃ by the end of the 21st century (2081–2100) due to the anthropogenic greenhouse gas emissions. In fact, global warming has profoundly affected the climate system and contributed to more extreme weather events (Banaji, 2022).

It has been proven that water-related weather hazards and multiple risks to ecosystems and human settlements tend to intensify with climate change (Huang and Swain, 2022; Nishant and Sherwood, 2021; Sammen et al., 2022), particularly in coastal cities at low elevations (Toimil et al., 2020). The overview of global disaster statistics during 1970–2019 indicates that weather- and water-related disasters had increased and reported losses accounted for the domination (WMO, 2021). Moreover, as global warming increases, such natural hazards are presumed to be more frequent and destructive that typically related to more record-breaking precipitation events under wetter and warmer atmospheric environments (He et al., 2022; Madakumbura et al., 2021; Papalexiou and Montanari, 2019). The water-holding capacity of the atmosphere would enhance with arising temperature and result in stronger moisture content, which can directly affect the magnitude of precipitation. Likewise, extreme precipitation is expected to increase robustly over most of the globe (Min et al., 2011).

However, at the scale of specific geographic areas, regional precipitation patterns diverge greatly and show heterogeneity characteristics because of specific atmospheric circulation situations (Tandon et al., 2018), as well as of the local thermodynamic environment (Ma et al., 2018). For example, changes in regional precipitation patterns over central Europe from 1950 to 2018 were related to the prevailing atmospheric configurations, that is, the low pressure or trough systems occurred along this area

(Hoffmann and Spekat, 2021). On the synoptic scale, the occurrences of extreme precipitation events are strongly related to the anomalies of large-scale atmospheric circulation, as well as the transportation and convergence of moisture airflows (Anandh and Vissa, 2022). A recent example reported is the catastrophic flood of August 2022 in Pakistan that was triggered by excessive monsoonal precipitation, with more than 1480 deaths and direct economic damage of over 30 billion dollars. In this case, the abnormally enhanced low-pressure system and water vapor transport exacerbated the devastating precipitation (Otto et al., 2022). In addition, a record-breaking extreme rainstorm hit the Zhengzhou city, China on 20 July 2021, with a maximum hourly rainfall of 201.9 mm. Contribution analysis showed that the "once in a thousand years" extreme event was mainly conditioned by the circulation anomalies of deepening upper-level trough and easterly flow, as well as the stable meridional water vapor from the adjacent sea (Nie and Sun, 2022; Qin et al., 2022). In order to understand the mechanisms of regional extreme precipitation, enormous studies have been conducted to identify the key atmospheric circulation configurations associated with such events (Beyene et al., 2022; Chikoore et al., 2021; Mastrantonas et al., 2022). Besides, behind the strong connections, the anomaly circulation fields are recognized as an important indicator to predict the occurrence probability of extreme precipitation events (Davenport and Diffenbaugh, 2021; Gao and Mathur, 2021), as well as the basic predictors in precipitation downscaling models (Araya-Osses et al., 2020; Wu et al., 2022a). Most empirical downscaling approaches for global circulation models (GCMs) are constructed based on the statistical properties between the precipitation aggregated at multiple sites and large-scale atmospheric variables (Pahlavan et al., 2018).

Our study area is the central-eastern China (CEC), which is one of the most densely populated regions and often suffers from serious flooding induced by excessive precipitation. Due to its geographic location, on the east side of Eurasia facing the Pacific Ocean, allows for large-scale circulation activities, e.g., the meridional movement of the Western Pacific Subtropical High (Wang et al., 2019) to promote amounts of water vapor transport from the oceans and facilitate the formation of precipitation. In particular, under climate warming, the future precipitation projections in previous studies suggest that this area would receive more intensified extremes (Lu et al., 2022). Despite enormous works conducted into the precipitation changes over CEC, the questions of which large-scale atmospheric circulation patterns are relevant to the extreme precipitation events have not yet

been completely understood, as well as the roles of circulation anomalous fields in the predictability of extreme precipitation. In addition, we still have knowledge gaps in the performances of the newest generation of GCMs in simulating the precipitation extremes and large-scale circulation patterns over CEC. Future projections of weather variables are highly depend on the GCM data, but large biases in their precipitation simulations have been found in regional research due to the coarse spatial resolution (Ayugi et al., 2021b; Nishant et al., 2022). Close these gaps will benefit us to select the GCMs for precipitation downscaling when using the large-scale atmospheric variables as the predictors and increase the confidence for future projections, especially for extreme events. There is a need to develop some statistical and downscaling models to accurately access and predict the extreme precipitation changes. Scientific and useful references for disaster prevention and mitigation strategies can be drawn in this thesis.

2. Literature reviews

2.1 Changes in extreme precipitation and possible causes

Statistically, precipitation extremes are rare events during a particular period, defined as the daily or hourly intensity exceeding the selected percentiles, thresholds, or return periods (Imran et al., 2023; Ritzhaupt and Maraun, 2023; Senent-Aparicio et al., 2023). Thereby, the change trends of extreme precipitation can be reported from the historical records over a specific region. When reviewing the publicly expressed papers, it is widely recognized that at the global mean scale, extreme precipitation had increased in frequency and intensity from in-situ and satellite-based observations over the past century(Nguyen et al., 2018; Sun et al., 2021). The fifth assessment report of the IPCC presents that the trend of increased heavy precipitation dominated over the land areas since 1950 (Hartmann et al., 2013). Papalexiou and Montanari (2019) observed that the number of rain gauges with positive changes in extreme precipitation frequency and intensity was higher than negative in the period of 1964–2013, on the global scale. In addition, evidence has proved that precipitation extremes are observed to increase in Europe (Cioffi et al., 2015; Zeder and Fischer, 2020), East Asia (Chang et al., 2020; Cui et al., 2019; Park et al., 2011), North America (Kirchmeier-Young and Zhang, 2020), and other regions. Blanchet et al. (2021) used a gridded product with 1×1 km to analyze extreme precipitation in the region of southwestern Alps during 1958–2017. They found that change characteristics of annual maxima varied on the seasons; while the atmospheric circulations and ocean

could regulate the extremes at the local scale. Osburn et al. (2021) analyzed the "once in two, ten, and one hundred years" events in Victoria, Australia from 1958 to 2014, based on gauge measurements. Results showed that an increase is able to observe, especially for most extremes. Takahashi and Fujinami (2021) confirmed a positive tendency in Meiyu heavy precipitation over East Asia during 1998–2019 from a satellite-based product.

For possible causes, previous studies suggested that there are two factors, that is, thermodynamic and dynamic contributing to the observed changes in extreme precipitation (Lee et al., 2017a; Pendergrass, 2020), which are discussed as follows.

2.1.1 Thermodynamic factor

Primarily, precipitation changes are constrained by the energy budget balance. More frequent and severe extreme precipitation around the world is expected under global warming (Donat et al., 2016; Song et al., 2022). The physical hypothesis is the "warmer atmosphere is also wetter" that ideally following the increasing rate of 6%–7% K^{-1} (the Clausius-Clapeyron rate) (O'Gorman and Muller, 2010), could condense into more water when rains (Chou et al., 2012). Many research demonstrated that global mean precipitation scaled more likely linear to global temperature change, accurately, increasing at a rate constrained by the 1.5–2% K^{-1} (Pendergrass et al., 2017; Salzmann, 2016); whereas the extremes are nearly 7% K^{-1} (Tabari, 2021). Moreover, the sensitivity of precipitation extremes to the temperature is more evident in the low latitude areas (Uribe et al., 2021). Over the tropical east Pacific, this rate is estimated to be above 25% K^{-1} when considering the dynamic forcing (Norris et al., 2019).

2.1.2 Dynamic factor

Compared to the thermodynamic scaling of temperature vs. precipitation, this factor refers to that large-scale atmospheric circulation has a broadly dynamic forcing on mesoscale rainfall systems (Cannon et al., 2018; Liu et al., 2020b). Changes in atmospheric conditions and water vapor transport belts shifted by circulation activities could potentially affect extreme precipitation (Angulo-Umana and Kim, 2023; Kautz et al., 2022; Ødemark et al., 2023). A sensitivity analysis showed that the intensification of moisture convergence mainly affects the precipitation areas, while precipitation

responds to the atmospheric instability manifested in intensity (Loriaux et al., 2017). Kim et al. (2019) found that dynamic forcing, i.e., the more southeastward extension of the jet contributed to the enhanced water vapor transport, led to an increase in precipitation over the coastal region of Northwest America. Moreover, the favorable large-scale circulation situations directly organized the regional and local factors in forcing extreme precipitation (Barlow et al., 2019).

Usually, large-scale atmospheric circulation refers to the air motions with horizontal scales of more than mesoscale systems above the earth, spanning from the surface layer to the troposphere vertically, and a time scale of at least one day or longer. These circulation activities at such scales are driven by the pressure gradient due to the differential heating surface and Coriolis effects. Conversely, circulation activities can be seen as bridges facilitating water vapor and energy transport, which are critical to the formation of extreme precipitation (Wu et al., 2022b). Often, parts of regional extreme precipitation events are conditioned by specific large-scale atmospheric circulation patterns (Olmo et al., 2020), which shape the processes of extreme events and their subsequent effects (Moustakis et al., 2020). For individual events, Ye and Qian (2021) analyzed how much the atmospheric circulation influenced an extreme precipitation event that occurred in the summer of 2020 over southern China. Simulations showed that the contribution of atmospheric circulation dominated more than 70% of the total precipitation. Similarly, atmospheric circulation was found to explain 47% of the intensity of heavy precipitation that happened in mid-August 2020 over southwestern China (Qian et al., 2022).

For the long-term climate changes, Feng et al. (2016) found that over central United States, the positive tendency of extreme precipitation in spring was influenced by an increased convective system. Cipolla et al. (2020) analyzed rainfall annual maxima events between 1928 and 2016 over Sicily, Italy. The results showed that most events were related to a dominant circulation mode. Shibuya et al. (2021) investigated the dynamical forcing during the development of reported catastrophic precipitation in western Japan. The anomalies circulation (i.e., positive of north Pacific subtropical high and cyclonic) ahead 7 to 2 days of the precipitation were responsible for the enhanced moisture. Ullah et al. (2021) also pointed out that most of the extreme monsoon precipitation was related to the leading circulation pattern in Pakistan. Ibebuchi (2022) investigated the circulation patterns associated with extreme precipitation from 1979 to 2021 in Germany. They found the

circulation pattern with the highest probability when extremes occur, especially this pattern also responsible for the record-breaking precipitation in July 2021. Undoubtedly, information on which circulation patterns are more prone to extreme precipitation events can help disaster prevention. Robust identification of circulation patterns is essential to understand the links between regional weather and synoptic drivers.

2.2 Objective classifications of large-scale atmospheric circulation

In recent years, objective weather classification techniques have been utilized to identify representative circulation patterns or circulation anomalies (Kotsias et al., 2023; Piotrowicz and Ciaranek, 2020). Specifically, circulation patterns extracted from reanalysis or observation data over different spatial domain sizes are corresponding to particular weather conditions, e.g., extreme precipitation (Marquardt Collow et al., 2016), drought (Odoulami et al., 2021), or high temperature (Yu et al., 2020) in order to reveal the interactions between circulation anomalies and climatological parameters. In a review of the existing classification techniques of large-scale atmospheric circulation, commonly used methods include four categories: dimensionality reduction, clustering, fuzzy rule-based, and neural network, as shown in Table 1-1. These methods have provided different frameworks for identifying circulation patterns.

2.2.1 Dimensionality reduction

Since the original datasets of atmospheric predictors, i.e., sea level pressure, geopotential height, and wind fields generally have high dimensions, this classification type of dimensionality reduction is known primarily for identifying the principal circulation patterns or features through linear or nonlinear transformation functions (Huth and Beranová, 2021; Mohammadpour et al., 2021; Yu and Zhai, 2021). Commonly, dimensionality reduction classification methods are including archetypal analysis (AA), empirical orthogonal function (EOF), and principal component analysis (PCA). The derivation processes of the latter two are essentially the same, both main goals are to decompose the main oscillations of key modes changing with time and to describe the decomposed circulation patterns spatially from the atmospheric variables.

Table 1-1. Summary for classification techniques.

Type	Method	Indicators of classification	References
Dimensionality reduction	archetypal analysis		Black et al. (2022)
	empirical orthogonal function	explained variance	Zhong et al. (2020)
	principle component analysis		Philipp (2009)
Clustering	*k*-means	distance to the *k*-center	Ku et al. (2021)
	analogy-based	the similarity of patterns	Blanc et al. (2022)
	probabilistic model	the probability distribution	Rust et al. (2010)
	ward's distance	distance to a cluster	Hu et al. (2019)
Fuzzy rule-based	fuzzy rule-based	maximize the objective function	Bliefernicht et al. (2022)
Neural network	self-organizing map	distance to the best-matching neurons	Kaesmacher and Schneider (2011)
	layerwise relevance propagation	the relevance to the trained neural network	Toms et al. (2021)

2.2.2 Clustering

Clustering aims to divide a dataset into a certain number of classes or clusters. The objects in the same cluster should get the highest possible similarity and be dissimilar from the others in different clusters. In synoptic climatology research, cluster analysis is often used to identify the dominant patterns from massive atmospheric data. For instance, for the *k*-means clustering method, the minimum Euclidean distance from the data points to the *k*-center while having the maximum inter-cluster variance was applied to divide a circulation field belongs which patterns (Torralba et al., 2021; Warren et al., 2021). The analogue method uses the mathematical metrics, e.g., S1 criterion, and Teweles-Wobus score to quantify the similarities of input (Blanc et al., 2022; Horton et al., 2018). Afterward, regional weather environments like extreme precipitation, droughts can be directly linked to these patterns by means of a well-statistical analysis, to investigate the possible connections.

2.2.3 Fuzzy-rule based

In 1990s, Bardossy et al. (1995) introduced the fuzzy-rule based algorithm for daily atmospheric circulation classification. This algorithm mainly includes two steps: 1) predefine the fuzzy rules. For each grid there is a fuzzy set that sufficient to cover the main circulation pattern characteristics; 2) for a given day, use the simulated annealing algorithm to optimize the objective function and obtain a cluster (Pringle et al., 2015). Since fuzzy classification allows flexible circumscriptions of patterns, this method hard to avoid the ambiguous classifications of atmospheric circulation and sensitive to the parameters (Enke et al., 2005; Kambalimath and Deka, 2020).

2.2.4 Neural network

In recent years, artificial neural network has become the representative tool for pattern classification. Among them, the self-organizing map (SOM) is an unsupervised neural network method of objective classification (Ghaseminezhad and Karami, 2011; Kiang, 2001; Kohonen, 1998) and superior to the based feature extraction methods, like principal component analysis and empirical orthogonal functions in interpreting the physical behavior of a yielded circulation field. Rousi et al. (2015) evaluated the principal component analysis and SOM methods in recognizing the teleconnection patterns of the winter 500 hPa geopotential height anomalies over Europe. Their comparison suggested that SOM could be the better choice in visualizing less pronounced patterns, especially for complex and diverse data. Consequently, SOM has been commonly used in related research (Nguyen-Le et al., 2017; Olmo and Bettolli, 2021). Agel et al. (2018) explored the links between tropopause height and extreme precipitation by using both the SOM and *k*-means clustering algorithms. Swales et al. (2016) used SOM method to relate localized extreme precipitation events to the synoptic conditions identified by vertically integrated water vapor transport (IVT) over the western United States. They demonstrated that about 70% of extreme precipitation were related to infrequent circulation patterns.

2.3 Predicting extreme precipitation events dominated by large-scale circulation

Analyses of the previous studies, presented in Section 2.1, suggest that extreme precipitation can be affected by large-scale atmospheric circulation activities (Agel et al., 2019; Kebacho, 2021), which as a dynamic forcing and be very important in constructing the regional and local precipitation conditions (Barlow et al., 2019). Conversely, the abnormal circulation features can be employed to

predict regional extreme precipitation (Rieger et al., 2021), which is an essential way to mitigate the risks of such events.

In general, studies with large-scale circulation for predicting regional weather or climate phenomena are available for years (Chattopadhyay et al., 2020; Mastrantonas et al., 2021). Prediction models widely used are regression, conditional probability, analog analysis, and machine/deep learning by developing the physical linkages between the regional precipitation and large-scale atmospheric variables (Cheng et al., 2021; Ma and Xie, 2020; Miller et al., 2021).

2.3.1 Regression model

In the field of synoptic-scale climate research, the regression model can be summarized as a common formulation in that the occurrences of extreme precipitation or precipitation intensity are the dependent variable and atmospheric predictors are the independent variables. Sohn et al. (2005) selected more than 40 atmospheric variables to construct the logistic regression and multiple linear regression model to statistically predict the heavy rainfall in South Korea. Zeng et al. (2011) compared three methods, i.e., support vector machine, Bayesian neural network, and multiple linear regression in predicting the seasonal extreme precipitation over Canada. The leading principal components of precipitation anomalies were the targets and the used predictors were the anomalous fields of sea surface temperature and GP at 500 hPa, and six circulation indexes. They found that the nonlinearity model outperformed the climate regions, where extreme precipitation was strongly influenced by the El Niño-Southern Oscillation. Shastri et al. (2017) proposed an extreme precipitation probabilistic forecast model over Mumbai. They used the censored quantile regression to link the predictors of ensemble circulation patterns and the percentile-based precipitation during the historical. At last, given a forecasted circulation pattern, it is possible to estimate the probability of extreme precipitation standing at the highest quantile.

2.3.2 Conditional probability model

Different from regressive methods, this approach is to construct a joint probability model based on the conditional event. Subsequently, predictions of extreme precipitation events can be extrapolated from a modeled conditional probability distribution. For instance, Vicente-Serrano et al. (2009) used

the generalized Pareto distribution to fit the historical extreme precipitation events conditioned by different circulation indices over northeast Spain and the precipitation probability was predicted during a given circulation phase. Lee et al. (2017b) fitted the occurrence probability of extreme precipitation events conditioned by a climate index over Asia and the empirical relationships were applied to give the prediction. When focus on the circulation patterns, Richardson et al. (2020) investigated the predictability of extreme precipitation on a given weather pattern, where the exceedance probabilities were calculated from the historical conditional distributions. Schroers and Martin (2022) adopted the anomalous fields of 500 hPa geopotential height and perceptible water to construct the conditional probability model, in order to predict extreme precipitation events in the United States.

2.3.3 Analog analysis

A general theory of analog analysis is that similar atmospheric conditions are prone to produce similar weather events. Accordingly, current predictions are achieved based on the similarities of the predictors in past events (Ben Daoud et al., 2011; Hamill and Whitaker, 2006; Horton et al., 2018). For this approach, the key issue is to quantify the analogous circulation features and produce extreme precipitation predictions (Hamill et al., 2015). Zhou and Zhai (2016) have tested the capability of analog analysis model over the Yangtze-Huai River valley. In their study, the cosine angular was selected to measure the similarities between two large-scale atmospheric patterns. The predictability of extreme precipitation on a given day was determined by the highest integral similarity score.

2.3.4 Deep learning model

Recent advances in deep learning, for example, the convolutional neural network (CNN) have shown tremendous potential in emulating high-dimensional geoscience data (Abdelmoaty et al., 2021; Goodfellow et al., 2016) and improved the predictive ability of extreme climate events (Knighton et al., 2019; Zhang et al., 2022). Specifically, CNN can learn the spatio-temporal features, i.e., location, intensity, or extent of anomaly atmospheric circulation associated with extreme weather events well. For instance, Davenport and Diffenbaugh (2021) trained a CNN model to learn the large-scale circulation features associated with the regional extreme precipitation events (95th percentile) over midwestern United States. Prediction results showed that CNN had an overall accuracy of 88% in

producing the binary classifications of extreme or non-extreme. Gao and Mathur (2021) compared CNN and analogue methods in predicting the winter and summer extreme precipitation occurrences over eastern and western regions of the United States based on meteorological patterns. They found that CNN demonstrated superior accuracy in their experiment. Dagon et al. (2022) trained a CNN model to identify the weather fronts and associated extreme precipitation over the United States. In addition, CNN also has been employed to recognize the "river-like" water vapor transport belts, cyclone systems, and monsoon events (Chapman et al., 2022; Griffin et al., 2022; Tang and Duan, 2021).

Besides, serval research has tried to investigate other deep learning models in predicting extreme precipitation. Chattopadhyay et al. (2020) employed the capsule neural network to predict the extreme precipitation using the GP at 500 hPa over North America. Huang (2022) developed a self-attention augmented neural network model for the task of extreme precipitation predictions over the United States. This study selected the anomalies of sea level pressure and GP as predictors and obtained an overall accuracy exceeding 90%. Healy et al. (2022) compared the multilayer perceptron (MLP) and long short-term memory (LSTM) in predicting thunderstorms over Miami based on the atmospheric conditions of temperature, humidity, air pressure, and wind fields.

2.4 Statistical downscaling and future projections of precipitation and its extremes

2.4.1 Statistical downscaling for GCMs

The Global Circulation Models (GCMs) are the most powerful tools for simulating the responses of climate system in the context of global warming (Grose et al., 2020). Over the past few decades, several generations of GCMs have been developed along with continuous updates of numerical and physical modeling techniques. In the 1990s, the first phase of Coupled Model Intercomparison Project (CMIP1) was proposed by the World Climate Research Programme, 10 GCMs participated in this community, whereas the latest sixth phase (CMIP6) has more than 100 "control runs" being produced. Different from the previous generations, the most recent CMIP6 experiments extend the new 21st century scenarios ranging from 2015 to 2100 within the Shared Socioeconomic Pathway and Representative Concentration Pathway (SSPs) framework (Tebaldi et al., 2021). This new framework mainly describes two guidelines as follows: 1) the trajectories of future socioeconomic, from

sustainability, middle to fossil-fueled developments; and 2) the magnitudes of climate forcing (e.g., greenhouse gas and aerosols emissions) and related climate responses (Riahi et al., 2017).

Despite the historical simulations and projections of GCMs being of great interest to meteorologists and decision-makers, yet many challenges remain. First, one of the Gordian knots is that the coarse spatial resolution of GCM projections has little feasibility for local or basin scale hydrology (Chen et al., 2021b; Christensen and Kjellström, 2020; He et al., 2021; Wang et al., 2020). Most GCMs of CMIP6 have a spatial resolution between 0.5° and 3°, on average, more than 100 kilometers in both north- and eastward directions for each grid point, whereas are too coarse to depict more precise features. As a general rule, the performances of the historical run of GCMs are evaluated against the observations or gridded precipitation products (e.g., satellite-based and reanalysis datasets) (Faye and Akinsanola, 2022; Papalexiou et al., 2021; You et al., 2021), which provides the uncertainties reference for future projections. For instance, Paik et al. (2020) did a sensitivity test for examining the anthropogenic signals in extreme precipitation changes on different spatial resolutions of GCMs, referencing observational data. They pointed out that although the coarse-resolution GCMs can capture long-term changes, the relevant mesoscale processes had been ignored. In addition, many GCMs have just scored basic on characterizing the storms and related tracks by a lack of resolution (Collins et al., 2018).

Another issue is that GCMs have remarkable biases in presenting precipitation (Cui et al., 2021), especially showing an even poorer capability in extreme estimation because of the limitations in the modeling process (Chen et al., 2021a). These inadequacies often yield non-negligible uncertainties in climate projections (Huang et al., 2020a; Norris et al., 2021; Yang et al., 2020). Plenty of accuracy evaluation works have been performed so far on different generations GCMs in precipitation simulations. Generally speaking, most CMIP6 models have many improvements in reporting precipitation relative to the previous phase 5 (Ayugi et al., 2021a; Xin et al., 2020; Zamani et al., 2020). Kim et al. (2020) compared the phases 5 and 6 models and found that CMIP6 can capture more intense precipitation than phase 5. Zhu and Yang (2020) confirmed that CMIP6 has higher reproducibility for precipitation over the arid climate areas. Nonetheless, at the global scale, there is a $\pm$10% difference against with the observations in annual maxima daily precipitation for most

GCMs of CMIP6 (Abdelmoaty et al., 2021). Particularly, in eastern Africa, CMIP6 models showed overestimation (underestimation) for the total wet day precipitation (very wet day precipitation) (Akinsanola et al., 2021). In east Asia, most CMIP6 models are hard to capture the spatial patterns of seasonal extreme precipitation (Liu et al., 2022). Indeed, these systematic biases in the historical control runs of GCMs further exacerbated the uncertainties in future projections (Iturbide et al., 2022).

In order to address the present issues that the poor representation of regional climate variables of the available GCMs, various downscaling techniques have been developed to translate the given coarse resolution information to a finer spatial scale during the historical period. When the downscaled variables can be considered more reliable by objectively validating some statistical metrics, in this situation, we can directly apply this downscaling model in future scenarios to facilitate the precipitation projection at the local scale (Mehrotra et al., 2013).

Traditionally, downscaling approaches can be directed into three types, i.e., dynamical, statistical, and their combinations. In dynamic downscaling, the GCMs provide the initial and lateral boundary conditions for the nested high-resolution regional climate model, thus far, to produce the finer scale information. For example, Wang and Kotamarthi (2015) selected the fourth version of the community climate system (CCSM4) model ($0.9° \times 1.25°$) of CMIP5 as the boundary conditions to derive the weather research and forecasting (WRF) model over north America and obtained an improved product that the spatial resolution was downscaled to 12 km. Chen et al. (2018b) used the WRF model to downscale the precipitation and surface air temperature of one GCM under two emission scenarios over China. Sivaramakrishna et al. (2022) implemented the WRF model to downscale the CCSM4 climate data to 25 km resolution in India. The downscaled simulations showed increased accuracy in areas with complex topography. However, due to the high computational costs of running dynamical downscaling, a limited number of GCMs, and the time length, this approach cannot compensate for this (Zhu et al., 2019).

An alternative approach is statistical downscaling, known as the local-scale relevant weather variables are considered as the predictands, whereas the large-scale atmospheric circulation information of GCMs are predictors. Accordingly, this downscaling is highly reliant on the well-done constructed

links between the predictands and predictors, via various statistical functions (Ahmed et al., 2019; Fan et al., 2021; Vandal et al., 2019). As investigated by Xoplaki et al. (2004), approximately 30% of the precipitation variabilities during the wet season over the Mediterranean can be explained linearly by the combination of GP and sea level pressure. Pichuka and Maity (2018) adopted the Bayesian function to model the statistical relationship between the large-scale circulation fields and monthly precipitation over India. Afterward, precipitation downscaling was conducted from the estimated stochastic parameters. Mesbahzadeh et al. (2019) successively used the copula to model the joint probability of precipitation and temperature in Iran. Over the past decades, many statistical downscaling studies have been done for various regions, Wilby and Wigley (1997) reviewed the commonly used statistical downscaling techniques to solve the problem of an insufficient resolution of climate models compared with observed data. These techniques can be divided into four categories: regression (Sharifi et al., 2019), weather typing (Bermúdez et al., 2020), stochastic weather generators (Chen et al., 2018a; Yu et al., 2022), and mesoscale modeling (Tomassetti et al., 2009). In general, there are two general conditionals. First, the spatio-temporal variabilities of the large-scale atmospheric circulation fields should be described well by the GCMs, because the statistics of daily precipitation are modeled by the timing evolution of predictors (Baghanam et al., 2020). For example, the commonly used stochastic downscaling approach, e.g., weather generators, in which the day-by-day variations in the circulation conditions formulated the changes in precipitation sequences (Jeong et al., 2012). Second, the formulated statistical linkage between the predictands and predictors in the future periods need to keep consistent with that of the historical (Araya-Osses et al., 2020; Meher and Das, 2022). Otherwise, the empirical statistical downscaling model may be unavailable for inferring the relevant behavior.

Several authors have examined the potentiality of the nonhomogeneous hidden Markov model (NHMM), a good representation of the weather generator and a very powerful diagnostic tool for detecting the stochastic parameters between multiple sites precipitation and large-scale atmospheric circulation variables (Cioffi et al., 2017; Shahriar et al., 2021; Siabi et al., 2021). Bates et al. (1998) applied the NHMM tool to fit the atmospheric circulation and precipitation data over the southwest parts of Australia. The results demonstrated that the downscaled simulations reproduced the wet or dry spells of precipitation well. Frost et al. (2011) compared six downscaling approaches with an

emphasis on simulating the statistical behaviours of multiple sites daily precipitation over southeastern Australia. They found that the NHMM performed better in capturing the spatial variabilities of precipitation.

In general, the basic assumptions of the NHMM downscaling approach are as follows: 1) the daily precipitation occurrence at multiple sites depends on a finite number of unobserved weather states (hidden states) (Hughes and Guttorp, 1994); and 2) state transition probabilities depend on the former state and time dependent atmospheric variables (predictors) (Bates et al., 2010). Relevant candidate predictors for the NHMM mainly include the GP, sea level pressure, wind fields, air temperature, humidity, and their combinations (Ghamghami and Bazrafshan, 2021; Zha et al., 2022). Since the high dimensionality of original datasets, the inputs must undergo the principal component analysis first to filter the noise and to find the most dominant behaviours of the large-scale atmospheric predictors (Ghamghami et al., 2019). For instance, Panda et al. (2022) only selected the first few principle components explaining 95% variance for each predictor. Guo et al. (2022) used a combination of the first 26 principle components of four predictors to run the NHMM downscaling. Nonetheless, the selection of such predictors for NHMM is empirical and the number of atmospheric predictors with the most significant over a specific study domain must be reduced (Cioffi et al., 2020). Liu et al. (2011) have referenced two indicators, that is, the explained variances and partial correlation to select the predictors from 20 candidate variables for daily precipitation downscaling over the Tarim river basin in China. It was recommended that predictors should be highly correlated with the predictands and satisfy the maximum differentiation. Phatak et al. (2011) presented a sparse variable selection model to choose the predictors for statistical downscaling. Cioffi et al. (2016) adopted statistical criteria, i.e., normalized log-likelihood to evaluate the accuracy of different combinations of potential predictors. Research on the transferability of predictor selection was conducted by Fu et al. (2018), who concluded that the NHMM using different groups of predictors tended to produce similar simulation results during the historical period, but the results showed divergent precipitation projections for future periods. They highlighted that the optimum predictors should be physically sensible in regional precipitation processes and reliable for projections. Additionally, in NHMM a multinomial logistic function is used to model the dependence of hidden state transition matrix on the exogenous variables. Despite the reliable results of precipitation variabilities obtained by NHMM

downscaling in several applications, the biggest challenge is to capture the extreme behavior of precipitation (Chen and Zhang, 2021) and yields inaccurate simulations of mid-latitude precipitation in spring and autumn (Cioffi et al., 2020).

2.4.2 Projections of extreme precipitation

Projections are looking to infer the possible state of Earth's climate in future decades that is conditioned by anthropogenic forcing (e.g., greenhouse gases concentrations, land use and land cover changes) and natural variabilities (e.g., volcanic activities) (Ribes et al., 2021). More specifically, future climate projections can provide such changes in atmospheric variables, i.e., temperature, precipitation, and sea level pressure, extending from unconstrained development to sustainability scenarios; and perform a primary reference for the research of climate change adaptation and mitigation, as well as for the formulations of the carbon emission policies (Matthews et al., 2018). In general, GCMs are widely used to project the future change trends of precipitation and its extremes around the globe.

Firstly, the global mean climate will be wetter without limiting warming. Projections of future water vapor flux showed that overall increases in atmospheric moisture are concluded (Watterson et al., 2021) and precipitation would be intensified approximately through the water cycle. By the late 21st century, global annual precipitation is projected to increase by more than 5% under the 2℃ warming scenario (Chen et al., 2020b). With respect to the average climate, precipitation extremes are more sensitive to the warming and wetting atmospheric conditions and are expected to stand heavier (Du et al., 2022). A scaling research was conducted by Wang et al. (2017) who used 25 CMIP5 models to project the changes in extreme precipitation over land under the RCP8.5 emission scenario. Their results showed that the 95th percentile precipitation significantly increases linear with the global warming magnitude, by approximately 21.1% $℃^{-1}$. Lenderink et al. (2021) investigated the climate responses for the hourly precipitation extremes to the dew point temperature. Analysis indicated that each degree of warming would result in a 10–14% increase in the most extreme event (99.9th percentile), consistent with 1.5–2 times the Clausius-Clapeyron rate. Thackeray et al. (2022) used two generations of models to document the changes in the precipitation above the 99th percentile. They suggested that relative to the period of 1980–2014, extremes will be 55±13% more frequent in

the future (2080–2100) under the worst emission scenario. Gründemann et al. (2022) found that the rarest precipitation events are more likely to increase than the common. In addition, Espinoza et al. (2018) also projected the mean atmospheric rivers frequency and intensity would increase by ~49% and 23% globally. The stronger integrated water vapor transport by climate warming would lead to considerable increasing risks in extreme precipitation along the coastline cities (Hagos et al., 2016; Kamae et al., 2021).

The thermodynamic mechanism governed the foremost changes in precipitation trends held at a global scale; whereas the quasi-hemispheric and regional precipitation extremes are affected by more underlying dynamic factors. Both the magnitude and vertical structure changes of atmospheric circulation would alter the precipitation conditions further (Nie et al., 2018). Moreover, regional precipitation changes are more scaling with local temperatures (John et al., 2022).

For the dynamic factor, several studies have revealed that changes in extreme precipitation in the northern hemisphere are associated with the Arctic amplification effects (Nakamura and Sato, 2022). Arctic warming may reduce the poleward pressure gradient, which can enhance the probabilities of slow-moving weather systems for extreme, and shift jet streams (i.e., Rossby wave) in the upper level (Coumou et al., 2018; Francis and Vavrus, 2012). Related projection results show that the 95th percentile precipitation by 2100 in the northern hemisphere would increase by 8.7% under the worst emission scenario, due to the intensified large-scale wave amplitudes (Liu et al., 2021a). Nonetheless, the theory still remains in scientific debate (Blackport and Screen, 2020; Vavrus, 2018).

In addition, simulations demonstrated that enhanced low-level atmospheric instabilities and deep convection boosted by the increase in Madden-Julian Oscillation (a leading intraseasonal mode of atmosphere in the tropic), especially in phases 2 and 5 would cause more extreme precipitation over tropical Asia and Australia in the future (Liang et al., 2022). While more stable atmospheric conditions are projected over the Mediterranean, due to the shifts of the subtropical high system and stronger anticyclones. This tendency will tend to be less precipitation in most parts of this region (Barcikowska et al., 2018).

In the mid-latitudes, studies demonstrated that a proportion of ~75% of extreme precipitation events during 1979–2011 were associated with fronts, especially the warm fronts (Catto and Pfahl, 2013). Dynamically, the increased temperature gradient and lifted airflow when across fronts could produce precipitation (Catto et al., 2015). Projections from multimodel showed that the frequency of fronts is likely to decrease, because of the weakened meridional temperature gradients under the worst-case scenario (Catto et al., 2014). Future responses of decreased extreme precipitation associated with fronts are found in Dagon et al. (2022)'s research.

Kitoh et al. (2013) examined the global and regional monsoonal extreme precipitation changes over the monsoon area. Results showed that end later and longer duration monsoon could be projected. The enhancement of monsoon precipitation is primarily of the anomalous water vapor flux convergence in the lower troposphere. Furthermore, these results are consistently confirmed in China. An enhanced land-sea pressure gradient is projected between the East Asia continent and the surrounding oceans and causes stronger northeasterly winds. Subsequently, this intensification of the East Asian summer monsoon would lead to more extreme precipitation events over east China by the end of the 21st century (Chen, 2013).

For the impacts of cyclones, Hawcroft et al. (2018) analyzed the future behaviours of extreme precipitation over Europe and North America tainted by extratropical cyclones. They found that less frequency but more intensely precipitating extratropical cyclones would generate more than a quadruple increase in total extreme precipitation amount. Similar change characteristics are also projected in tropical cyclones, see Bacmeister et al. (2018)'s research, the storm precipitation of tropical cyclones is becoming more common.

Brief summary here, increases in regional extreme precipitation could be attributed to the dynamic forcing, such as the large-scale atmospheric circulation activities (Barton et al., 2016; Marquardt Collow et al., 2016), as well as to the thermodynamic effects of a warming climate (Wentz Frank et al., 2007) and combined influences. When facing ongoing climate warms, it is necessary to allow improvements to be made for understanding regional extreme precipitation changes. Accordingly, it is crucial to establish strategies to significantly reduce such uncertainties in future projection,

especially for extreme precipitation.

3. Literature comments

3.1 Issue 1: study on the links between the large-scale atmospheric circulation and extreme precipitation over central-eastern China

Central-eastern China (CEC) is one of the most populated zones in East Asia, highly developed cities such as Shanghai, Nanjing, Hangzhou, and others cities have a high risk of extreme precipitation and related disasters (Gu et al., 2022). Its geographic location, on the east side of Eurasia facing the Pacific Ocean, precipitation over CEC is strongly affected by the thermodynamic and dynamic forcing of the land-sea contrast. Typically, the Western Pacific Subtropical High (WPSH), blocking high, quasi-stationary front, and cyclones are the important large-scale circulation systems associated with extreme precipitation. Previous studies have proved that most of the persistent extreme precipitation events over CEC were related to two typical circulation configurations, i.e., the double- and single-blocking high types (Chen and Zhai, 2014). Moreover, when abnormal circulation combined with stable water vapor transport could cause devastating precipitation events. For example, a record-breaking extreme rainstorm hit the Yangtze river valley in 2020 with a total accumulated rainfall of more than 600 mm (Wang et al., 2021). In that case, the extreme event was conditioned by the strengthened westerly jet and strong water vapor transport from the adjacent seas. Dynamically, the anomalous east Asia summer monsoon provided a favorable background for moisture convergence (Li et al., 2021). In July 2021, the “once in a thousand years” extreme precipitation event occurred in Henan province, China (Huang et al., 2022). The large-scale atmospheric circulation, including the WPSH and tropical cyclone, strongly affected the precipitation system. Therefore, the roust identification of large-scale atmospheric circulation configurations driving possible increased extreme precipitation is fundamental to forecasting such events in order to reduce the hydraulic risk.

In addition, because the seasonal north-south movement of WPSH, there are non-negligible time lags or synchronization in the occurrences of extreme precipitation between rain gauges within CEC. Regions with similar climatic and surface conditions where extreme precipitation is more homogeneous or synchronized (Zhou et al., 2023). For instance, an evident rainstorm corridor

accompanied by excessive precipitation often occurred due to the dynamic forcing, that is, the Meiyu-front (Guan et al., 2020). Extreme precipitation in this narrow belt showed strong concurrent. Besides, previous studies showed that the peak time of extreme precipitation in the north CEC is significantly later than that in the south (Li et al., 2013). However, the current understanding of identifying the large-scale atmospheric circulation is insufficient, due to little work of objective weather classification that has been conducted to depict the spatio-temporal differences of extreme precipitation over CEC. More importantly, earlier studies revealed that change points can be detected in extreme precipitation over CEC (Deng et al., 2018). To date, knowledge of the question "was it related to the circulation pattern changes?" remains weak.

3.2 Issue 2: performances of the regional extreme precipitation prediction models

As presented in Section 2.3, Chapter 1, we have seen many works utilizing large-scale atmospheric circulation fields to predict regional extreme precipitation events. A few pros and cons of different approaches should be noted.

(1) Despite the promising results derived from the regression, conditional, and analog analysis models, the predictions of extreme precipitation still have significant errors. The evident insufficiency is that event-based statistical models struggle to capture the nonhomogeneity of extreme precipitation (Elison Timm et al., 2013).

(2) It should be noticed that due to the rarity of extreme precipitation in number, the deep learning algorithm is susceptible to being hampered by the imbalanced samples and getting a false alarm or miss (Kellenberger et al., 2018).

Instead of applying the oversampling and adjusting weights (Fernando and Tsokos, 2021), the hybrid model approach has been designed to result in better accuracy by combining multiple hierarchical layers. Generally speaking, the hybrid modeling approach aims to concatenate two or more models together to obtain more accurate predictions (Ahmed et al., 2022; Jena et al., 2021; Lin et al., 2021). In Reichstein et al. (2019)'s review paper published in *Nature* journal, they addressed that hybrid models will be an opportunity for the development of machine and deep learning in earth system

science. More importantly, this combination model often performs better than the individual in dealing with hydrological or other related problems. For instance, Li et al. (2022) compared three machine learning models in forecasting the 3-hour precipitation levels over an inland city in China. However, they found that these separate models were hard to ideal for all precipitation levels, due to the class of sample being severely imbalanced. Subsequently, they combined the CNN and long short-term memory (LSTM) models and obtained an improved accuracy of 77%. Khan and Maity (2020) presented a hybrid model to predict daily precipitation over the central India. The obtained results showed that the hybrid model consisting of CNN and multilayer perceptron (MLP) performed better than the individual CNN and MLP, especially for extreme precipitation. Dong et al. (2021) discussed the combination of recurrent neural network and a fully convolutional network for flood predictions in Harris County. Sha et al. (2022) incorporated the analog ensemble, minimum divergence Schaake shuffle, and CNN models for the forecasting of 3-hourly precipitation using the post processed total precipitation.

Overall, using the predictability of large-scale atmospheric circulation in regional extreme precipitation to produce the precursory signal will benefit numerical weather forecasting and related research. However, few studies have focused on this useful information which directly infers the extreme precipitation over CEC. Their potential practicality has not been specifically focused on so far. Although deep learning is an effective tool in the community of extreme weather research, how to use reliable and scientific models to predict extreme precipitation dominated by large-scale atmospheric circulation should be provided with a more detailed investigation.

3.3 Issue 3: the reliability of GCMs and future projections of extreme precipitation

It has been recognized in Sections 2.1 and 2.4 (Chapter 1), changes in regional extreme precipitation are very complicated due to the influences of thermodynamic and dynamic factors. Such GCMs with coarse spatial resolution underestimated extreme precipitation seriously and makes it impossible to yield reliable projections of extremes at regional scale. The NHMM avoids this problem by simulating the stochastic parameters between multiple sites precipitation and large-scale atmospheric circulation variables to accomplish precipitation downscaling. However, the limitations of NHMM precipitation downscaling should be adequately considered, not only in the statistical of precipitation variabilities

but also in extreme precipitation simulations, in order for this approach to be more robust for projections.

Additionally, a contribution analysis showed that circulation changes facilitated a dipole pattern of "wetter in the south but dry in the north" over eastern China over the past 53 years (Zhou et al., 2021a). However, disaster statistics showed that the extreme precipitation events in recent years (e.g., "once in a thousand years" extreme precipitation event occurred in Henan province, China) did not occur in the traditionally rainy south China, but in the north, where the climate is considered dry and rainless. Both large-scale atmospheric circulation and water vapor anomalies were indispensable factors leading to these events. There is no general understanding of the role of large-scale atmospheric circulation in changing extreme precipitation in the future. More reliable scenario data are needed to explore these critical but poorly knowledgeable questions.

4. Objectives and structure of the thesis

4.1 Key scientific questions and research objectives

From the perspective of the above literatures reviewed, the thesis dedicated to answer the following three scientific questions: (1) Which circulation patterns were prone to the extreme precipitation in the last decades over CEC? (2) Can large-scale atmospheric circulation anomaly information be used for regional extreme precipitation predictions over CEC? And the associated accuracy. (3) How will the future extreme precipitation over CEC be affected by thermodynamic and dynamic factors, that is, large-scale atmospheric circulation and global warming?

Figure 1-1 shows the technology map of this thesis. Several statistical techniques, objective weather classification, and hybrid deep learning models were used to characterize the main circulation patterns affecting extreme precipitation and their roles in predicting such events. A new precipitation downscaling framework was proposed to improve the reliability of GCMs in precipitation simulations and future projections.

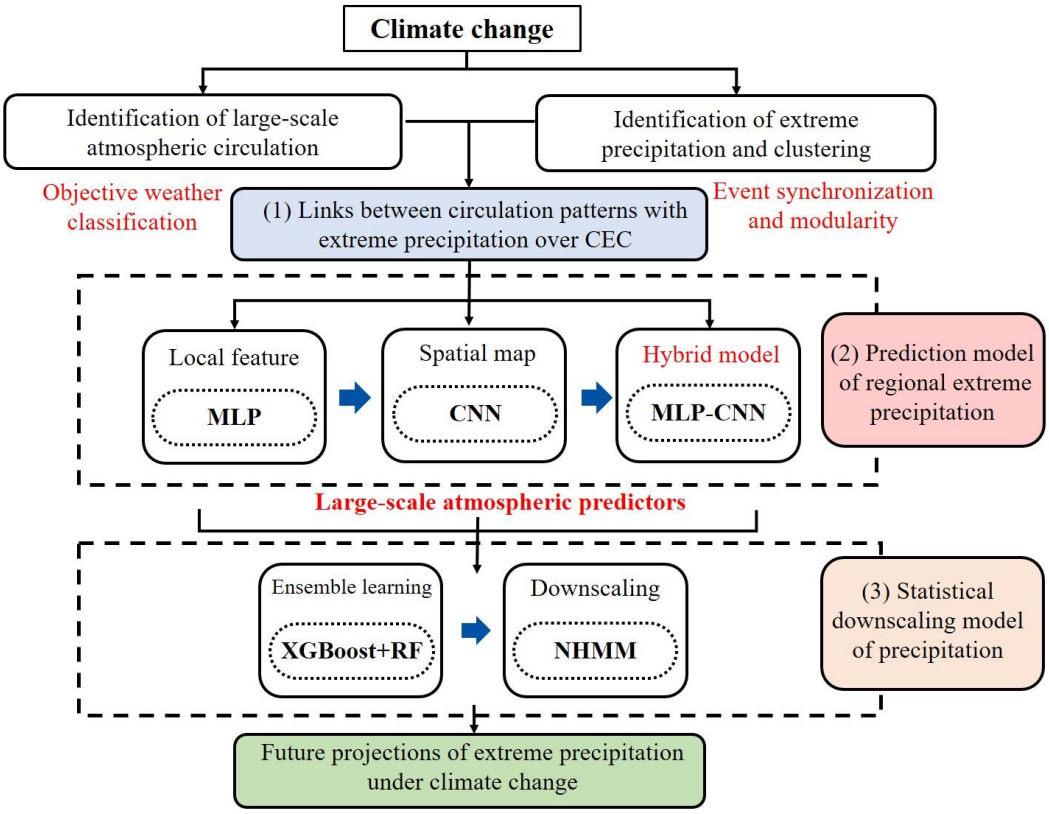

Figure 1-1. Technology map of this study.

The detailed contents of this thesis are listed. First of all, the mid-level geopotential height data was taken to represent the atmospheric circulation features. Indeed, anomalous fields of geopotential height at 500 hPa can provide important indications of some weather systems, like blocking high, troughs and ridges at high altitudes, WPSH, etc., which are closely related to extreme precipitation over China (Chen et al., 2019; Yuan et al., 2020). Besides, atmospheric moisture transport is a predominant factor indispensable for sustaining the development and evolution of extreme precipitation (Feng and Zhou, 2012; Liu et al., 2020a). At current, different approaches have been designed to identify the atmospheric water vapor and its trajectory path information. For example, the data-driven atmospheric dispersion modeling systems (for example, HYSPLIT, Stein et al. (2015); FLEXPART, Pisso et al. (2019)) by recognizing moist air parcel trajectories based on Lagrangian models. Additionally, another alternative way is to adopt quantitative indicators, like vertically integrated water vapor transport (IVT, Ralph et al. (2019)) or vertically integrated water vapor content (IWV, McClenny et al. (2020)) to retrieve the atmospheric rivers. Prince et al. (2021) found that extreme IVTs were associated with hazardous atmospheric river events and more conducive to extreme precipitation. Eiras-Barca et al. (2021) also confirmed that intense IVTs were expected with higher amounts of precipitation. Overall, the quantitative estimates based on IVT provide an effective

indicator to characterize the potential atmospheric river-induced precipitation events. In this study, IVT composites were considered to quantify the water vapor transport and to understand its potential links with extreme precipitation. One of the objective classification methods, the SOM, was used to identify the dominant large-scale circulation patterns in the range of 10°S–70°N and 40°E–170°W, where the weather systems affecting CEC are spatially covered. The links between the circulation patterns and extreme precipitation were quantified by event synchronization.

After exploring their relationships, how to predict extreme precipitation via the anomaly signals of large-scale atmospheric circulation is a challenging issue. To answer the second scientific question, a hybrid deep learning model that combined the multilayer perceptron and convolutional neural networks was proposed. This model was trained to learn the local and spatial features from the large-scale atmospheric conditions associated with extreme precipitation and to give binary predictions.

At last, since precipitation especially extreme precipitation, is poorly simulated by the coarse spatial resolution GCMs, the resulting future precipitation projections may be insufficient in depicting the regional change trends over CEC. To obtain the precipitation characteristics for each single rain gauge and improve the reliability of future projections, we developed a new statistical downscaling framework based on the NHMM. The GP at 500 hPa and IVT we still selected as the predictors to accomplish precipitation downscaling of GCMs. Subsequently, this downscaling model was applied to future scenario data to project the possible changes over CEC under low-, medium-, and high-emission scenarios.

Overall, the main objectives of this paper are fourfold, summarized as follows. (1) Identify the key large-scale atmospheric circulation patterns prone to extreme precipitation events over CEC. (2) Propose a hybrid deep learning model to accurately predict the occurrence of extreme precipitation over CEC using large-scale atmospheric predictors. (3) Evaluate the accuracy of GCMs from CMIP6 in simulating extreme precipitation and large-scale circulation patterns. (4) Develop a new precipitation downscaling framework that stacked ensemble learning and NHMM to improve the accuracy of downscaled precipitation from GCMs and project the future precipitation and extremes over CEC under different warming scenarios.

4.2 Structure of thesis

Figure 1-2 shows the structure of this thesis, which briefly introduces the research topics of each chapter. In Chapter 2, I will present the SOM and event synchronization to allow the identification of large-scale circulation patterns associated with the extreme precipitation. The detailed methodology about the combination of multilayer perceptron and convolutional neural network, as well as its capability in predicting extreme precipitation, are presented in Chapter 3. Considering the performance of GCMs on depicting the circulation variabilities could affect the resulting downscaled precipitation, I prefer to select a model to conduct the downscaling not the multimodel average. Chapter 4 describes how I choose the GCMs model, which includes the content of evaluation works for extreme precipitation simulations and related circulation characteristics. In Chapter 5, I will describe the work of precipitation downscaling based on the large-scale atmospheric circulation during the historical period and attempt to explain the thermodynamic and dynamic factors underlying projected precipitation changes. Finally, the conclusions are summarized in Chapter 6.

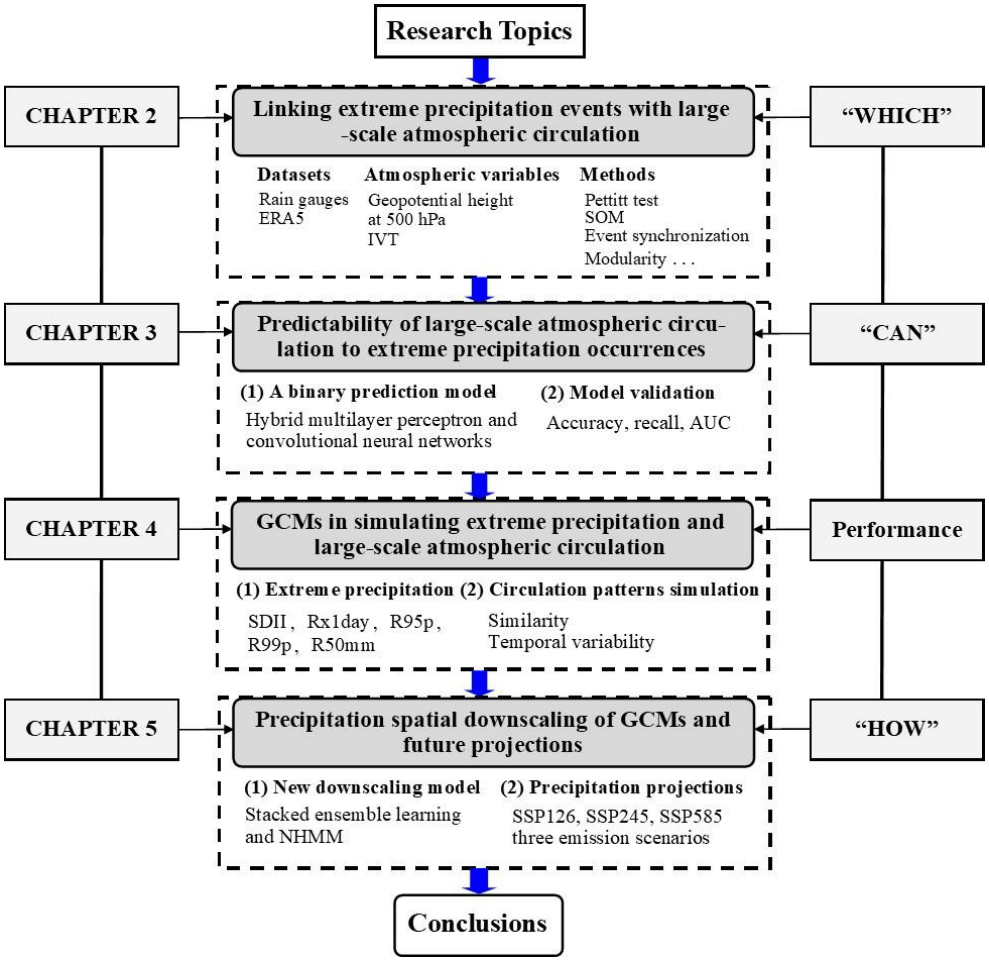

Figure 1-2. Structure of this study.

CHAPTER-2. Linking extreme precipitation events with large-scale atmospheric circulation over central-eastern China

Summary

To an extent, large-scale circulation situations and moisture transport are responsible for extreme precipitation occurrence. The aim of this chapter is to investigate the possible modifications of circulation patterns (CPs) in driving extreme precipitation over Central-Eastern China (CEC). The self-organizing map (SOM) and event synchronization methods were used to link the extreme precipitation events with CPs. Results show that 23% of rain gauges have a significant change point (at the 90% confidence level) in annual extreme precipitation from 1960 to 2015. Based on the identified change points, we classified the data into two periods, i.e., 1960 to 1989 and 1990 to 2015. Overall, CPs characterized by obvious positive anomalies of 500 hPa geopotential height over the Eastern Eurasia continent and negative values over the surrounding oceans are highly synchronized with extreme precipitation events. During 1990–2015, the predominant CPs are more related to the extreme precipitation with enhanced event synchronization. We found that the CP changes produce an increase in extreme precipitation frequency from 1960–1989 to 1990–2015.

1. Study area

Our study area is the central-eastern China (CEC) (25°N–35°N, 106°E–123°E, see Figure 2-1), where highly developed cities such as Shanghai, Nanjing, Hangzhou. Figure 2-1 shows the topography of CEC (obtained from the NASA's Shuttle Radar Topography Mission), which consists of mountains in the west, hills in the southeastern region, and low plains in the north. Generally, the CEC is characterized by subtropical monsoon climate. Precipitation over CEC is greatly influenced by the synoptic-scale circulation systems, e.g., Meiyu-front and typhoon cyclone. During mid-June and mid-July, a quasi-stationary front (or called Meiyu-front) is formed over the mid-lower reaches of the

Yangtze River, which usually relates to the poleward moisture transport from the ocean derived by Western Pacific Subtropical High (WPSH) and low-level south-westerly jet (Ding et al., 2020). The Meiyu rain band in the lower troposphere is usually observed on the northern boundary of the front and feeds the precipitation system development and maintenance. Furthermore, rainstorm corridors accompanied by excessive precipitation often occurred due to the Meiyu-front (Guan et al., 2020). Another important aspect is the tropical cyclone activities. It was proved that the tropical cyclone circulation system, including frontal clouds and outward spiraling rain band, could favor intensified precipitation over CEC (Tang et al., 2021).

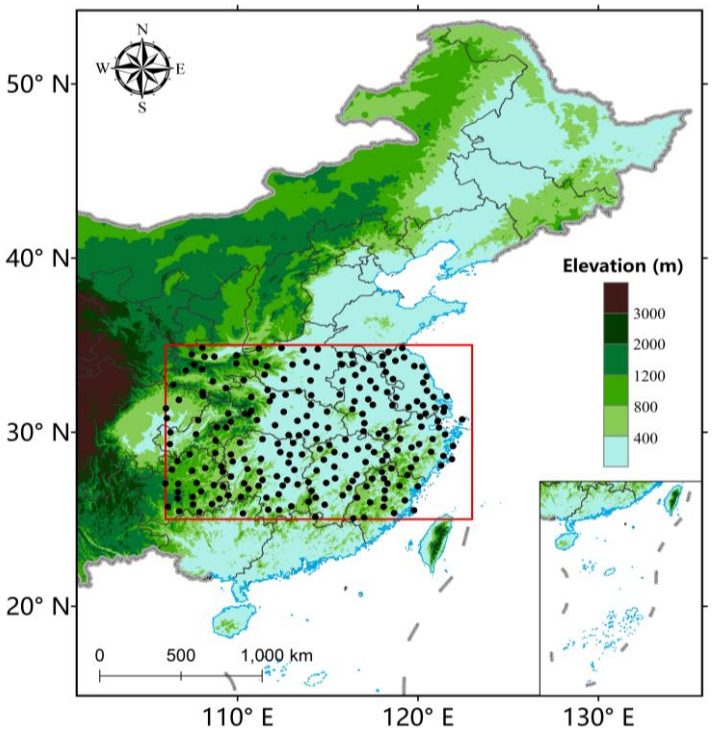

Figure 2-1. Location of study region. Rain gauges are marked with black circles.

The aims of this chapter is to answer the first question "Which circulation patterns were prone to the extreme precipitation in the last decades over CEC?". Additionally, the above analysis in Section 3, Chapter 1awakens us to some new questions: 1) was there a step-change in extreme precipitation frequency in the last decades over CEC; 2) was it related to the circulation pattern (CP) changes? 3) and what are the possible causes. To answer those, in this chapter, we examined the change points in extreme precipitation over CEC from 1960 to 2015, and used the self-organizing map (SOM) and some statistical methods to investigate the links between large-scale atmospheric CPs with changing extreme precipitation. Specifically, vertically integrated water vapor transport (IVT) composites are

considered to quantify the water vapor transport, the links between CPs (identified by SOM) and heavy precipitation (daily precipitation amount exceeding the 95th percentile) are explored by event synchronization following the approach suggested by Conticello et al. (2020); Conticello et al. (2018). They found that this approach was effective in identifying the causality between CPs and extreme events occurrence.

2. Datasets

Several datasets were used in this study: 1) The daily rain records over CEC were downloaded from the China Meteorological Data Service Centre (http://data.cma.cn/). Available period is January 1960 until December 2015. Figure 2-1 shows the detailed distribution; 2) the fifth generation atmospheric reanalysis product ERA5, which developed by the European Centre for Medium-Range Weather Forecasts. The used reanalysis variables included geopotential height (z, m) at 500 hPa, eastward (u, m s^{-1})/northward (v, m s^{-1}) components of the wind, specific humidity (q, kg kg^{-1}) from 1000 to 300 hPa with a spatial resolution of 0.25° × 0.25°. Here, for identifying the moisture transport magnitude, we calculated the IVT values (kg m^{-1} s^{-1}) for each 0.25° grid in the range of 10°S–70°N and 40°E–170°W, referenced to Lavers et al. (2012)'s method.

$$\mathrm{IVT} = \sqrt{(\frac{1}{g}\int_{1000}^{300} qu\mathrm{d}p)^2 + (\frac{1}{g}\int_{1000}^{300} qv\mathrm{d}p)^2} \quad (2\text{-}1)$$

where g and $\mathrm{d}p$ are the acceleration of gravity (9.8 m s^{-2}) and the difference between two adjacent pressure levels.

3. Methods

Our work was inspired by the recent research proposed by Conticello et al. (2020) and followed the methods they used for CPs identification. The involved methodology was consisted of five main parts: 1) used the Pettitt test to examine the potential change points in the time series of extreme precipitation from 1960 to 2015 and classified the data into two sub-periods; 2) For each gauge, after obtained the binary sequence of extreme precipitation events (1 represents extremes occurred and 0 otherwise), event synchronization was chosen to describe the simultaneities of extreme precipitation occurrence; and 3) as the input for the modularity algorithm to divide these rain gauges into some spatially and temporally coherent clusters; 4) SOM was used to identify a finite number of CPs

defined on the standardized geopotential height at 500 hPa pressure level in different periods. The daily geopotential height field belongs to which CP was determined by the *k*-nearest neighbor method. Then, event synchronization applied again to identify the synchronized CPs related to the extreme precipitation events for each cluster; 5) adopted the local logistics regression to model the nonlinearity relation between extreme precipitation occurrence and IVT intensity; 6) and used the quantitative partitioning technique to investigate the percentage of extreme precipitation frequency changes attributed to CPs variations.

3.1 Pettitt test

In this paper, extreme precipitation was defined as the daily precipitation occurred in the top 5% heaviest precipitation events of wet days (≥ 0.1 mm/day) during 1960 to 2015. For each gauge, the total number of extreme precipitation events and their accumulated rainfall amounts within the 5% range per year can be obtained. Supposed that the step changes occurred in annual extreme precipitation frequency and amount over the interested area, the non-parametric approach Pettitt test aims to discover the shifts in the central tendency across the time series (Pettitt, 1979). Moreover, Pettitt test has the advantage of examining the sensitivity when considering varied record length (Ryberg et al., 2020).

Let $X_1, \dots, X_t$ and $X_{t+1}, \dots, X_T$ are two samples in a same population, T is the total sample size. The nonparametric statistic K_T can be defined as:

$$K_T = \max\left|U_{t,T}\right|, 1 \le t < T \tag{2-2}$$

with

$$U_{t,T} = \sum_{i=1}^{t}\sum_{j=i+1}^{T} sgn(X_i - X_j) \tag{2-3}$$

$$sgn(X_i - X_j) = \begin{cases} 1 & if \;\; X_i > X_j \\ 0 & if \;\; X_i = X_j \\ -1 & if \;\; X_i < X_j \end{cases} \tag{2-4}$$

where $U_{t,T}$ indicates the Pettitt test index, which is a version of Mann-Whitney two-sample test. The change point of the time series was occurred at the location of K_T that stands the highest value. Given a significance level of α, if the p-value is less than the α means changes are statistically significant.

Additionally, in order to make the resulting change points more robust, the series of annual extreme precipitation frequency and amount per gauge were undergone the 3-yr lowpass filter first to remove the noises. Figure 2-2 shows the gauges with a statistically significant (at 90% significance level) changing point for annual extreme precipitation frequency and amount. These rain gauges accounting for 23.26% and 20.61% of total samples. Moreover, the average of the Pettitt test index corresponding to the significant change points are 29.06 and 29.21 (counting since 1960). Therefore, we classified the data into two periods, 1960 to 1989 and 1990 to 2015 (before and after the location of the mean change point) to visualize the CPs respectively.

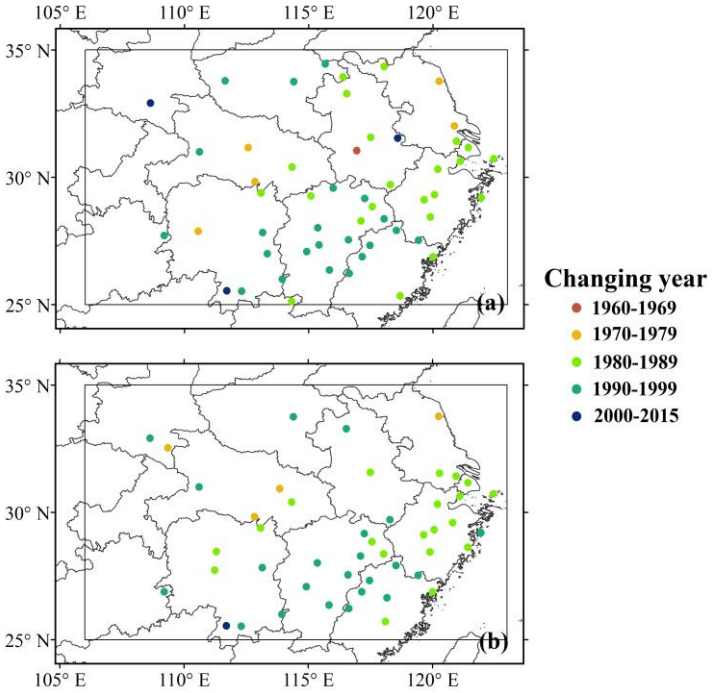

Figure 2-2. Gauges with a statistically significant change point for (**a**) annual extreme precipitation frequency and (**b**) amount from 1960 to 2015.

3.2 Self-organizing map

We used the SOM toolbox encapsulated in MeteoLab of MATLAB 2021a to cluster the daily geopotential height at 500 hPa into a certain number of CPs over the spatial domain of 10°S–70°N and 40°E–170°W. The identified CPs are called nodes in SOM, which best capture the feature information in observed datasets.

Detailed interpretations of SOM has been presented in previous research (Kiang, 2001; Kohonen, 1998). In short, we only described the basic steps here: 1) Input data preprocessed: before SOM model

training, the daily geopotential height at 500 hPa were converted to dimensionless value through the z-score standardization method to eliminate the influence of outliers; 2) Training processes: randomly assigned the number and initial weights for nodes. The Euclidean distances between each training sample and the weight vector of nodes were computed to find the best-matching unit, whose weight vector is the closest to the input. The weights of best-matching unit and its neighboring neurons within the neighborhood kernel were adjusted iteratively according to the learning rate, in order to let the best-matching unit move closer to the input vector; 3) The output of SOM were evaluated upon two indicators, quantization error (QE) and topographic error (TE) to determine the optimal size of nodes. QE indicates the average distance between each data point and the node, and TE is the ratio of the data points that the best-matching unit un-adjacent with the secondary. Optimal nodes size depends on the trade-off between low QE and low TE; 4) At last, the classification of daily standardized geopotential height fields during two periods was determined by the *k*-nearest neighbor method (Rajagopalan and Lall, 1999) and produced the binary time sequences per SOM node. For an identified node, 1 represents its occurrence; otherwise 0. We tested the QE and TE of different node sizes (from 2×2 to 9×9, see Figure 2-3). The 5×5 node sizes are more reasonable with relatively lower errors.

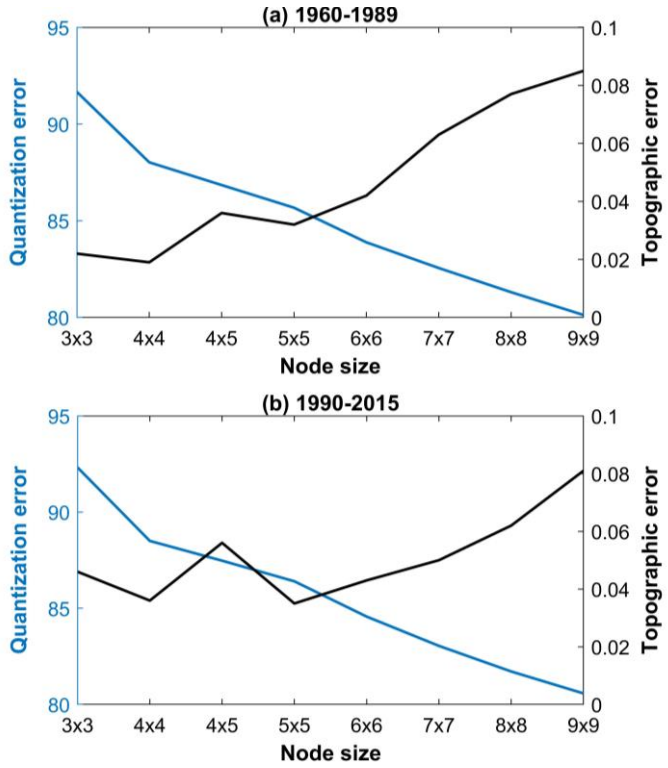

Figure 2-3. Quantization error and topographic error of different node sizes during (**a**) 1960–1989 and (**b**) 1990–2015.

3.3 Event synchronization

The event synchronization method proposed by Quiroga et al. (2002) and modified by Conticello et al. (2018) to measure the synchronization degree and time delay between two binary series. In this study, we used it to quantify the simultaneities of extreme precipitation events among the rain gauges.

Assuming that x_n and y_n, $n = 1, \dots, N$ are two binary sequences of extreme precipitation occurrence, t_i^x and t_i^y $(i = 1, \dots, m_x;\ j = 1, \dots, m_y)$ represent the time index of recorded extreme events; m_x and m_y denote the total number of recorded extreme events for the two sequences. Preset the time window τ between two sequences, we had the number of event happens in x shortly after it happens in y, that is, $F^\tau(x|y)$.

$$F^\tau(x|y) = \sum_{i=1}^{m_x} W_i \tag{2-5}$$

with

$$W_{ij}^\tau = \begin{cases} 1 & if \quad \exists\ \min(\left|t_i^x - t_i^y\right| \le \tau) \\ 0 & else \end{cases} \tag{2-6}$$

Similarly, $F^\tau(y|x)$ can be proved. Then, the synchronization of the extreme events is calculated as follows:

$$S_{x,y}^\tau = \frac{F^\tau(x|y) + F^\tau(y|x)}{m_x + m_y} \tag{2-7}$$

Summarizing, $0 \le S_{x,y}^\tau \le 1$. If $S_{x,y}^\tau = 1$, the extreme precipitation events are fully synchronized. Furthermore, the event synchronization method was also used to examine the simultaneous degree between extreme precipitation recorded by rain gauges and the binary sequences per CP. In our study, the time window τ was set to 3 days to quantify the robustness links between two binary sequences.

3.4 Rain gauges clustering by modularity

In characterizing the structural consistency of extreme precipitation events recorded by rain gauges, a community detection approach was applied. The modularity (Newman, 2004, 2006) is defined as follows:

$$\mathrm{Q} = \frac{1}{2q} \sum_{i,j} \left[A_{ij} - \frac{k_i k_j}{2q} \right] \delta(c_i, c_j) \tag{2-8}$$

where Q indicates the modularity, $-0.5 \le Q < 1$. k_i and k_j are the number of edges for nodes i and j, and $2q$ is the total edges of all nodes. A_{ij} represents the adjacency matrix, ranging between

1 or 0. When nodes i and j belongs to a same group, $\delta(c_i, c_j)$ having a value of 1, otherwise 0.

3.5 Local logistics regression

Local logistics regression, was used to fit the occurrence probability of extreme precipitation events conditioned by IVT values for a given circulation pattern. Assuming that H is a binary response series, a positive indicates at least one rain gauge has recorded the extreme precipitation in a cluster, otherwise is 0. I indicates the IVT predictor (i.e., independent variable) that averaged by the 0.25° grids closet to the rain gauge. We selected the generalized linear model with a logit link function and Bernoulli distribution for fitting the conditional probability of binary responses (Conticello et al., 2020; Loader, 2006). The logistics regression model is formulated as follows:

$$H_t = \text{Logit}(p_t) = \epsilon_t + \beta(I_t) = \ln(\frac{p_t}{1-p_t}) = \gamma_t \quad (2\text{-}9)$$

$$P(H_t = 1|I_t) = p_t \quad (2\text{-}10)$$

$$P(H_t = 0|I_t) = 1 - p_t \quad (2\text{-}11)$$

where p_t is the probability that $H = 1$ at time t. ϵ_t and β are the error term and unknown function, respectively. $\ln(\frac{p_t}{1-p_t})$ indicates the logistic link function that can be converted to $\frac{e^{\gamma t}}{1+e^{\gamma t}} = p_t$. Defining the bandwidth and moving window, we used the local logistic likelihood to estimate $\beta(I)$ in Eq. 1-10. In this study, Bisquare kernel function was used to estimate the local bands. The local logistics regression constructed in Rstudio with the R version of 4.1.3, using the locfit() library.

3.6 Quantitative partitioning technique

Some previous studies suggested that the changes in extreme precipitation frequency between two different periods could be separated into three components by quantitative partitioning technique (Cassano et al., 2007). Assuming that EP_{all1} is the total frequency of extreme precipitation event in the first period.

$$EP_{all1} = Y_1 * \sum_{i=1}^{C} P_i mf_i \quad (2\text{-}12)$$

where Y_1 is the total number of years for initial period, P_i is the annual mean number of CP i occurrences, and mf_i is the annual mean number of extreme precipitation events recorded by this CP. C is the total number of node size. Then, the total extreme events in the second period (EP_{all2})

can be calculated as follows:

$$EP_{all2} = Y_2 * \sum_{i=1}^{C}(P_i mf_i + \Delta P_i mf_i + P_i \Delta mf_i + \Delta P_i \Delta mf_i) \quad (2\text{-}13)$$

where Y_2 is the total number of years for second period, $\Delta P_i mf_i$ is the component that extreme precipitation frequency changes attributed to CP i number variation from the initial to the second period. $P_i \Delta mf_i$ and $\Delta P_i \Delta mf_i$ represent the changes attributed to the variations in the average number of extreme precipitation events for a CP and the combined, respectively. Then, for the observed change in mean extreme precipitation frequency for CP i ($\Delta P_i mf_i + P_i \Delta mf_i + \Delta P_i \Delta mf_i$), we can calculate the percentage that the three components account for.

4. Results

4.1 Identified circulation patterns by SOM

Figure 2-4 shows the identified CPs by SOM in the two periods, which are arrayed in five columns (labeled A to E and A′ to E′, respectively) and five rows (labeled 1 to 5). The shadow indicates the anomalous fields of standardized geopotential height at 500 hPa, and projected circulation configurations for each CP are plotted in black contours. It is found that these CPs are governed by four distinct nodes (e.g., A1, A5, E1, and E5 in the period of 1960–1989) and some transition types, and their morphological information demonstrates similarity occurs in the adjacent nodes. For the period of 1960–1989, CPs on the diagonals of the top-left and bottom-right have an obvious north-south opposing situation, bounded by 20°N. CPs A4–A5 and B4–B5 are dominated by the positive anomalies over the Eastern Eurasia continent and negative anomalies over the surrounding oceans (e.g. the South China Sea, Bay of Bengal, and the Arabian Sea); CPs D1–D2 and E1–E2 are the opposite. CPs A1 and B1 are controlled by a stable positive anomaly; while negative anomalies can be seen for D5 and E5. Also, the identified CPs in the period of 1990–2015 show similar consistent node characteristics. In terms of the circulation situation, we can find the WPSH's location (the contour of 5880 gpm at 500 hPa was used to indicate its extent) and its seasonal movement. For CPs C3 to E5 (C′3 to E′5), the WPSH are very weak and an obviously cold low-pressure system distributes over the Eastern Siberia. For CPs E2 to C1 (E′2 to C′1), the increase in 500 hPa geopotential height over the south Pacific, the South China Sea, and India ocean has enhanced the north-south barometric

gradient and promoted the enhancement and northward of WPSH. In addition, the strong WPSH and the blocking high over the Lake Baikal region are mainly circulation systems for A1 and B1 (A′1 and B′1). For CPs A2 to B5, the WPSH moves southward and its intensity becomes weak.

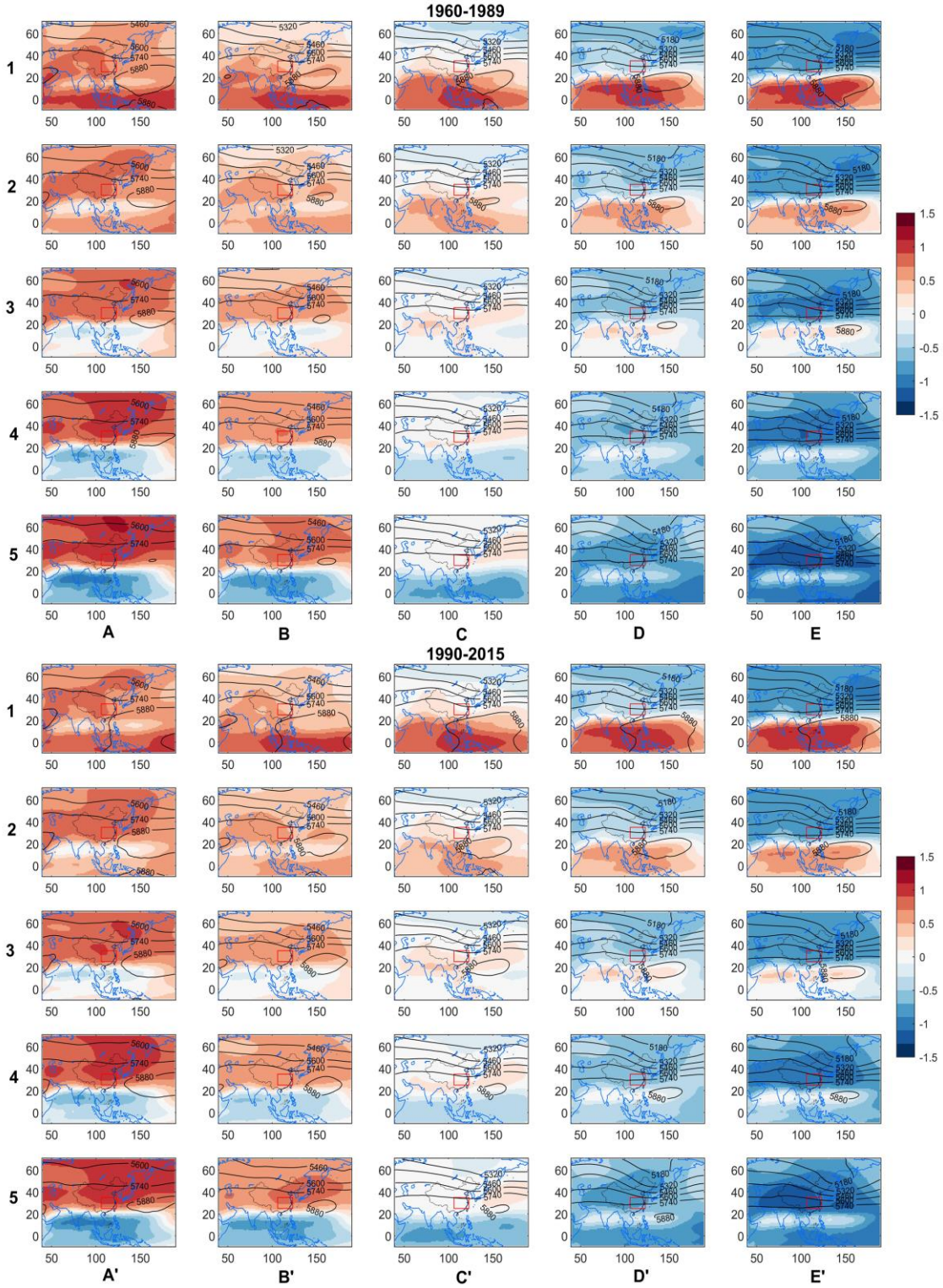

Figure 2-4. The identified circulation patterns of standardized geopotential height at 500 hPa during 1960 to 1989 and 1990 to 2015 periods. Shadow indicates anomalous fields of standardized geopotential height at 500 hPa, black contour is the geopotential height composite (unit: gpm).

Matrix Euclidean distance and correlation coefficient were adopted to investigate the similarities of identified CPs between the two periods, as shown in Figure 2-5. When compared to the period of 1960–1989, the CPs in 1990–2015 standing at the diagonal have the minimum Euclidean distance and high correlation. This reflects that the category of identified CPs in the latter period generally remains almost unchanged.

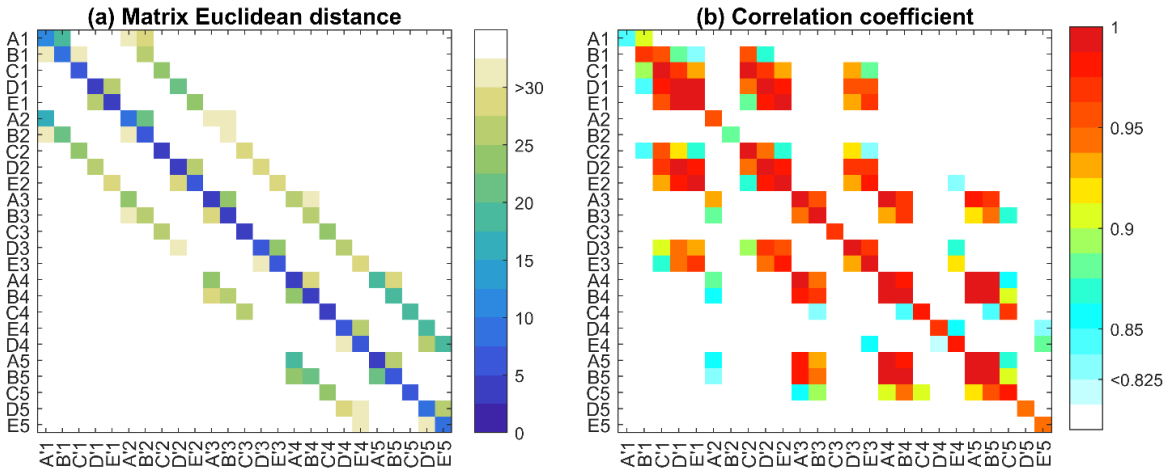

Figure 2-5. Matrix Euclidean distance and correlation coefficient of the circulation patterns between two periods.

Figure 2-6 shows the composites of daily precipitation anomalies related to per CP. For each rain gauge, this anomaly was achieved by the deviation from their average daily precipitation from 1960 to 2015. Positive value indicates more precipitation than the average, while negative is the opposite. Meanwhile, the time distribution of identified CPs during the two periods is displayed in Figure 2-7. It can be found that the changes in precipitation anomalies are associated with the evolution of circulation situations, which driven by the north-south propagation of the WPSH. From January to March, the frequent CPs belong to E5 to E1 (E′5 to E′1) for the period of 1960–1989 (1990–2015) (Figure 2-7), the WPSH intensity of these CPs are generally weak (Figure 2-4) and precipitation composites over CEC are dominated by negative anomalies compared to the climatology (Figure 2-6). From April to May, the occurrence proportion of CPs C1 and B1 (C′1 and B′1) are the highest, we can find that the intensity of WPSH has strengthened and its ridge line locates at 18°N. At the same time, precipitation over the south CEC also tends to increase. For A1 to A5 (A′1 to A′5), due to the northward expansion of the WPSH, the rain belt moves from the south to the north CEC from June to August. After that, the WPSH begins to move southward with weakened intensity, and the anomalously high precipitation belt over CEC also disappeared during October and December.

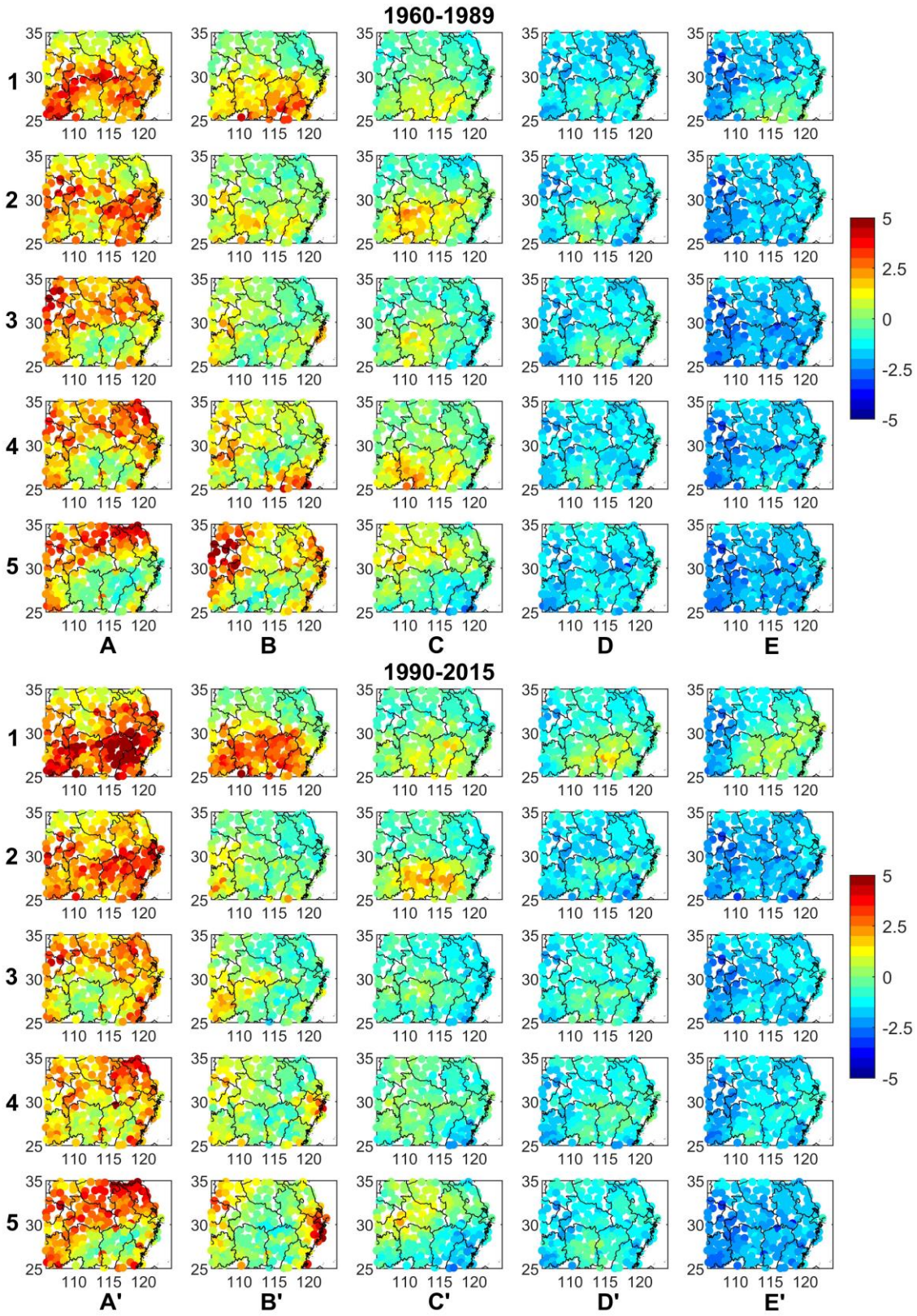

Figure 2-6. Composites of precipitation anomalies for each CP during 1960 to 1989 and 1990 to 2015 periods (unit: mm).

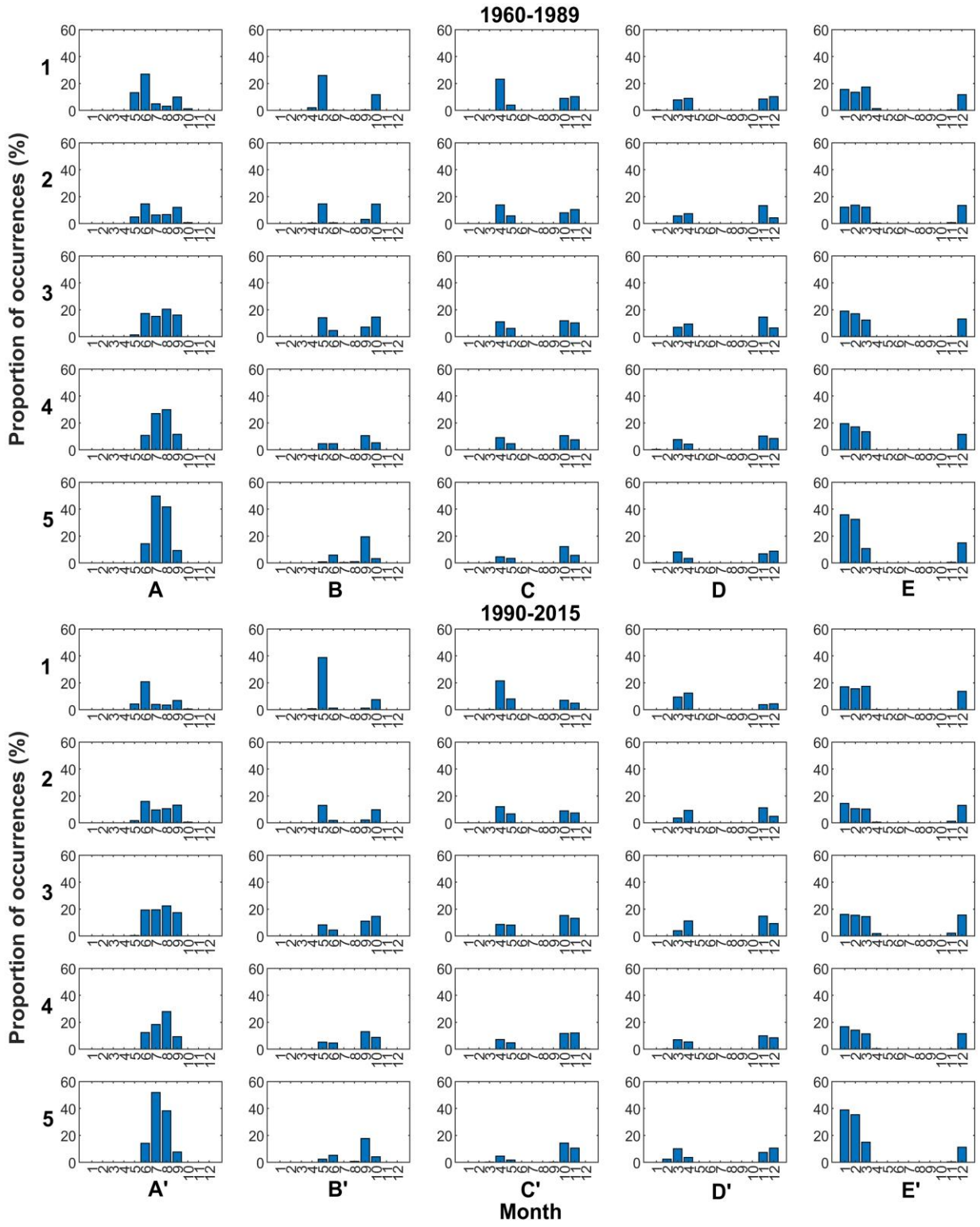

Figure 2-7. Monthly distribution of the identified circulation patterns during 1960 to 1989 and 1990 to 2015 periods.

4.2 Synchronized circulation patterns with extreme precipitation

In different periods, rain gauges with synchronized characteristics of extreme precipitation were

clustered together by the modularity method. The modularity values reached the maximum (that is, 0.287 of 1960–1989 and 0.279 of 1990–2015 respectively) when the number of clusters set to 4. Figure 2-8 shows the identified rain gauge clusters over CEC, which labeled as 'East', 'West', 'North', and 'South' according to their geographic location. There is some difference in the clusters in the two periods. Synchronized extreme rainfall in Figure 2-8a and b seems to show a slight different spatial coherence. Fundamentally, cluster East in the second period extends toward west, while cluster South reduce its extension on the north side. Overall, our results show that the synchronous clusters have strong concurrent characteristic and the latitudinal factor stands dominant in modulating extreme precipitation synchronization. Guan et al. (2020) found that the narrow corridor of extreme precipitation over CEC mainly forced by the Meiyu-front.

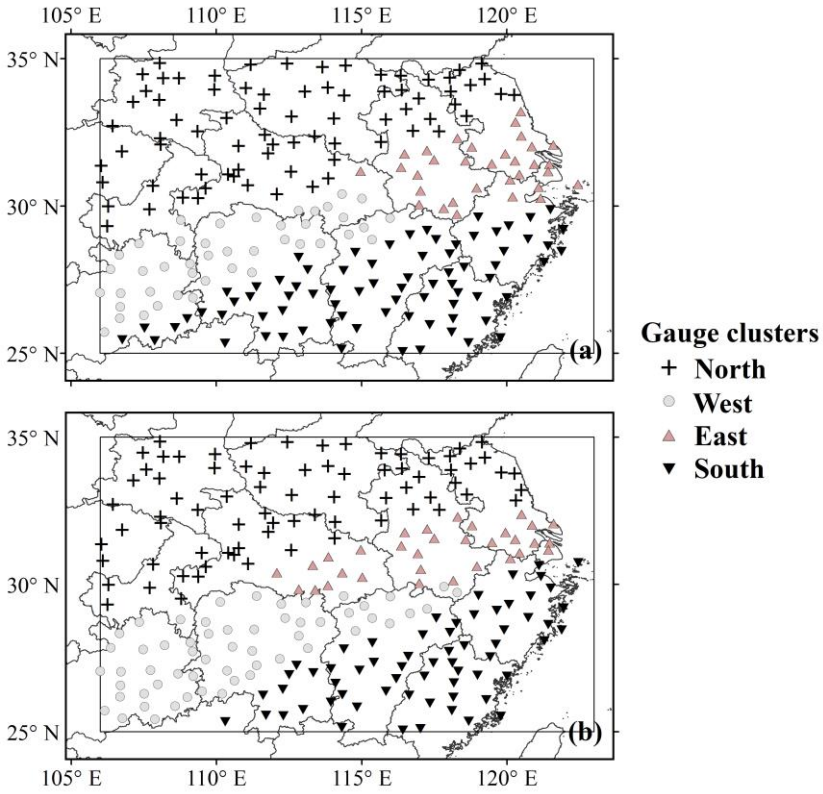

Figure 2-8. Clusters of rain gauges based on modularity method during (**a**) 1960–1989 and (**b**) 1990–2015 periods.

For each cluster, we calculated the synchronization degree between the binary sequence of extreme precipitation events recorded by each gauge with CPs, respectively. As displayed in Figure 1-9, the gauge-averaged synchronization matrix allows us to find the CPs highly synchronized with extreme precipitation events across the four clusters. Overall, CPs A1 to A5 are strongly synchronized with

extreme precipitation over CEC during 1960–1989. Specifically, CP A4 (A1) has the highest scores with extreme precipitation events for the East (West) cluster, while is A5 (A2) for the North (South) cluster (Figure 2-9a). In the period of 1990–2015, CPs A′1 to A′5, and B′1 are more related to the extreme precipitation in terms of the event synchronization degree (Figure 2-9b).

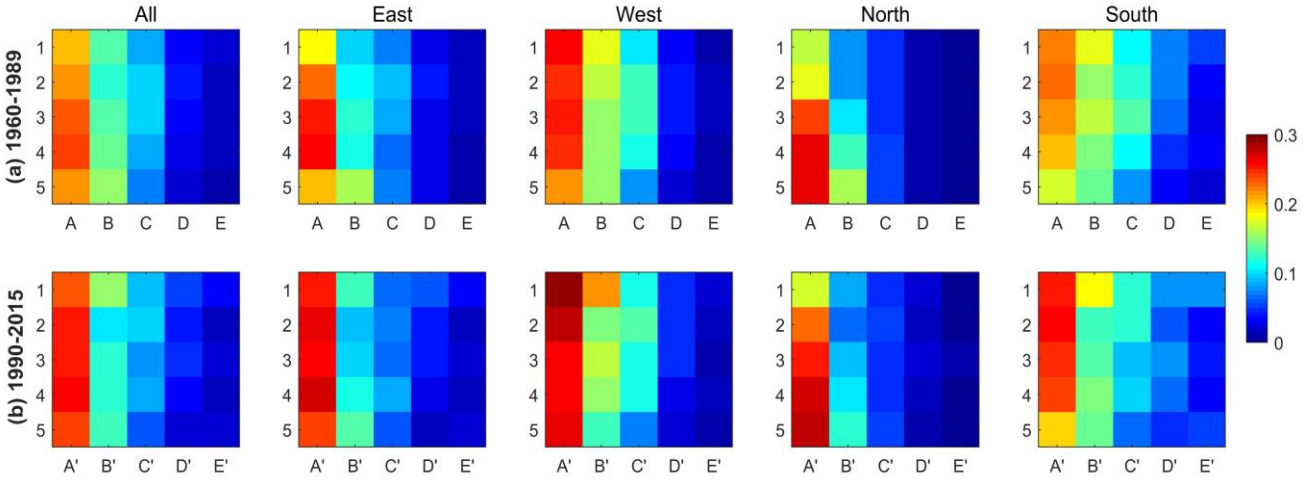

Figure 2-9. Mean synchronization degree for the identified circulation patterns with extreme precipitation events in the whole CEC, East, West, North, and South clusters during (**a**) 1960 to 1989 and (**b**) 1990 to 2015 periods.

To further demonstrate the influence of CP variations and their configuration on extreme precipitation, in the following, we mainly focus on the representative CPs (mean synchronization degree > 0.20) analysis. For each cluster, the local logistics model regresses the probabilities of at least one rain gauge has recorded the extreme precipitation. Figures 2-10–11 show the probabilities of extreme precipitation occurrences (black lines) conditioned by the IVT predictor when during the representative CPs. Overall, the conditional probabilities of extreme precipitation are expected to steadily increase with increasing IVT values. For the East, North, and South clusters, the conditional probability curves present a higher tail. Extreme precipitation occurrence in North cluster is highly related to the intensity of IVT, with the steepest probability curves in the range of 50~500 kg m^{-1} s^{-1}. In addition, for CP B1 and B′1, the IVT-extreme precipitation relationship is weak consistent with the results in Figure 2-9, but the fitted conditional extreme precipitation probability for the five cluster in CP B′1 is higher than that of the former.

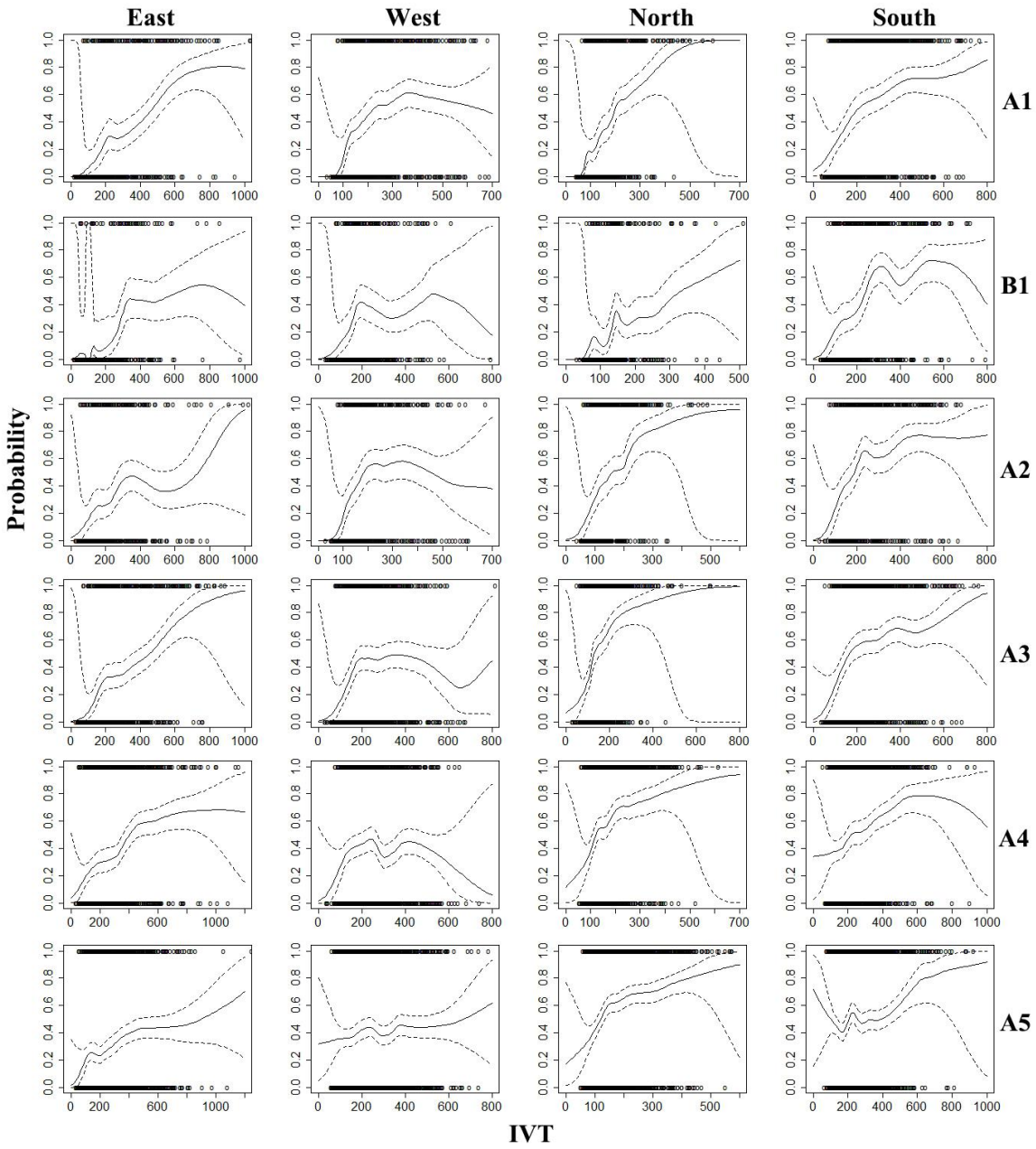

Figure 2-10. Probability of extreme precipitation occurrence conditioned by IVT (unit: kg m^{-1} s^{-1}) when during the representative circulation patterns for the East, West, North, and South clusters during 1960 to 1989 period. Dashed lines are the 95% confidence interval.

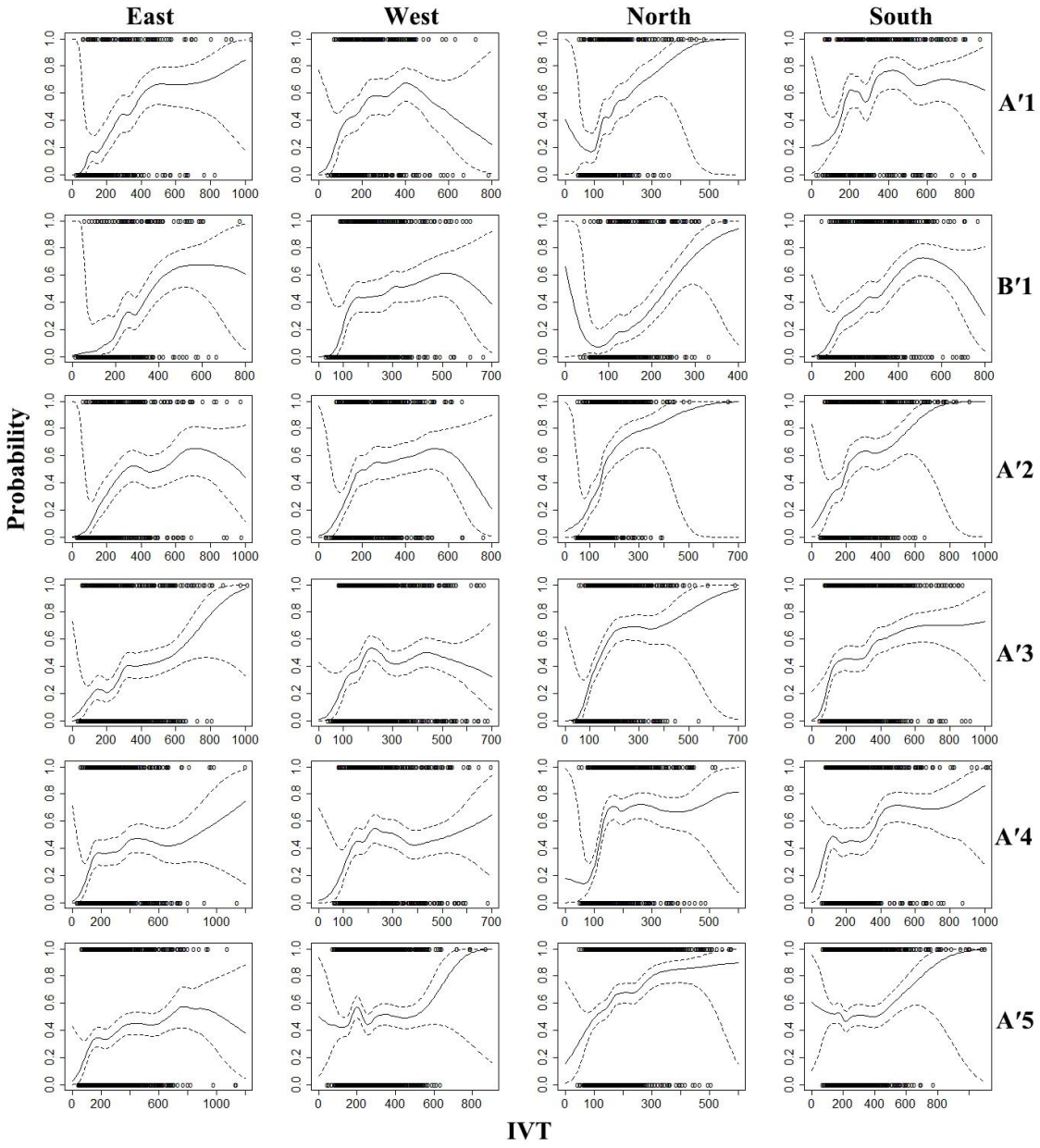

Figure 2-11. Same as Figure 2-10, but for the period of 1990–2015.

Figure 2-12 shows the IVT composites and wind fields at 850 hPa for the representative patterns in the two periods. An obvious water vapor channel that originates from the northern Indian Ocean can be found for A1 to A5 (A′1 to A′5), the IVT values higher than 350 kg m^{-1} s^{-1} over the Arabian Sea. Forced by the southwesterly flow, the humidity air mass would affect Eastern China via the Indian Peninsula and the Bay of Bengal. Another is the southeast airflow that originates from the western Pacific. Because the wind fields over CEC for A5 and A′5 are stronger than other CPs, causing the water vapor forced by southwesterly flow would continue toward the north CEC, which can explain the extreme precipitation across the North cluster are more related to CP A5 (A′5) (Figure 2-9).

Additionally, the circulation situations show that the mid-latitude shallow trough of A3 to A5 (A′3 to A′5) is located more northerly, which also contributes to the precipitation. However, less water vapor is found due to the relatively weak wind fields and IVT intensities of B1 and B′1, extreme events associate to B1 and B′1 may be less produced. Overall, specific circulation configuration and stable water vapor transport are two factors necessary for the occurrence of extreme precipitation over CEC.

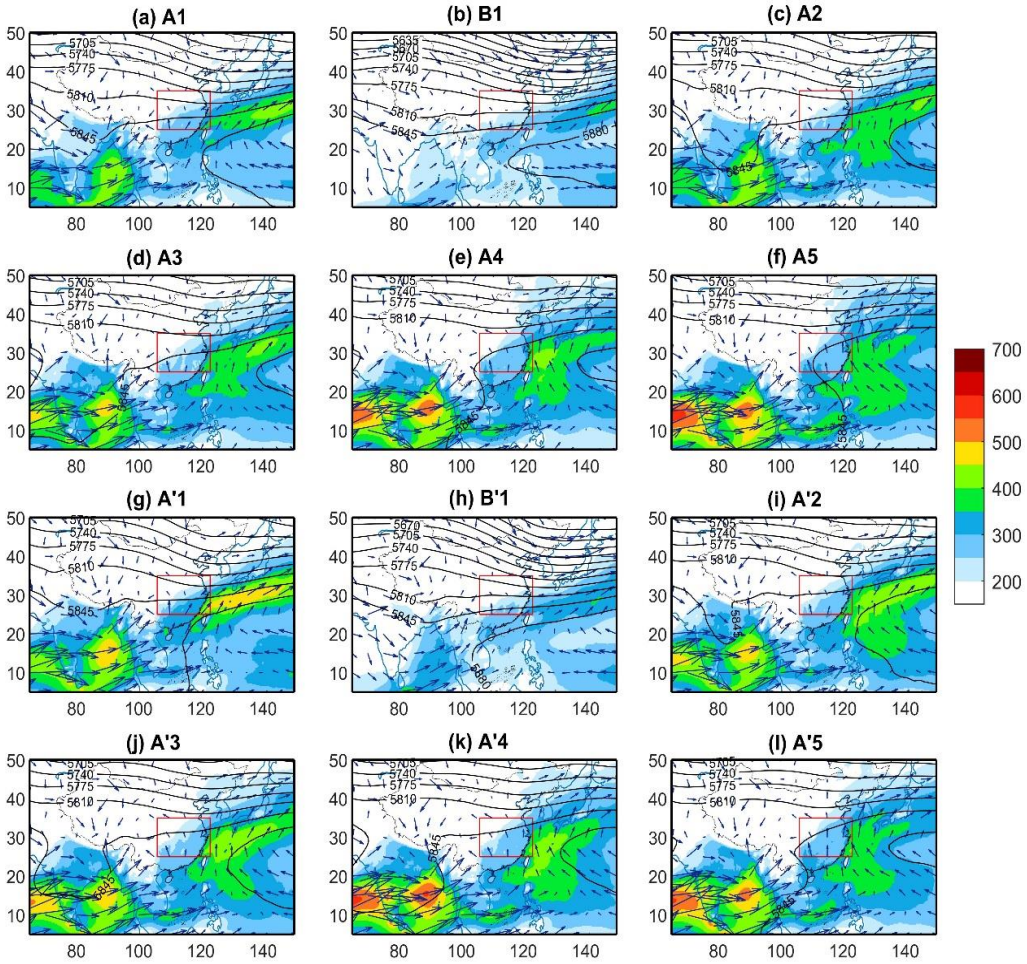

Figure 2-12. IVT composite (kg m^{-1} s^{-1}) for the representative circulation patterns during 1960–1989 and 1990–2015 periods, vector arrows are wind composites at 850 hPa.

4.3 Contribution analysis of extreme precipitation changes

Since the CP categories in the two periods remained the same, here we compared the frequency differences for the same CP type from 1960–1989 to 1990–2015 to analyze how their variations act on extreme precipitation frequency. Figure 2-13a, b shows the mean annual number of identified CPs in the two periods. Among the representative CPs, B′1, A′2, and A′3 become more frequent in 1990–2015, but a decreased number is found for A′1, A′4, and A′5. Figure 2-13c indicates the period

changes (from 1960–1989 to 1990–2015) in the recorded mean annual frequency of extreme precipitation events (sums of $\Delta P_i mf_i$, $P_i \Delta mf_i$, $\Delta P_i \Delta mf_i$, see Eq.2-11) for each CP. The mean number of extreme precipitation events in 1990–2015 for CP A′1 and A′4 are decreased compared to that for A1 and A4 in 1960–1989. Figure 2-13d shows the percentage that extreme precipitation frequency changes attributed to CP variation. We can find that for the increased extreme precipitation events in A′3 and A′5, 118.7% and 48.67% could be attributed to the relatively increased CP number, respectively. However, for CP A′1, the decreased extreme precipitation event only 26.92% can be attributed to the reduced CP number. For CP A′1 and B′1, these effects on extreme precipitation frequency are relatively weak.

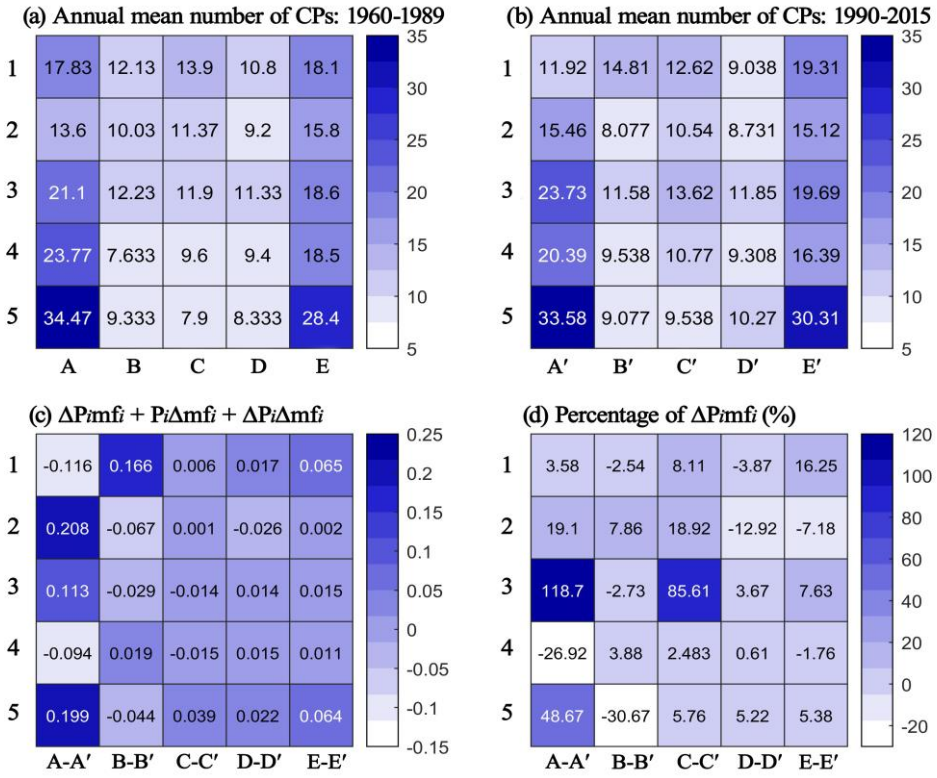

Figure 2-13. Annual mean number of identified circulation patterns in (**a**) 1960–1989 and (**b**) 1990–2015. (**c**) Changes in the recorded annual mean number of extreme precipitation events for each CP and (**d**) the percentage that extreme precipitation frequency changes attributed to the changes in circulation pattern frequency.

5. Discussion-The potential mechanism for large-scale circulation patterns change

Due to more frequent extreme weather events on land, many studies tried to explain this change by analyzing their links with large-scale atmospheric circulation variations (Pendergrass, 2018). For

example, Swain et al. (2016) demonstrated that the variations in zonal gradient of geopotential height at 500 hPa were closely related to seasonal storm tracks in California. Lennard and Hegerl (2015) also found that increase in extreme precipitation was associated with the more frequent key summer circulation modes. In general, the variations in the atmospheric circulation involve intraseasonal, interannual, decadal, and multidecadal time scales. We know that daily changes in the atmospheric horizontal motion are formulated by the gravity and pressure gradient force (e.g., land-sea and pole-equator pressure contrasts) and showed bewildering characteristics; while the year-to-year variabilities are much more manifested (Collins et al., 2010). For example, the intraseasonal periodic north-south shifts of the WPSH. As it migrates northward and arrives at its most northern climatological-mean position, then southward. Interannual variabilities are often forced by the interactions between the atmosphere and ocean conditions. The most prominent mode is known as the El Niño and Southern Oscillation (ENSO) (Dong et al., 2006; Wang et al., 1999). The anomalous sea surface temperature (SST) in the tropical Pacific is responsible for the circulation anomalies in the equatorial Pacific. Previous studies found that the lower-frequency (3–5 year) oscillation in WPSH may be caused by the ENSO cycle (Huang et al., 2020b). Moreover, the more slowly varying warm or cool anomalies of SST in the Pacific and Atlantic oceans may also modulate the decadal behaviors of the large-scale circulation activities (Scafetta, 2014; Valdés-Pineda et al., 2018). As the intermediary bridge connecting the ocean, atmospheric circulation could transfer the decadal-scale climate variability of oceanic to affect regional precipitation (Ning et al., 2017; Zhou et al., 2021b).

In this study, the synchronized CPs with extreme precipitation events over CEC have been identified in the periods of 1960–1989 and 1990–2015. We find that for the increased extreme precipitation events in A′3 and A′5, 118.7% and 48.67% could be attributed to CP changes. However, the possible causes for the representative CPs frequency changes are not well understand. In this section, we selected the Niño 3.4 index and two climate indices, that is, the Pacific Decadal Oscillation (PDO) and the Atlantic Multidecadal Oscillation (AMO) to investigate the potential physical mechanism influencing the variations in frequency of the representative CPs. The Niño 3.4 index was used to quantify the warm (El Niño) and cold (La Niña) swings of ENSO, and the PDO/AMO indices were defined as the first principal component of monthly mean SST anomalies in the North Pacific and North Atlantic, respectively. Figure 2-14 shows the time series of Niño 3.4 index, PDO, and AMO

indices. The interannual signals of ENSO (or interdecadal variabilities of PDO and AMO) were obtained by the 3–yr (12–yr) lowpass filter, which allow us to clearly find their phase transition characteristics. The time periodic signals in the annual frequency of representative CPs were decomposed into some sub-ingredients, called intrinsic mode functions (IMFs) by the empirical mode decomposition method (Rilling et al., 2003).

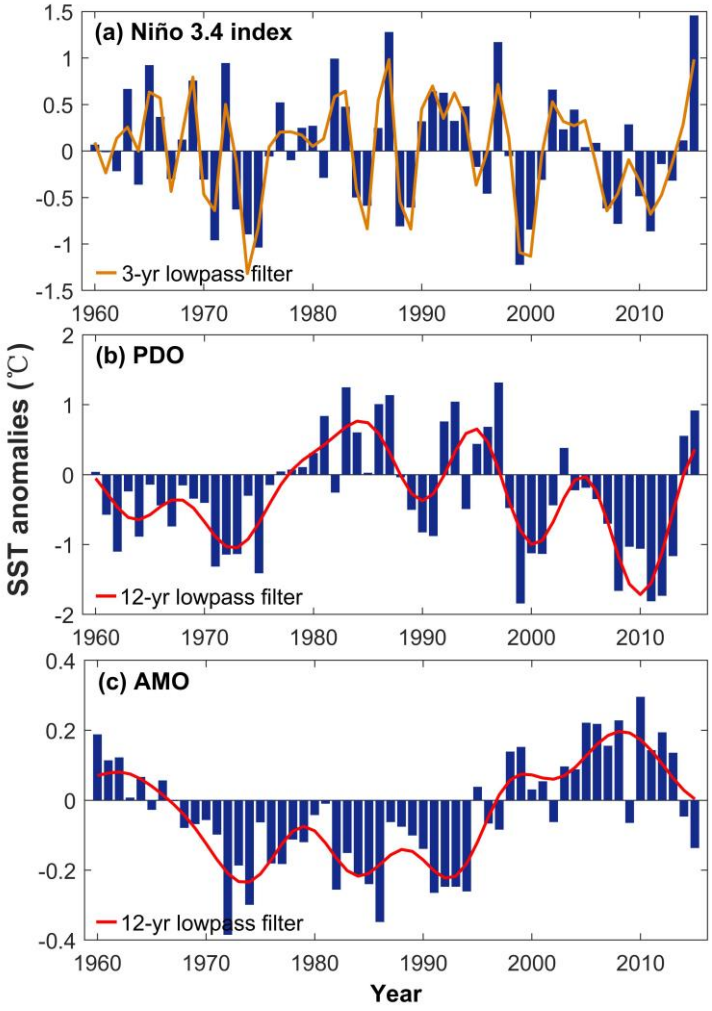

Figure 2-14. Time series of (**a**) ENSO, (**b**) PDO, and (**c**) AMO indices from 1960 to 2015.

Figure 2-15 displays the decomposed IMFs in the annual frequency of representative CPs from 1960 to 2015. Table 2-1 indicates the correlation coefficients between the decomposed IMFs and the climate variabilities of ENSO/PDO/AMO. We can find that the 2–4 yr and 8–10 yr quasi-periodic signals (IMF1 and IMF2) in the representative CPs have no correlation with PDO and AMO, but the 2–4 yr oscillation in A1-A′1, B1-B′1, and A2-A′2 is positively related to the phase of ENSO (at 99% statistical significance level), for A5-A′5 is the opposite. Previous studies showed that the East Asia Summer Monsoon (EASM) is tends to stronger when is an El Niño event, and to shift the WPSH

more northward; while La Niña is the opposite (Xu et al., 2021). Because CP A5-A′5 is dominated by the relatively weak WPSH (Figure 2-4), it is natural to have a negative relationship with ENSO. The 20–25 yr and 42–50 yr periodic oscillations (IMF3 and IMF4) in A1-A′1, B1-B′1, A2-A′2, and A3-A′3 are correlated well with the phase of PDO; while AMO is an important factor affected the 28–30 yr (50 yr) periodic oscillation in A4-A′4 (A5-A′5).

Figure 2-16 shows the shape, intensity, and location of the summer (i.e., July to August) WPSH in different PDO (AMO) phases. When the PDO is warm (or the AMO is cold), the WPSH tends to be enhanced and more western. The weak WPSH is the opposite. This can explain that the long-period variations of A1-A′1 to A3-A′3 (A5-A′5) are positively (negatively) related to the PDO phase and negatively (positively) to the AMO phase.

Overall, the potential mechanism for CP changes has been discussed in this section. The interannual variations of the representative CPs frequency are associated with ENSO, while the Pacific and Atlantic SSTs modulate the longer periodic. However, as shown by other studies, the amplitude and periodic length of PDO are influenced by global warming (Zhang and Delworth, 2016). An increase in anthropogenic aerosols also affects atmospheric circulation (Murakami, 2022). The changes in atmospheric circulation and SST results by complex external forcing (e.g., greenhouse gas emission) and inner variability. Identifying the robustness of such links in a warming climate is challenging and it is beyond the scope of this paper. To sum up, our results confirmed that changes in extreme precipitation frequency can be found from 1960 to 2015 over CEC, these changes are related to circulation patterns activities that can mainly be motivated by the atmospheric and oceanic interactions. This study also provides valuable information for using circulation situations to predict extreme events.

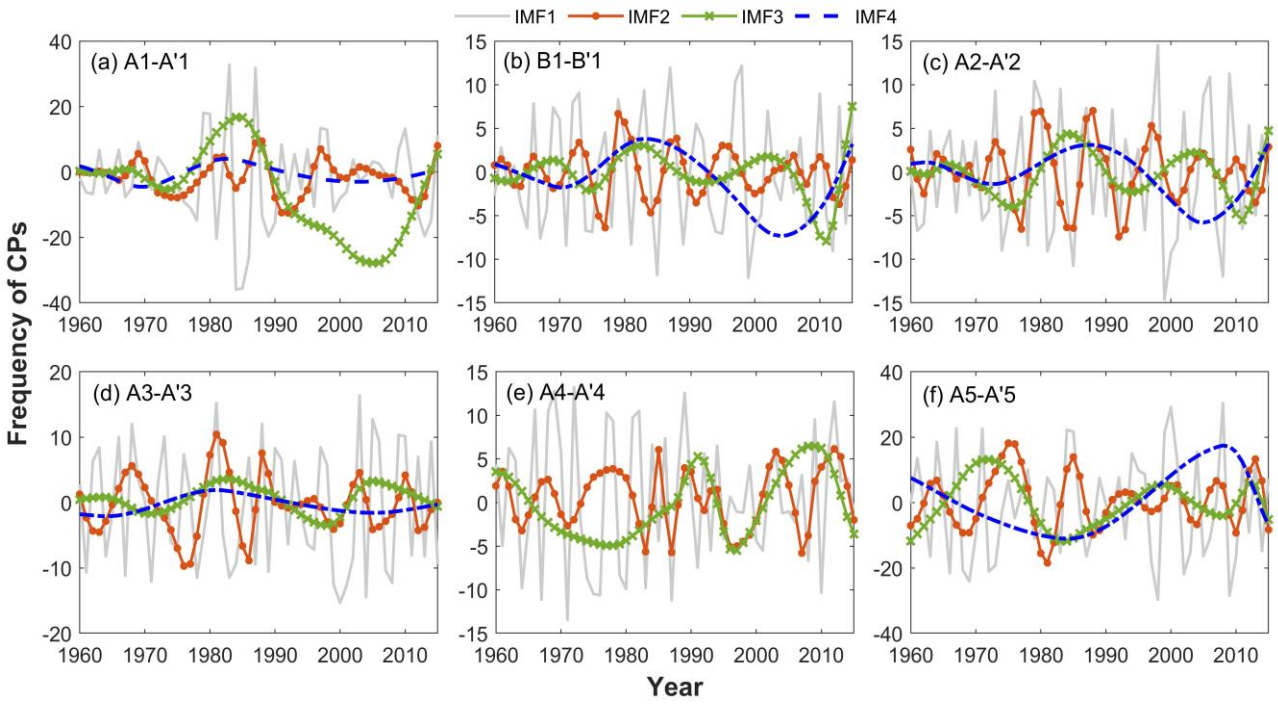

Figure 2-15. Decomposed IMFs in the annual frequency of representative circulation patterns from 1960 to 2015.

Table 2-1. Correlation coefficients between the decomposed IMFs in the annual frequency of representative CPs and the Niño 3.4 index, and 12-yr lowpass filter of PDO/AMO. Bold fonts indicate statistically significant correlation at the 99% confidence levels.

	A1-A′1	B1-B′1	A2-A′2	A3-A′3	A4-A′4	A5-A′5
IMF1	**0.44**/-0.08/0.11	**0.57**/0.07/-0.07	**0.42**/0.09/0.02	0.32/-0.02/0.01	0.16/0.02/0.05	**-0.48**/0.11/-0.03
IMF2	0.21/0.27/0.20	0.07/0.12/0.04	0.11/0.00/0.13	0.17/0.11/-0.02	-0.14/-0.16/0.05	-0.29/-0.16/-0.16
IMF3	0.17/**0.49**/**-0.59**	**0.35**/**0.65**/-0.30	0.29/**0.57**/-0.06	0.09/0.20/0.11	-0.02/-0.34/**0.52**	-0.23/-**0.53**/-0.05
IMF4	0.16/**0.62**/**-0.37**	0.21/**0.57**/**-0.67**	0.26/**0.58**/**-0.64**	0.05/**0.54**/**-0.73**	/	-0.18/-**0.58**/**0.89**

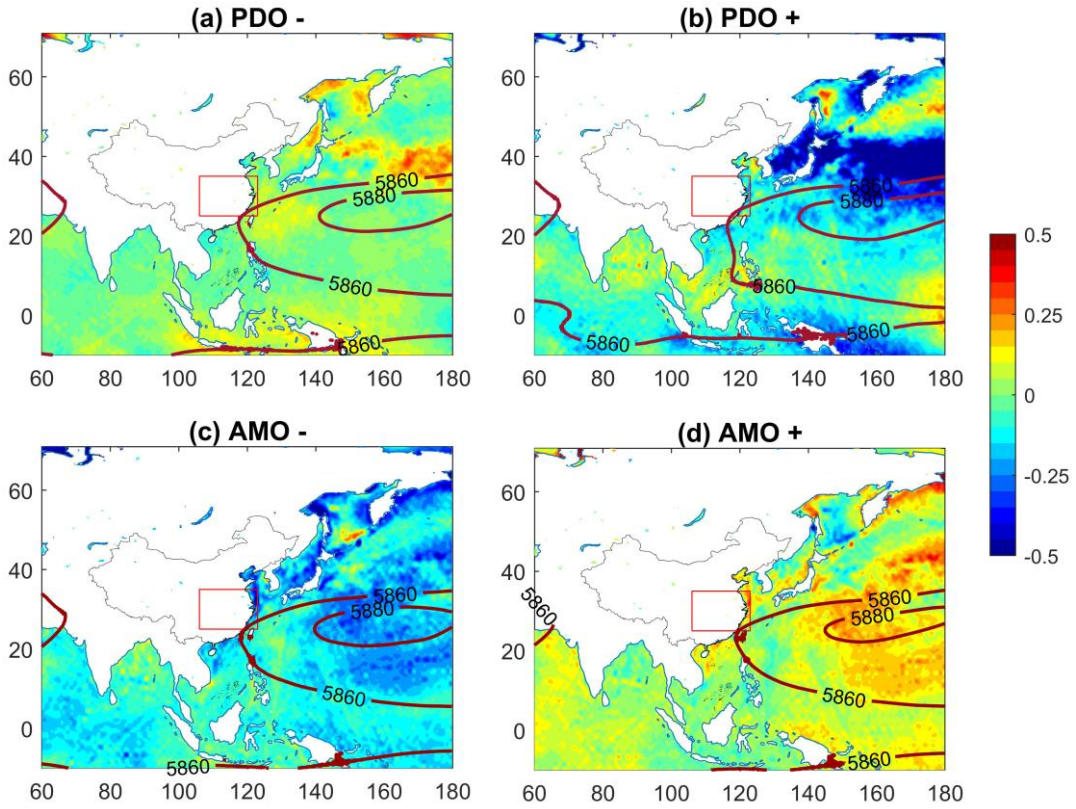

Figure 2-16. Location of 500 hPa WPSH (5880 contours, unit: gpm) and composite of sea surface temperature anomalies (shadow, unit: ℃) in the (**a**) negative, (**b**) positive phase of PDO, and the (**c**) negative, (**d**) positive phase of AMO during June to August.

6. Conclusions

In this study, we have investigated the characteristics of large-scale circulation patterns and water vapor transport related to the extreme rainfall over CEC from 1960 to 2015. Based on the changing points of extreme precipitation over CEC, we objectively choose 5×5 SOM nodes during 1960 to 1989 and 1990 to 2015 periods to identify the atmospheric CPs respectively, based on the standardized geopotential height field at 500 hPa. The SOM and event synchronization methods are effective in classifying and capturing the representative atmospheric circulation, which allows us to find robust links between extreme precipitation events and CPs.

We found that regional extreme precipitation events over CEC are closely related to the evolution of large-scale CPs. Over the four rain gauge clusters, the predominate CPs that synchronized with extreme precipitation events are different. In addition, water vapor transport also plays an important

role in shaping the extreme precipitation. Highly intense precipitation over CEC is primarily associated with the strong southerly moisture flows.

In summary, we have investigated the statistical relationship between circulation patterns and extreme precipitation over CEC. Existing studies argued that the intensity and frequency of precipitation extremes will increase in a warming climate (Kao and Ganguly, 2011; Papalexiou and Montanari, 2019; Zhan et al., 2020). Based on the findings in this study, one possible direction of future work is to use the methodology presented in this paper to explore the linked relationship and to forecast the occurrence probability of future extreme precipitation under different climate scenarios.

CHAPTER-3. Predictability of large-scale atmospheric circulation to extreme precipitation occurrences based on hybrid deep learning model

Summary

Rapid developments in deep learning algorithms provide a tool that enables the meteorologist to predict extreme precipitation from massive atmospheric data. In this chapter, a hybrid multilayer perceptron and convolutional neural networks (MLP-CNN) for binary predictions of extreme precipitation was proposed. In the case study of central-eastern China (CEC), the MLP-CNN model obtains an overall accuracy of 86% in predicting the extreme or non-extreme precipitation days using the anomalous fields of two large-scale atmospheric predictors, that is, geopotential height (GP) at 500 hPa and vertically integrated water vapor transport (IVT). Evaluation metrics illustrate that MLP-CNN outperforms the independent predictions from MLP and CNN, and two machine learning models (random forest and support vector machine). Finally, we examined the performance of MLP-CNN for 1–15 days ahead predictions. The 1–2 days' advance predictions can be considered as the reference to identify the extreme precipitation events.

1. Motivations

It has been shown that which patterns of large-scale atmospheric circulation and water vapor transport were relevant to extreme precipitation over CEC in Chapter 2. The aims of this chapter are to answer the second question "Can large-scale atmospheric circulation anomaly information be used for regional extreme precipitation predictions over CEC?", as well as to improve the prediction skill of deep learning through hybrid multiple models.

In Section 3.3 (see Chapter 1), we summarized a considerable opportunity for using deep learning models in extreme precipitation predictions. In this chapter, we constructed a hybrid deep learning

model, incorporating multilayer perceptron and convolutional neural networks (MLP-CNN) for predicting the occurrence probability of regional extreme precipitation over CEC. The MLP outperforms in nonlinearity data and low computing cost (Arulampalam and Bouzerdoum, 2003) and CNN has superior capabilities in learning and classifying the circulation patterns associated with extreme precipitation, as discussed in previous studies (Gao and Mathur, 2021). Furthermore, based on the analysis in Chapter 2, geopotential height (GP) at 500 hPa and vertically integrated water vapor transport (IVT) are two significant factors associated with extreme precipitation over CEC. Due to the large-scale atmospheric circulation dominating the foremost changes in extreme precipitation, the small-scale storm might be insufficiently reflected. Therefore, in this chapter, we only considered the regional extreme precipitation events identified from multi-gauges not the local events for each rain gauge.

Consequently, this chapter focuses on investigating the predictability of regional extreme precipitation using the anomalies of the two predictors. The motivations of this study were summarized as follows: (1) design a hybrid deep learning approach called MLP-CNN, which can learn the local and spatial features from the large-scale atmospheric conditions associated with extreme precipitation; (2) improve the accuracy of the predictability of extreme precipitation over CEC.

This chapter is organized as follows. Section 2 presents the datasets. Section 3 introduces the hybrid multilayer perceptron and convolutional neural networks model proposed to predict the occurrence of regional extreme precipitation over CEC. In section 4, we investigated the skill of the hybrid model. Further discussions on the hybrid model and one case study are presented in sections 5 and 6, respectively. Section 6 presents the conclusions.

2. Datasets

As mentioned in Chapter 2, the rain gauge data over CEC were obtained at the daily temporal resolution, from 1960 to 2015 (20454 days). The daily fields of 500 hPa GP and IVT in the range of 10°S–70°N and 40°E–170°W were available at the spatial resolution of 0.25°. In this study, anomalies of GP and IVT were selected as the predictors, which are important driving factors of extreme

precipitation occurrence over CEC.

3. Methodology

Now we present the hybrid multilayer perceptron and convolutional neural network (MLP-CNN) for extreme precipitation prediction. Figure 3-1 shows the brief framework of the MLP-CNN model, in which the MLP and CNN were constructed independently to extract related information from the numerical data at grid-point scale and spatial features from images respectively. Subsequently, we combined the two models to give the final classification as extreme or non-extreme precipitation. The proposed MLP-CNN model was built in the Spyder of Python 3.8 using Keras Sequential API. Detailed descriptions of each module are presented in the following sub-sections.

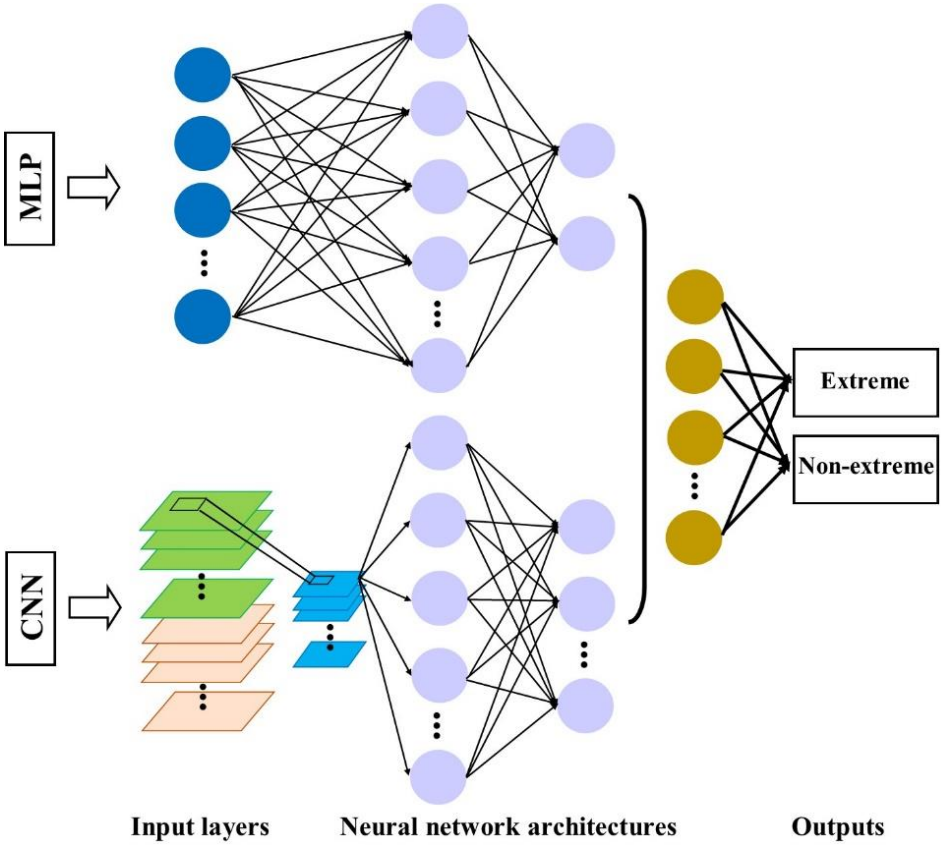

Figure 3-1. Flow chart of the MLP-CNN model.

3.1 Data preprocessing

First, extreme precipitation refers to daily records exceeding the 95th threshold from 1960 to 2015 (only days with an amount above 0.1 mm are considered). For each rain gauge, the total amount and frequency of extreme precipitation per year were obtained. In Chapter 2, rain gauges over CEC were

divided into four clusters respectively, in two time periods, 1960–1989 and 1990–2015, when considering the step changes in extreme precipitation (Figure 1-8). Within the same cluster, extreme precipitation events had a high degree of synchronization degree. Noted that the synchrony degree matrix of extreme precipitation events among the 228 rain gauges was calculated with the event synchronization method. Subsequently, the rain gauges were clustered into four groups by looking at the modularity values of the synchrony degree matrix. This chapter used the existing gauge clustering results, but a new cluster named "Central," was categorized (including the rain gauges whose communities differed between the two periods) as shown in Figure 3-2. The remaining clusters are labeled as 'East', 'West', 'North', and 'South'.

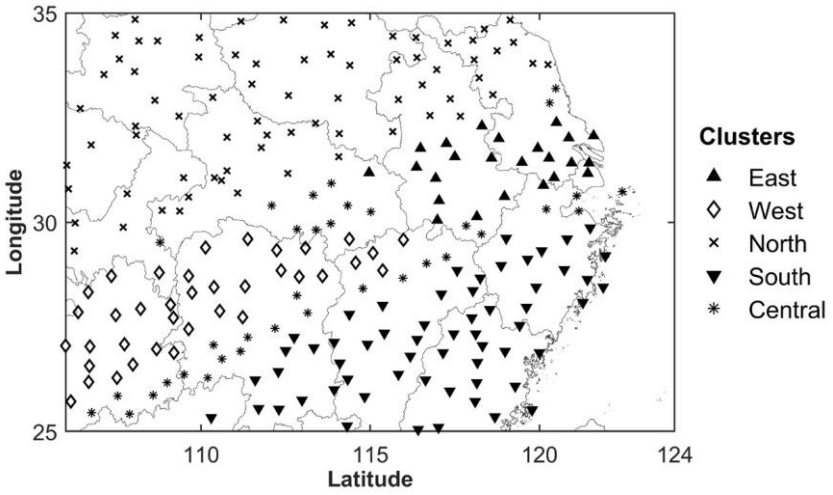

Figure 3-2. Spatial distributions of five rain gauge clusters.

Regional extreme precipitation event was defined as the mean precipitation (calculated from the ensemble average of multiple rain gauges in the cluster) exceeding the 95th threshold for the entire study period. This average approach was validated by previous studies to identify the regional extreme precipitation events (Davenport and Diffenbaugh, 2021). We then produced the binary time sequences of regional extreme precipitation event per rain gauge cluster. 1 represents its occurrence; otherwise 0. Table 3-1 shows the total days of identified regional extreme precipitation events for the five clusters, where the extreme and non-extreme cases are non-uniformly distributed.

Table 3-1. Total days of regional extreme precipitation events for the five clusters.

	East	West	North	South	Central
Days	556	729	679	760	749

For each 0.25° grid, the anomalous fields of GP at 500 hPa and IVT were calculated by subtracting the mean and dividing the standard deviation during the period 1960–2015, respectively.

3.2 Multilayer perceptron neural network

MLP is a feedforward neural network that commonly composes of input, hidden, and output layers. It uses the backpropagation training algorithm to minimize the quadratic error (Gardner and Dorling, 1998; Murtagh, 1991). In this study, we constructed a three-layers of MLP based on the numerical data of IVT and GP at 500 hPa anomalies. 1) input layers: the input for MLP is a two-dimensional vector $I_{t,m},\ t = 1, \dots, T;\ \ m = 1, \dots, M.$ T and M represent the total days of sample and number of pixels, respectively. In this study, only pixels covering the location of rain gauges were considered; 2) two hidden layers: 32 and 2 neurons were contained respectively, in which each neuron has a rectifier linear unit (ReLU) activation function, where $ReLU(x) = \max(0, x)$ (Ramchoun et al., 2016; Varshney and Singh, 2021). The hidden layer fully connects the next two hidden layers of CNN by weights, which presented at section 3.4. For MLP, it aims to learn the function $f(\cdot): I_{t,m} \rightarrow T_{t,o}$. T is the output and o indicates the desired columns.

3.3 Convolutional neural networks

CNN is a popular deep learning algorithm developed by LeCun et al. (2015) and designed to learn and recognize the target feature from images automatically. We built a deep CNN consisting of one input, two convolutional, and two fully connected layers. The network architecture of CNN is shown in Table 3-2.

1) Input layer. First, the inputs to CNN are the anomalous fields of daily GP at 500 hPa and IVT has a size of 40×75×2. 40 and 75 represent the total steps of latitude and longitude of an image, with 2 channels.

2) Convolutional layer. Each convolutional layer contains 20 filters of 3×3 kernel size with a ReLU activation function. The number of filters was tested from the candidate set {16, 20, 32, 40}. Both layers allow us to filter the irrelevant information from the previous layer through feature extraction and obtain a smaller image. The first layer mainly extracts the basic features, such as the edges and

corners; while the high-level layer is more complicated (Mairal et al., 2014). The detailed convolutional process was explained by Albawi et al. (2017)'s research, which can be mathematically formulated as follows:

$$X_j^l = ReLU(\sum_{i=1}^{S} X_i^{l-1} \otimes k_j^l + b_j^l) \quad (3\text{-}1)$$

where X_j^l is the lth feature map of the jth layer that calculated from the ith layer through convolutional operation. $ReLU(\cdot)$ represents the activation function, X_i^{l-1} is the output of $l-1$th feature map of the ith layer, $\otimes$ represents the convolutional operation, k_j^l and b_j^l indicate the weight matrix and bias vector, respectively.

Table 3-2. Architecture of CNN

Layer (type)	Descriptions*	Output shape	Parameter
Input layer	40×75×2	(None, 40, 75, 2)	0
Conv2D	Filters 20 3×3	(None, 38, 73, 20)	380
Activation	ReLU	(None, 38, 73, 20)	0
MaxPooling2D	2×2	(None, 19, 36, 20)	0
Dropout	0.5	(None, 19, 36, 20)	0
Conv2D	Filters 20 3×3	(None, 17, 34, 20)	3620
Activation	ReLU	(None, 17, 34, 20)	0
MaxPooling2D	2×2	(None, 8, 17, 20)	0
Dropout	0.5	(None, 8, 17, 20)	0
Flatten	/	(None, 2720)	0
Dense	32	(None, 32)	87072
Activation	ReLU	(None, 32)	0
Dropout	0.5	(None, 32)	0
Dense	16	(None, 16)	528
Activation	ReLU	(None, 16)	0

Notes: *Denotes the size of layers, convolutional filters, and max-pooling windows respectively, as well as the used activation function and dropout rate.

Additionally, the max-pooling and dropout layers were sequentially added after each convolutional layer. Max-pooling layer reduces the feature dimension by aggregating the pixels from the convolutional layer to mitigate the model's sensitivity (Wu and Gu, 2015) and dropout regularization aims to prevent overfitting by randomly ignoring a certain portion of neurons in each training batch (Garbin et al., 2020; Hinton et al., 2012). We set a dropout rate of 0.5, which was determined by the candidate set {0.2, 0.25, 0.4, 0.5, 0.7}. The strides of these layers same with the convolutional layers are set to be 1×1.

3) Fully connected layer. After configuring the Flatten layer converted the feature map to a vector, two dense layers with 32 and 16 neurons respectively, were fully connected to the previous layers. Both dense layers had the ReLU activation functions, but a dropout layer (dropout rate = 0.5) was added after the first dense layer. In addition, the L2 regularization penalty (regularization value = 0.0005) was added to each convolutional and fully connected layer to reduce model overfitting.

3.4 Hybrid model of MLP and CNN

At the last stage, CNN receives the last layer of MLP and two dense layers were added. The first fully connected dense layer had 16 neurons with the ReLU activation function. For the final output layer with 2 neurons of the MLP-CNN, a softmax activation function (Liu et al., 2016; Sharma et al., 2017) was used to transform the preliminary outputs to the normalized probability of both classes (p_c).

$$p_c = \frac{e^{z_c}}{\sum_{k=0}^{1} e^{z_k}},\ c = \{0,1\} \tag{3-2}$$

where c indicates the number of predicted classes. 1 represents an extreme precipitation predicted by MLP-CNN; otherwise 0. z is the input vector to the softmax activation function. $\sum_{k=0}^{1} e^{z_k}$ is the normalization term, it ensures that the probabilities of all classes of a day must add up to 1. Therefore, for any given day, the class with a higher occurrence probability we take it as the final predicted results of the MLP-CNN.

The hybrid MLP-CNN model was trained on the 80% of the samples, and its test was performed on the remaining. Since the samples contain less extreme cases (see Table 3-1), we divided the samples by stratified sampling method (Parsons, 2017), which allows the training and testing sets have the

same proportion of positive or negative labels. The random sate of split was set to 20. In addition, the class weight was employed to solve this problem further. $\text{weight}_c = \frac{C}{2C}$, where C is the total number of a class during the training process. 400 subsamples were imported into the training one time. Batch size = 400, selected from the candidate set {32, 64, 200, 400, 1024}. For the binary classifications problem, the categorical cross-entropy loss function (Ho and Wookey, 2020) was implemented to train the model along with the adaptive learning algorithm, i.e., Adam optimizer (Khan et al., 2018). Assuming that p and $1-p$ are the resulting predicted probabilities of the binary classes. The categorical cross-entropy loss function ($Lossf$) can be expressed as follows.

$$Lossf = -\frac{1}{SN}\sum_c [y_c \cdot log(p_c) + (1-y_c) \cdot log(1-p_c)] \quad (3\text{-}3)$$

where SN represents the number of training sample, y_c and p_c indicate the target label and predicted probability, respectively.

The learning rate was set to 0.001, which tuned from the set {0.1, 0.01, 0.001, 0.0001}. We adopted the early stopping technique to monitor the $loss$ value at validation to prevent model from overfitting. When setting 400 epochs to train the MLP-CNN, the model will stop if the $loss$ is no longer reduced after 10 rounds. In this study, we used the HyperTuner model (Li et al., 2018b) to tune the architecture parameters (e.g., size of convolutional filters, level of layers, number of neurons) and Hyperparameters (e.g., learning rate, dropout rate, batch size, regularization value) of MLP-CNN. The final selected values after model tuning have described above.

3.5 Evaluation metrics

Three metrics, i.e., accuracy, recall, and the area under the receiver operating characteristics curve (AUC) were used for investigating the extreme precipitation predictability of MLP-CNN. Accuracy indicates the overall ratio of correctly predicted class on the samples. In the case of extreme and non-extreme precipitation predictions task, correctly classifying the positive class should be highlighted rather than missing. Recall measures the model's capability in predicting the positives with respect to all positives. AUC is a more balanced indicator (Hand and Till, 2001; Huang and Ling, 2005) that comprises the correctly predicted or false alarms for extreme precipitation, defined in Eq. 3-6.

$$accuracy = \frac{TN+TP}{n} \times 100\% \quad (3\text{-}4)$$

$$recall = \frac{TP}{P} \times 100\% \quad (3\text{-}5)$$

$$AUC = \frac{S-P(P+1)/2}{N \times P} \quad (3\text{-}6)$$

$$S = \sum_{i \in positives} rank_i \quad (3\text{-}7)$$

where TN and TP are the number of correctly classified negatives and positives, respectively. n and P (N) represent the total days and extreme (non-extreme) precipitation days of used subsets, respectively. S is the rank of a positive sample.

4. Results

4.1 Analysis of extreme precipitation events and related circulation features

We calculated the accumulative days of extreme precipitation in each calendar month from 1960 to 2015 over CEC. Figure 3-2 shows the monthly ratio of extreme precipitation days for the five clusters. In general, extreme precipitation mainly falls from May to July. Across the five clusters, June generally has a high ratio of extreme precipitation day, but the North cluster receives the largest occurrence of extreme precipitation in July, followed by June and September (Figure 3-2d).

Figure 3-3 shows the composite anomalies of IVT and GP at 500 hPa associated with the extreme precipitation events for the five clusters. At each grid the anomalies are calculated by taking the mean field of extreme precipitation days subtracting the average from 1960 to 2015. Evident positive anomalies of GP can be found over almost region of eastern Eurasia (the north of 20°N). The intensified pressure gradient can enhance the moisture transportation to east China. Additionally, the anomalous center with strong water vapor transport generally locates at the north side of Western Pacific Subtropical High (the contours of 5880 and 5860 gpm), and coincides with the locations of the near-front rainfall system. For example, the anomalous IVT of the North cluster is north than that of the South cluster.

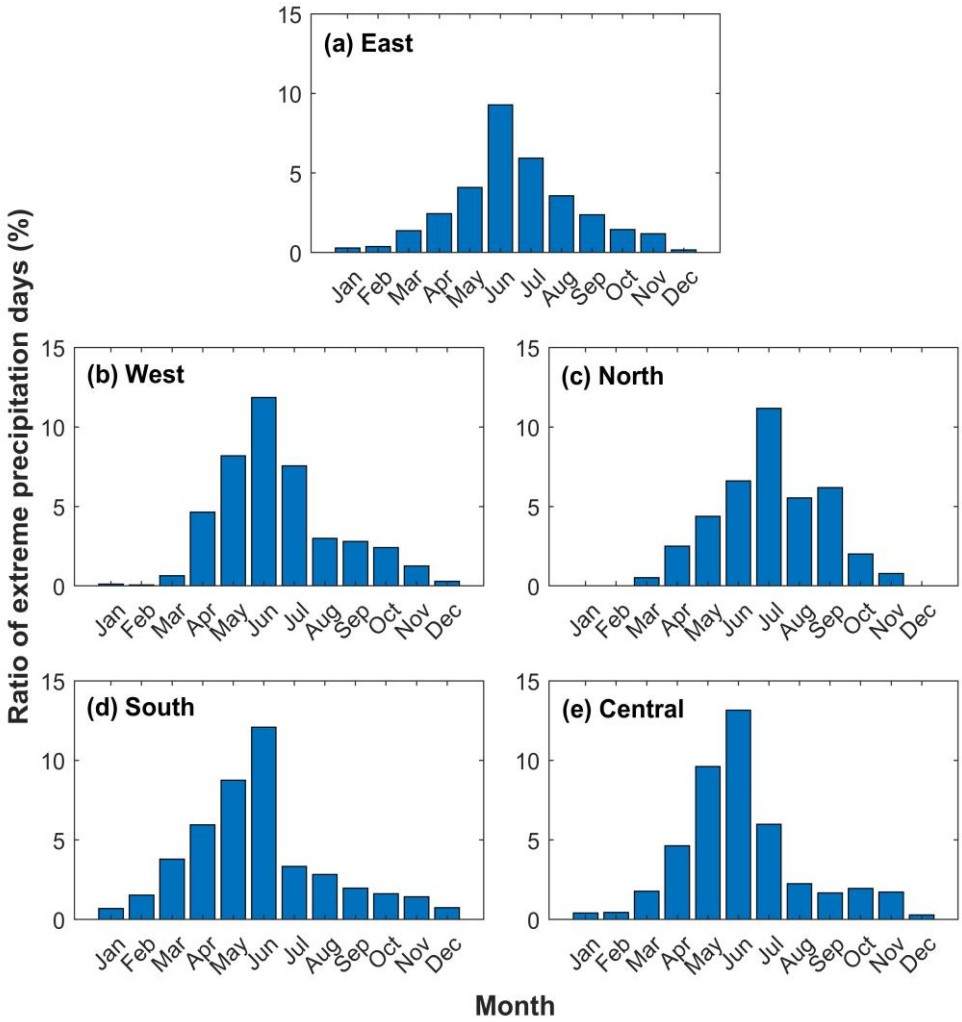

Figure 3-2. Monthly ratio (%) of extreme precipitation days for (**a**) East, (**b**) West, (**c**) North, (**d**) South, and (**e**) Central clusters from 1960 to 2015.

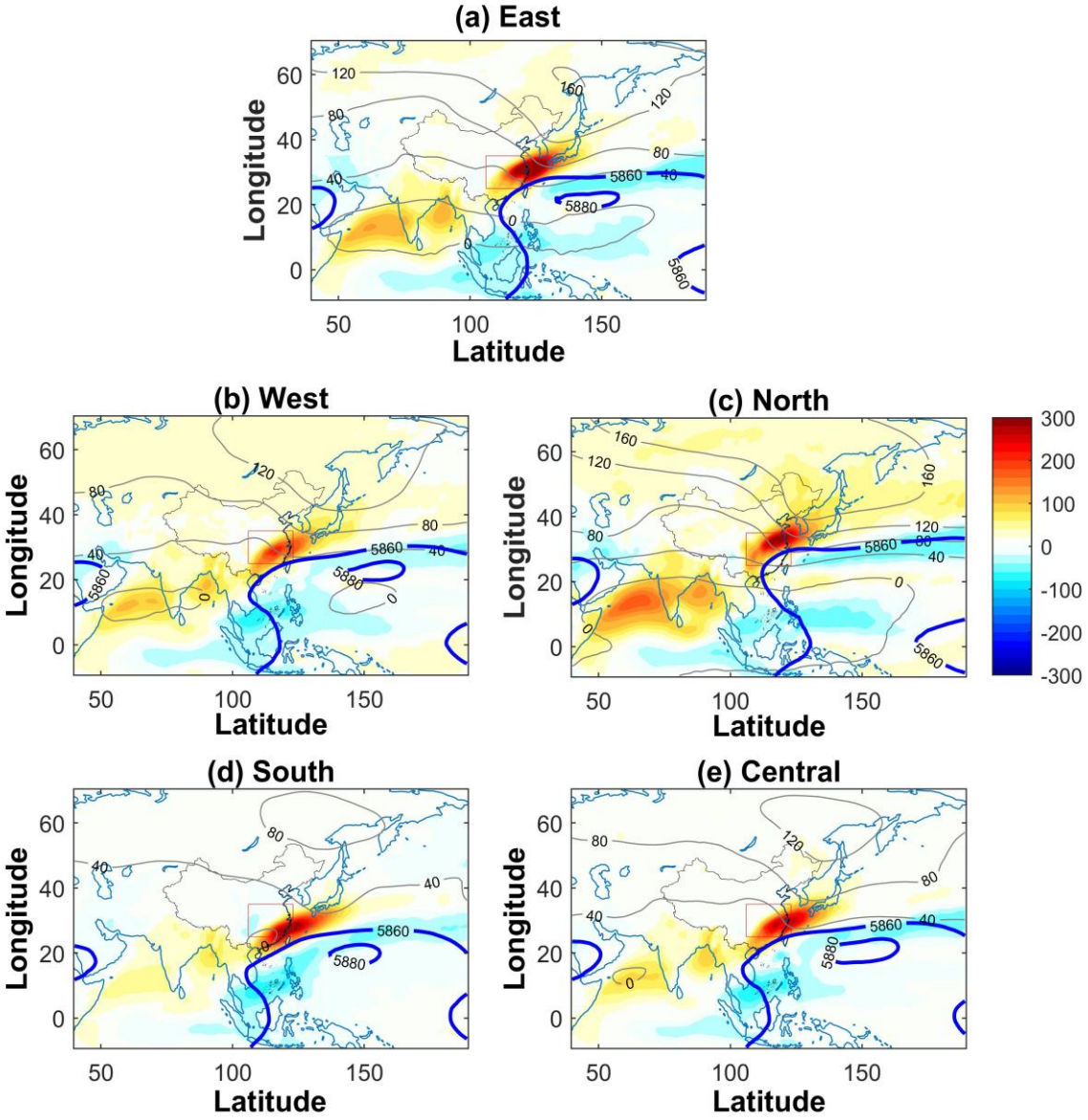

Figure 3-3. Composites of anomalous fields of IVT (shadow, unit: kg m^{-1} s^{-1}) and geopotential height at 500 hPa (grey contours, unit: gpm) under the extreme precipitation day for the (**a**) East, (**b**) West, (**c**) North, (**d**) South, and (**e**) Central clusters. Bold contours represent the 5860 and 5880 gpm.

4.2 Performance of MLP-CNN in predicting extreme precipitation

Figure 3-4 shows the performance of the hybrid MLP-CNN model in classifying the extreme and non-extreme events using the anomalies of geopotential height and IVT. Overall, the MLP-CNN achieves 86% accuracy for binary classifications across the five clusters, with a slightly better performance of 89% and 88% for the north and south respectively. For the extreme precipitation day, the MLP-CNN could correctly predict 91% (81%) of events on training (testing) sets. However, the Recall metric is generally worse for the West cluster (72%). The MLP-CNN also produces a fairly

high AUC (average of 0.93) across the five clusters, indicating this model can give convincing predictions for the occurrence probability of extreme precipitation over CEC.

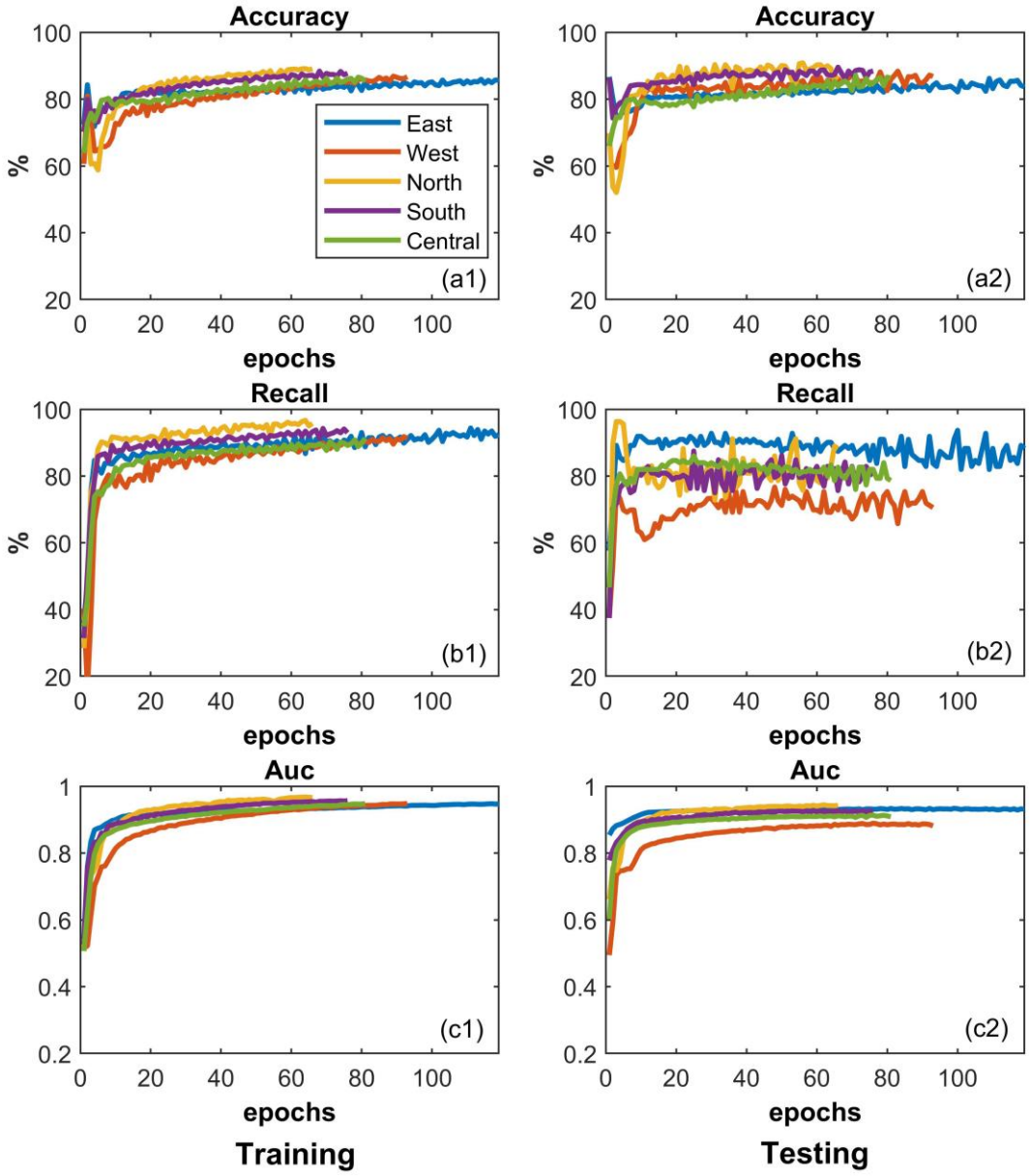

Figure 3-4. Training and testing results of MLP-CNN in predicting the occurrences of extreme and non-extreme precipitation on the training (left column) and testing (right column) sets, for the five clusters.

Figure 3-5 shows the performance of MLP-CNN for predicting extreme precipitation day in different seasons. The accuracies of MLP-CNN on both training and validation sets are relatively higher in autumn and winter, at a range of 89%~100%. This is largely due to extreme precipitation over CEC mainly falls from May to July (see Figure 3-2). Fewer positive samples often lead to a high accuracy.

In addition, no extreme precipitation was recorded in winter for the North cluster (Figure 3-2c), both recall and AUC values are null. Overall, considering the AUC of the four seasons, the MLP-CNN provides a skilled prediction for extreme precipitation.

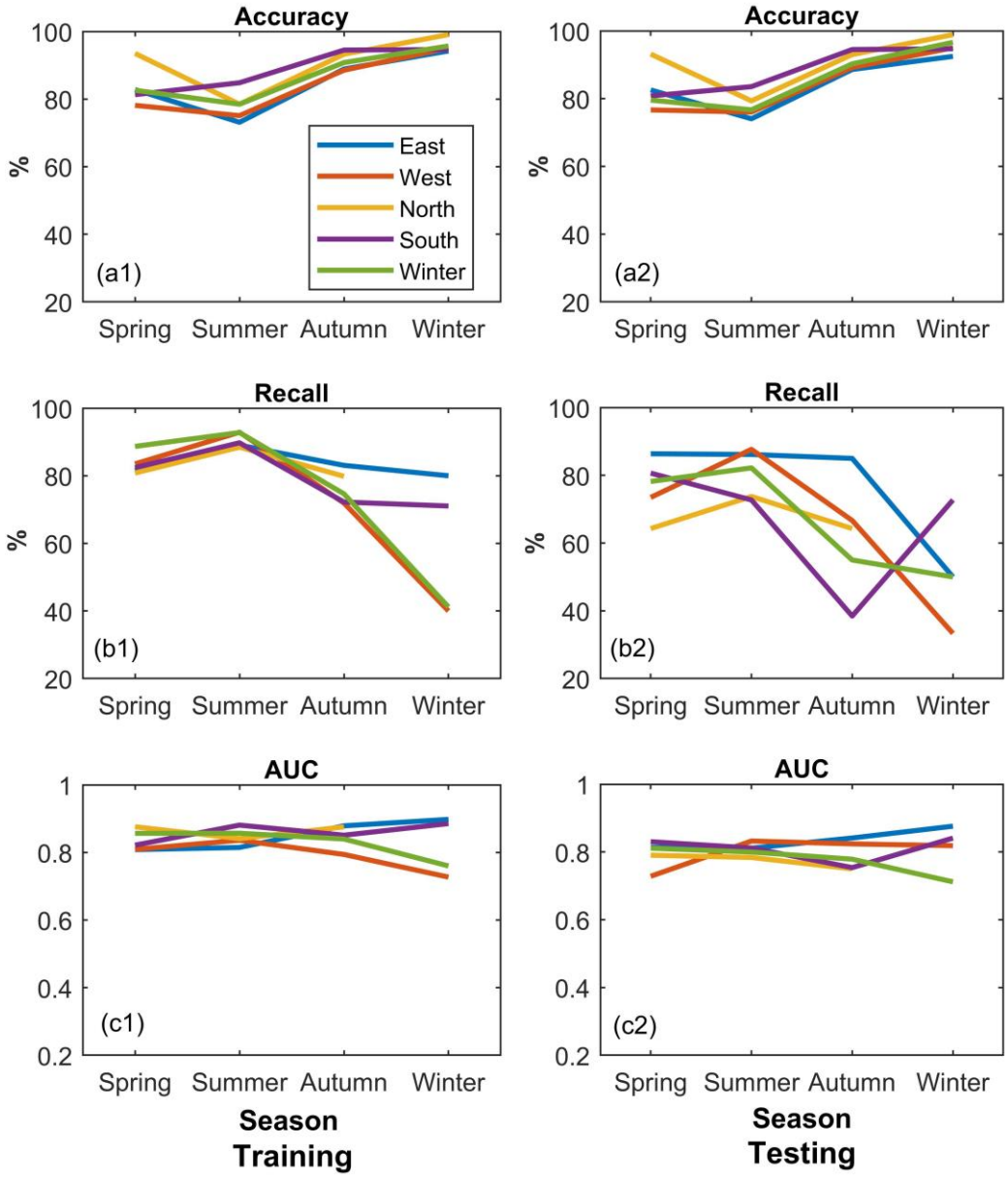

Figure 3-5. Seasonal performances of MLP-CNN in predicting extreme and non-extreme precipitation day on the training (left column) and testing (right column) sets, for the five clusters.

4.3 Comparison with other deep and machine learning models

The capability of MLP-CNN was compared with the independent predictions from MLP and CNN and two machine learning models, i.e., random forest (RF) and support vector machine (SVM) further. RF proposed by Breiman (2001) is a widely used ensemble learning model for classifications and

regressions using the bagging strategy, whereas the key concept of SVM is to maximize the distance between sample points and the hyperplane (Noble, 2006). We used the identical inputs of MLP to train the two machine learning models. Network architectures of RF and SVM were constructed based on the classification algorithms. Hyperparameters of RF (e.g., number of trees, max depth of a tree) and SVM (e.g., penalty parameter C, kernel function) were tuned by the Grid Search optimization approach (Liashchynskyi and Pavlo, 2019; Syarif et al., 2016). For MLP and CNN, the last layers were set consistent with the MLP-CNN, that is, 2 neurons fully connected layer with the softmax activation function.

Table 3-3 summarizes the evaluation results of our proposed hybrid approach and the four individual models on the training and testing sets. As expected, the MLP-CNN outperforms the four individual models on a daily scale. On average, the accuracy was improved by 11.6% and 18.5%, 2.6% and 278% of recall, 5.1% and 83.8% of AUC compared to MLP and CNN. MLP has more convincing predictions than CNN, while CNN shows poor capability in predicting extreme precipitation occurrences. On the training set, CNN only can correctly predict 43% of extreme precipitation days and prone to over train, which caused a considerable miss can be seen on the testing set. This limitation also can be found in the RF and SVM. They are not able to correctly classify the extreme precipitation days in this case, with very poor recall values. Actually, each model can achieve at least 95% accuracy if their predictions are insensitive to the minority samples. But it should be noted here only the model has equivalent performance among the majority and minority classes that could be considered to deal with the prediction task of extreme precipitation. Due to the imbalanced classes, it is critical for an individual machine or deep learning model to achieve promising predictions and the hybrid deep learning approach is suggested.

Table 3-3. Performance of different deep learning models in predicting the extreme and non-extreme precipitation for the five clusters.

Model	Cluster	Training			Testing		
		Accuracy (%)	Recall (%)	AUC	Accuracy (%)	Recall (%)	AUC
MLP-CNN	East	83.88	90.71	0.94	83.12	87.78	0.93
	West	84.01	88.66	0.93	85.20	71.88	0.88
	North	87.88	95.01	0.96	88.80	81.89	0.94
	South	86.59	92.24	0.95	87.66	80.73	0.92
	Central	84.34	88.66	0.94	83.62	81.42	0.91
MLP	East	79.37	87.24	0.92	79.17	88.78	0.92
	West	70.29	73.74	0.81	70.06	73.66	0.80
	North	81.64	88.88	0.95	81.16	85.25	0.92
	South	77.98	88.65	0.93	77.95	88.88	0.90
	Central	74.52	80.10	0.85	73.66	81.95	0.85
CNN	East	58.37	40.90	0.50	67.07	4.66	0.50
	West	47.81	54.15	0.51	84.78	2.63	0.50
	North	63.64	36.79	0.51	95.91	0.79	0.49
	South	63.10	37.97	0.51	92.25	3.25	0.51
	Central	56.76	44.50	0.51	91.97	1.67	0.52
RF	East	98.06	28.76	0.64	97.33	7.21	0.57
	West	96.89	12.99	0.57	96.38	4.11	0.55
	North	97.78	33.27	0.67	96.65	8.09	0.53
	South	97.50	33.93	0.69	96.55	13.16	0.61
	Central	97.25	25.17	0.65	96.50	9.33	0.58
SVM	East	94.77	3.60	0.51	94.25	0.79	0.52
	West	93.07	2.91	0.51	93.52	4.71	0.52
	North	93.77	6.07	0.52	93.86	4.41	0.52
	South	93.18	8.36	0.55	92.95	6.58	0.56
	Central	93.03	4.67	0.53	92.73	2.67	0.53

5. Discussion-Performances of MLP-CNN in the ahead predictions for extreme precipitation

Since extreme precipitation is a nonstationary and hazardous weather phenomenon, various statistical and physically-based models have been developed for its predictions. Deep learning algorithms which are known for their powerful and automatic interpretation advantages are adopted for solving this issue. In this study, we designed a hybrid MLP and CNN architecture for predicting the occurrence probabilities of extreme and non-extreme precipitation over CEC. One focus is how this model works using the large-scale atmospheric predictors of geopotential height and IVT. Evaluation metrics demonstrate that the MLP-CNN performs well in the training and testing sets. There is no lag-time between the predictors and the occurrence day of extreme precipitation. However, the large-scale atmospheric circulation has not only an immediate trigger effect on regional extreme precipitation, but the lagging influences are also important (Cavazos, 1997; Tabari and Willems, 2018). Teixeira and Satyamurty (2007) investigated the 1–3 days circulation features preceding the heavy precipitation events over the southern Brazil. They found that these features were significantly different from that of non-heavy precipitation and may be precursors to precipitation episodes. Hong and Ren (2013) analyzed the links between circulation anomaly and heavy precipitation over the east Asian coastal region. Results showed the anomalous circulation associated with heavy precipitation developed from the previous days' systems. Giannakaki and Martius (2016) found that circulation patterns affecting the extreme precipitation in southern Switzerland often need certain day to elongate meridional. 1-2 days' circulation before extreme precipitation events shaped the moist air transport.

In this section, we traced back 1, 2, 3, 5, 7, 10, and 15 days of the circulation anomalies advance the extreme precipitation episodes to train the MLP-CNN model, to discuss whether the precursors can be used to predict the occurrence probabilities of extreme precipitation over CEC. For the reason of brevity, only AUC results are discussed due to this metric being more comprehensive. Figure 3-6 presents the evaluation results of MLP-CNN on different leading days in predicting extreme precipitation. It can be seen that the predictions without ahead times are the best for the five clusters. The performance of MLP-CNN tends to decrease with the increasing leading days of circulation anomalies, e.g., the AUC of the East cluster decreases from 0.83 (1 day ahead) to 0.63 (15 days ahead). Noticed that advanced 1–2 days of knowledge of extreme precipitation occurrences could be a good

auxiliary for the final predictions.

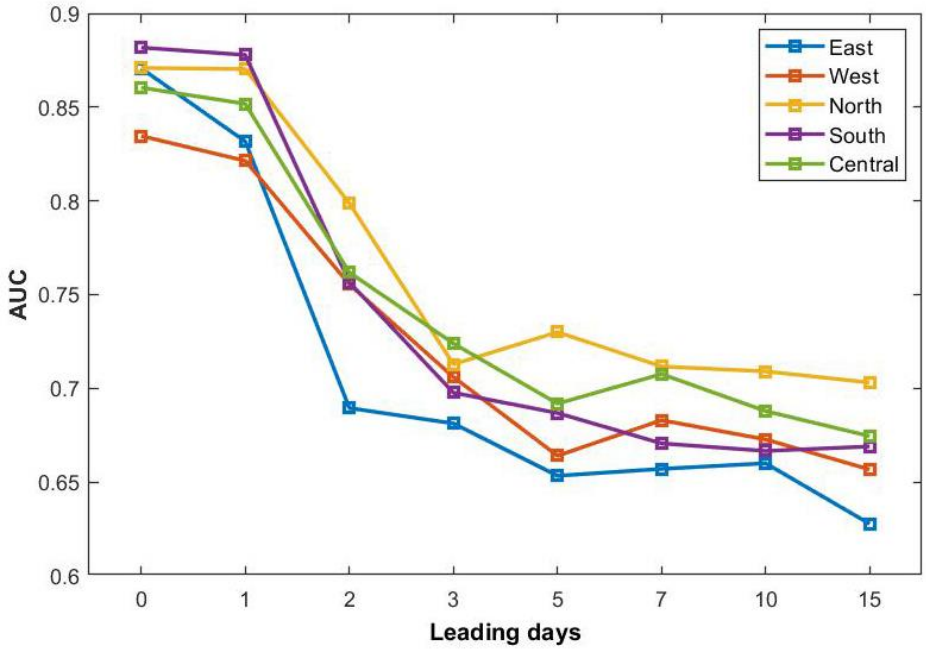

Figure 3-6. AUC metrics of MLP-CNN in predicting extreme and non-extreme precipitation day at different leading days for the five clusters.

6. Case study-Performances of MLP-CNN in July 2021 extreme rainstorm in Henan province, China

The extreme rainstorm of 19–21 July, 2021 in Henan province, China was triggered by circulation anomalies of the enhanced upper-level trough and easterly flow, as well as the stable water vapor transport from the ocean (Nie and Sun, 2022; Qin et al., 2022), with more than 300 deaths and direct economic damage of over 20 billion dollars. Statistically, the Henan province experienced a record-breaking rainstorm in the 21st century. According to the rainfall records at *Zhengzhou* station from the National Meteorological Center of China, the daily precipitation was higher than 600 mm on 20 July.

Figure 3-7 shows the daily precipitation distribution over east China during 19–21 July 2021, estimated from the ERA5 data. Precipitation areas are observed over north CEC. At the same time, the associated water vapor transport and GP at 500 hPa are presented. An obvious water vapor channel that originates from the northern Indian Ocean and an extremely intense vortex structure under a typhoon can be found, and the IVTs reveal the enhanced convergence centers (> 300 kg m^{-1} s^{-1}) over

north CEC. We used the MLP-CNN to predict the probability of regional extreme precipitation during the three days, and the results are higher than 90% for the north cluster (Red fonts). To some extent, this model shows good performance. It is noted that this approach can provide the probability and classification information for regional extreme precipitation occurrences from large-scale atmospheric circulation, those precursory signals will benefit numerical weather forecasting and related research, but it lacks information about the intensity and geographic locations.

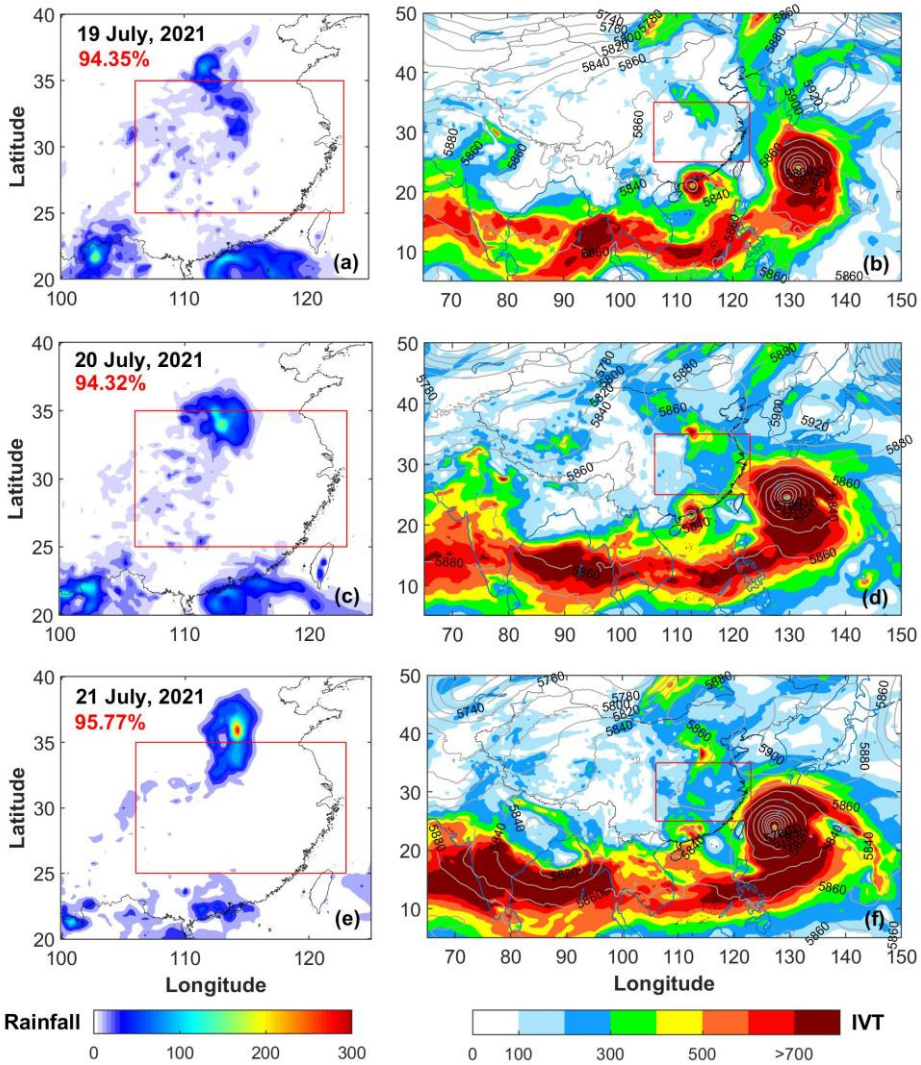

Figure 3-7. Daily precipitation ((**a**), (**c**), (**e**); unit: mm/day); and (**b**, **e**, **f**) composites of IVT (shadow, unit: kg m^{-1} s^{-1}) and geopotential height at 500 hPa (grey contours, unit: gpm) during 19–21 July, 2021. Red fonts represent the predicted probability of regional extreme precipitation occurrence for the North cluster.

7. Conclusions

In this study, we proposed a hybrid model combining the multilayer perceptron and convolutional

neural network for predicting extreme precipitation over CEC, based on the anomalous fields of 500 hPa geopotential height and IVT. Conclusions are summarized as follows:

(1) The hybrid MLP-CNN model has the potential to predict the occurrence probabilities of extreme precipitation over CEC. It achieves convincing performance for binary classifications across the five clusters, with an average accuracy of 86%. MLP-CNN can correctly predict 91% (81%) of extreme precipitation days on training (testing) sets. For the seasonal extreme precipitation, the MLP-CNN accomplishes a balanced prediction.

(2) We conducted a comparison of MLP-CNN with the independent predictions from MLP and CNN, and two machine learning models (i.e., random forest and support vector machine). In terms of the three statistical evaluation metrics, MLP-CNN outperforms other models. Poor predictions of CNN and the two machine learning models mainly come from their insufficient learning abilities on imbalanced samples.

(3) Experiment of predictions in advance shows that the performance of MLP-CNN tends to decrease with the increasing leading days of circulation anomalies, but the 1–2 days' advance predictions can be considered as the reference to identify the extreme precipitation.

In summary, the hybrid MLP and CNN model is critical for improving the predictability of extreme precipitation, despite this approach lacks the information about the intensity and geographic locations. Thus, continued works are recommended to improve the usability of MLP-CNN, e.g., considering the region-based neural network, an approach for location recognition (Girshick et al., 2015; Lu et al., 2020; Yang et al., 2022b). Future works will encourage the comparisons of other deep learning models and broaden the applications in predicting extreme precipitation information in a warming climate.

CHAPTER-4. Performance of global circulation models in simulating extreme precipitation and large-scale atmospheric circulation

Summary

Global circulation models (GCMs) are the primarily tool for simulating the responses of climate system in the context of global warming. The objective of this study is to evaluate the performances of 10 CMIP6 GCM control runs in the simulations of extreme precipitation and large-scale atmospheric circulation over Central-Eastern China (CEC). Four indices were selected for the extreme precipitation evaluation. Referenced to the gauge-based daily precipitation analysis dataset (from 1960 to 2015) over the Chinese mainland (CGDPA), all GCMs have poor skill in simulating the extreme precipitation with severe underestimations. The self-organizing map was used to identify the circulation patterns (CPs) of GCMs based on the geopotential height at 500 hPa. Compared with the results of ERA5, GCMs can reflect most categories of the identified CPs. The MPI-ESM1-2-HR could be considered excellent according to its correctly capture the pattern labels.

1. Motivations

For the sixth phase of CMIP, more than 20 Model Intercomparison Projects (MIPs) were endorsed. They contain the atmospheric variables across the historical, future scenario, detection and attribution experiments for simulating and projecting climate changes. Compared to the previous generations, many improvements were included in the scientific focuses, physical modeling processes, and spatial resolutions of the global circulation models (GCMs) from CMIP6 (Stouffer et al., 2017). Furthermore, in order to know their data reliabilities and increase confidence for future projections, enormous evaluation works have been conducted on GCMs for precipitation and other atmospheric variables (Pimonsree et al., 2023; Srivastava et al., 2020; Wehner et al., 2020). However, little knowledge is

about the accuracies of GCMs in the identification of large-scale atmospheric circulation patterns (CPs) over CEC. To fill this gap, in this chapter, I focused on two research issues. 1) the accuracy of selected GCMs in estimating the historical extreme precipitation over CEC; and 2) their abilities to reproduce the spatial similarity and time variability of large-scale CPs. These evaluations can be received as a reference for selecting GCMs to conduct the precipitation downscaling in Chapter 5.

This chapter is structured as follows. After this section, the used datasets are presented. Section 3 describes the evaluation metrics. Because the meteorology of self-organizing map (SOM) was detailed in Chapter 2, we mentioned this approach here briefly. Section 4 presents the evaluation results on extreme precipitation and the large-scale circulation simulations of GCMs. Conclusions are summarized in section 5.

2. Datasets

2.1 Gauge-based data

The gauge-based daily precipitation analysis dataset (from 1960 to 2015) over the Chinese mainland (CGDPA) with 0.25°×0.25° spatial resolution was downloaded from the China Meteorological Data Service Centre (http://data.cma.cn/). This dataset was interpolated by more than 2400 rain gauges using the optimal climatological fields and its accuracy has been validated in previous studies (Shen and Xiong, 2016). In this study, CGDPA was selected as the "ground reference" to evaluate the performances of GCM historical data in precipitation simulation, rather than using gauge observations directly. It has been widely proven that point-to-pixel comparisons may produce errors from the spatial mismatch (Li et al., 2018a; Tostes et al., 2017).

2.2 ERA5

The fifth-generation atmospheric reanalysis (ERA5) of European Centre for the Medium-Range Weather Forecasts. This product provided the 0.25° daily geopotential height at 500 hPa pressure level for the period of 1960 to 2015, as well as the "reference of CPs classification" to evaluate the performance of GCMs.

2.3 GCMs

In this study, evaluation variables are the total precipitation (unit: mm/day, converted from the precipitation flux, kg m^{-2} s^{-1}) and geopotential height at 500 hPa (unit: gpm). We examined all GCMs available in CMIP6 and found that only 14 models included these two variables in both historical and future scenarios. Besides, some models are missing data over the Qinghai-Tibet Plateau. Finally, 10 GCMs of CMIP6 were downloaded from the World Climate Research Programme (https://esgf-data.dkrz.de/search/cmip6-dkrz/). These include the low resolution version of Hadley Centre Global Environment Model in the Global Coupled configuration 3.1 (HadGEM3-GC31-LL), the United Kingdom Earth System Model (UKESM1-0-LL), the new version of Australian Community Climate and Earth System Simulator coupled model (ACCESS-CM2), the Canadian Earth System Model version 5 (CanESM5), the Flexible Global Ocean-Atmosphere-Land System Model Grid-Point Version 3 (FGOALS-g3), the IITM Earth System Model (IITM-ESM); the medium resolution models of the Norwegian Earth System Model (NorESM2-MM), the Model for Interdisciplinary Research on Climate version 6 (MIROC6), the Meteorological Research Institute Earth System Model version 2.0 (MRI-ESM2-0); and the high resolution version of the Max Planck Institute for Meteorology Earth System Model (MPI-ESM1-2-HR). These GCMs were coupled atmospheric, ocean, sea ice, and land-surface models. For instance, MPI-ESM1-2-HR used the ECHAM6.3 for atmospheric (95 levels), MPIOM for the ocean and sea ice, and JSBACH for the land-surface models (Müller et al., 2018). The spatial resolution and variant label of the 10 GCMs are presented in Table 4-1.

Table 4-1. Detailed information for used GCMs.

Model	Resolution	Variant label	Sub models*	Reference
HadGEM3-GC31-LL	T144×T192	r1i1p1f3	MetUM-HadGEM3-GA7.1, NEMO-HadGEM3-GO6.0, CICE-HadGEM3-GSI8, JULES-HadGEM3-GL7.1	Andrews et al. (2020)
UKESM1-0-LL	T144×T192	r1i1p1f2	MetUM-HadGEM3-GA7.1, NEMO-HadGEM3-GO6.0, CICE-HadGEM3-GSI8 JULES-ES-1.0	Sellar et al. (2019)

ACCESS-CM2	T144×T192	r1i1p1f1	MetUM-HadGEM3-GA7.1, ACCESS-OM2, CICE5.1.2, CABLE2.5	Bi et al. (2020)
CanESM5	T64×T128	r1i1p1f1	CanAM5, NEMO3.4.1, LIM2, CLASS3.6/CTEM1.2	Swart et al. (2019)
FGOALS-g3	T80×T180	r1i1p1f1	GAMIL2, LICOM3, CICE4.0, CLM4	Li et al. (2020)
IITM-ESM	T94×T192	r1i1p1f1	IITM-GFSv1, MOM4p1, SISv1, NOAH LSMv2.7.1	Krishnan et al. (2019)
NorESM2-MM	T192×T288	r1i1p1f1	CAM-OSLO, MICOM, CICE, CLM	Seland et al. (2020)
MIROC6	T128×T256	r1i1p1f1	CCSR AGCM, COCO4.9, MATSIRO6.0	Tatebe et al. (2019)
MRI-ESM2-0	T160×T320	r1i1p1f1	MRI-AGCM3.5, MRI.COM4.4, HAL1	Oshima et al. (2020)
MPI-ESM1-2-HR	T192×T384	r1i1p1f1	ECHAM6.3, MPIOM, JSBACH	Müller et al. (2018)

Notes: *Atmospheric, ocean, sea ice, and land-surface models in sequence.

Considering the available period of historical data is only up to 2014, the simulation data from 2015 under the highest greenhouse gases emission scenario that is more close to the current states (Schwalm et al., 2020) were used as the historical data, in order to be consistent with the time period of ERA5. Additionally, all GCMs were resampled into a resolution of 0.25°×0.25° regular pixel using the nearest interpolation.

3. Methods

3.1 Extreme precipitation indices

Five precipitation indices recommended by the World Meteorological Organization (Alexander et al., 2020; Karl et al., 1999) were used in this study, which include 1) SDII: mean daily precipitation amount for the wet days (daily precipitation >0.1 mm) per year; 2) Rx1day: annual maximum daily precipitation amount; 3) R95p: annual accumulated precipitation amount from the wet days exceeds

the 95th threshold during 1960 to 2015; 4) R99p: same as 4) but for the 99th percentile; 5) R50mm: annual accumulated precipitation amount from the days higher than 50 mm. The last four indices indicate the behaviours of extreme precipitation.

3.2 Clustering of circulation patterns

CPs of the four GCMs were identified by the SOM based on the standardized GP at 500 hPa. Detailed methodology of SOM was presented in Section 3.2 (Chapter 2). In this chapter, we referenced the SOM node size of ERA5 (i.e., 5×5) to identify the CPs of GCMs during the periods 1960–1989 and 1990–2015. Subsequently, the binary time sequences per CP of GCMs were obtained.

3.3 Evaluation metrics

Two aspects of GCMs behavior are crucial: their performance for precipitation estimations, especially for extreme precipitation. Another is on the simulations of large-scale CPs. Firstly, two indicators, i.e., coefficient of variation of root mean square error (CVRMSE) and relative bias (RB) were used to evaluate the accuracy of GCMs in extreme precipitation estimations. The CVRMSE measures the normalized error of GCMs and RB quantifies the bias of GCMs. The negative (positive) value of RB represents an underestimation (overestimation) of GCMs to the reference dataset.

$$\mathrm{CV}RMSE = \frac{\sqrt{\frac{1}{n}\sum_{i=1}^{n}(G_i - R_i)^2}}{\bar{R}} \tag{4-1}$$

$$RB = \frac{\sum_{i=1}^{n}(G_i - R_i)}{\sum_{i=1}^{n} R_i} \times 100 \tag{4-2}$$

where G_i (R_i) is the precipitation estimates from GCMs and CGDPA during 1960–2015, respectively. n indicates the number of target samples.

The matrix Euclidean distance (EUdistance) was selected for the examination of whether the GCMs simulate the identified CPs well during the two periods 1960–1989 and 1990–2015. It provides us with the spatial similarity information of GCMs to the ERA5.

$$EUdistance = \sqrt{\sum_{k=1}^{K}(x_{c,k} - y_{c,k})^2} \tag{4-3}$$

where $x_{c,k}$ ($y_{c,k}$) indicates the two-dimensional CP identified by GCMs (ERA5). c and k are the row and column index of a pixel. K is the total number of pixels.

Subsequently, the performances of GCMs in reproducing the temporal variabilities of identified CPs were investigated using two indicators, that is, frequency and persistence, which followed Gibson et al. (2016)'s research.

$$Frequency_j = \frac{N_j}{m} \times 100 \tag{4-5}$$

$$Persistence_j = \frac{ND2_j}{ND1_j} \tag{4-6}$$

where $Frequency_j$ is the percentage for a CP j occurrence during a period. N and m represent the total days of CP j and samples, respectively. $Persistence_j$ quantifies the ratio of the total number of events for CP j that occurs for two or more consecutive days ($ND2_j$) to only one day ($ND1_j$).

4. Results

4.1 Evaluation of extreme precipitation simulations

4.1.1 General analysis of annual precipitation

Figure 4-1 shows the spatial distributions of the mean annual precipitation during 1960–2015 estimated by CGDPA and GCMs. Overall, except for the FGOALS-g3, most GCMs can reproduce the main climatological patterns of annual precipitation, that is, the southeast coastal receives more precipitation than the north and northwest areas. Noted that a wet bias is prominent over the southern CEC among HadGEM3-GC31-LL, UKESM1-0-LL, and ACCESS-CM2. The three GCMs used the MetUM-HadGEM3-GA7.1 atmospheric sub-model coupled in the physical and parameterization processes, which has been discussed in previous studies this sub-model had errors in modeling cloud cover (Kuma et al., 2020) and tropospheric circulation that may lead to the biased precipitation (Liu et al., 2021b). Besides, CanESM5, IITM-ESM, NorESM2-MM, and MIROC6 (FGOALS-g3) over (under) predicted precipitation over northwestern CEC.

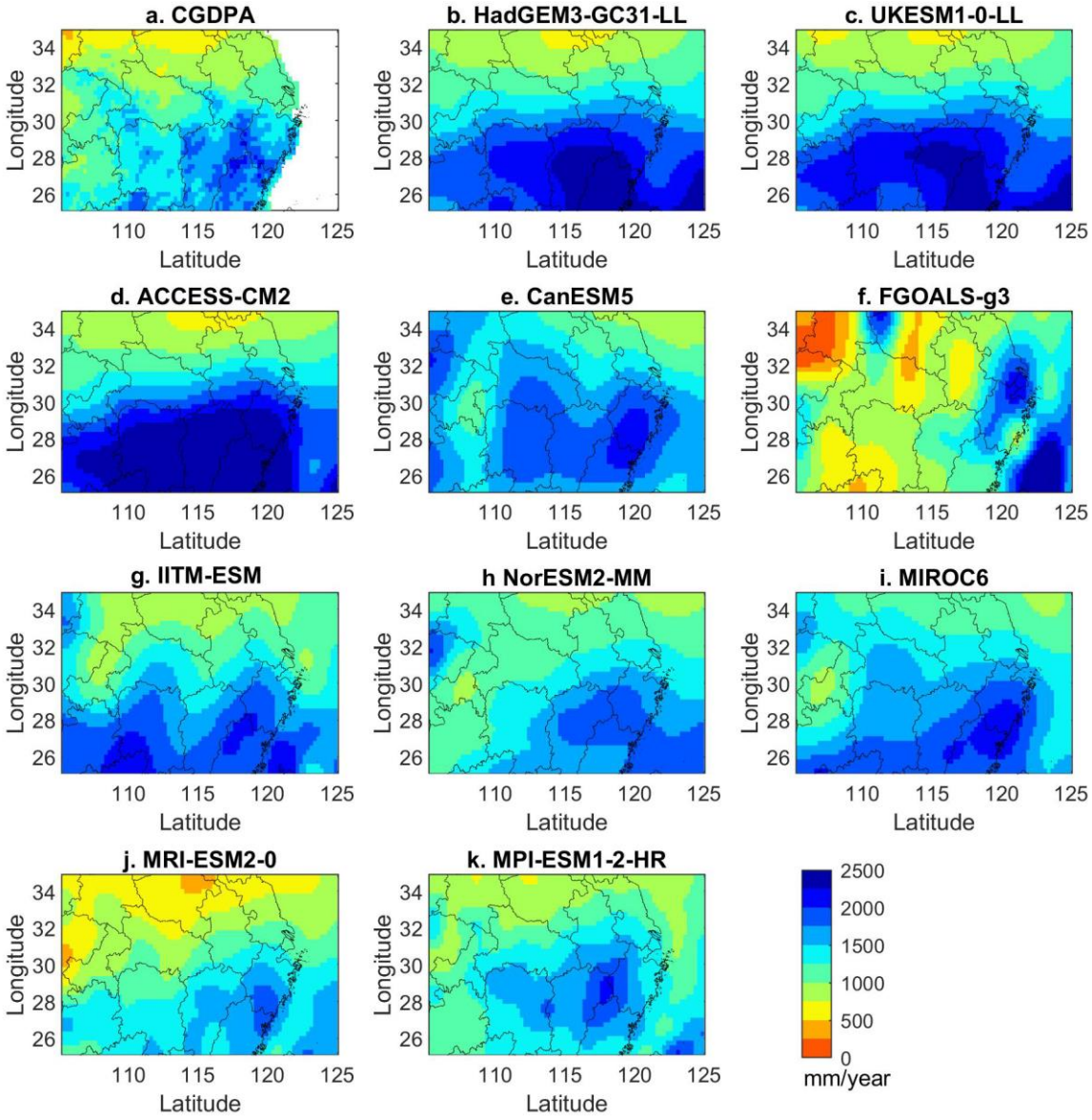

Figure 4-1. Spatial distributions of mean annual precipitation from 1960 to 2015 for (**a**) CGDPA and (**b-k**) GCMs.

4.1.2 Error metrics

A comparison of GCM precipitation against the CGDPA was implemented, by the statistics of CVRMSE and RB. As shown in Figure 4-2, all GCMs exhibit large errors in simulating extreme precipitation amounts reflected by the CVRMSE values, as well as an evident underestimation, in terms of the RB indicator. Except for the SDII, the underestimations of GCMs in the remaining metrics are higher than 85%. Even for the higher resolution GCM (~0.9°), MPI-ESM1-2-HR also exhibit severe underestimation in representing the extreme precipitation. These results inform us that do not directly use the precipitation variable from GCMs to examine the extreme precipitation.

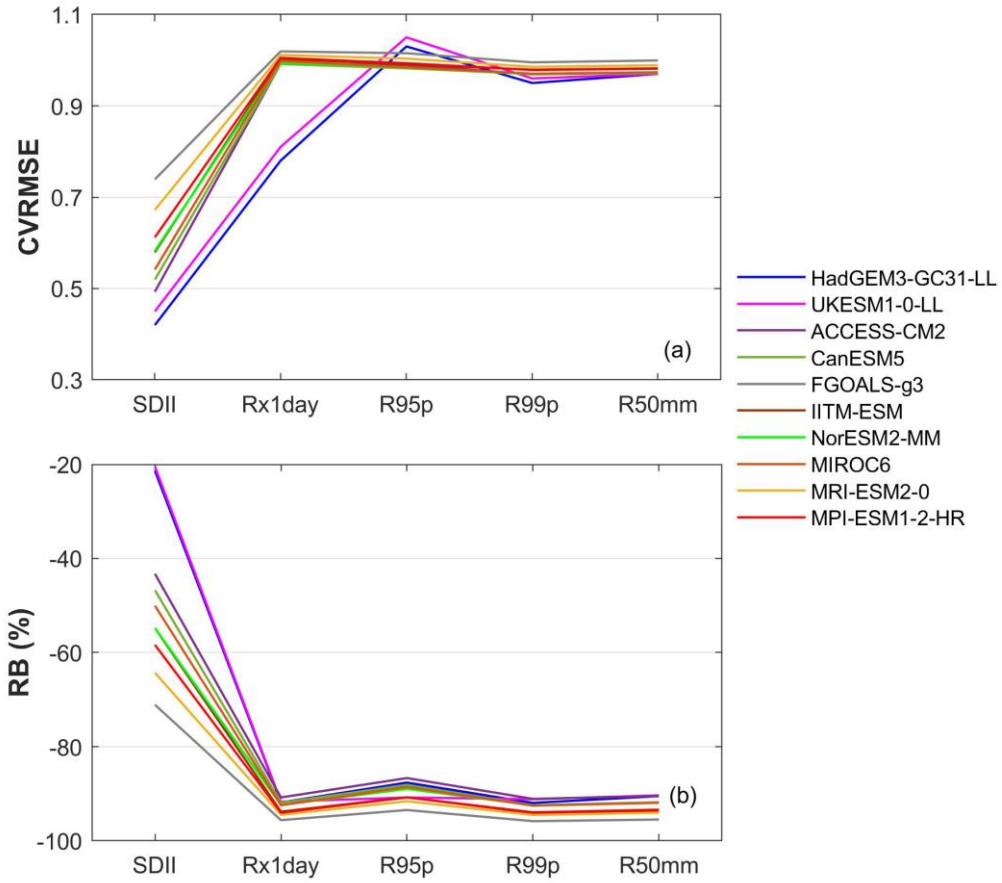

Figure 4-2. Error metric results for the GCMs.

4.2 Evaluation of circulation patterns simulation

4.2.1 Geopotential height at 500 hPa

Figure 4-3a represents the time series of regional-averaged, annual mean GP at 500 hPa derived from ERA5 and the 10 GCMs. Obviously, GCMs of CMIP6 have a marked bias compared to the ERA5. FAOALS-g3, MPI-ESM1-2-HR, and NorESM2-MM show a positive bias, whereas large underestimation is predominant for IITM-ESM and MIROC6. In order to eliminate these systematic deviations, the original data of ERA5 and 10 GCMs were subtracted its own average of 1960–2015, respectively. As shown in Figure 4-3b, after the simple bias correction procedure, most GCMs can reproduce the increasing trends of GP at 500 hPa, while the annual anomalies of GP depicted by the NorESM2-MM performs the worst compared with that of ERA5, followed by CanESM5.

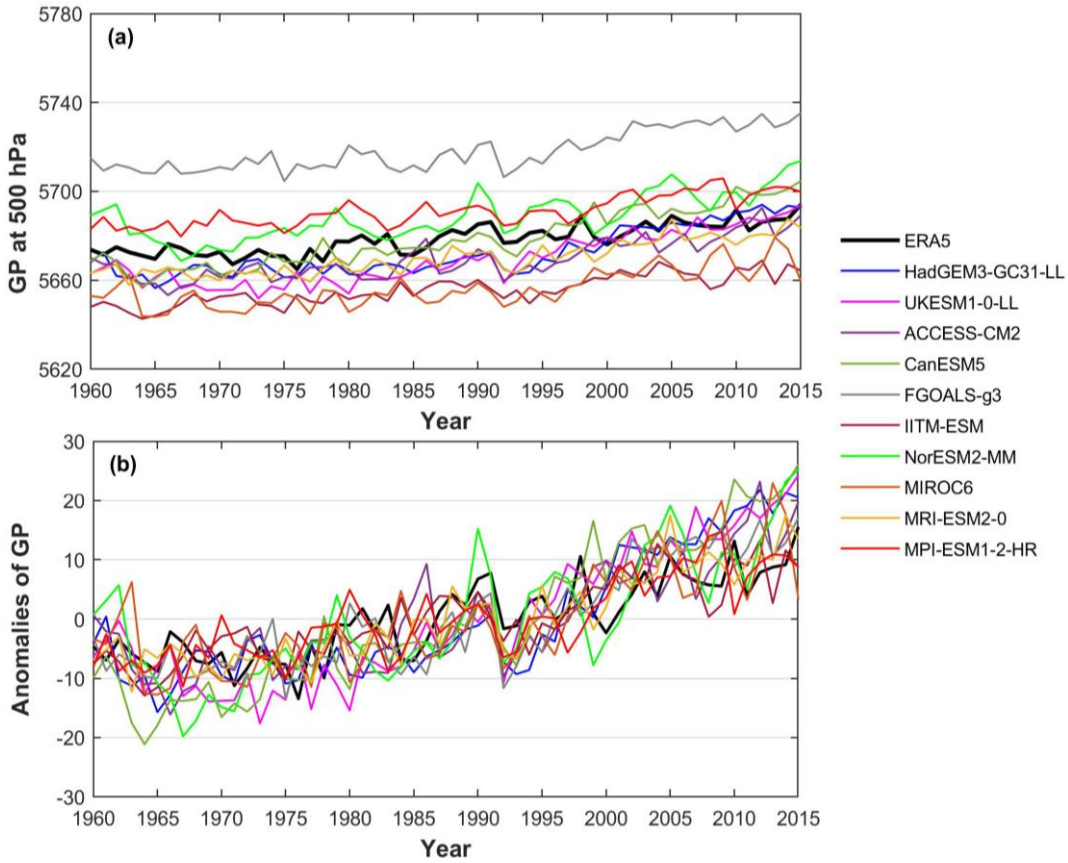

Figure 4-3. Changes of (**a**) regional-averaged, annual mean of geopotential height at 500 hPa of ERA5 and GCMs and (**b**) anomalies of geopotential height during the period 1960–2015.

4.2.2 Identified circulation patterns of GCMs

In order to rank the skills of the 10 GCMs in simulating the large-scale atmospheric circulation, we constructed the 5×5 SOM maps for each GCM independently. The identified CPs by GCMs were examined on spatial similarities and related statistic characteristics (e.g., frequency and persistence) with respect to the results of ERA5. Considering space limitations, we only used the HadGEM3-GC31-LL, NorESM2-MM, and MPI-ESM1-2-HR (representing the low, medium, and high spatial resolution models, respectively) as examples; The detailed description is as follows. Figures 4-4–4-6 show the identified CPs by SOM of HadGEM3-GC31-LL, NorESM2-MM, and MPI-ESM1-2-HR during the two periods of 1960–1989 and 1990–2015. These maps are arrayed in five columns (labeled A to E and A′ to E′, respectively) and five rows (labeled 1 to 5). Shadows represent the anomalous fields of each CP. Obviously, there are dominated by a strong positive anomaly over the east Eurasian and adjacent oceans for CPs A1 to B2 (and A′1 to B′2), whereas CPs D4 to E5 (and D′4 to E′5) display the opposite modes. CPs on the diagonals of the top-left and bottom-right differ

substantially from the north-south anomalies information of GP. The principal features of the morphological information demonstrate that during the two periods, the identified CPs from GCMs are visually consistent with the results of ERA5 presented in Section 4.1, Chapter 2.

Despite the resulting similar anomalies distributions, the four GCMs also exhibit some discrepancies compared to ERA5. For example, HadGEM3-GC31-LL underestimates the positive anomalies over southeast Asia of CPs A1 and B1, while overestimates the positive anomalies over north Asia of CPs A′2 and A′3 (Figure 4-4); NorESM2-MM shows weaker positive anomalies over north Asia of CPs A4–A5 and A′5–B′5 (Figure 4-5); and an underestimation of the positive anomalies over the southeast Asia is found in C1, E1, and E′1 for MPI-ESM1-2-HR (Figure 4-6).

(1) Spatial similarity

To fairly know how similar, the identified CPs of GCMs are to ERA5, the matrix Euclidean distance and correlation coefficient were computed to measure the pattern structure differences. In general, referencing the results of ERA5, when the corresponding CP identified by GCMs (on the diagonal) has the lowest Euclidean distance and higher correlation coefficient indicates that GCMs can simulate this CP well. Otherwise, suggesting that models are hard to give ascertain classifications and identified CPs are dissimilar to that of ERA5. Figures 4-7–4-8 shows the matrix of Euclidean distance for the identified CPs of GCMs compared to that of ERA5 in the period 1960–1989 and 1990–2015. Overall, GCMs can reproduce most types of the CPs identified by ERA5. CPs on the diagonal of UKESM1-0-LL, HadGEM3-GC31-LL, and MPI-ESM1-2-HR in the period 1960–1989 and the latter two in the period 1990–2015 are closed to the ERA5, with the lowest Euclidean distance. The dissimilarity of CPs is also found when details are analyzed. CP A2 of ACCESS-CM2 is dissimilar to that one of ERA5, due to the CP A1 having the lowest Euclidean distance (Figure 4-7c). Similarly, we can prove that C1 of CanESM5, A1 of FGOALS-g3, IITM-ESM, NorESM2-MM and MIROC6, E1 of MRI-ESM2-0, A′1 of UKESM1-0-LL, CanESM5, FGOALS-g3, IITM-ESM, NorESM2-MM and MIROC6 are dissimilar to that of ERA5.

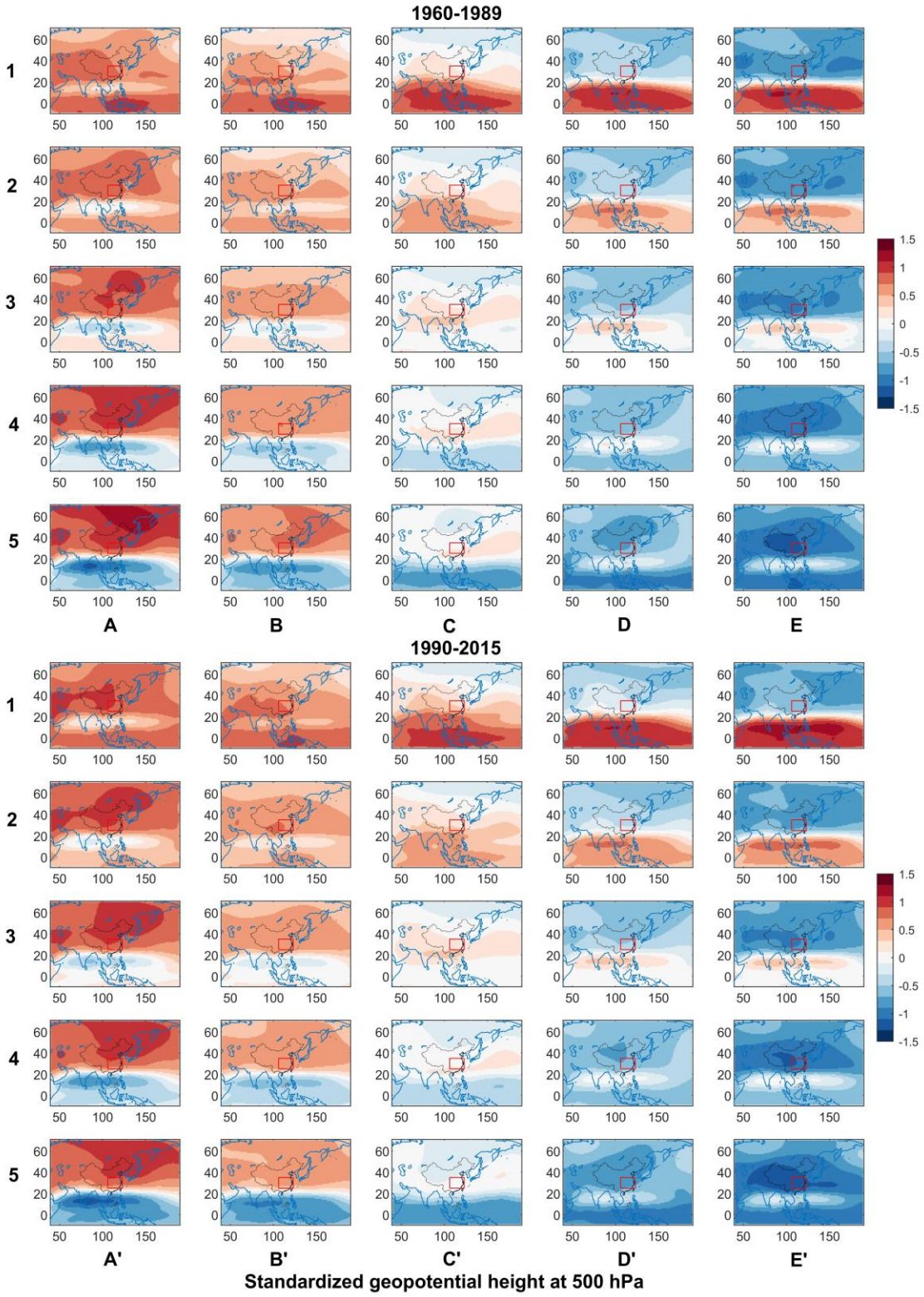

Figure 4-4. The identified circulation patterns of standardized geopotential height at 500 hPa from the HadGEM3-GC31-LL during the periods 1960–1989 and 1990–2015, respectively. Shadow indicates the anomaly fields.

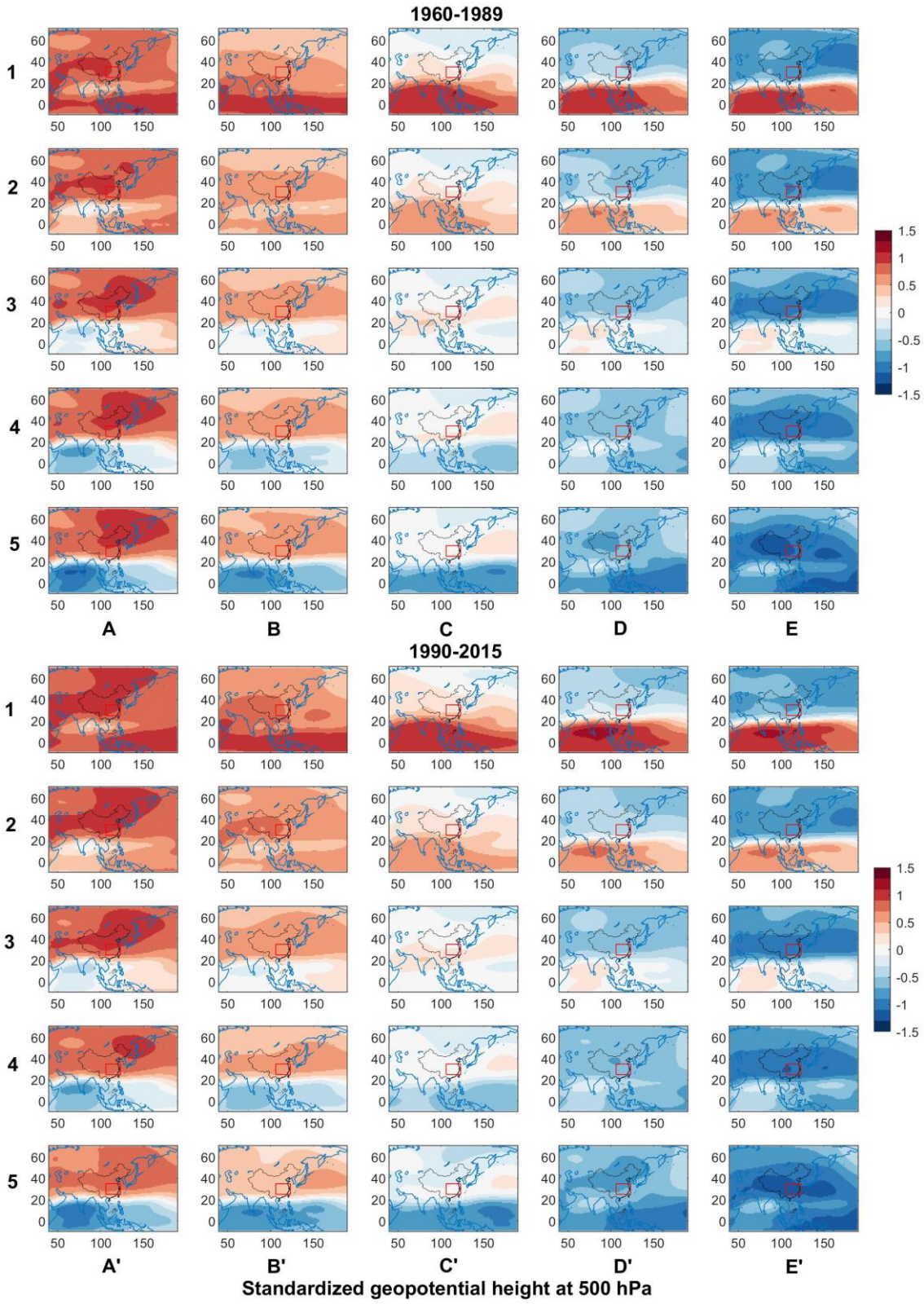

Figure 4-5. Same as Figure 4-4, but for NorESM2-MM.

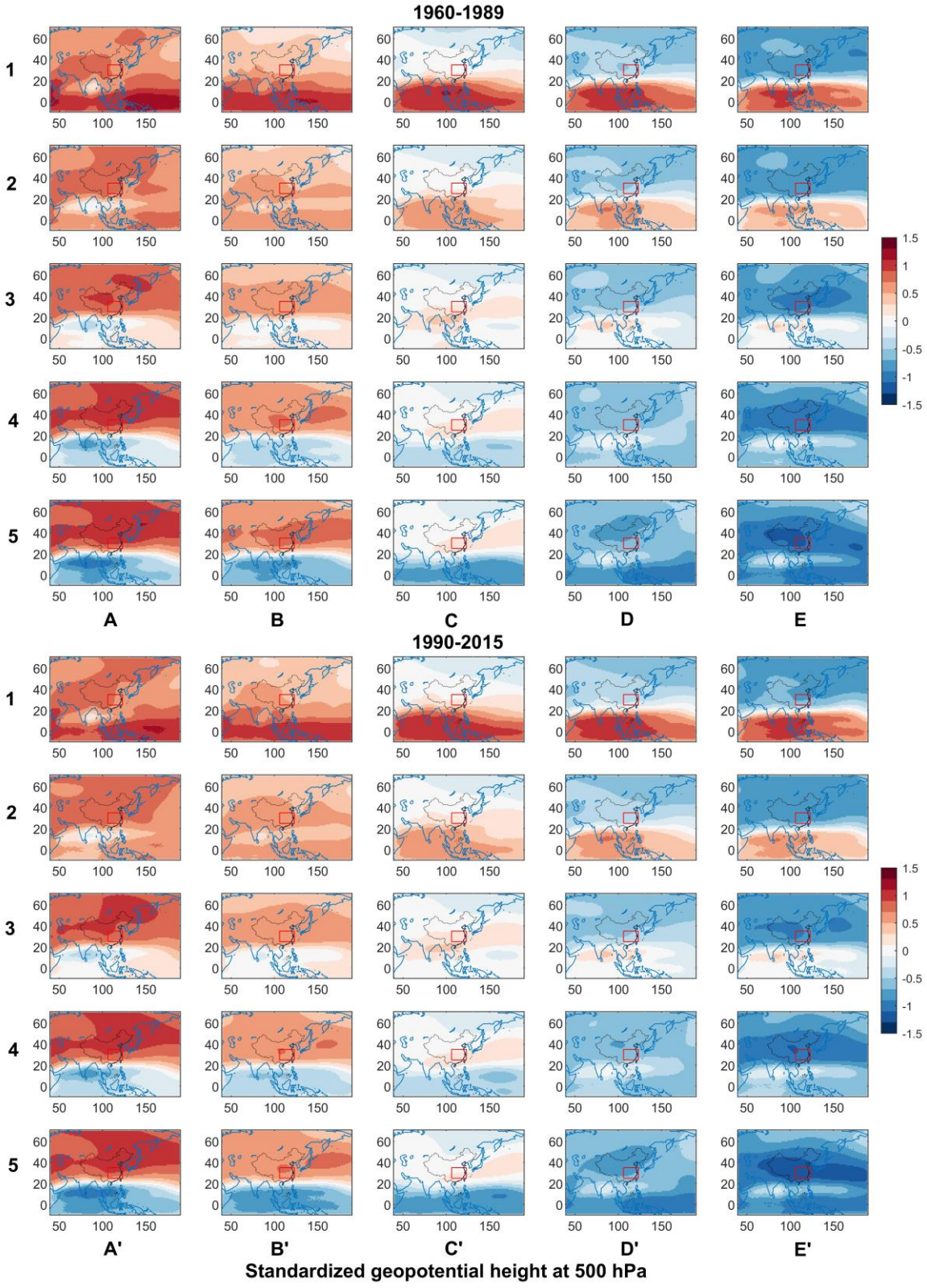

Figure 4-6. Same as Figure 4-4, but for MPI-ESM1-2-HR.

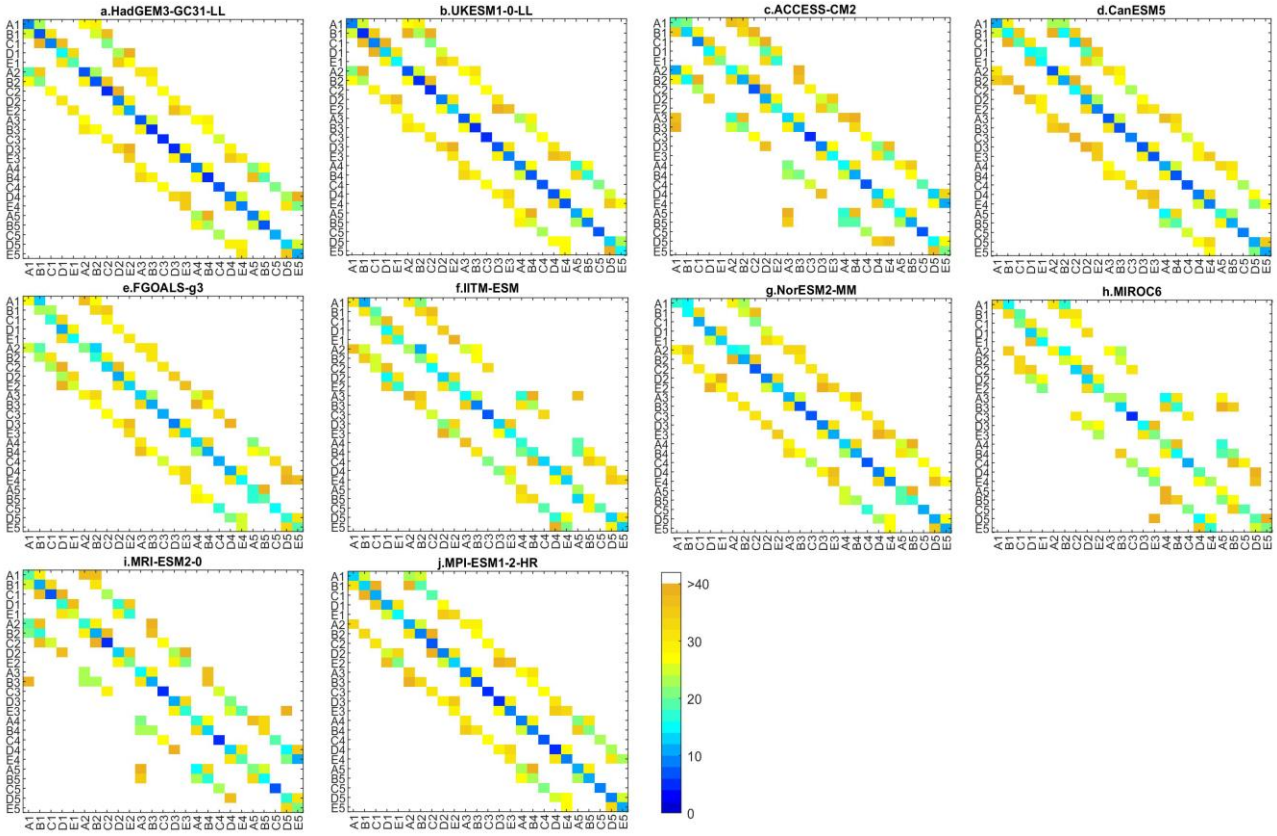

Figure 4-7. Matrix of Euclidean distance for the identified circulation patterns of GCMs compared to that of ERA5 in the period 1960–1989.

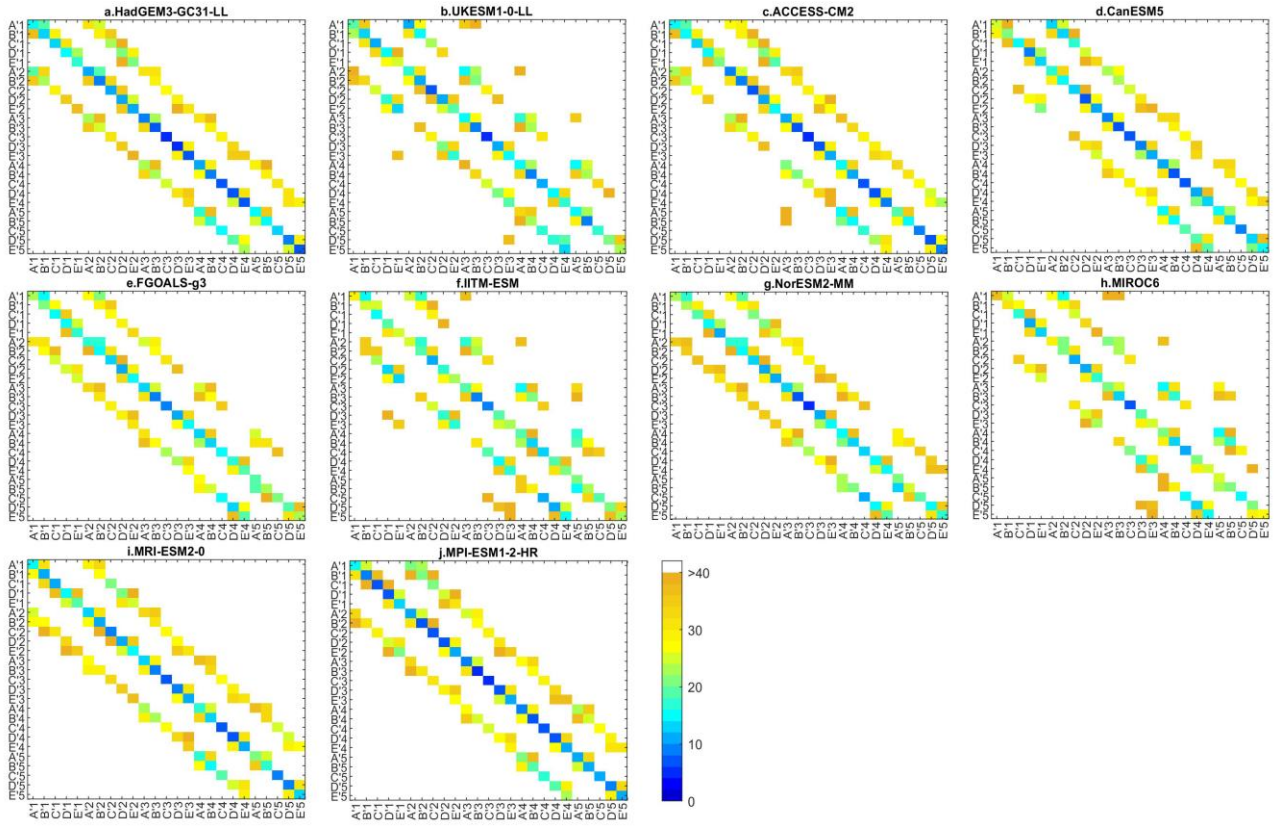

Figure 4-8. Same as Figure 4-7, but for the period 1990–2015.

Figure 4-9 shows the Euclidean distance and correlation coefficient for the CPs identified by GCMs with respect to ERA5. In most cases, the CPs of FGOALS-g3, IITM-ESM, and MIROC6 are poor than other models, with a large Euclidean distance and low correlation. MPI-ESM1-2-HR could be considered excellent because its produced CPs are considerably convincing.

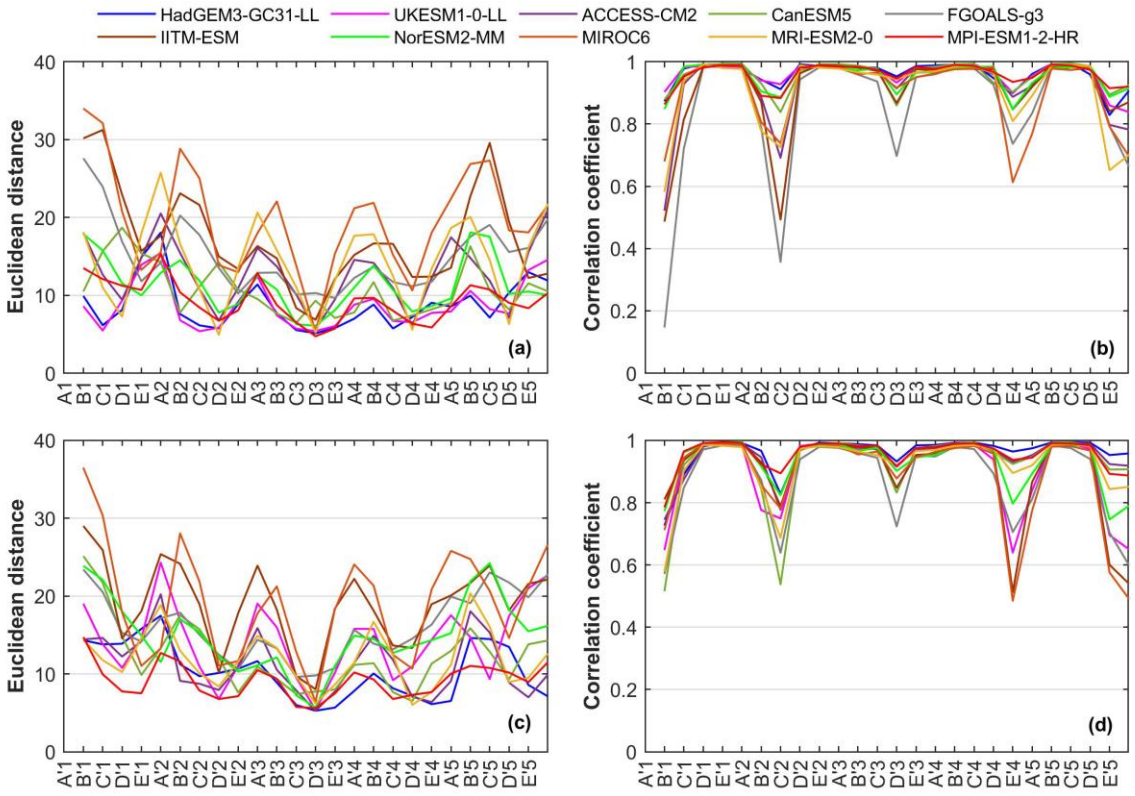

Figure 4-9. Euclidean distance and correlation coefficient for the identified circulation patterns of GCMs compared to that of ERA5 in the two periods (**a**) 1960–1989 and (**b**) 1990–2015.

(2) Temporal variabilities

Figures 4-10–4-11 show the frequency and persistence of the identified CPs of ERA5 and GCMs during the two periods. Overall, CPs A5 and A′5 had the highest occurrences (9.35%, 9.19%) in 1960–1989 and 1990–2015, respectively, followed by E5 and E′5. FGOALS-g3, IITM-ESM, and MIROC6 false alarmed the dominant CP and overestimated the frequency of CPs A1 and A′1. CanESM5 and MRI-ESM2-0 (UKESM1-0-LL, NorESM2-MM, and MPI-ESM1-2-HR) showed an overestimation (underestimation) of CPs A5 and A′5 frequencies. Meanwhile, GCMs generally exhibits worse performance in reproduce the persistence of CPs A5 to E5 and A′5 to E′5. Additionally, ACCESS-CM2 (HadGEM3-GC31-LL) has a systematic overestimation at the number of CPs C1 to E1, A′1, and E′1 (C1, C′1, and D′1). In terms of pattern persistence, MPI-ESM1-2-HR performs best (Table

4-3). Overall, GCMs display promising skill in simulating large-scale circulation patterns and related time variabilities.

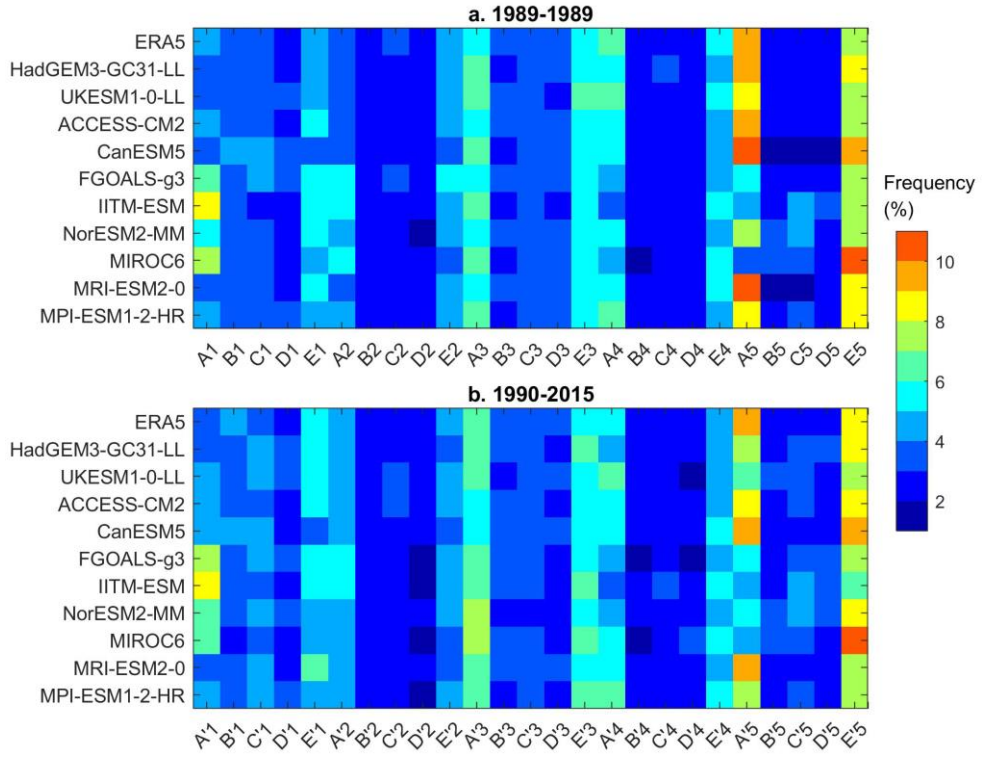

Figure 4-10. Frequency (%) of the identified circulation patterns of ERA5 and GCMs during the two periods (**a**) 1960–1989 and (**b**) 1990–2015.

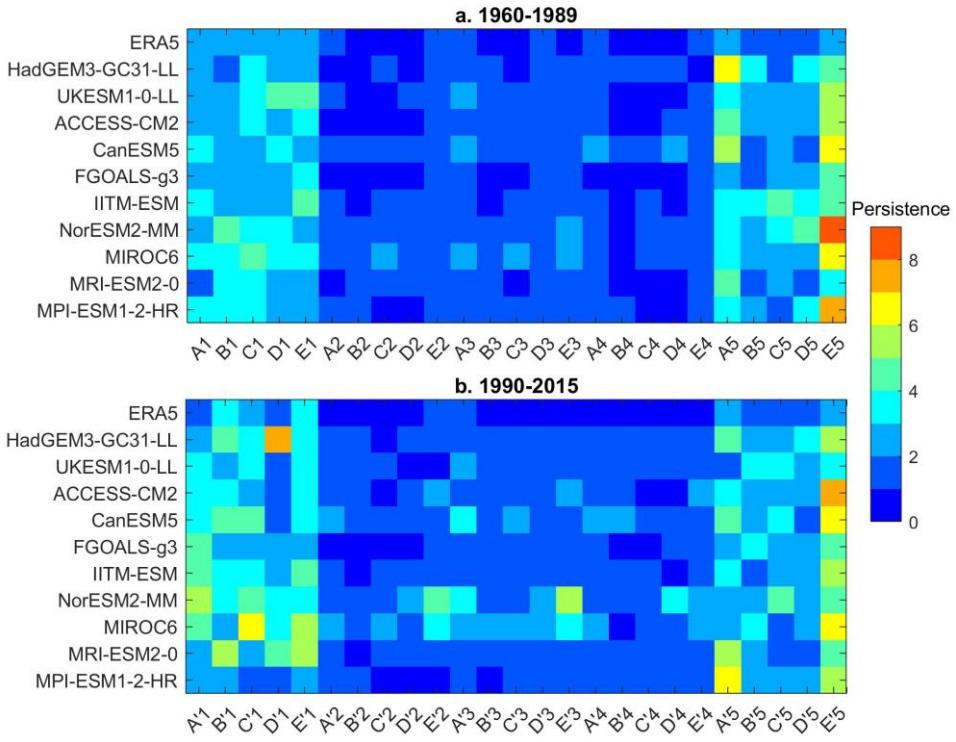

Figure 4-11. Persistence of the identified circulation patterns of ERA5 and GCMs during the two periods (**a**) 1960–1989 and (**b**) 1990–2015.

5 Conclusions

In this study, the performances of 10 GCMs of CMIP6 in extreme precipitation and large-scale atmospheric circulation simulations were evaluated over CEC. Conclusions are summarized as follows.

(1) Four indices (i.e., SDII, Rx1day, R95p, R99p, R50mm) were selected to define the extreme precipitation. Compared to the gauge-based daily precipitation analysis dataset over the Chinese mainland (CGDPA), GCMs are difficult to accurately estimate the extreme precipitation amounts. Extreme precipitation from GCMs are weaker than CGDPA, with an underestimation exceeds 80%.

(2) The GCMs can reproduce the observed increasing trends of geopotential height at 500 hPa well. Relative to the identified CPs of ERA5, GCMs can reflect most categories accurately, and MPI-ESM1-2-HR could be considered excellent according to its correctly capture the pattern labels. In terms of two indicators, that is, frequency and persistence, GCMs display promising skills.

The present study provides a reference for selecting GCMs to conduct the precipitation and circulation patterns simulations. We assume that GCMs cannot be directly used for extreme precipitation studies, therefore a possible direction is to improve the reliabilities of GCMs in estimating extreme precipitation.

CHAPTER-5. Precipitation downscaling and future projections using large-scale atmospheric circulation features

Summary

Global climate models (GCMs) are routinely used to project future climate conditions worldwide, as temperature and precipitation. However, inputs with a finer resolution are required to drive impact-related models at local scales. The nonhomogeneous hidden Markov model (NHMM) is a widely used algorithm for the precipitation statistical downscaling for GCMs. To improve the accuracy of the traditional NHMM in reproducing spatio-temporal precipitation features of specific geographic sites, especially extreme precipitation, we developed a new precipitation downscaling framework. This hierarchical model includes two levels: 1) established an ensemble learning model to predict the occurrence probabilities for different levels of daily precipitation aggregated at multiple sites; and 2) constructed a NHMM downscaling scheme of daily amount at scale of single rain gauge using the outputs of ensemble learning model as predictors. As the results obtained for the case study in the central-eastern China, show that our downscaling model is highly efficient and performs better than the NHMM in precipitation variability and extreme precipitation simulations. Finally, our projections indicate that CEC may receive more precipitation in the future. Compared with ~26 years (1990–2015), the extreme precipitation frequency and amount would significantly increase by 21.9–48.1% and 12.3–38.3% respectively, by the late century under the worst emission scenario. We believe that our model can advance downscaling tools and lead to further improvement in future simulations.

1. Motivations

In an attempt to overcome the limitations of NHMM downscaling presented in Section 2.4.1, Chapter 1, a slight modification of this downscaling framework based on which an intermediate exogenous predictor was introduced, that is, the daily precipitation probabilities at different percentiles of an ensemble of rain gauges. The dependence of such intermediate predictors on atmospheric predictors

was learned and predicted using machine learning models. The proposed scheme can be considered as a hierarchical model with the occurrence probability prediction of the aggregate behavior of the ensemble of multi-site precipitation at the first level. Subsequently, statistical precipitation characteristics for each single rain gauge were obtained using the NHMM.

It remains how the daily precipitation amount can be classified into more than two levels and give the occurrence probabilities to modelling the stochastic process of precipitation. Based on the development of machine learning techniques, it is possible to construct a model that combining the classifiers (e.g., random forest, RF; support vector machine, SVM; gradient boosting, GB) to directly handle the prediction tasks with multi-class classification (Tsoumakas and Katakis, 2007). Conventionally, ensemble-based approach is famous for "put heads together" on one learning task, which allows for optimally combining the outputs of different basic learners to give the best prediction (Ahmed et al., 2020; Zhou, 2021; Zounemat-Kermani et al., 2021). When adopted for class-imbalanced data, ensemble learning generally, achieves good performance through fast iteration (Bansal et al., 2021). For instance, Kadavi et al. (2018) constructed an ensemble model with four meta classifiers to estimate the levels of landslide susceptibility in South Korea. Rahman et al. (2021) developed a multi-class flood probabilities assessment model for Bangladesh by stacking different meta classifiers to maximize the accuracy. The results showed that the ensemble model had the lowest overfitting possibility. However, studies on ensemble learning for multi-level daily precipitation probabilities prediction using the large-scale atmospheric circulation factors are scarce.

Therefore, we considered the ensemble learning to predict the occurrence probability of different levels of daily precipitation aggregated at multiple sites. The geopotential height (GP) at 500 hPa and the vertically integrated water vapor transport (IVT) were selected as key factors affecting the precipitation occurrence (Conticello et al., 2018). Furthermore, the predicted probabilities were used as the predictors to model the transitional probabilities of hidden states in the NHMM. We determined if such a difference in predictors can improve the accuracy of downscaled precipitation of the NHMM results. The aims of this chapter were as follows: (1) design an ensemble learning model for predicting the probability of daily precipitation events with different intensities; (2) improve the accuracy of the NHMM model with respect to precipitation simulation, especially on extreme events; (3) project the future precipitation and extremes possible changes over central-eastern China (CEC) under low-,

medium-, and high- emission scenarios; and (4) attempt to explain the thermodynamic and dynamic factors in affecting the projected changes.

This chapter is comprised of six sections. Datasets are introduced in Section 2. The proposed stacked ensemble learning and NHMM downscaling model and the basic steps of the methodology are described in Section 3. Detailed results are provided in Section 4, discussion and conclusions are presented in Section 5 and 6, respectively.

2. Datasets

Daily precipitation observations (1960–2015) were recorded at 228 gauges. One reanalysis product, the fifth generation ECMWF atmospheric reanalysis (ERA5) with 0.25° spatial resolution was obtained from the Copernicus Climate Change Service (C3S) Climate Date Store. One Global Circulation Model (GCM) of the Coupled Model Intercomparsion Project Phase 6 (CMIP6), that is, MPI-ESM1-2-HR (0.9°×0.9°) was downloaded from the Max Planck Institute for Meteorology, Germany. We have examined the performances of 10 GCM models to estimate the GP at 500 hPa, presented in Chapter 4 and found MPI-ESM1-2-HR yielded the best accuracy. The results of previous studies also confirmed that MPI-ESM1-2-HR can be applied to the NHMM for simulations (Guo et al., 2022). Thus, we only used MPI-ESM1-2-HR and obtained its historical simulation (from 1960 to 2014) and three climate scenarios with different shared socioeconomic pathways (SSP126, SSP245, and SSP585 from 2015 to 2100) to analyze the future precipitation projection. The three scenarios with different levels of radiative forcing, limit the possible states of the Earth's future. Among them, the dominant factor is the level of anthropogenic influence (Meinshausen et al., 2020), including human-induced greenhouse gas and aerosol emissions and land use changes, etc. SSP126 represents the SSP-1 with low emission scenario limiting global warming on land to 1.61 ℃ by 2100. SSP245 is a medium radiative forcing scenario with SSP-2 socioeconomic conditions. SSP585 is the worst forcing pathway based on SSP-5 and has the highest emissions (Tebaldi et al., 2021). To be consistent with the rain gauge period, data from 2015 under the SSP585 scenario were used as the historical data. Additionally, the spatial resolution of the MPI-ESM1-2-HR was resampled to 0.25° using the nearest interpolation method. The used variables of ERA5 and MPI-ESM1-2-HR are GP at 500 hPa, specific humidity and u/v wind fields from 250 to 1000 hPa.

3. Methodology

In this study, we describe the stacked ensemble learning and nonhomogeneous hidden Markov models ("Ensemble-NHMM") which is proposed for precipitation downscaling (Figure 5-1).

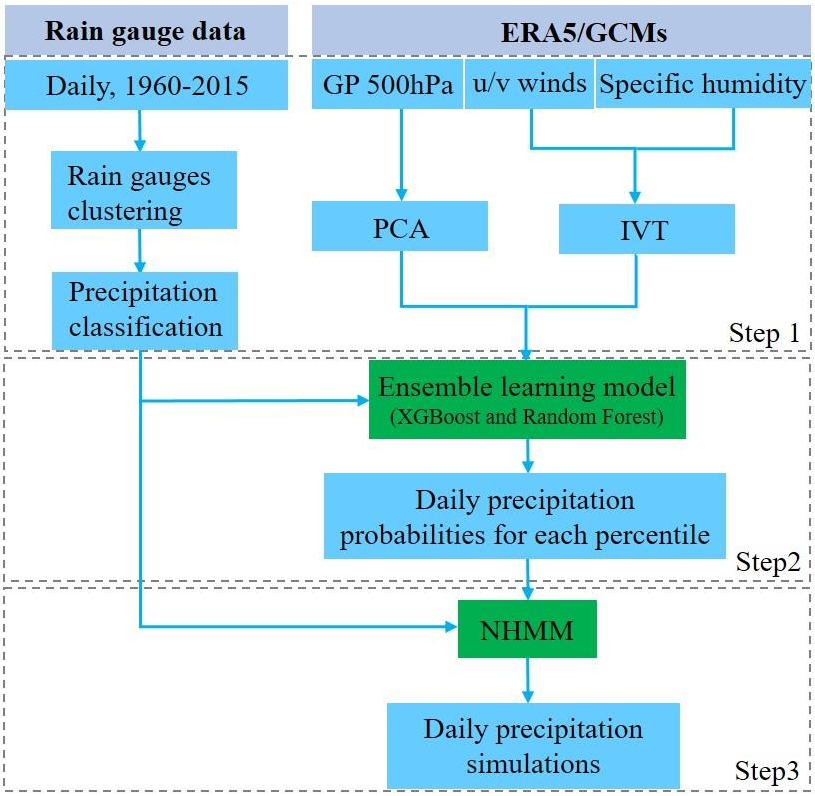

Figure 5-1. Flow chart of the proposed downscaling framework.

The overall structure consists of three steps: data preprocessing, ensemble learning model, and NHMM. We first elaborate on the preprocessing approaches for daily precipitation and reanalysis data. In step 2, we provide the details for predicting the multi-level daily precipitation probabilities based on the ensemble learning model. In the following subsection, a brief summary of the use of the NHMM based on the results of the ensemble learning model for precipitation downscaling is presented.

3.1 Data preprocessing

The network of gauges had been classified into different clusters through a community detection algorithm, by looking at the event synchronization degree of extreme precipitation occurrences among these rain gauges. This chapter uses the existing gauge clustering results, as shown in Figure

3-2 (Chapter 3).

Secondly, the daily precipitation was converted into categorical data. Let Y_t be a vector that denoting the observed precipitation levels on day t.

$$Y_t = max(Pr_t \geq Pr_x^*) \quad (5\text{-}1)$$

where Pr_t is the original precipitation amount averaged by all rain gauges across a cluster, Pr_x^* indicates the precipitation thresholds of Pr_t at different percentiles (no rain; 0.1 mm/day, 30th, 60th, and 95th), and $max(.)$ is a transform function that yields maximum levels on day t for Pr_t. Table 5-1 shows the specific intervals corresponding to the different precipitation percentiles for the five clusters. Based on the intervals, we named the precipitation levels as follows: no event (I), very light precipitation (II), light precipitation (III), moderate precipitation (IV), and heavy precipitation (V).

Table 5-1. Classifications of daily precipitation for the five clusters.

	I	II	III	IV	V
East		[0.1, 0.95)	[0.95, 4.19)	[4.19, 23.29)	≥23.29
West		[0.1, 0.86)	[0.86, 3.48)	[3.48, 19.58)	≥19.58
North	[0, 0.1)	[0.1, 0.66)	[0.66, 2.54)	[2.54, 14.08)	≥14.08
South		[0.1, 1.23)	[1.23, 4.55)	[4.55, 21.16)	≥21.16
Central		[0.1, 1.09)	[1.09, 3.91)	[3.91, 17.62)	≥17.62

Furthermore, GP at 500 hPa and the IVT were utilized as the large-scale atmospheric circulation predictors. We chose the two predictors based on the following considerations: IVT quantifies the intensity of moisture transport which affects a given specific geographic region and thus the probable intensity of precipitation. The GP represents the atmospheric circulation features and in particular the fluid flow structure. Together, these two predictors are able to describe the direction and intensity of humidity transport.

Before training, the two predictors must be subjected to data preprocessing (e.g., standardization and dimensionality reduction). Daily IVT and GP sequences were standardized by using the z-score method, which is dimensionless. We then extracted the standardized IVT values corresponding to the geographical location of the rain gauges and as an independent variable $IVT\_set_{t,m}$ ($t = 1, \dots, T;\ m = 1, \dots, M$), where T and M are the total numbers of days from 1960 to 2015 and the

rain gauges in a cluster, respectively. For GP, the principal component analysis (PCA) was applied to discover the leading behavior of the domain of interest (10°S–70°N and 40°E–170°W). Here, in order to greatly interprets the circulation variations, the first 50 PCs that explained more than 96% of the total variance were selected as the second predictor $GP\_50_{t,p}$ with p columns, $p = 1, \dots, 50$. Thus, the input of the ensemble learning model is represented by $I = \{(IVT\_set_{t,m}, GP\_50_{t,p}, Y_t)\}$, where $Y_t \in \{1, 2, 3, 4, 5\}$.

3.2 Ensemble learning model

The task of the ensemble learning model is to learn and predict the possible probability of our predefined daily precipitation levels (introduced in section 3.1) based on the basic and meta classifiers. Relevant methodologies are introduced in the following subsections.

3.2.1 Extreme Gradient Boosting

XGBoost, which was developed by Chen and Guestrin (2016) is a new ensemble learning tool based on tree boosting. In this study, XGBoost was used to solve multi-class classification problems.

Let the training dataset $D = \{(x_i, y_i)\}$, features $x_i \in \{(IVT\_set_{t,m}, GP\_50_{t,p})\}$ that has the maximum number of $\mathrm{m} + p$, and the corresponding label $y_i \in \{Y_t\}$. Then, a predicted result $\hat{y}_i$ at point i can then be formally determined via the XGBoost model.

$$\hat{y}_i = \emptyset(x_i) = \sum_{k=1}^{K} f_k(x_i), f_k \in \mathcal{F} \tag{5-2}$$

where K is the number of trees in the model, $\mathcal{F}$ represents all possible classification and regression trees, $f_k(x_i)$ represents the output at the k-th tree of the i-th sample, and f_k is an independent tree. The XGBoost aims to minimize the objective function O, which is expressed in the Eq. 5-3.

$$O(\emptyset) = \sum_i l(y_i, \hat{y}_i) + \sum_k \Omega(f_k) \tag{5-3}$$

$$\Omega(f_k) = \gamma\alpha + \frac{1}{2}\lambda\|w\|^2 \tag{5-4}$$

where LF indicates the training loss function that measures the difference between y_i and $\hat{y}_i$. Ω is a regularization term that quantifies the complexity of the model to avoid overfitting. Typically, γ and λ are the penalty coefficients of each leaf, α and w are the total number of leaf nodes and the weight of leaf nodes in the decision tree, respectively.

The XGBoost algorithm uses incremental learning to optimize the objective function. In the t-th iteration a new tree f_t is greedily added as follows:

$$O^t = \sum_{i=1}^{n} LF\left(y_i, \hat{y}_i{}^{(t-1)} + f_t(x_i)\right) + \Omega(f_t) \quad (5\text{-}5)$$

where n is the number of samples. The second-order Taylor expansion of the loss function is given by

$$O^t \cong \sum_{i=1}^{n}[LF\,(y_i, \hat{y}_i{}^{(t-1)}) + g_i f_t(x_i) + \frac{1}{2} h_i f_t^2(x_i)] + \Omega(f_t) \quad (5\text{-}6)$$

$$g_i = \partial_{\hat{y}_i(t-1)} l(y_i, \hat{y}_i(t-1)) \quad (5\text{-}7)$$

$$h_i = \partial^2_{\hat{y}_i(t-1)}\ l(y_i, \hat{y}_i(t-1)) \quad (5\text{-}8)$$

where g_i and h_i are the first- and second-order partial derivatives of LF, respectively. Thus, the loss reduction after a split can be obtained by

$$O_{split} = \frac{1}{2}\left[\frac{(\sum_{i\epsilon I_L} g_i))^2}{\sum_{i\epsilon I_L} h_i + \lambda} + \frac{(\sum_{i\epsilon I_R} g_i))^2}{\sum_{i\epsilon I_R} h_i + \lambda} - \frac{(\sum_{i\epsilon I} g_i))^2}{\sum_{i\epsilon I} h_i + \lambda}\right] - \Upsilon \quad (5\text{-}9)$$

where I_L and I_R are the left and right nodes after the split, respectively.

3.2.2 Random Forest

RF is one of the most popular ensemble learning algorithms based on decision trees (Breiman, 1996). The key concept of RF is that multiple trees or networks can obtain more robust and accurate predictions than individual trees or networks (Genuer et al., 2017). In this study, we used the classification algorithm of RF in which the output is determined by a majority vote of the trees. The basic steps are as follows: (1) Randomly generate sample sets by using bagging sampling from a given dataset. (2) Let each tree grow to the largest extent possible without pruning. At every nodes of the tree, randomly select $mtry$ variables for splitting. We then obtained the prediction results from each decision tree. (3) Determines the class label of the sample based on the voting results from each classification.

3.2.3 Implementing ensemble learning with XGBoost and RF models

We developed an ensemble learning model that integrates the XGBoost and RF for multi-class probability predictions of daily precipitation. Figure 5-2 shows the workflow of the ensemble learning model. Its core concept is to use predictions from the lower level cast into the higher level for the

meta classifier and minimize the errors. At level 1, 90% of the samples were randomly separated as the training set to train the first XGBoost model. At level 2, 30% of the training set was randomly separated again to train the RF model, then the temporary outputs of RF (Tem_RF1) were predicted from the remaining and as an additional feature fed into the second XGBoost model (meta classifier). The target was the daily precipitation level in the 70% training set. Model training was done by repeating the processes at level 2 N times. For the prediction task, all samples were applied to the first XGBoost and RF models to obtain preliminary outcomes (Pre_XGB1) and the additional features (Tem_RF2) on each day, respectively. The experiment at level 2 was conducted 120 rounds (N=120). Subsequently, for each round, the Tem_RF2 and the original feature data were fed into the second XGBoost model to make the 2nd prediction (Pre_XGB2). Finally, for the ensemble results, we chosen the average method. The predictions of the basic learner (level 1) were stacked with those of meta classifiers (level 2) to output the final decision (Meta_pro), which is the average of the $N+1$ independent predictions. The output Meta_pro is a two-dimensional vector with c columns and T rows and contains the predicted probability of each data point belonging to each class. In this study, c should be 5, which is ranked by increased daily precipitation levels. Therefore, possible weather states on day t can be quantified using the probability information contained in the five columns. The sum of the predicted probabilities of the five precipitation levels on day t should be 1.

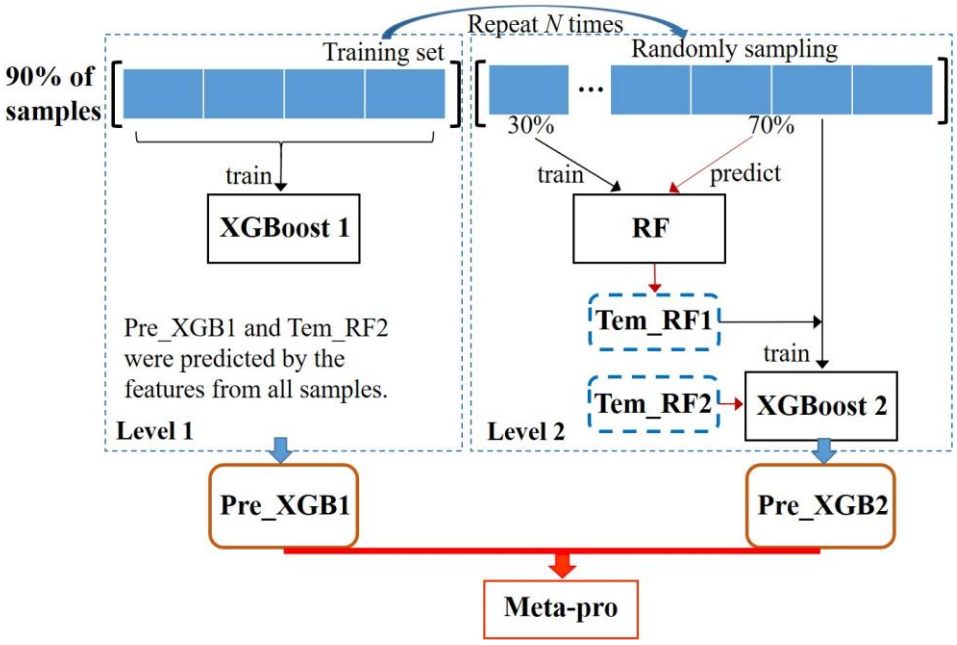

Figure 5-2. Flowchart of the ensemble learning model.

3.2.4 Parameters tuning and model validation

The ensemble learning model was implemented in Rstudio using the R version 4.1.3. Table 5-2 summarizes the specific parameter settings and explanations of the XGBoost and RF models. First, the ratio of training samples was set to 0.8 to tune the hyperparameters, for example, tree depth (max. depth), learning rate (eta), and leaf node weight (min_child_weight) for XGBoost. The tuning task was to minimize the training logloss of multi-classes. In the RF, the out of bag score was referenced to select the number of trees (ntree) and candidates at each split (ntry). For the final predictions, we referred to the confusion matrix (see Table 5-3) to evaluate the model's performance in simulating the probabilities of different precipitation levels.

Table 5-2. Parameter settings in the ensemble learning model.

	Parameter	Explanation	Value
XGBoost	booster	Specify the type of booster	gbtree
	objective	Specify the learning task of the model	multi:softprob
	max.depth	Maximum depth of a tree	8*, 11**
	eta	Learning rate	0.1*, 0.46**
	nrounds	Number of rounds	1200*, 60**
	min_child_weight	Minimum weight for a child leaf node	3*, 10**
	subsample	Ratio of training samples	0.8
	eval_metric	Evaluation metrics for validation	mlogloss
RF	ntree	Number of trees	100
	ntry	Number of variables randomly used as candidates at each split	7

Notes: *XGBoost 1, **XGBoost 2.

Table 5-3. Descriptions of the confusion matrix.

		Predicted levels				Accuracy rate (%)
		I	II	…	V	
Actual levels	I	$hist_{1,1}$	$False_{1,2}$		$False_{1,5}$	(Number of $hist_{1,1}$/total number of class I)*100
	II	$False_{2,1}$	$hist_{2,2}$		$False_{2,5}$	
	…				…	…
	V	$False_{5,1}$	$False_{5,2}$	..	$hist_{5,5}$	(Number of $hist_{5,5}$/total number of class V)*100

3.3 Nonhomogeneous hidden Markov model

Typically, the NHMM is a double stochastic process composed of two parts, that is, an observation sequence and discrete hidden states (Hughes and Guttorp, 1994; Hughes et al., 1999), which are defined as follows:

(1) Observation sequence R_t: Let $R_t = (R_t^1, \dots, R_t^M)$ be an multivariate vector that records the precipitation amount from M rain gauges in a cluster on day t. Let $R_{1:T} = (R_1, \dots, R_T)$ represents the daily precipitation sequence using a Markov chain with hidden states.

(2) Hidden states S_t: Let $S_t = (1, \dots, s)$ be the weather state at day t, whose state transition probability $P(S_t|S_{1:\,t-1}) = P(S_t|S_{t-1})$ is modeled by the first-order Markovian process.

Subsequently, the log-likelihood of the data under the NHMM model can be formulated as

$$l = \log P(R|X) = log \sum_S [P(S_1|X_1) \prod_{t=2}^{T} P(S_t|S_{t-1}, X_t)][\prod_{t=1}^{T} P(R_t|S_t)] \quad (5\text{-}10)$$

where $P(R_t|S_t)$ is the emission probability of R_t from state S_t, $P(R_t|S_{1:t}, R_{1:t-1}) = P(R_t|S_t)$; X_t represents additional observed variables with o columns; and S_t depends on both S_{t-1} and X_t. In this study, the external variables were the time dependent atmospheric circulation factors.

We used multinomial logistic regression to model the multivariate hidden state transitions:

$$P(S_t = j|S_{t-1} = i, X_t = x) = \frac{\exp\ (\sigma_{ji} + \rho_j x^t)}{\sum_{h=1}^{H} \exp(\sigma_{jh} + \rho_h x^t)} \quad (5\text{-}11)$$

where H denotes the number of hidden states. An independent delta–gamma function was selected to model the emission probabilities. The best NHMM fits the conditional probability of observation sequence is determined using the expectation–maximization technique (Moon, 1996). The most likely weather state sequence can then be generated from the NHMM using the Viterbi algorithm (Forney, 1973). Log-likelihood criteria and Bayesian criteria were selected to identify the most appropriate number of hidden states. After testing the number of hidden states from 2 to 10, the optimum number of hidden states was determined to be 6. In this study, leave-5 fold-out cross-validation was used to train the NHMM.

Compared with the traditional method of directly using the atmospheric circulation data to construct the NHMM downscaling model, we propose a new downscaling framework that uses the occurrence

probabilities of different precipitation levels from the ensemble learning model outputs as the predictors. Therefore, two downscaling experiments were conducted for each cluster. The first was the stacked ensemble learning and NHMM (Ensemble-NHMM) downscaling model based on the daily precipitation probability. The other was the NHMM, which uses the original sequence of the standardized IVT and the first leading 50 PCs of GP at 500 hPa. Noted that we have conducted 100 simulations for each model during the simulation process.

3.4 Evaluation indicators

Two indicators were selected to stratify the performance of the Ensemble-NHMM and NHMM. The first is the coefficient of variation of the root-mean-squared error (CVRMSE), which quantifies the standard deviation of the differences between simulations and observations without unit (Chakraborty and Elzarka, 2018). The other is the correlation coefficient (CC), which is used to estimate the linear relationship between simulations and observations.

$$CVRMSE = \frac{\sqrt{\frac{1}{n}\sum_{i=1}^{n}(sim_i - obs_i)^2}}{\frac{1}{n}\sum_{i=1}^{n} obs_i} \tag{5-12}$$

$$CC = \frac{\sum_{i=1}^{n}(sim_i - \overline{sim})(obs_i - \overline{obs})}{\sqrt{\sum_{i=1}^{n}(sim_i - \overline{sim})^2}\sqrt{\sum_{i=1}^{n}(obs_i - \overline{obs})^2}} \tag{5-13}$$

where sim and obs indicate the simulations and observations from the Ensemble-NHMM (or NHMM) and rain gauge, respectively, and n is the total number of samples.

4. Results

4.1 Ensemble learning model performance in daily precipitation classification

For each rain gauge cluster, the outcome of the ensemble learning model was a two-dimensional vector that contains the predicted occurrence probability of the five predefined levels of daily precipitation from 1960 to 2015. To investigate the performance of the ensemble learning model, we selected the one with the highest occurrence probability as the eventually predicted level on a daily basis and compared it with the real observed value [Y_t, in Eq.(5-1)]. Table 5-4 shows the confusion matrix of the predicted and observed daily precipitation levels for the five clusters. The accuracy rate was calculated by referring to the equations in Table 5-3. Overall, the ensemble learning model shows

a superior capability in classifying no rain or rain and predicting moderate precipitation events for the five clusters (accuracy rates exceed 88% and 83% respectively). A relatively lower accuracy rate was observed at very light and heavy precipitation levels; the confusion matrix indicates that some heavy precipitation events were misclassified as moderate.

Table 5-4. Confusion matrix of the predicted and observed daily precipitation levels for the five clusters and related accuracy rate.

Cluster	Precipitation level		Predicted					Accuracy rate (%)
			I	II	III	IV	V	
East	Actual	I	**8922**	107	133	165	1	95.65
		II	908	**2008**	179	241	0	60.19
		III	634	127	**2094**	476	2	62.83
		IV	364	83	182	**3250**	8	83.61
		V	13	3	10	169	**361**	64.93
West	Actual	I	**5204**	273	180	201	0	88.84
		II	721	**2922**	325	408	0	66.77
		III	401	285	**2993**	693	2	68.43
		IV	204	163	347	**4374**	15	85.71
		V	13	12	16	217	**471**	64.61
North	Actual	I	**6384**	156	186	135	0	93.05
		II	899	**2616**	310	250	0	64.20
		III	397	195	**2841**	636	4	69.75
		IV	126	80	299	**4224**	23	88.89
		V	0	2	1	236	**440**	64.80
South	Actual	I	**4633**	357	126	96	1	88.87
		II	559	**3279**	400	327	3	71.78
		III	226	470	**3183**	685	4	69.68
		IV	100	213	362	**4635**	21	86.94
		V	1	4	6	262	**487**	64.08
Central	Actual	I	**4875**	316	165	108	0	89.22
		II	629	**3112**	407	349	0	69.20
		III	267	392	**3183**	646	2	70.89
		IV	115	188	376	**4539**	22	86.62
		V	1	4	11	230	**503**	67.16

Furthermore, daily precipitation was classified into different months to evaluate the capability of ensemble learning model in depicting precipitation seasonality. As shown in Figure 5-3a, the ensemble learning model yields better performance in the non-rainy season (from October to March) for the five clusters, with an average classification accuracy rate of 82.14%; while the reported accuracy is 77.43% in the rainy season (from April to September). The lowest accuracy rate can be found in the East cluster during July to August.

To further understand the capability of the ensemble learning model, we also separately examined the accuracy of only using the RF or XGBoost to predict the probabilities of multi-level daily precipitation. Figure 5-3b demonstrates the overall performance of the ensemble learning, RF, and XGBoost for the five clusters. The statistical results indicate that the ensemble learning model obtains better prediction skills than the RF and XGBoost. The accuracy rate of the ensemble learning model ranges from 78.10% to 81.38%, while 57.16% to 65.47% for the RF and 72.80% to 77.69% for the XGBoost, respectively. The combination of poor performance base learners can improve the capability of the multi-class probability predictions model of daily precipitation.

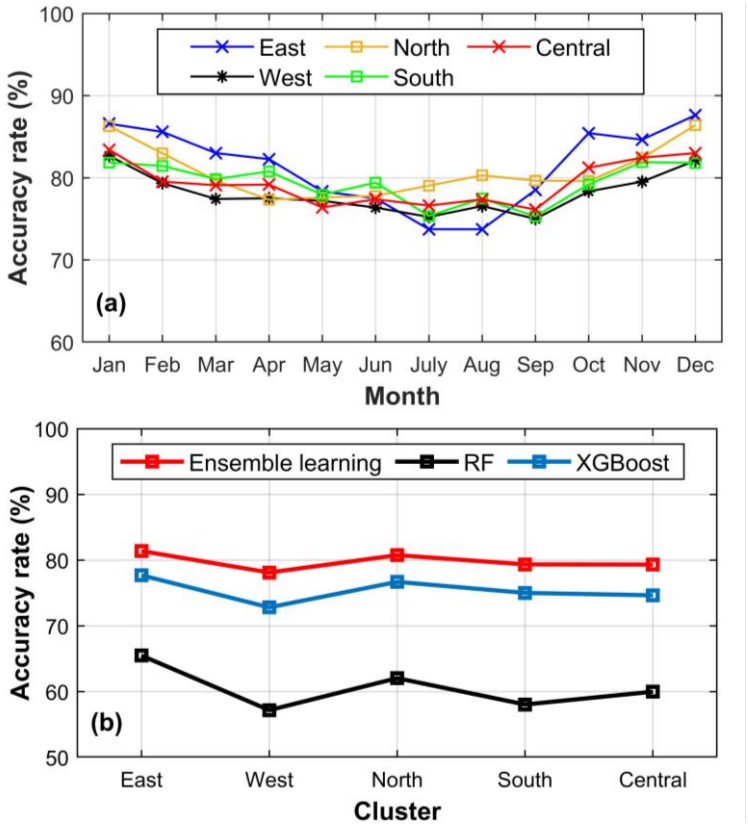

Figure 5-3. Accuracy rate of the ensemble learning model in the different months (**a**) and (**b**) the overall performance of the ensemble learning, RF, and XGBoost models for the five clusters.

4.2 Comparison of Ensemble-NHMM and NHMM

Atmospheric circulation substantially affects the variability of regional precipitation and magnitudes of extreme precipitation events under global warming (Zhang et al., 2021). Hence in this section, we focus on testing the two models for depicting the precipitation variability and extreme precipitation simulations. Note that the two models differ depending on how the atmospheric predictors affect the conditional hidden states transitional probability: in NHMM by Eq. (5-11), that is, directly using the PCs of the atmospheric predictor in the multinomial logistic regression. In Ensemble-NHMM, introducing an intermediate predictor depends on atmospheric predictors in a more complex way.

4.2.1 Precipitation variabilities

For each rain gauge, 100 downscaled precipitation events were predicted by the Ensemble-NHMM and NHMM models on any given day. Comparisons with observations were first conducted for monthly precipitation. Daily precipitation was accumulated on a monthly scale. Next, across the five clusters, we examined the CVRMSE indicator, which was calculated by comparing the monthly precipitation averaged by the rain gauges and the simulations of Ensemble-NHMM and NHMM. Tables 5-5 and 5-6 present the results calculated from the median and mean of the 100 simulations, respectively. For CEC as a whole, the Ensemble-NHMM has a lower error (average CVRMSE of 0.26) with respect to monthly precipitation simulations compared with the NHMM (average CVRMSE of 0.45).

Furthermore, the temporal variations in the monthly mean precipitation for the five clusters agree more closely with the observations (Figure 5-4). This means that the Ensemble-NHMM can reproduce the seasonality of the precipitation very well over CEC when using the probabilities of different precipitation levels as predictors. The results of the NHMM are shown in Figure 5-5. The boxplots reveal that the NHMM has large errors in estimating the precipitation that occurred in May and June, especially for the west, south, and central clusters.

Table 5-5. CVRMSE of the simulated (median) monthly precipitation for the Ensemble-NHMM and NHMM.

		Jan	Feb	Mar	Apr	May	Jun	Jul	Aug	Sep	Oct	Nov	Dec
Ensemble -NHMM	East	0.37	0.28	0.22	0.25	0.29	0.34	0.26	0.24	0.25	0.36	0.32	0.43
	West	0.35	0.27	0.18	0.23	0.28	0.24	0.25	0.22	0.22	0.27	0.27	0.36
	North	0.41	0.34	0.25	0.31	0.24	0.23	0.22	0.20	0.27	0.27	0.29	0.40
	South	0.22	0.21	0.16	0.17	0.22	0.24	0.23	0.17	0.22	0.31	0.29	0.37
	Central	0.26	0.20	0.18	0.20	0.27	0.27	0.22	0.22	0.22	0.22	0.26	0.32
NHMM	East	0.72	0.52	0.31	0.31	0.29	0.44	0.34	0.39	0.34	0.48	0.41	0.82
	West	0.77	0.63	0.35	0.27	0.35	0.39	0.38	0.34	0.37	0.35	0.38	0.83
	North	1.40	1.05	0.39	0.33	0.27	0.33	0.30	0.31	0.35	0.35	0.54	1.51
	South	0.64	0.52	0.29	0.22	0.29	0.37	0.31	0.34	0.30	0.44	0.40	0.71
	Central	0.59	0.41	0.26	0.27	0.38	0.41	0.33	0.34	0.28	0.32	0.33	0.68

Table 5-6. CVRMSE of simulated (mean) monthly precipitation for the Ensemble-NHMM and NHMM.

		Jan	Feb	Mar	Apr	May	Jun	Jul	Aug	Sep	Oct	Nov	Dec
Ensemble -NHMM	East	0.40	0.30	0.21	0.22	0.25	0.31	0.27	0.26	0.24	0.34	0.29	0.45
	West	0.47	0.36	0.22	0.20	0.25	0.22	0.25	0.23	0.24	0.25	0.28	0.47
	North	0.65	0.52	0.26	0.26	0.20	0.21	0.20	0.20	0.24	0.28	0.29	0.67
	South	0.25	0.23	0.17	0.16	0.19	0.23	0.26	0.18	0.24	0.29	0.26	0.38
	Central	0.35	0.26	0.20	0.17	0.24	0.24	0.23	0.24	0.27	0.21	0.25	0.40
NHMM	East	0.89	0.64	0.36	0.32	0.27	0.41	0.34	0.38	0.33	0.56	0.48	1.03
	West	1.00	0.80	0.42	0.25	0.32	0.36	0.36	0.33	0.39	0.35	0.43	1.09
	North	1.99	1.43	0.55	0.32	0.24	0.28	0.28	0.29	0.32	0.44	0.71	2.07
	South	0.76	0.59	0.32	0.23	0.26	0.35	0.30	0.32	0.30	0.50	0.47	0.85
	Central	0.75	0.50	0.28	0.23	0.34	0.37	0.31	0.34	0.30	0.34	0.38	0.86

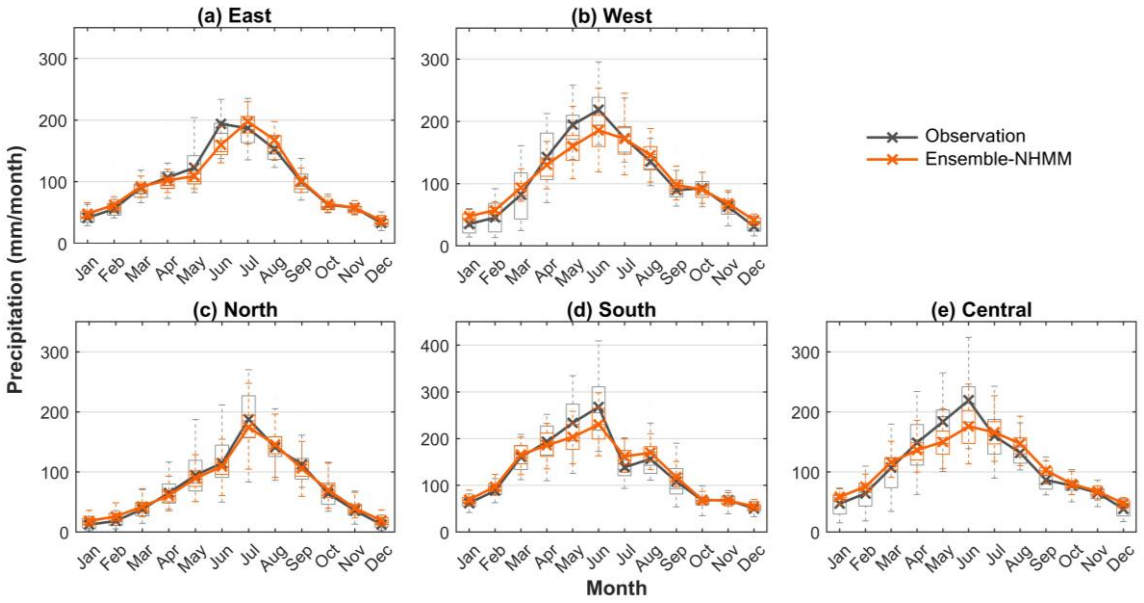

Figure 5-4. Boxplots of the observed and simulated mean monthly precipitation amount for the (**a**) East, (**b**) West, (**c**) North, (**d**) South, and (**e**) Central clusters based on the Ensemble-NHMM. Thick lines represent the average.

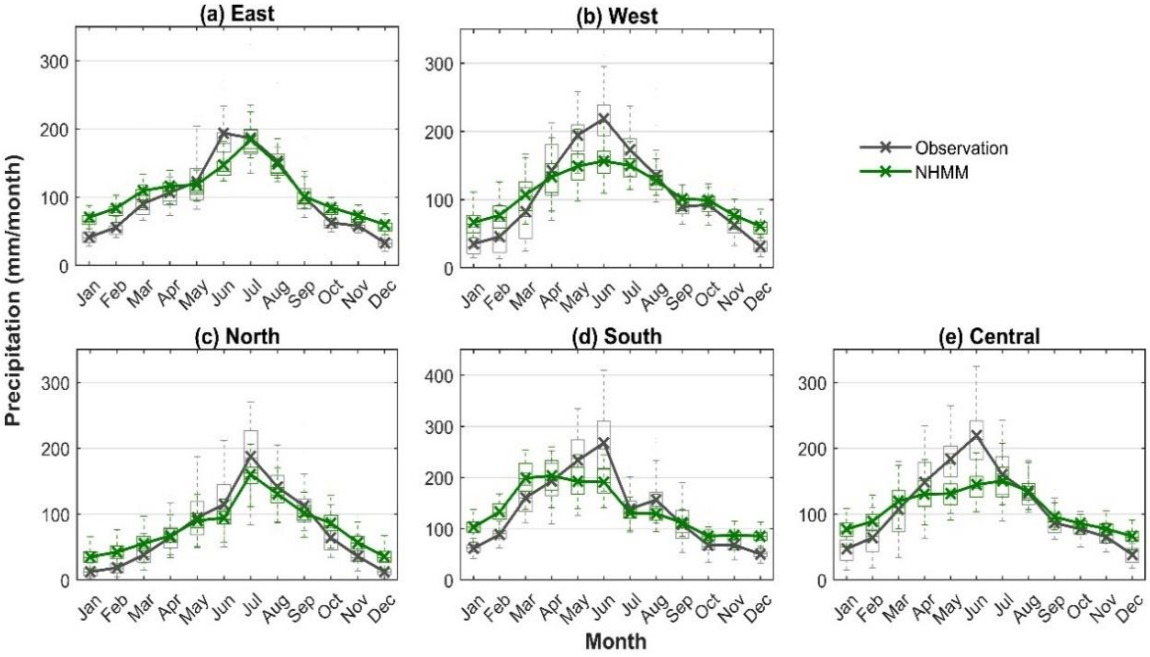

Figure 5-5. Boxplots of the observed and simulated mean monthly precipitation amount for the (**a**) East, (**b**) West, (**c**) North, (**d**) South, and (**e**) Central clusters based on the NHMM. Thick lines represent the average.

We compared the Ensemble-NHMM and NHMM for annual precipitation simulations that accumulated from daily precipitation data. Table 5-7 summarizes the CVRMSE between the

observations and simulations, considering different lengths of moving windows for the annual precipitation. This indicator was calculated from the median of the 100 simulations. Overall, the ability of Ensemble-NHMM performs better than the NHMM, with a lower CVRMSE. The CVRMSE tends to decrease with the increasing length of moving windows. Table 5-8 presents the mean results from the mean of the 100 simulations. As expected, the Ensemble-NHMM obtains satisfactory results.

Table 5-7. CVRMSE of simulated (median) annual precipitation trends under three periodic moving averages for the Ensemble-NHMM and NHMM.

	Ensemble-NHMM				NHMM			
	1a	5a	15a	20a	1a	5a	15a	20a
East	0.161	0.080	0.047	0.040	0.202	0.122	0.100	0.096
West	0.151	0.070	0.043	0.037	0.161	0.104	0.079	0.057
North	0.197	0.088	0.047	0.039	0.218	0.115	0.084	0.078
South	0.142	0.066	0.036	0.030	0.156	0.081	0.054	0.049
Central	0.162	0.076	0.047	0.042	0.171	0.083	0.057	0.052

Table 5-8. CVRMSE of simulated (mean) annual precipitation trends under three periodic moving averages for the Ensemble-NHMM and NHMM.

	Ensemble-NHMM				NHMM			
	1a	5a	15a	20a	1a	5a	15a	20a
East	0.160	0.078	0.046	0.039	0.205	0.127	0.106	0.102
West	0.150	0.069	0.041	0.035	0.160	0.103	0.082	0.066
North	0.196	0.088	0.047	0.039	0.220	0.120	0.090	0.085
South	0.142	0.066	0.036	0.030	0.158	0.083	0.057	0.053
Central	0.162	0.075	0.046	0.041	0.169	0.081	0.054	0.049

Figures 5-6–5-8 show the observed and simulated mean annual precipitation series under different lengths of moving windows for the five clusters, which were averaged by their respective rain gauges. We observed that the Ensemble-NHMM was able to capture the year-to-year and interannual variations in precipitation over CEC, whereas the NHMM tended to overestimate the annual precipitation for the five clusters and failed to capture the peak value in 1997 for the West cluster and in 2000 for the Central cluster. In addition, because the median of 100 simulations obtains better

statistical results on the monthly scale than that of the mean, we only used the former for the subsequent analysis.

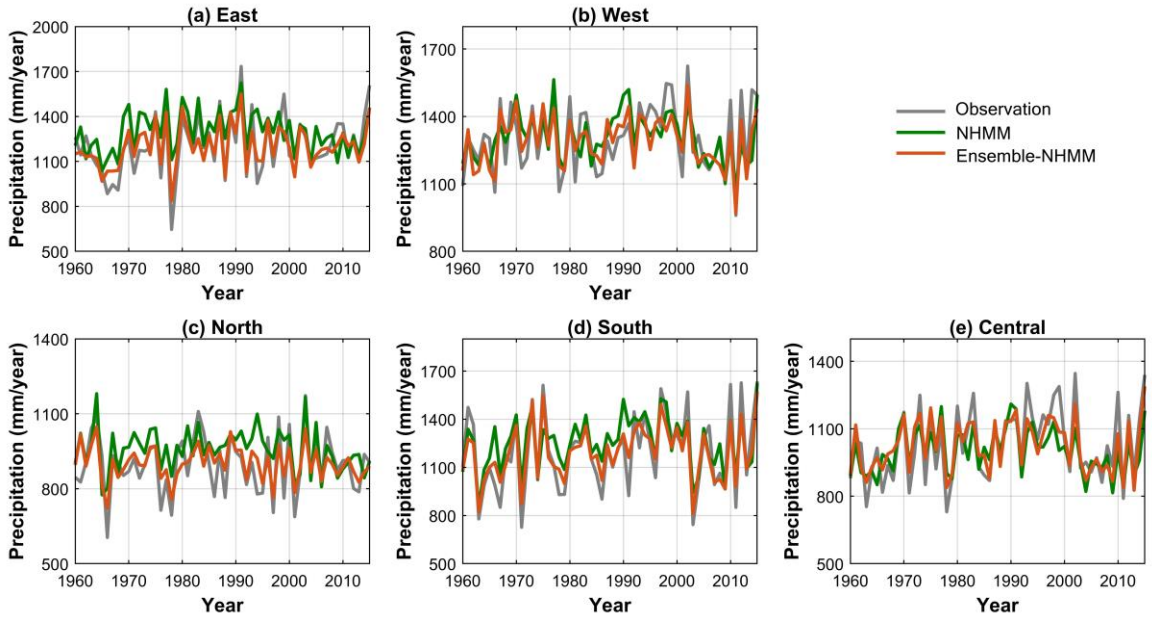

Figure 5-6. Observed and simulated mean annual precipitation amount for the (**a**) East, (**b**) West, (**c**) North, (**d**) South, and (**e**) Central clusters.

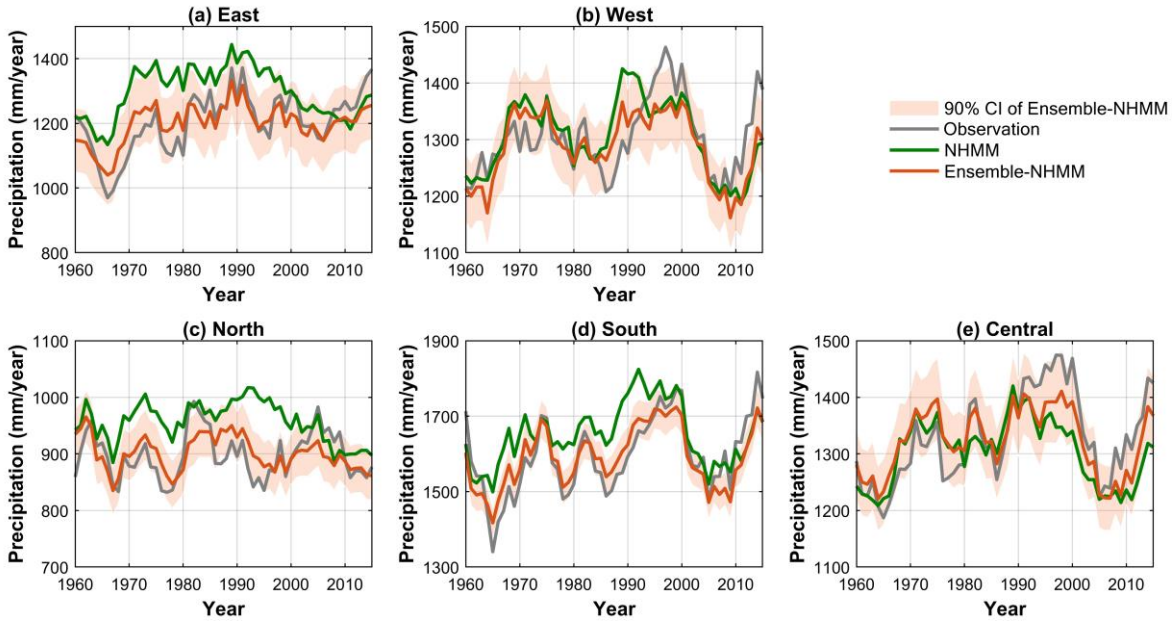

Figure 5-7. Observed and simulated mean annual precipitation amount under the 5a moving window for the (**a**) East, (**b**) West, (**c**) North, (**d**) South, and (**e**) Central clusters. Shadow represents the 90% confidence interval (CI) of Ensemble-NHMM.

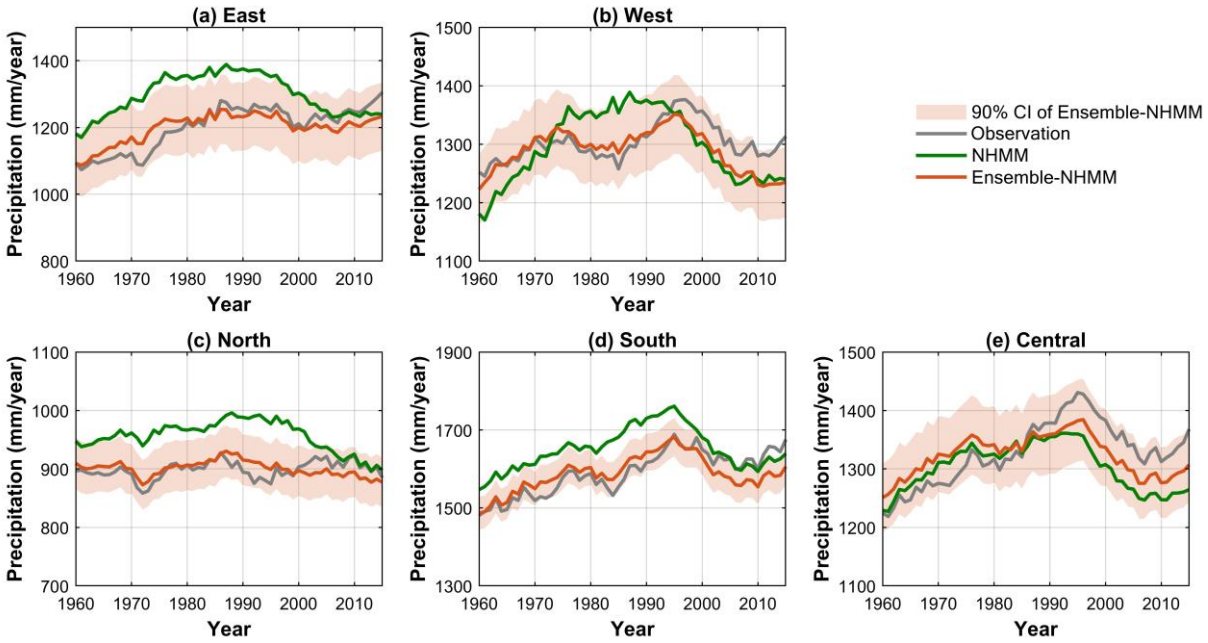

Figure 5-8. Same as Figure 5-7, but for the 15a moving window.

4.2.2 Extreme precipitation

The 95th percentile of the wet days (daily precipitation ≥ 0.1 mm/day) was used to define the extreme precipitation for each rain gauge. For the simulations, extreme precipitation was directly calculated when considering the observation thresholds. Subsequently, we obtained the total frequency and amount exceeding the 95th percentile from 1960 to 2015. Figure 5-9 compares the means of the total extreme precipitation frequency and amount over the 56 years for the observations and simulations. The gauges are represented by dots. Referring to the 1:1 lines (dotted lines) and evaluation results presented in these figures, we confirm the Ensemble-NHMM provides good approximations of the climatology of extremes across all gauges. The NHMM also performs well in reproducing the extremes but there is a relatively worse CC for extreme precipitation frequency. In addition, the Ensemble-NHMM is better in characterizing annual extreme precipitation than the NHMM. The Ensemble-NHMM clearly captures the means of the total extreme precipitation frequency and amount between observations.

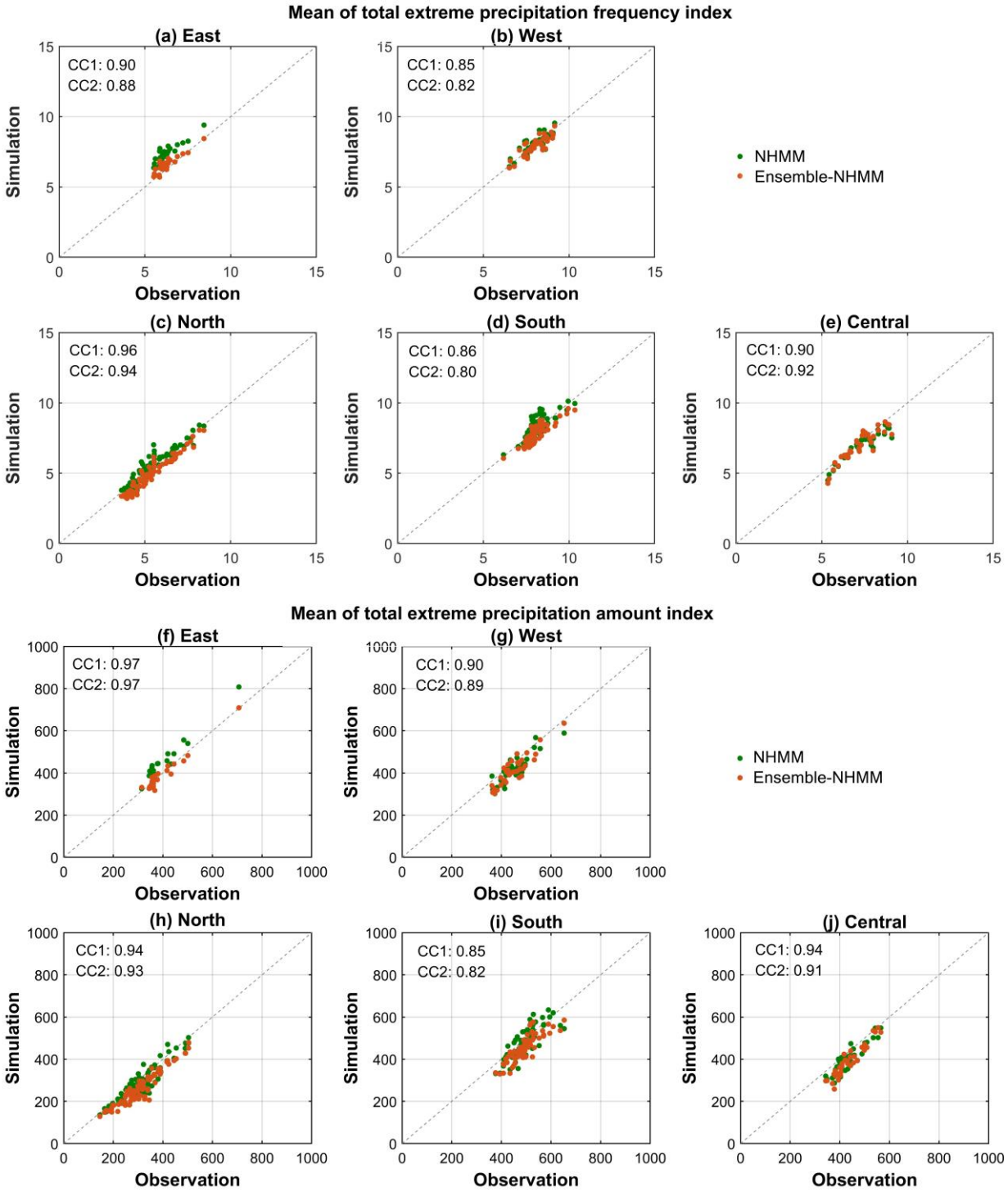

Figure 5-9. Scatterplots of the means of total extreme precipitation frequency and amount (unit: mm/year) index for observations against the simulations for the (**a, f**) East, (**b, g**) West, (**c, h**) North, (**d, i**) South, and (**e, j**) Central clusters. Numbers 1 and 2 represent the Ensemble-NHMM and NHMM, respectively.

4.3 Future precipitation projection under different climate change scenarios

4.3.1 Analysis of the historical period

In the above-mentioned analysis, we explored the feasibility of Ensemble-NHMM in downscaling precipitation using the multi-level daily precipitation occurrence probabilities, which were predicted by the GP at 500 hPa and IVT from the ERA5 data. We further analyzed how the GCM model, that is, MPI-ESM1-2-HR, performs in the Ensemble-NHMM during the same historical period. All steps of the Ensemble-NHMM were repeated using the MPI-ESM1-2-HR data. Because the Ensemble-NHMM is a data-driven model, changes in the data source could directly affect the recognition of the hidden states and its most probable sequence, which has a considerable influence on the simulated sequence of daily precipitation. We selected six-hidden states and examined the goodness of fit the hidden states sequence based on MPI-ESM1-2-HR with the results of ERA5. During the period of 1960–2015, the consistency rate of hidden state occurrence was as high as 98% (98.62%, 98.56%, 99.69%, 98.01%, and 96.63% of the East, West, North, South, and Central clusters respectively), indicating that MPI-ESM1-2-HR can capture the statistical behavior of actual observations.

We then evaluated the accuracy of the downscaled precipitation based on MPI-ESM1-2-HR. Tables 5-9–5-10 list the evaluation results of the mean monthly, annual and extreme precipitation simulations for the MPI-ESM1-2-HR. Monthly CVRMSE statistics ranges between 0.22 and 0.59, with an average of 0.34. MPI-ESM1-2-HR performed better in the non-rainy months. The annual CVRMSEs of MPI-ESM1-2-HR were close to those of ERA5. Figures 5-10–5-11 show the observed and simulated annual precipitation amount using the MPI-ESM1-2-HR under the 5a and 10a moving windows. The results show that MPI-ESM1-2-HR can produce reliable trend simulations by using the Ensemble-NHMM. Furthermore, when considering MPI-ESM1-2-HR in the estimations of the mean of the total extreme precipitation frequency and amount, the CVRMSEs do not exceed 0.12 and 0.20 respectively. In summary, compared with the that results produced by the ERA5 (see Tables 5-5, 7 and Figure 5-9), the performance of MPI-ESM1-2-HR is satisfactory. We can fully consider the GCM data for future scenarios.

Table 5-9. CVRMSE of simulated (median) monthly precipitation using the Ensemble-NHMM model based on the GCM data.

	Jan	Feb	Mar	Apr	May	Jun	Jul	Aug	Sep	Oct	Nov	Dec
East	0.44	0.47	0.37	0.34	0.29	0.35	0.35	0.31	0.34	0.53	0.52	0.56
West	0.33	0.35	0.22	0.27	0.23	0.23	0.34	0.23	0.26	0.30	0.33	0.37
North	0.46	0.53	0.41	0.42	0.31	0.30	0.28	0.25	0.33	0.37	0.43	0.53
South	0.39	0.35	0.26	0.21	0.22	0.25	0.28	0.23	0.25	0.42	0.52	0.59
Central	0.33	0.33	0.24	0.23	0.24	0.26	0.31	0.25	0.29	0.34	0.42	0.42

Table 5-10. CVRMSE of simulated (median) annual precipitation trends under three periodic moving averages using the Ensemble-NHMM model based on the GCM data.

	Moving window			
	1a	5a	15a	20a
East	0.178	0.083	0.048	0.042
West	0.157	0.065	0.036	0.030
North	0.208	0.088	0.049	0.042
South	0.164	0.074	0.040	0.036
Central	0.174	0.082	0.051	0.045

Table 5-11. CVRMSE of the means of the total extreme precipitation frequency and amount using the Ensemble-NHMM model based on the GCM data.

	Frequency		Amount	
	CVRMSE	CC	CVRMSE	CC
East	0.06	0.90	0.04	0.98
West	0.05	0.86	0.10	0.90
North	0.11	0.96	0.19	0.93
South	0.07	0.89	0.12	0.86
Central	0.08	0.90	0.12	0.90

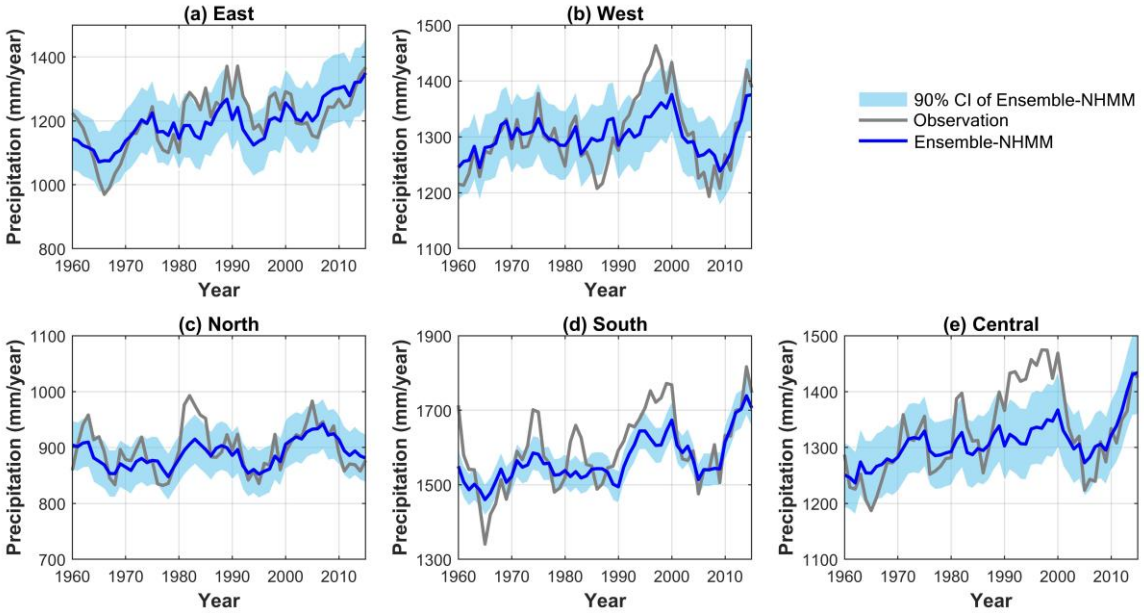

Figure 5-10. Observed and simulated annual precipitation amount (using GCM) under the 5a moving window for the (**a**) East, (**b**) West, (**c**) North, (**d**) South, and (**e**) Central clusters. Shadows represent the 90% confidence intervals.

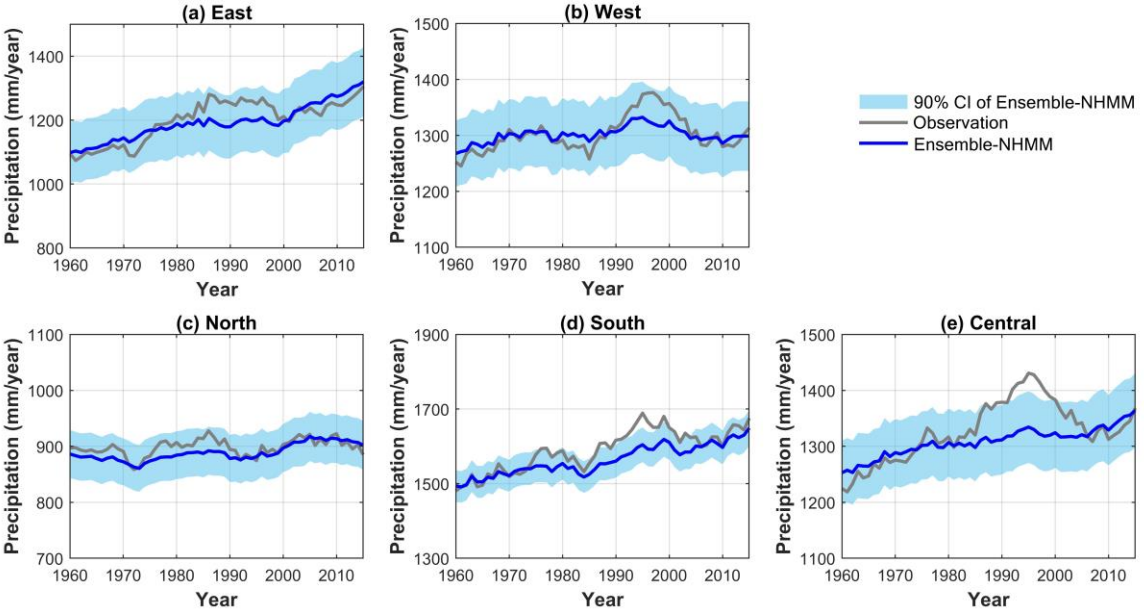

Figure 5-11. Same as Figure 5-10, but for the 15a moving window.

In the historical period, we analyzed the spatial distributions of the anomalies of daily precipitation and circulation configurations of the identified hidden states based on the MPIESM1-2-HR, as shown in Figures 5-12 and S5-1 to S5-4 in the supporting materials. Precipitation anomalies at the sites were obtained by taking the mean values within the date of a specific hidden state and subtracting the mean values from 1960 to 2015 (the definition of circulation anomalies uses the same approach). A positive

result indicates that the hidden states belongs to the wet pattern; otherwise, they are considered to be dry. The precipitation conditions for each hidden state in each cluster are summarized in Table 5-12. Considering space limitations, we only used the East cluster as an example; the detailed description is as follows:

(1) State 1 represents a very wet and homogeneous condition for all rain gauges. Precipitation for the gauges located in the western part is relatively higher and occurs most frequently in spring, followed by summer (see Figure 5-13).

(2) State 2 is dominated by a very wet and homogeneous conditions. In this case, all gauges recorded high precipitation. This state appears mainly in the summer.

(3) State 3 is a wet pattern that is nearly homogeneous. A few gauges located west showed slightly negative anomalies.

(4) State 4 is a wet pattern but non-homogeneous. Locally, dry conditions are observed in the west. It mainly occurs in late summer and early autumn.

(5) State 5 is dominated by a very dry and homogeneous conditions. This state had the higher occurrences from 1960 to 2015.

(6) State 6 represents dry conditions. This state had the fewest number (low frequency) but also significantly affects the precipitation occurrences.

The atmospheric circulation anomaly fields for every hidden state show that the dry or wet weather conditions are closely related to the surrounding water vapor transport. For instance, for hidden states 1 and 2, the east cluster is completely controlled by the positive anomalies of IVT and abnormal cyclone-like airflows at 850 hPa, resulting in abundant precipitation (Figures 5-12a, b). During the hidden state 5 period, the IVTs showed a negative abnormal situation, resulting in less precipitation (Figure 5-12e). Because the pathway of water vapor transport is easterly, located over the East China Sea, for hidden states 3 and 4, the precipitation in the eastern and western parts of the East cluster presents different anomalous status (Figure 5-12c, d). For hidden state 6, we observed that the WPSH system was located at 23°N, and the westward extension ridge point was near 108°E (contour of 5860 gpm). At this time, eastern and northern China were controlled by abnormally high pressure, which led to low precipitation over CEC (Figure 5-12f).

Table 5-12. Precipitation conditions of the six hidden states for the five clusters.

	State 1	State 2	State 3	State 4	State 5	State 6
East	very wet and homogeneous	very wet and homogeneous	wet, nearly homogeneous	wet, but for the southeast part	very dry and homogeneous	dry, nearly homogeneous
West	dry, nearly homogeneous	very dry and homogeneous	very dry and homogeneous	dry, but for the western part	dry, but for the eastern part	very wet and homogeneous
North	wet and homogeneous	very dry and homogeneous	dry, nearly homogeneous	dry, nearly homogeneous	wet, nearly homogeneous	very wet and homogeneous
South	very wet and homogeneous	dry, but for the western part	very dry and homogeneous	very dry and homogeneous	wet, but for the southern part	wet (dry) for the northern (southern)
Central	very wet and homogeneous	dry, but for the east part	dry, but for the western part	very dry and homogeneous	very dry and homogeneous	wet, but for the eastern part

The same conclusion can be reached for other clusters (see Figures S5-1–S5-4). The location and intensity of water vapor transport and circulation features play important roles in shaping the regional precipitation. For the West cluster, only hidden state 6 belongs to the wet pattern. The anomalous southwesterly airflow draws abundant moisture from the oceans and converges to the west of the CEC, which corresponds to the precipitation locations. In the other five dry hidden states, weak water vapor transport and wind fields were responsible for the poor precipitation (Figure S5-1). For the North cluster, we found that the center of the positive precipitation anomalies corresponded to the strong water vapor transport belt (Figure S5-2). The dry patterns of the South cluster were mainly influenced by the anticyclone-like airflow and insufficient water vapor transport (Figure S5-3). The anomalous cyclone-like airflow provides dynamic forcing for the precipitation development over the central region, coupled with abundant moisture that could produce more precipitation (Figure S5-4). Figure 5-13 shows the 10-day moving average of the identified hidden states occurrences for the five clusters during the calendar year. The wet hidden states are identified by the bold lines, whereas the dry hidden states are plotted as dotted lines. The seasonality of their occurrence shows that wet hidden states mainly occur during the rainy season. The wet hidden states are dominant from the summer to early autumn for the North cluster, whereas they are dominant in spring in the South cluster. For the West and Central clusters, the wet state occurs most frequently in spring and early summer.

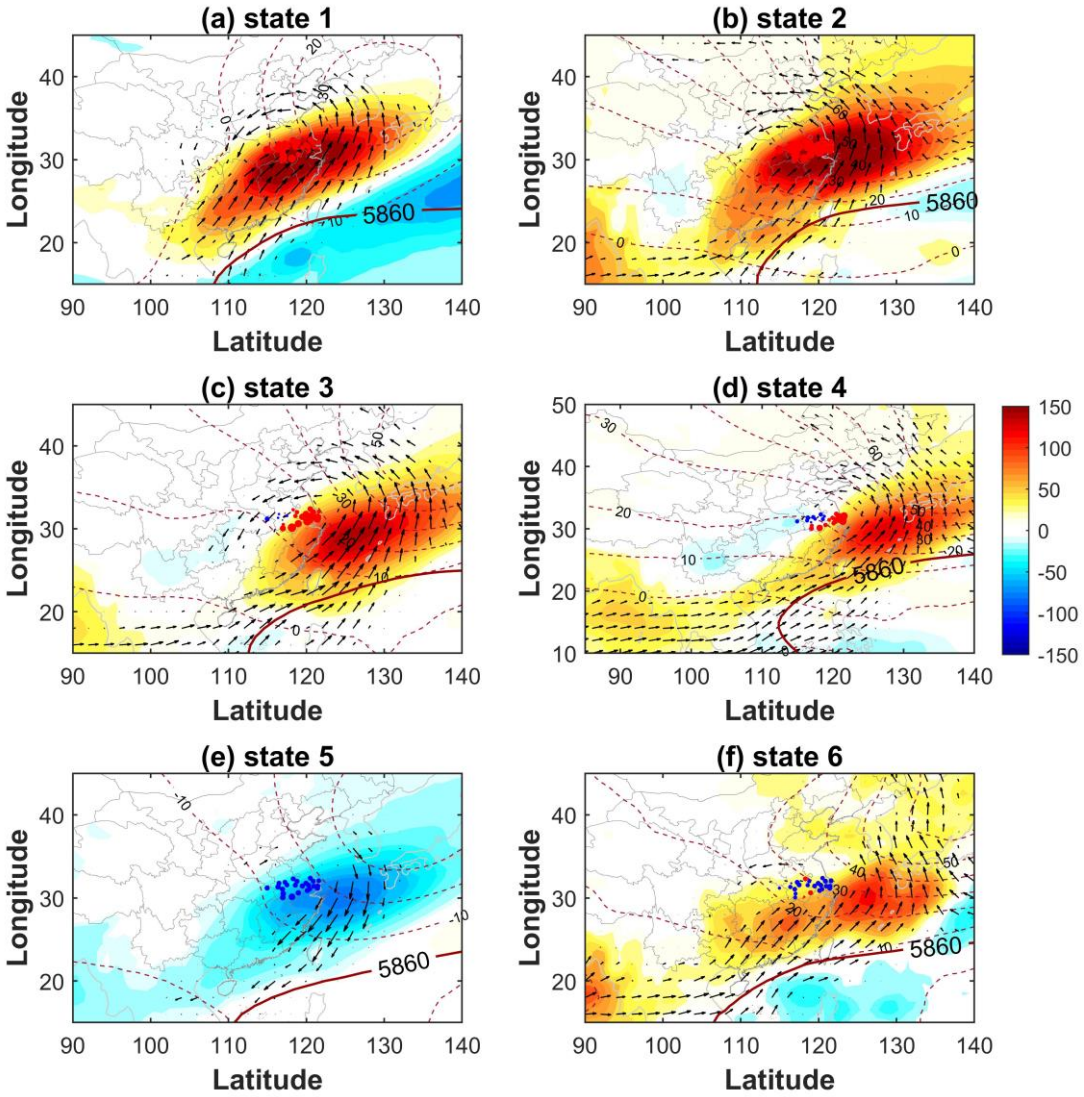

Figure 5-12. Identified hidden states for the East cluster and their corresponding atmospheric circulations. The red or blue solid circles represent the positive or negative anomalies the daily precipitation amount under a hidden state compared with the average from 1960 to 2015; their size represents the severity. Vector arrows indicate the wind anomalies at 850 hPa (unit: m s^{-1}) and shadow and dotted lines show the anomalous fields of IVT (unit: kg m^{-1} s^{-1}) and geopotential height at 500 hPa, respectively. Bold contours represent the 5860 gpm.

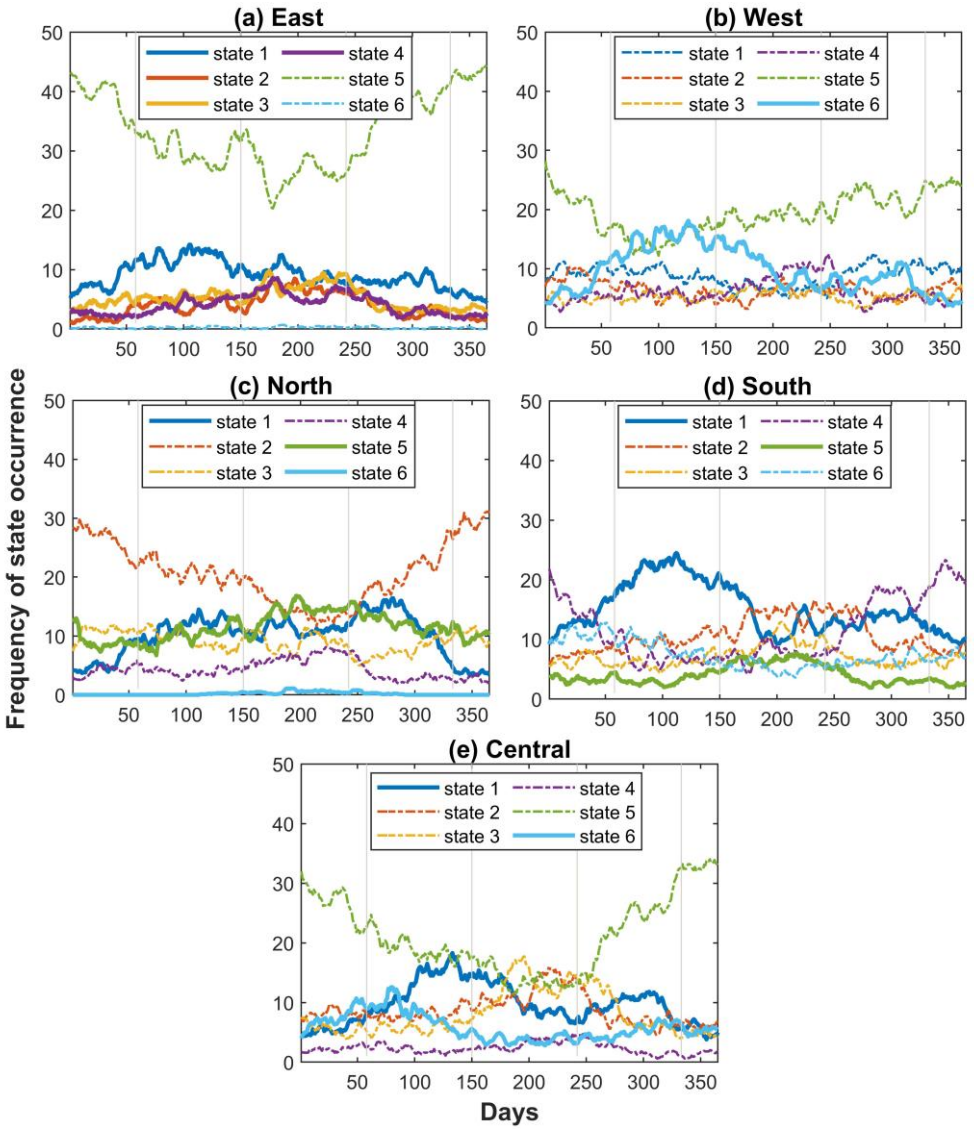

Figure 5-13. Ten-day moving average of the identified hidden states occurrence during the calendar year (from 1960 to 2015) for the five clusters. Wet and dry hidden states are identified by the bold and dotted lines, respectively.

4.3.2 Future precipitation projection

Before the projection of precipitation, we must state that there is a basic assumption that the future atmospheric circulation features of GCMs must respect the statistical consistency in the historical period (Cioffi et al., 2016). Thus, we restructured the PCs in the period of 2016–2100 for the three emission scenarios to be consistent with the mean and variance of those in the historical period, respectively. Subsequently, the restructured first 50 leading PCs of GP at 500 hPa and IVT were used to simulate the multi-level daily precipitation probabilities from 2016 to 2100 based on the ensemble

learning model trained by the historical data of MPI-ESM1-2-HR. Thus, we can directly use the Ensemble-NHMM directly to perform the projections.

Figure 5-14 shows the mean annual precipitation projections under a 15a moving average window for the five clusters. Under the SSP245 and SSP585 emission scenarios, the annual precipitation over CEC may significantly increase in the next 85 years. The largest boost is found in 2060–2100 under the SSP585 scenario. While limiting the anthropogenic greenhouse gas at the lowest emission scenario, precipitation over CEC is projected a relatively slight increase in the 2016–2070 period, whereas a decreasing trend in the last 30 years of the 21st century.

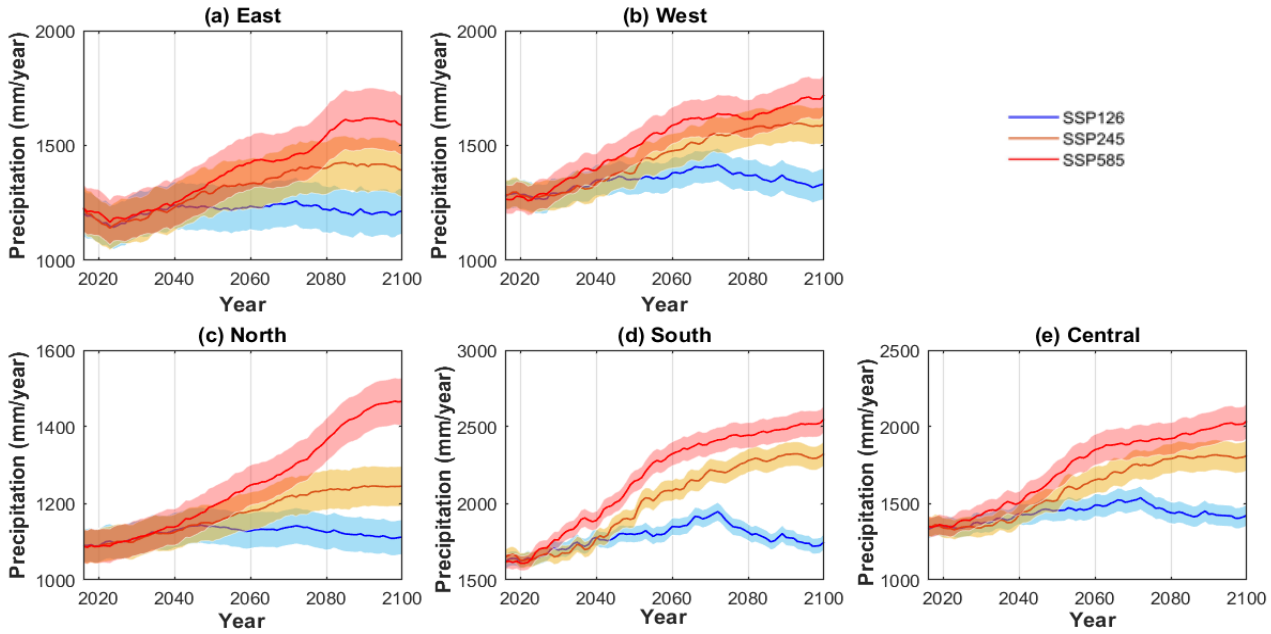

Figure 5-14. Annual precipitation projections under 15a moving average window for the (**a**) East, (**b**) West, (**c**) North, (**d**) South, and (**e**) Central clusters. Shadows represent the 90% confidence intervals.

The future scenarios are divided into three sub-time periods with a 26-year interval, that is, 2023–2048, 2049–2074, and 2075–2100, representing the early, mid, and late 21st century, respectively. Projected changes in precipitation can be revealed based on the difference compared with the historical 26-year period (1990–2015). Projected relative changes in the mean annual precipitation amount are presented in Figure 5-15. Positive and negative values indicate more and less precipitation in the projection period than in the historical period, respectively. In the early 21st century, the mean annual precipitation amount indicates a slight drying tendency over the northeastern CEC and sites in the center under the three emission scenarios (Figures 5-15a, d, g). The projected decrease remained

over the northeastern CEC in the mid- and late century under the SSP126 scenario (Figures 5-15b and c). However, over the southern and western parts of CEC, a slightly wetter condition was projected in the early 21st century under the three scenarios. Furthermore, this wetter tendency is expected to be notable in the mid- and late periods, especially under the SSP585 scenario, with an increasing percentage beyond 30% (Figures 5-15f, i).

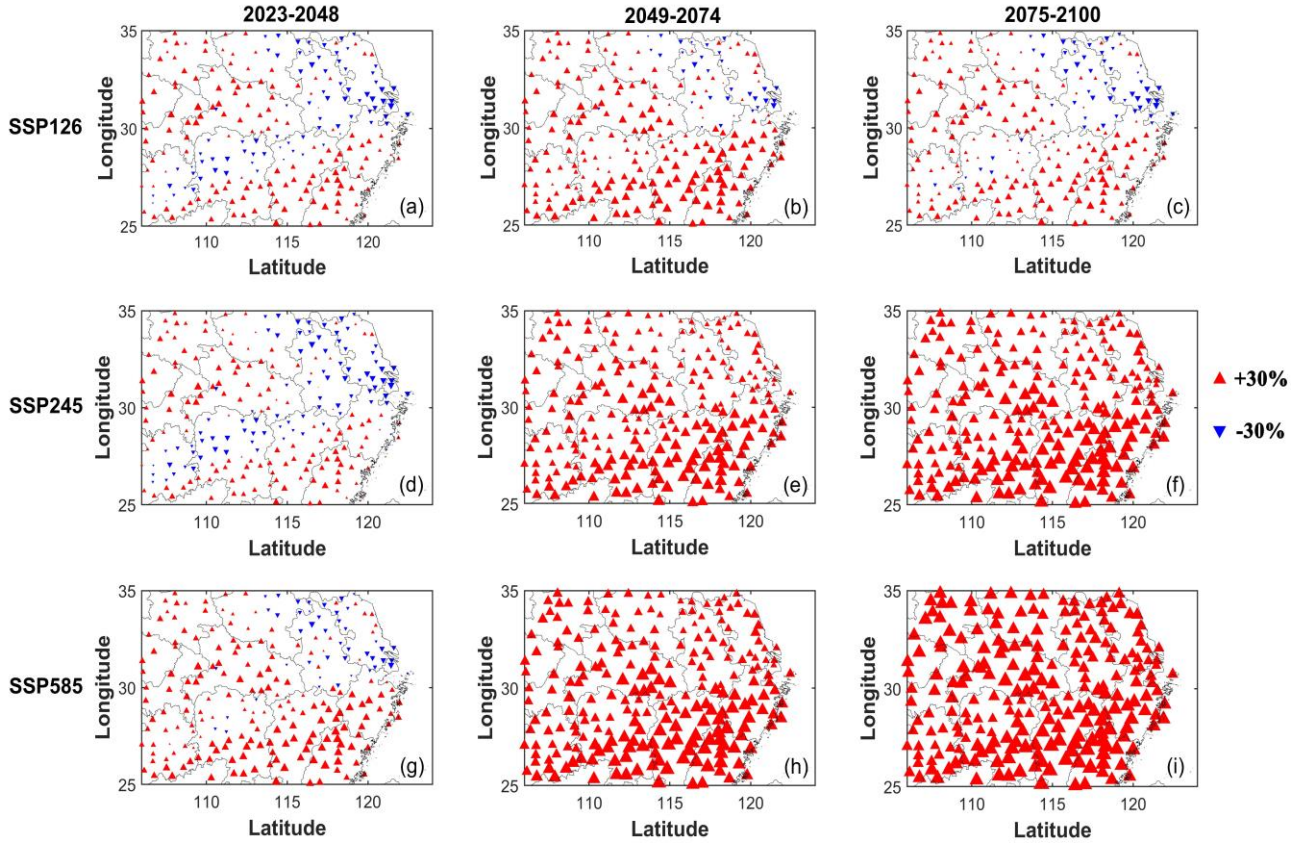

Figure 5-15. Relative changes (%) of the projected mean annual precipitation amount in the early, mid, and late 21st centuries under different emission scenarios compared with the historical period 1990–2015.

Figure 5-16 show the boxplots of the means of the total extreme precipitation frequency and amount index for the historical and future projections under different warming scenarios. The relative changes for the early, mid, and late 21st centuries compared with the historical period of 1990–2015 are summarized in Table 5-13. The bold font indicates statistically significant changes at the 95% confidence level. For the early 21st century, the projected changes in the mean of the total extreme precipitation frequency show regional differences under the three scenarios. Except for a slight increase found for the east cluster, the remaining regions are likely to face less frequent extreme

precipitation. Meanwhile, weakened extreme precipitation intensity is found over CEC. In particular, for the North cluster, the negative changes are projected to decrease by -14.91%, -15.42%, and -14.86% under the SSP126, SSP245, and SSP585 scenarios, respectively. By the mid-21st century, projected changes in extreme precipitation in most areas will switch from negative to positive. Except for the North cluster, the mean of the total extreme precipitation frequency for the remaining clusters is projected to increase under the SPP245 and SSP585 scenarios. Accordingly, it produces the largest magnitude ranging from 15.33%–38.79% in the worst scenario. For example, the projected mean extreme frequency of the South cluster increases to 11.89 per year under the SSP585 scenario, which is higher than that of the historical period (8.76 per year). However, under the SSP126 scenario, the projected extreme amount may decrease by -0.89% to -13.88% for the five clusters. In the late century, the projected increases in precipitation extremes over CEC are expected to be larger than those in the early- and mid-periods. The means of the total extreme precipitation frequency and amount significantly increase by 21.93%–48.07% and 12.32%–38.33% respectively, in the scenario with the highest emission scenario. The change rates of the North and West clusters were relatively smaller than those of the East, South, and Central clusters. For the most severe cluster, the mean extreme precipitation amount can increase to 751.50 mm per year in the worst scenario. As expected, the projected extreme precipitation shows a continuous decrease over CEC when under the SSP126 scenario.

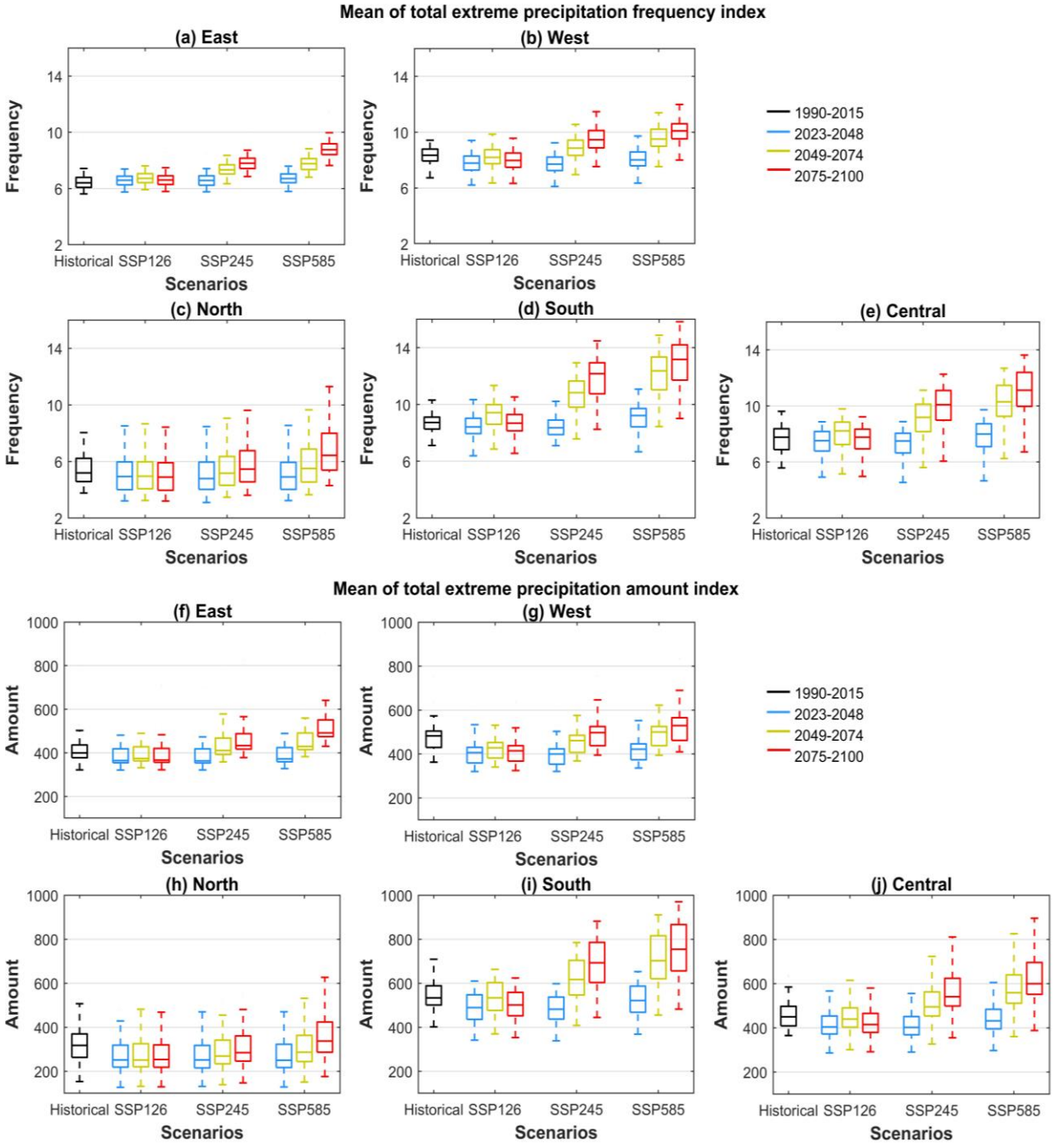

Figure 5-16. Boxplots of the means of the total extreme precipitation frequency and amount (unit: mm/year) index for the historical period (1990–2015) and the future projections for three sub periods (early, mid, and late 21st centuries) under different warming scenarios. (**a, f**) East, (**b, g**) West, (**c, h**) North, (**d, i**) South, and (**e, j**) Central cluster.

Table 5-13. Relative changes (%) of the projected means of the total extreme precipitation frequency and amount in the early, mid, and late 21st centuries under different emission scenarios compared with the historical period 1990–2015. Bold fonts represent statistically significant changes at the 95% confidence level.

		2023-2048			2049-2074			2075-2100		
		SSP126	SSP245	SSP585	SSP126	SSP245	SSP585	SSP126	SSP245	SSP585
Frequency	East	1.78	1.75	3.61	4.24	**13.52**	**19.76**	2.17	**20.07**	**35.73**
	West	**-6.11**	**-7.07**	-2.65	-0.74	**6.67**	**15.33**	-3.54	**14.75**	**21.93**
	North	-7.75	-8.28	-7.68	-6.63	-1.08	4.84	-7.86	4.20	**23.22**
	South	-2.87	-3.95	4.04	**6.44**	**22.41**	**38.79**	-0.56	**35.70**	**48.07**
	Central	-4.26	-5.05	1.68	3.70	**16.87**	**32.31**	-1.81	**28.75**	**42.82**
Amount	East	-5.50	-5.58	-3.68	-3.13	5.44	11.28	-5.12	11.48	**26.21**
	West	**-13.65**	**-14.50**	**-10.41**	-8.64	-1.78	6.17	**-11.24**	5.68	**12.32**
	North	**-14.91**	**-15.42**	**-14.86**	**-13.88**	-8.75	-3.42	**-15.06**	-3.90	**16.61**
	South	**-9.69**	**-10.68**	-3.19	-0.89	**14.19**	**29.62**	**-7.55**	**26.68**	**38.33**
	Central	**-10.60**	-11.32	-4.95	-3.06	9.25	**23.85**	-8.31	**20.54**	**33.82**

5. Discussion-Possible impacts of climate change on future precipitation changes

In Section 4.3, we described the selection of a GCM model for precipitation projections. Our results show that the annual and extreme precipitation over CEC have increased under global warming. Most regions will experience unprecedented precipitation and extremes in the late 21st century under the scenario with the highest emission. This increase is expected to be more severe over the southern CEC. Under the lowest emission scenario, the annual precipitation of the northeast CEC and most of the extreme precipitation are projected to be lower than the historical values (1990–2015). Because the results described in the previous section were mainly obtained via a statistical approach, in this section, the explanations of the increased precipitation were conducted from a point of view of the possible causes.

5.1 Future projections of water vapor transport

In general, changes in regional precipitation due to global warming can be decomposed into two contributors: 1) the thermodynamic effects (Wentz Frank et al., 2007) and 2) the dynamic forcing (Barton et al., 2016; Marquardt Collow et al., 2016). All increase in temperature results in a higher evaporation rate (Giorgi et al., 2011). Furthermore, the enhanced atmospheric water-holding capacity with increasing global temperature that approximately in accordance with the theoretical rate of the Clausius-Clapeyron equation (Koutsoyiannis, 2012; Lehmann et al., 2015) could increase the water vapor contents and affect the magnitude of the precipitation (Emori and Brown, 2005; Gorman and Schneider, 2009). Previous studies have demonstrated that the increased water vapor transport and convergence will boost precipitation and its extremes (Ayantobo et al., 2022; Patricola et al., 2022; Pendergrass et al., 2015). Lavers et al. (2015) used 22 GCMs from CMIP5 to examine the possible changes of the mean, standard deviation, and extreme thresholds of IVT in the historical simulation (1979–2005) and two emission scenarios (2073–2099) on a global scale. They concluded that under the highest emission scenario, the intensified water vapor flux in the lower atmosphere would lead to higher IVTs (increases 17%) when referencing the average of multi-model. Moreover, 30%–40% increase in IVTs over the northern hemisphere storm tracks. Warner et al. (2015) simulated the atmospheric rivers over the west coast of northern United States in the periods 1970–1999 and 2070–2099. Results showed that increased IVTs were predicted under the highest emission scenario and the average winter precipitation has increased by 11%–18%, especially on extreme IVT days, this trend reached 15%–39%. In particular, Neelin et al. (2022) investigated the temperature dependence of precipitation extremes. They suggested that increases in moisture will exacerbate the probability of precipitation extremes.

In the eastern China region, the atmospheric moisture content would also change in response to global warming (Sun and Ding, 2010; Zhang et al., 2019a). In this section, we projected the possible changes in water vapor transport (quantified by IVT) in the future, an important indicator of atmospheric moisture status. Figure 5-17 shows the mean annual IVT intensities and temperature changes from 1960 to 2100 over CEC, based on the GCM data. Relative to the historical period 1960–2015, the projected IVT significantly increases associated with the warming temperature under the three emission scenarios.

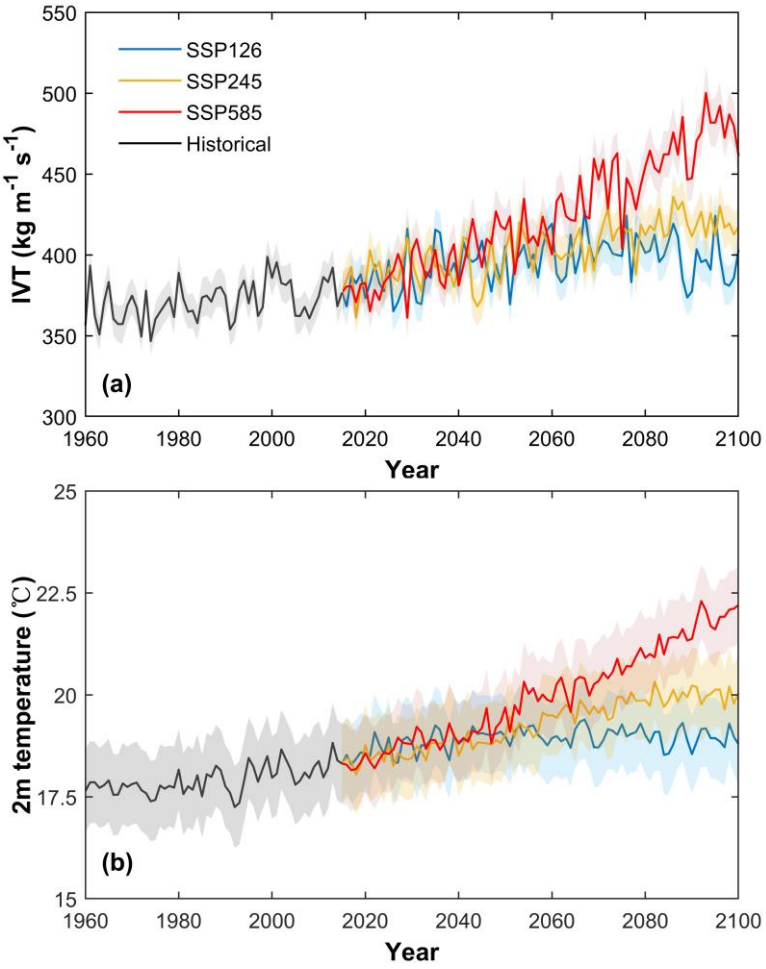

Figure 5-17. Historical (1960–2015) and projected (2016–2100) mean of the **(a)** annual IVT and **(b)** 2m temperature under SSP126, SSP245, and SSP585 emission scenarios over the study domain.

Changes in the probability distributions of the mean daily IVT values (averaged by the 0.25° grids closet to the rain gauge) from historical to the projected periods are shown in Figure 5-18. The fitted probability density functions were calculated by kernel density estimation. Black lines indicate the historical values in the periods 1960–1989 and 1990–2015. Compared with the period 1990–2015, the peaks of projected IVT in all sub-periods moved to the right and have a longer tail, especially in the late 21st century under the SSP585 scenario. It is projected that warmed atmospheric will result in large water vapor transport and convergence more frequently over CEC, which may affect extreme precipitation.

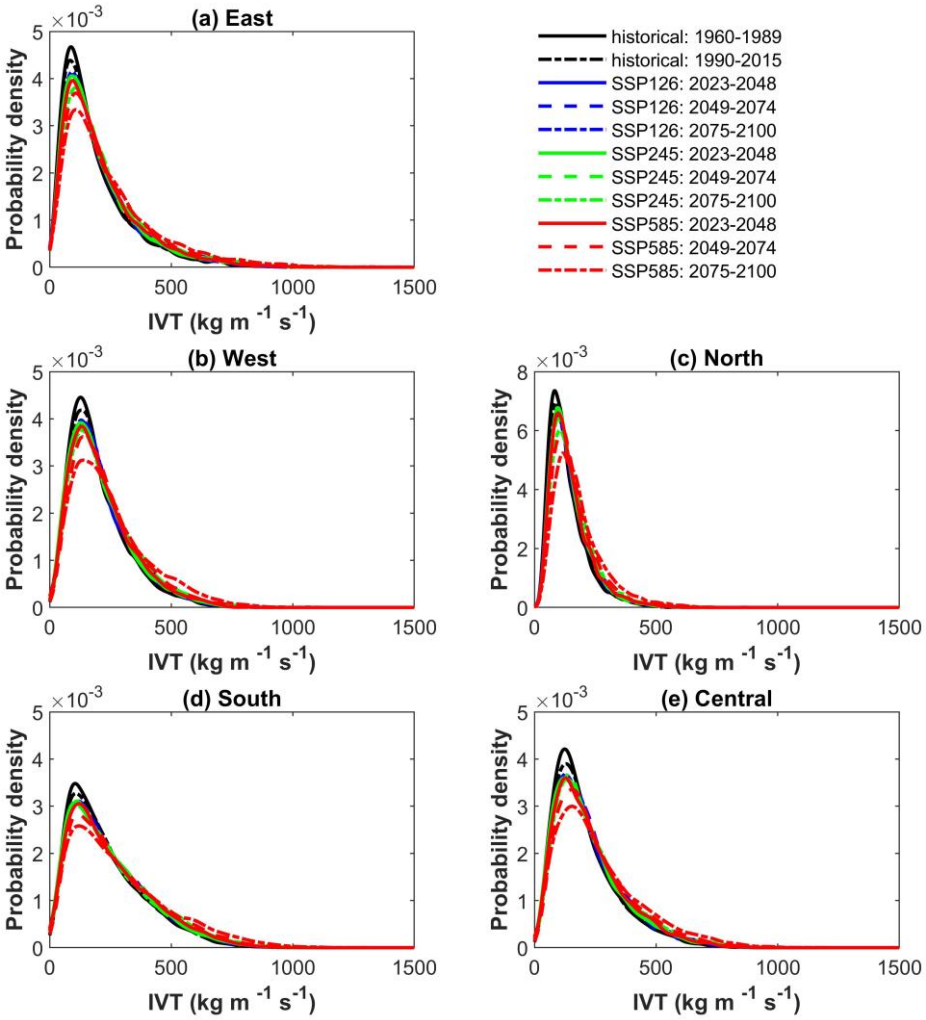

Figure 5-18. Probability distributions of the historical period (1960–1989, 1990–2015) and projected of the mean daily IVT values under SSP126, SSP245, and SSP585 emission scenarios for the five clusters.

To future explore the roles of climate warming in altering the occurrence probability on a particular IVT threshold, the event attribution analysis that proposed by Allen (2003) was used. Assuming that P_0 and P_1 are the probabilities of a particular IVT threshold in the historical period 1990–2015 and projected future world, respectively. The fraction attributable risk (FAR) can be formulated by the Equation, $\mathrm{FAR} = 1 - P_0/P_1$, where $\mathrm{FAR} = 0.5$ indicates a doubled occurrence probability of this IVT threshold in projected scenarios and climate changes contribute to 50% (Stott et al., 2016). Figure 5-19 shows the FARs for the projected IVT at five thresholds (80th, 90th, 95th, 99th, and 99.5th) under different warming scenarios, where referenced to the historical 1990–2015. In general, with the increasing IVT threshold, the contributions of climate changes are likely to magnify because more evident signals indicated by the FARs can be detected. The estimated FARs under the three scenarios

are ranging from 0.05–0.18 for the heavy IVT (at 80th percentile) in the period 2023–2048; whereas for the 95th threshold, the FAR is projected to be above 0.2 for the five clusters in the worst scenario. In addition, for the IVT extremes exceeding the 99.5th threshold, roughly 65% of increases in the occurrence probability are attributable to the increased CO_2 by the end of this century.

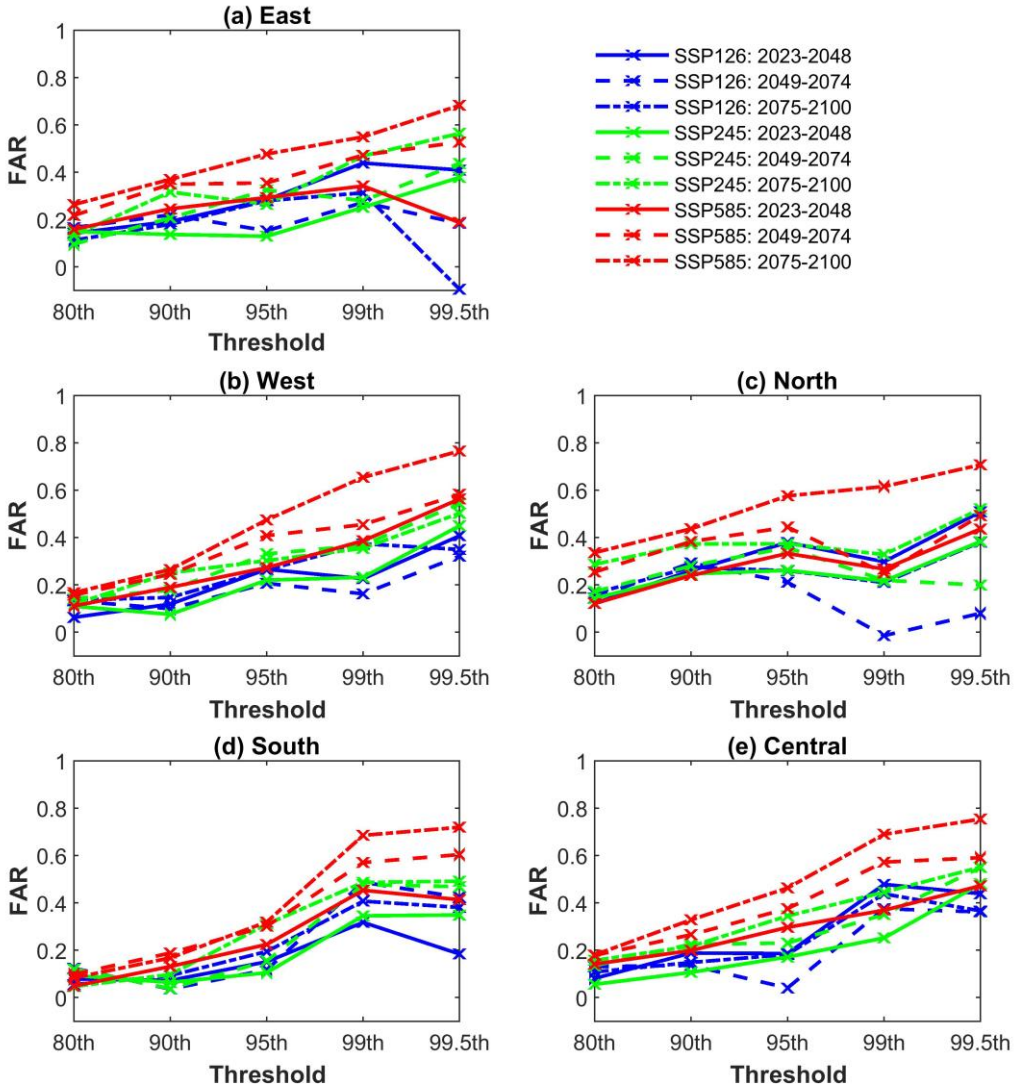

Figure 5-19. The fraction attributable risks for the mean daily IVT at five thresholds under different warming scenarios.

5.2 Future projections of weather states and circulation patterns

Stronger water vapor transport may result in the enhancement of the potential wet weather conditions (Pfleiderer et al., 2019). To clarify this, we assumed the projected daily downscaling precipitation (from 2016 to 2100) simulated by the Ensemble-NHMM as the most likely observation

sequence “occurring in the future,” and imported the data into the Ensemble-NHMM trained with GCM historical data. The Viterbi algorithm was used to obtain the most likely hidden state sequence of the future cycle. Because 100 simulation values are obtained every day, we performed the Viterbi algorithm 100 times for each cluster respectively. Because of the limitation of the NHMM, whose emission probabilities associated with the hidden states do not change in the future, the hidden weather states remain the same, only the frequency. Wet or dry conditions referring to the historical period. Figure 5-20 shows the time series of the projected annual frequency of the six hidden states (median of the 100 simulations) under the three emission scenarios for the South cluster, where projected precipitation will increase most severely in the future. The results for the remaining clusters are presented in Figures S5-5–S5-8. The blue title indicates that the state belongs to the wet type; otherwise, it is dry. The frequency of wet hidden states in the South cluster is projected to increase in the future, especially under the SSP585 scenario. In contrast, the dry hidden states are projected to decrease. Under the SSP126 scenario, the wet (dry) hidden states exhibit an increase (decrease) in the first 50 years but a decrease (increase) in the last 30 years. Similar conclusions can be drawn for the other clusters.

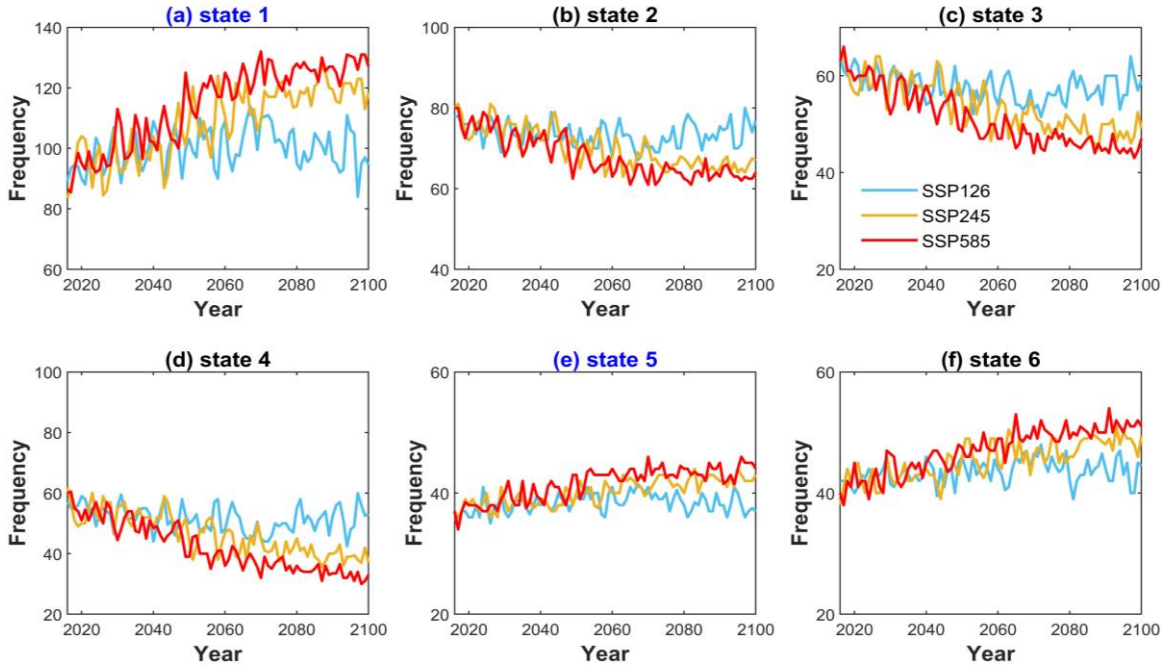

Figure 5-20. Time series of the projected annual frequency of the six hidden states under the three emission scenarios for the South cluster. The blue title indicates that the state belongs to the wet type.

Table 5-14 summarizes the correlation coefficients between the annual frequency of the hidden states and mean annual IVT intensities under the different warming scenarios. From the low to high emission scenario, the linear relationship between the occurrence of hidden states and IVT becomes more notable. In other words, changes in the weather conditions are more sensitive to an increased water vapor transport intensity. Wet weather conditions occur more frequently.

Table 5-14. Correlation coefficients between the annual frequency of the hidden states and mean annual IVT intensities under three emission scenarios. Wet states are shown in bold fonts.

		State 1	State 2	State 3	State 4	State 5	State 6
	East	**0.26**	**0.30**	**0.26**	**0.29**	-0.33	0.06*
	West	0.37	-0.48	-0.48	0.14*	-0.40	**0.44**
SSP126	North	**0.38**	-0.13*	-0.19	0.40	**-0.27**	**0.16***
	South	**0.50**	-0.49	-0.52	-0.44	**0.43**	0.29
	Central	**0.50**	-0.21	-0.27	-0.17*	-0.36	**0.38**
	East	**0.73**	**0.72**	**0.70**	**0.67**	-0.74	0.26
	West	0.64	-0.71	-0.76	0.58	-0.72	**0.75**
SSP245	North	**0.72**	-0.58	-0.61	0.55	**-0.55**	**0.35**
	South	**0.77**	-0.75	-0.77	-0.75	**0.76**	0.71
	Central	**0.76**	-0.10*	-0.22	-0.08*	-0.76	**0.74**
	East	**0.88**	**0.86**	**0.84**	**0.85**	-0.88	0.46
	West	0.72	-0.77	-0.80	0.81	-0.83	**0.81**
SSP585	North	**0.91**	-0.89	-0.83	0.85	**-0.80**	**0.54**
	South	**0.84**	-0.79	-0.83	-0.85	**0.76**	0.80
	Central	**0.85**	0.36	-0.21*	-0.03*	-0.85	**0.80**

Notes: *This value failed to reach the 95% confidence level.

Global warming leads to changes in atmospheric circulation characteristics relevant to specific geographic precipitation (Mindlin et al., 2021). Zhou et al. (2021a) analyzed the frequency differences in summer circulation pattern under anthropogenic and only natural forcing. They found that anthropogenic influences could alter the likelihood of wet CPs which favors the rainfall over east China. The self-organizing map was used again to identify the CPs of MPI-ESM1-2-HR during the three sub-periods, results are shown in Figures S5-9–S5-11. Relative changes in the projected mean

annual frequency of the identified CPs under three emission scenarios compared with the historical of 1990–2015 are shown in Figure 5-21. As presented in Section 4.2, Chapter 2, A′1 to A′5 CPs related to the extreme precipitation occurrence over CEC, while CPs A′1 and A′2 are controlled by a stable positive anomaly of geopotential height at 500 hPa, A′4 and A′5 dominated by the positive (negative) anomalies over the Eastern Eurasia continent (surrounding oceans). Due to the different configurations of circulation anomalies, CP A′1 and A′5 in producing extreme precipitation are more relevant to the South and North clusters over CEC respectively. It is noted that the projected mean annual frequencies of CPs A′1 and A′5 show a converse change trend under the three emission scenario. A′1 is occurring more often in the future, e.g., with an increase rate of 5 to 10 days per year under SSP245 and SSP585 scenarios in the early 21st century; while CP A′5 is the opposite.

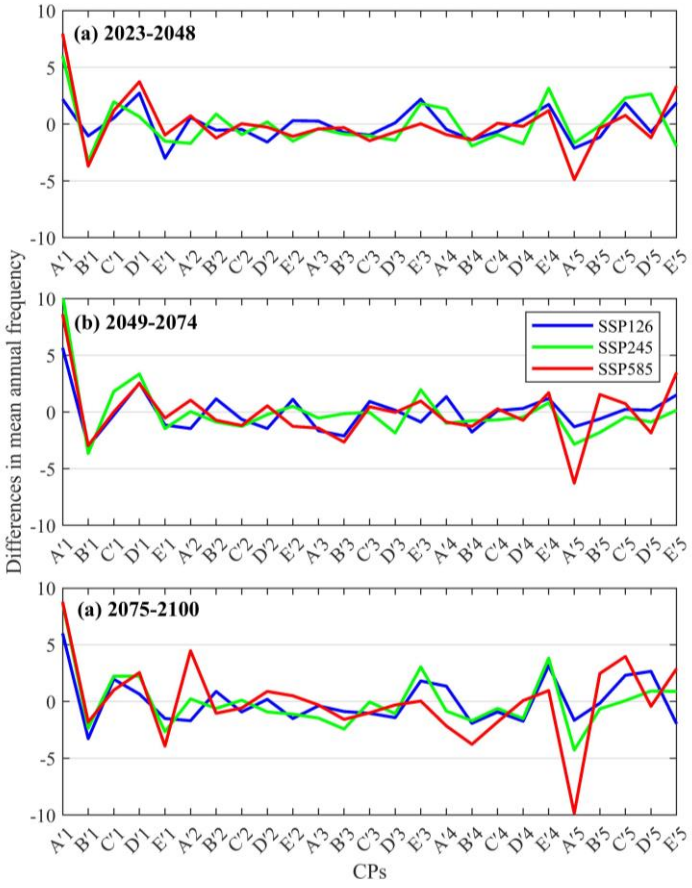

Figure 5-21. Relative changes in the projected mean annual frequency of circulation patterns in the early, mid, and late 21st centuries compared with the historical 1990–2015.

Furthermore, these changes in the circulation system can further affect the water vapor path further (Liu et al., 2020a). For instance, Wang et al. (2022) pointed out that an intensified land–sea thermal contrast would strengthen the East Asian summer monsoon meridional circulation and thereby forces

more moisture from the ocean into inland areas, eventually causing more precipitation over the northern China. Yang et al. (2022a) showed that strengthening the WPSH under global warming could also cause more moisture transport from the ocean to East China and induces heavy precipitation. Figure 5-22 shows the anomaly fields of GP at 500 hPa and IVT during the rainy season (April to September) in the early, mid, and late 21st centuries compared with the historical period 1990–2015. The figure shows that the GP at 500 hPa over CEC tends to increase due to global warming, but the contour lines of the anomaly fields denote an inhomogeneous feature in the horizontal direction during different sub-periods. First, significant changes in GP at 500 hPa and IVT anomalies between the three scenarios can be detected only starting from the mid-21st century. Based on Tebaldi and Friedlingstein (2013), significant climate effects of different emission pathways cannot be detected very quickly; this process requires 30–45 years at the regional scale. In addition, the ridge lines with an enhanced pressure gradient located in the coastal areas would promote the water vapor transport from the ocean to the south CEC, especially under the SSP585 scenario. It is clear that in the mid- and late centuries, under different emission scenarios, the south of CEC would receive stronger water vapor transport than the north, which could explain why the annual precipitation and precipitation extremes are expected to be more severe over the South cluster.

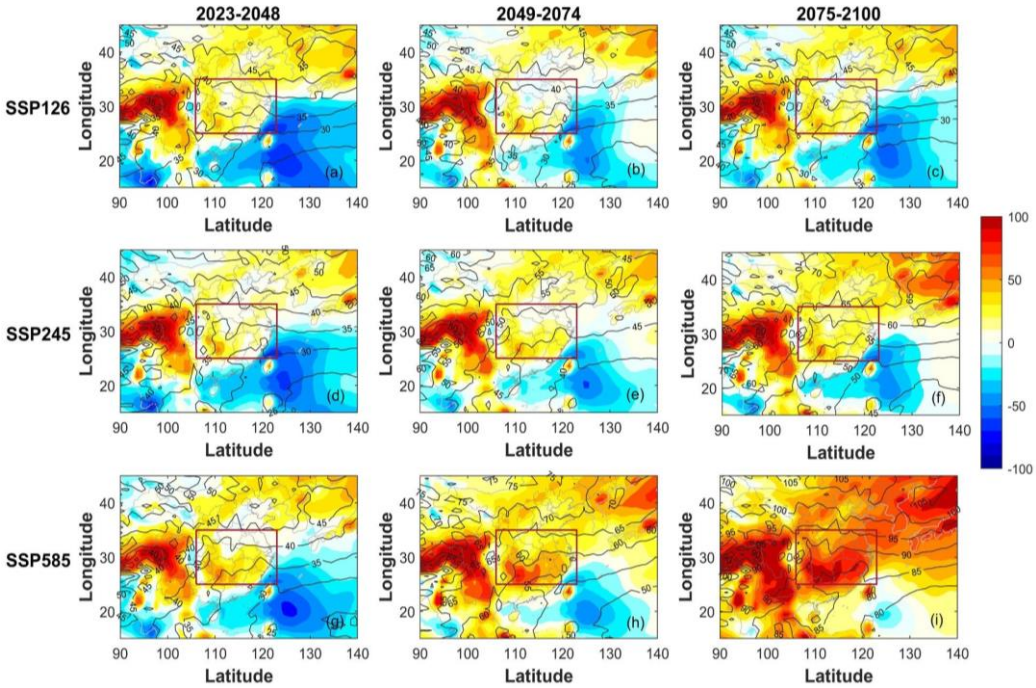

Figure 5-22. Under three emission scenarios, the anomalies fields of GP at 500 hPa (contours, unit: gpm) and IVT (shadow, unit: kg m^{-1} s^{-1}) during the rainy season of the periods of 2023–2048, 2049–2074, 2075–2100 compared with the historical period 1990–2015.

6. Conclusions

In this study, we proposed a new two-step precipitation hierarchical downscaling framework consisting of an ensemble learning model that combines XGBoost and RF for predicting the probability of multi-level daily precipitation events for an ensemble of clustered rain gauges. Predicted probabilities were used as predictors for the NHMM to conduct the precipitation downscaling at the scales of the individual rain gauges. The downscaling model, that is, Ensemble-NHMM, projects future trends in the daily precipitation amount over central-eastern China under different SSPs. The conclusions can be summarized as follows:

1) Our proposed ensemble learning model shows a superior capability in predicting the occurrence probabilities of multi-class daily precipitation. It obtains better prediction skills than the individual machine learning of RF and XGBoost.

2) Evaluation results show that the occurrence probability of different precipitation levels is a good predictor for the NHMM model. The Ensemble-NHMM performs well in simulating annual and extreme precipitation compared with the traditional NHMM, which directly uses the sequence of standardized IVTs and the first leading 50 PCs of GP at 500 hPa as the atmospheric predictors. We examined one of the CMIP6 models (MPI-ESM1-2-HR) for precipitation downscaling via the Ensemble-NHMM during 1960–2015. Based on the statistical metrics, the downscaled results of MPI-ESM1-2-HR produce reliable trend simulations.

3) Based on the precipitation projection results of the MPI-ESM1-2-HR, the central-eastern China may receive more precipitation in the period of 2016–2100, especially under the SSP245 and SSP585 emission scenarios. However, in the SSP126 scenario, the mean annual precipitation would decrease in the last 30 years of the 21st century. Furthermore, compared with ~26 years (1990– 2015), a slight drying tendency projected over the northeastern CEC under the three emission scenarios. The extreme precipitation frequency and amount will increase throughout the whole century (2016–2100). In the late century, the extreme precipitation frequency and amount may significantly increase by 21.9%–48.1% and 12.3%–38.3%, respectively, in the case of the worst emission scenario.

4) Enhanced water vapor transport and strengthened pressure gradient would be the possible factors responsible for the increased precipitation. To increase the likelihood of extreme events under the highest emission scenarios, it is necessary to limit global warming to reduce the future risks.

In summary, the Ensemble-NHMM exhibits a good performance with respect to precipitation downscaling, which can lead to further improvements in hydrological modeling.

CHAPTER-6. Extended summary and prospect

1. Main conclusions

Precipitation extremes are key factors for rainfall-induced disasters. Both observations from different measurements and simulations derived by numerical models demonstrate that extreme precipitation is increasing and expected to keep going more in the future. The occurrences of extreme precipitation events are strongly related to the favorable large-scale background of atmospheric circulation, as well as the anomaly of water vapor transport. There are still insufficient in investigating the roles of large-scale atmospheric circulation to extreme precipitation over central-eastern China (CEC). Moreover, the key scientific issue about "Can large-scale atmospheric circulation anomaly information be used for regional extreme precipitation predictions" should be solved. In the context of global warming, changes in atmospheric circulation and water vapor transport would lead to an increase in extreme precipitation. The future precipitation projections at the regional scale have large uncertainties due to the limitations of insufficient resolution of global circulation models.

In the PhD thesis, I filled these gaps by using self-organizing map (SOM) and event synchronization methods to investigate the linkages between extreme precipitation and large-scale atmospheric circulation; proposed a new hybrid deep learning model for extreme precipitation predictions, as well as a new downscaling framework to improve the historical simulations and future projections of GCMs. The major conclusions are summarized as follows.

(1) From 1960 to 2015, 23% of rain gauges in the CEC showed significant changes in annual extreme precipitation by the nonparametric Pettitt test, and the average of the Pettitt test index corresponding to the significant change points were 29.06 and 29.21 (counting since 1960) for annual extreme precipitation frequency and amount respectively. Meanwhile, rain gauges with synchronized characteristics of extreme precipitation can be clustered into four clusters by using the modularity method. 25 CPs were identified by SOM in each period of 1960–1989 and 1990–2015. The CPs characterized by obvious positive anomalies of 500 hPa geopotential height over the Eastern Eurasia continent and negative values over the surrounding oceans were highly synchronized with extreme

precipitation events. Contribution analysis of extreme precipitation changes indicate that the variations in CPs A′3 and A′5 could produce an increase in extreme precipitation frequency from 1960–1989 to 1990–2015. The 2–4 yr oscillation in the annual frequency of representative CPs was closely related to the phase of El Niño and Southern Oscillation; while the 20–25 yr and 42–50 yr periodic oscillations were correlated with the Pacific Decadal Oscillation and the Atlantic Multidecadal Oscillation.

(2) A hybrid deep learning model for the binary perdition of regional extreme precipitation occurrences was developed. Constructed by the anomalies of geopotential height at 500 hPa and water vapor transport, results showed that the MLP-CNN model exhibited an overall accuracy of 86% in the classification task of extreme or non-extreme precipitation days. For extreme precipitation events, MLP-CNN can correctly predict 81% of samples on the testing set and outperformed MLP, CNN, and two machine learning models (i.e., random forest and support vector machine). Additionally, the precursor signals of 1–2 days' circulation anomalies can be auxiliary to identify the extreme precipitation events, although the prediction time shifted from 1 to 15 days ahead, the reliability of MLP-CNN tended to decrease.

(3) The accuracies of 10 global circulation models (GCM) in extreme precipitation and atmospheric circulation simulations were evaluated. Five indices (i.e., SDII, Rx1day, R95p, R99p, R50mm) were selected to quantify the extremes. Compared to the gauge-based daily precipitation analysis dataset over the Chinese mainland (CGDPA), GCMs are difficult to accurately estimate the extreme precipitation amounts. Extreme precipitation from GCMs are weaker than CGDPA, with an underestimation exceeds 80%. Relative to the identified CPs of ERA5, GCMs can reflect most categories accurately, and MPI-ESM1-2-HR could be considered excellent according to its correctly capture the pattern labels.

(4) In Chapter 5, a new statistical downscaling framework was designed. This framework consisting the multi-level precipitation probability prediction based on the ensemble learning technique and NHMM downscaling. The ensemble learning model constructed by extreme gradient boosting (XGBoost) and random forest (RF) was used to predict the occurrence probabilities for the different

levels of daily precipitation aggregated by multiple sites. Accuracy validations show that ensemble learning model shows a superior capability in classifying no rain or rain and predicting moderate precipitation events for the five clusters. The precipitation downscaling was done using the predicted occurrence probabilities as the predictors for the NHMM. Statistical metrics show that the Ensemble-NHMM downscaled results are match well to the observations in precipitation variabilities and extreme precipitation simulations. In addition, the downscaled precipitation from a GCM model (MPI-ESM1-2-HR) can simulate the precipitation well. The consistency rate of the time series of hidden state identified by MPI-ESM1-2-HR exceeds 98% to the results of ERA5.

(5) The Ensemble-NHMM downscaling model was applied to future scenarios to conduct precipitation projection. Three climate scenarios with different Shared Socioeconomic Pathways (i.e., SSP126, SSP245, and SSP585) were selected. Projection results show that the precipitation over CEC would increase in the future. Compared with the ~26 years (1990–2015), the extreme precipitation frequency and amount may significantly increase by 21.9%–48.1% and 12.3%–38.3%, respectively, in the late century when under the worst emission scenario. The increased probability of stronger water vapor transport relevant to the regional warming. More wet weather states due to the enhanced water vapor transport and the strengthen pressure gradient would be the possible factors for the increased precipitation.

2. Revisiting the research questions and future work

The research questions discussed in the thesis relating to 1) the atmospheric circulation patterns associated with the extreme precipitation over central-eastern China; 2) the extreme precipitation predictability when using the large-scale atmospheric variables; and 3) future projections of extreme precipitation under different warming scenarios and the possible causes. To investigate these issues, I developed some statistical/climatic models to predict and project extreme precipitation events dominated by large-scale atmospheric circulation. These scientific and useful tools can be referenced for the similar research.

There are some limitations should be addressed.

(1) First, although large-scale atmospheric circulation dominates the foremost changes in regional

extreme precipitation, the small-scale-storm might be reflected insufficient. In some cases, locally vertical convection also plays an important role in triggering the short time heavy precipitation in summer over east China (Li et al., 2019; Zhang et al., 2019b). In addition, we assumed that the leading features of future atmospheric circulation remains the same. Some studies suggested that the nonstationary of precipitation should be considered under climate changes (Chen and Zhang, 2021; Cheng and AghaKouchak, 2014; Hertig and Jacobeit, 2015). To solve the limitations in the thesis, accordingly, two issues should be considered in the futures. More atmospheric variables, e.g., column water vapor, and water vapor flux convergence at different vertical levels will under considerations. Previous studies suggested that the deep convective precipitation is highly related to the column water vapor (Holloway and Neelin, 2009; Schiro et al., 2016). For the downscaling technique, the key issue is to adjust the conditional transition probabilities consider the nonstationary of precipitation (Holsclaw et al., 2017).

(2) The hybrid deep learning model was used to predict the occurrence probability of extreme precipitation events. The multilayer perceptron and convolutional neural network were trained to mine the local and spatial feature information of large-scale atmospheric circulation associated with the extreme precipitation. Despite reliable predictions are obtained, this hybrid deep learning model is insufficient in the explanations of related physical mechanism. In future research, how to improve the interpretability of the deep learning model in regional extreme precipitation predictions is also one of the directions.

(3) In the research on the future predictions of precipitation, the possible factors of precipitation changes over CEC were analyzed from the projected large-scale atmospheric circulation fields and the water vapor transport under different warming scenarios. The influences of climate change were quantified on the basis of thermodynamic and dynamic factors. Strengthen the physical mechanisms and attribution research of precipitation changes can provide more reliable and comprehensive reference for exploring the impact of climate change.

Appendix

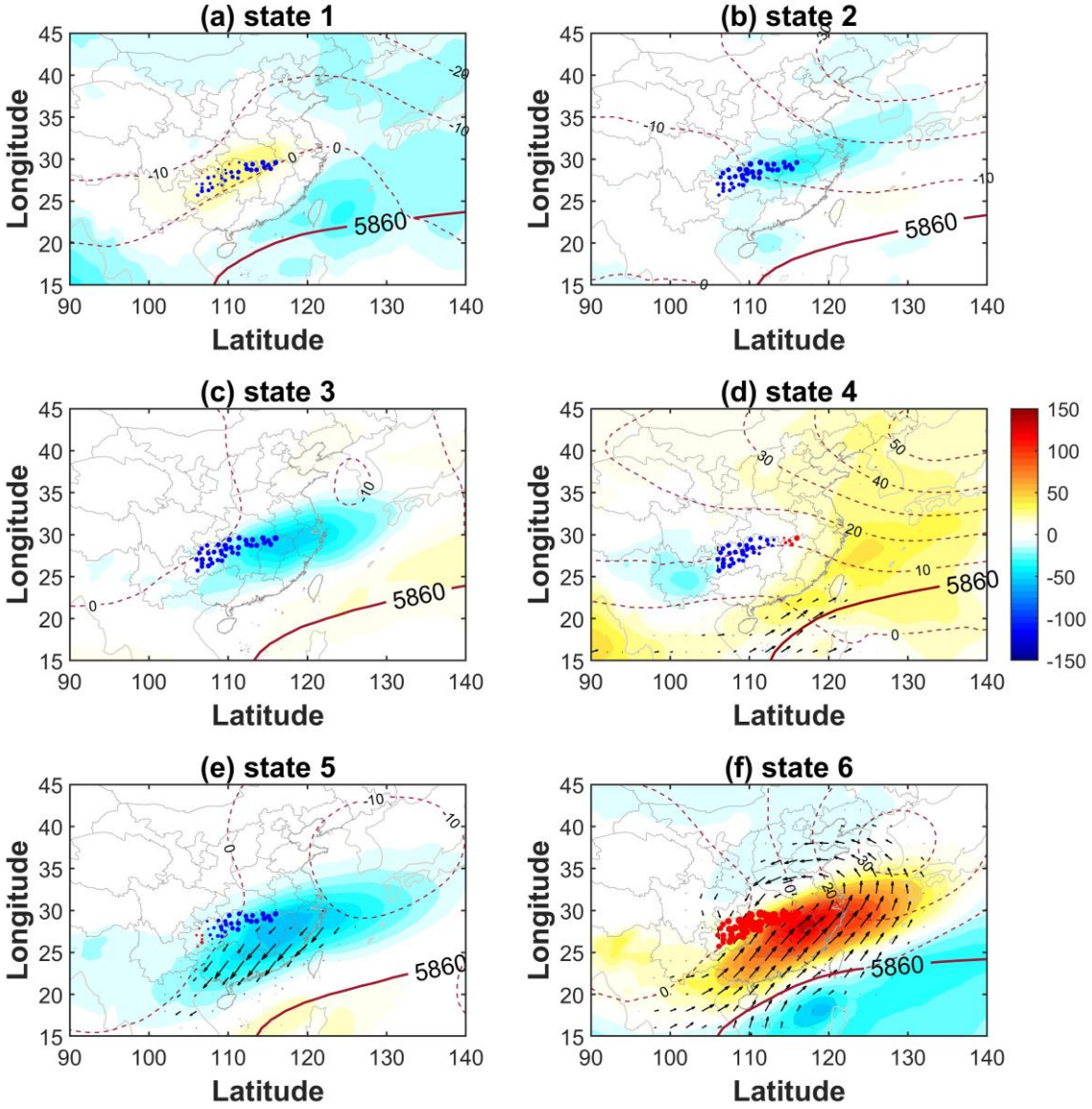

Figure S5-1. Identified hidden states for the West cluster and their corresponding atmospheric circulations. The red or blue solid circles represent the positive or negative anomalies the daily precipitation amount under a hidden state compared with the average from 1960 to 2015; their size represents the severity. Vector arrows indicate the wind anomalies at 850 hPa (unit: m s^{-1}) and shadow and dotted lines show the anomalous fields of IVT (unit: kg m^{-1} s^{-1}) and geopotential height at 500 hPa, respectively. Bold contours represent the 5860 gpm.

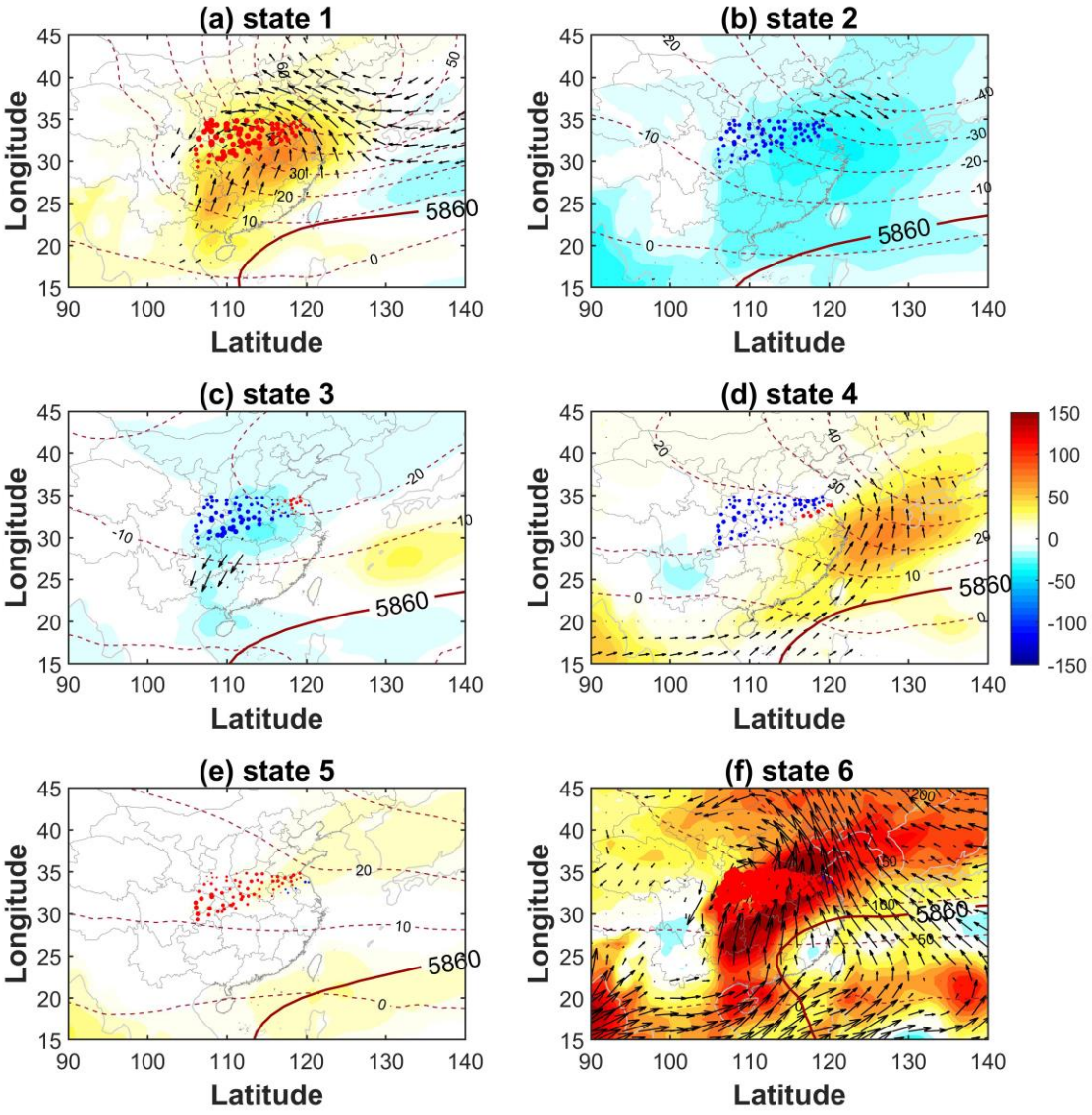

Figure S5-2. Same as Figure S5-1, but for the North cluster.

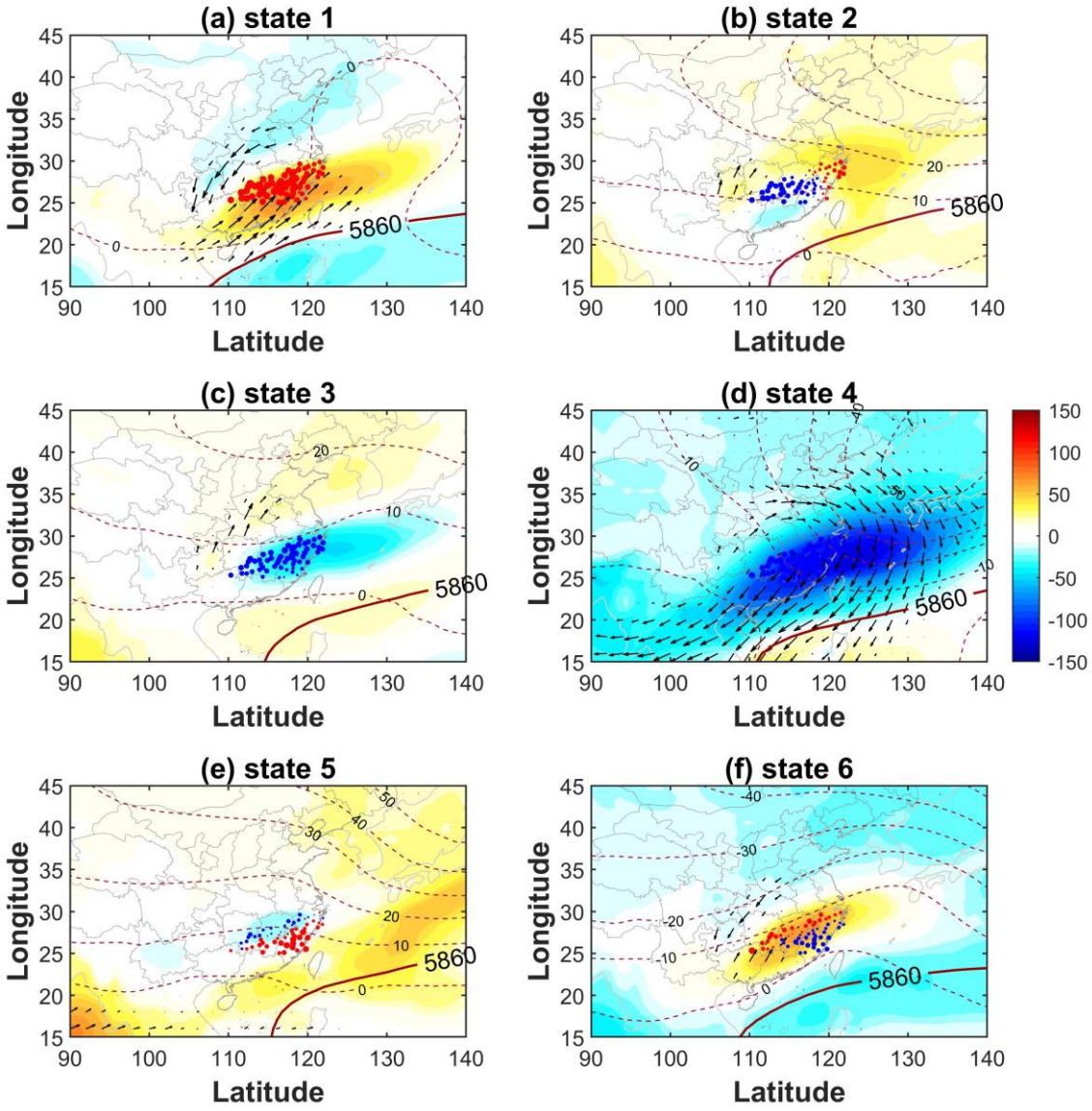

Figure S5-3. Same as Figure S5-1, but for the South cluster.

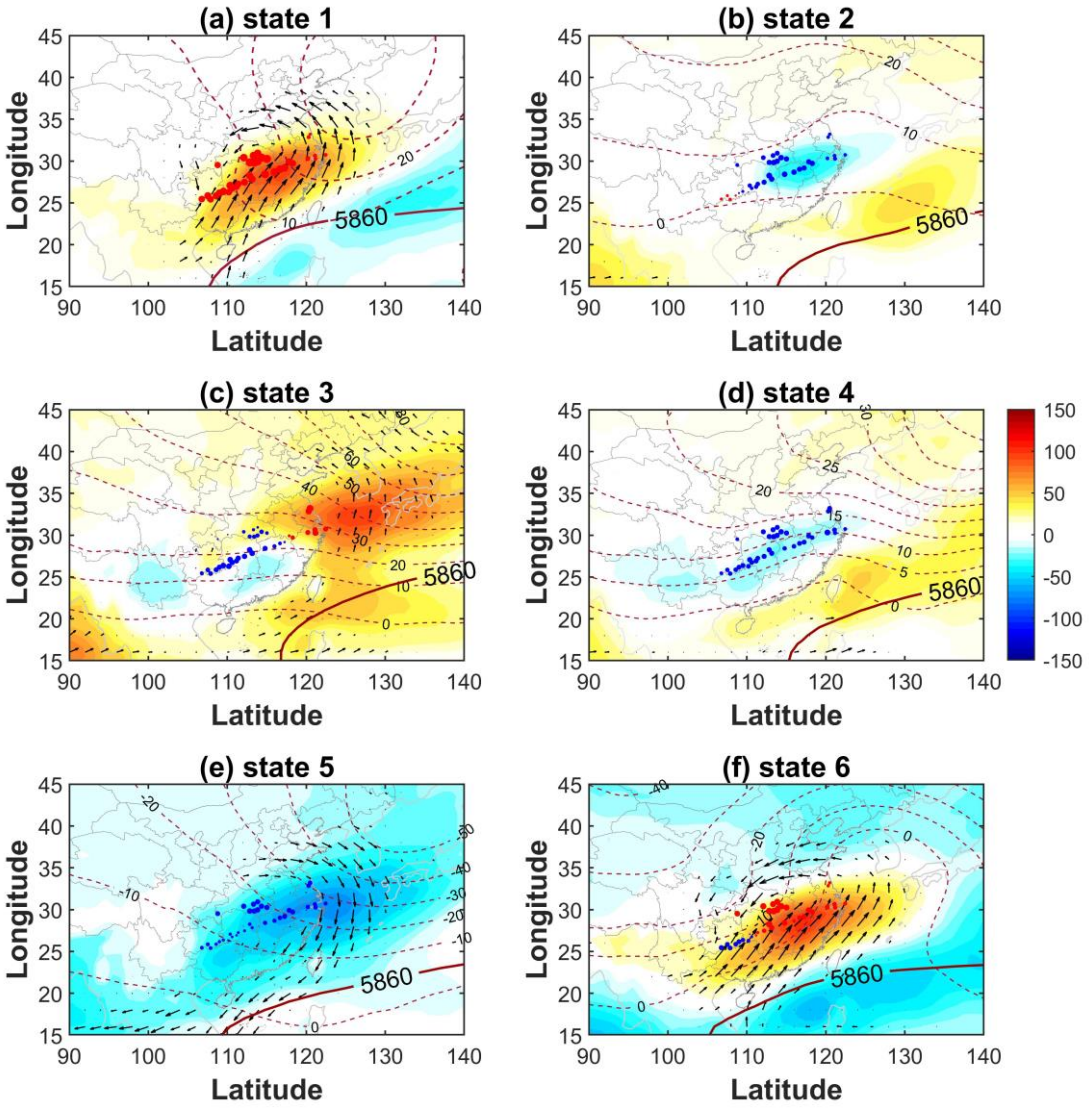

Figure S5-4. Same as Figure S5-1, but for the Central cluster.

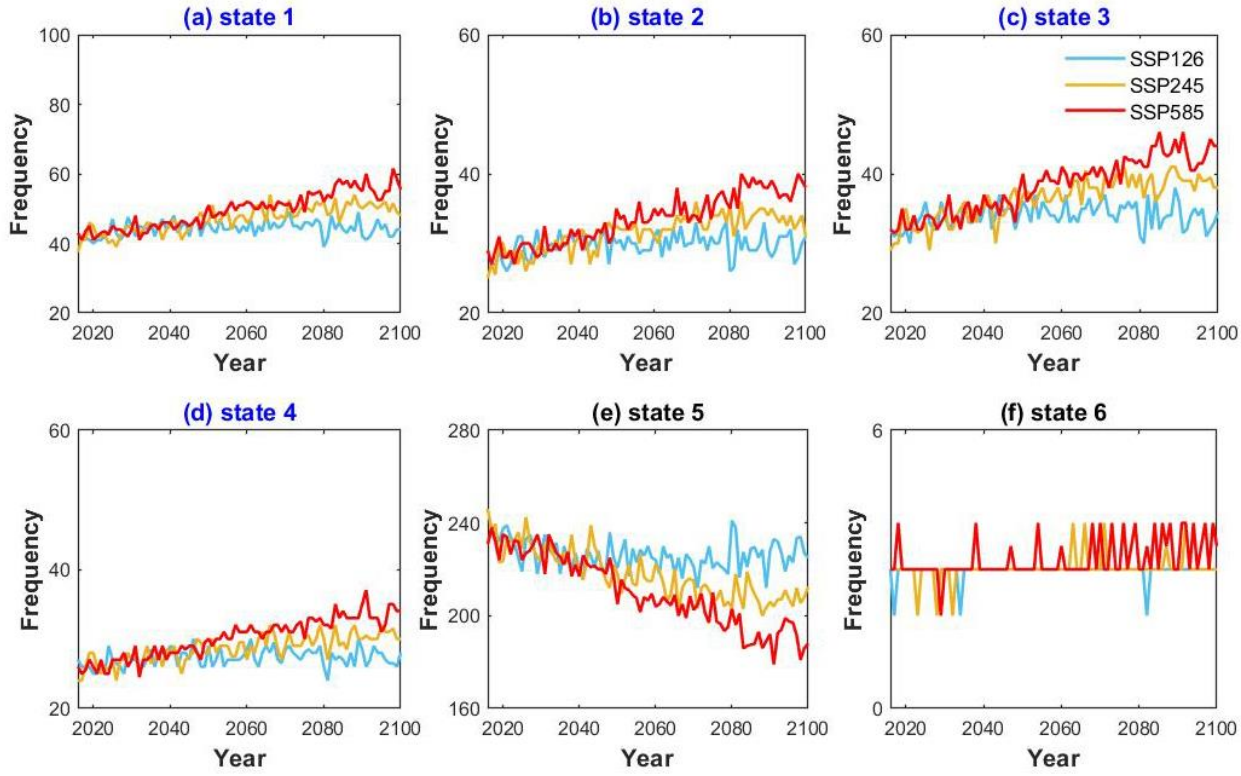

Figure S5-5. Time series of projected annual frequency of the six hidden states under the three emission scenarios for the East cluster. The blue title means the state belongs to the wet type, otherwise dry.

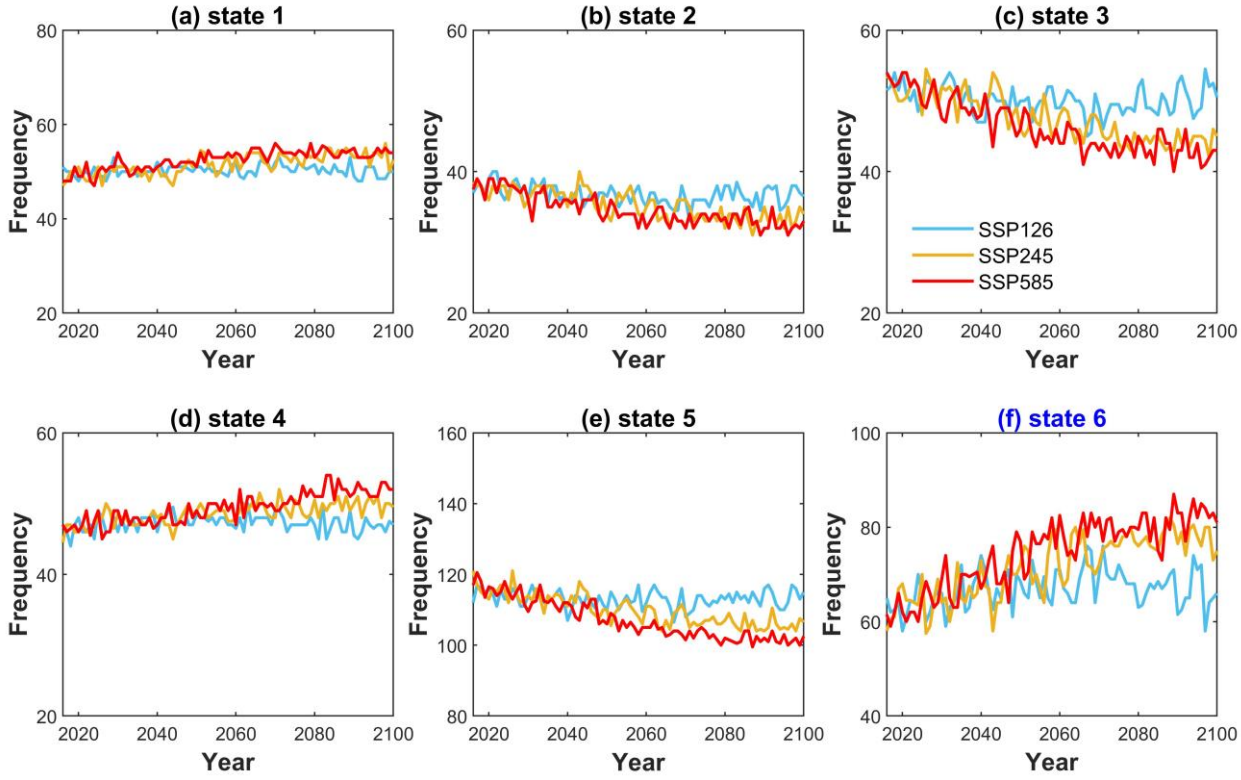

Figure S5-6. Same as Figure S5-5, but for the West cluster.

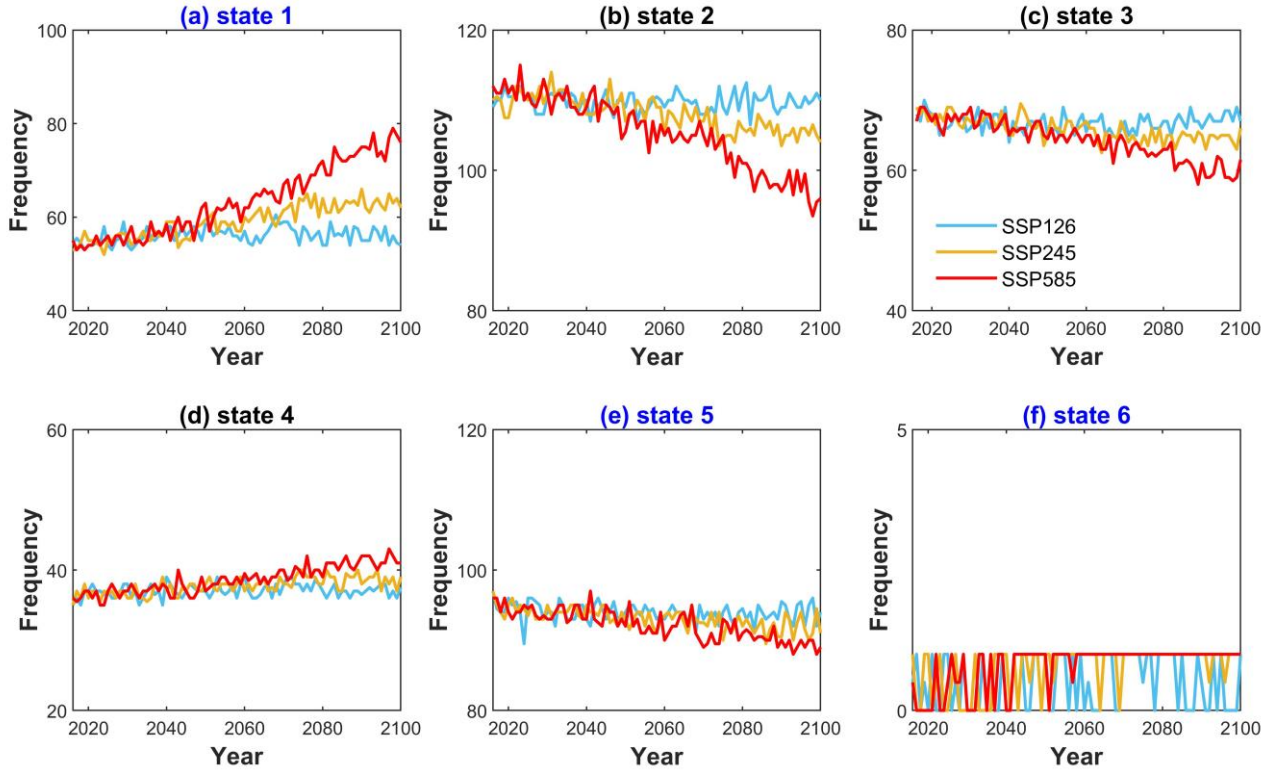

Figure S5-7. Same as Figure S5-5, but for the North cluster.

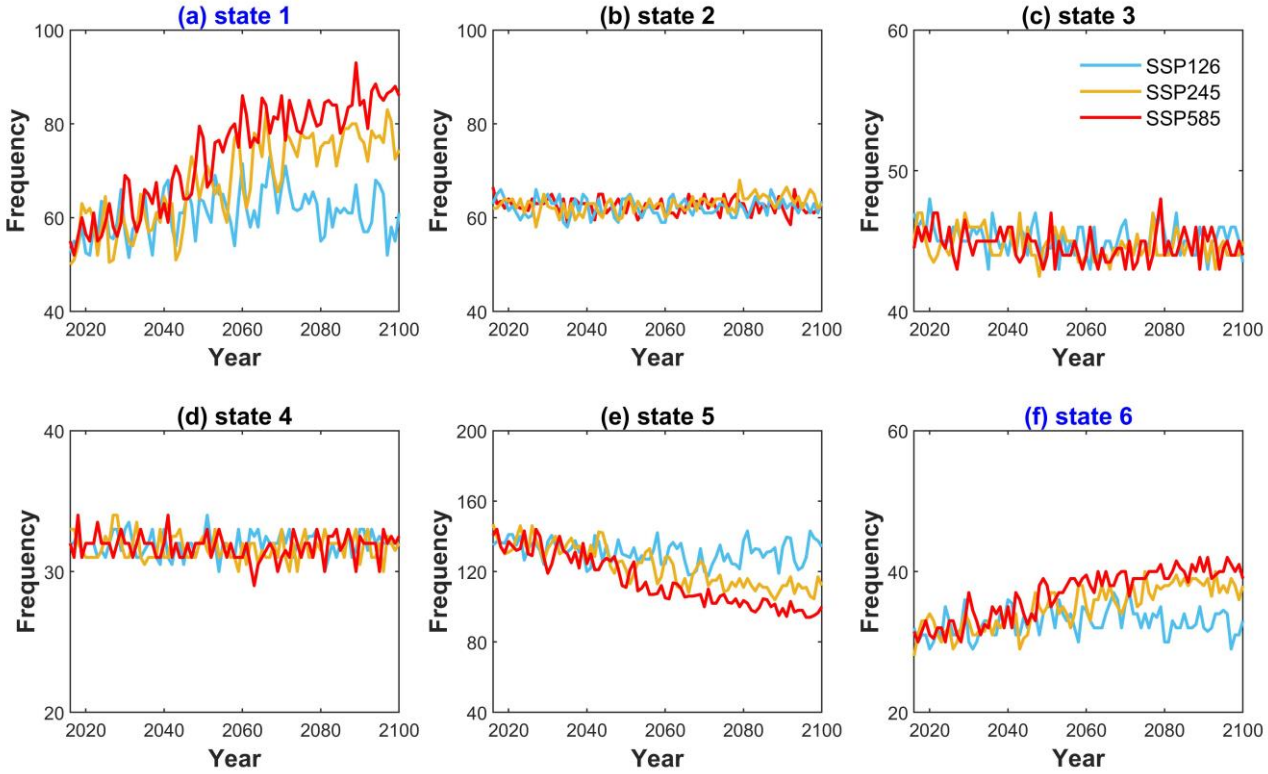

Figure S5-8. Same as Figure S5-5, but for the Central cluster.

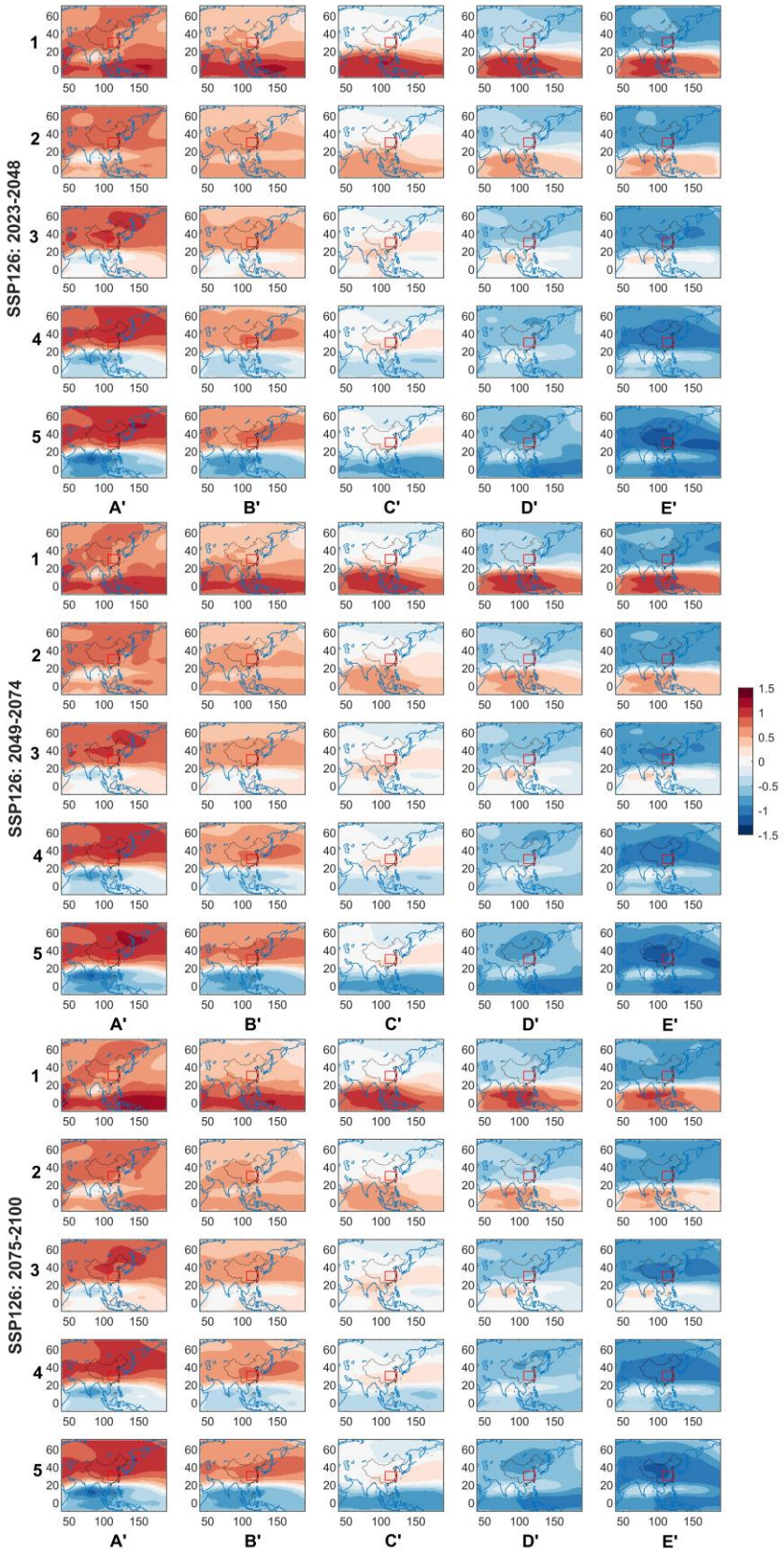

Figure S5-9. The identified circulation patterns from the MPI-ESM1-2-HR in the future periods under the SSP126 scenario. Shadow indicates anomalous fields of standardized geopotential height at 500 hPa.

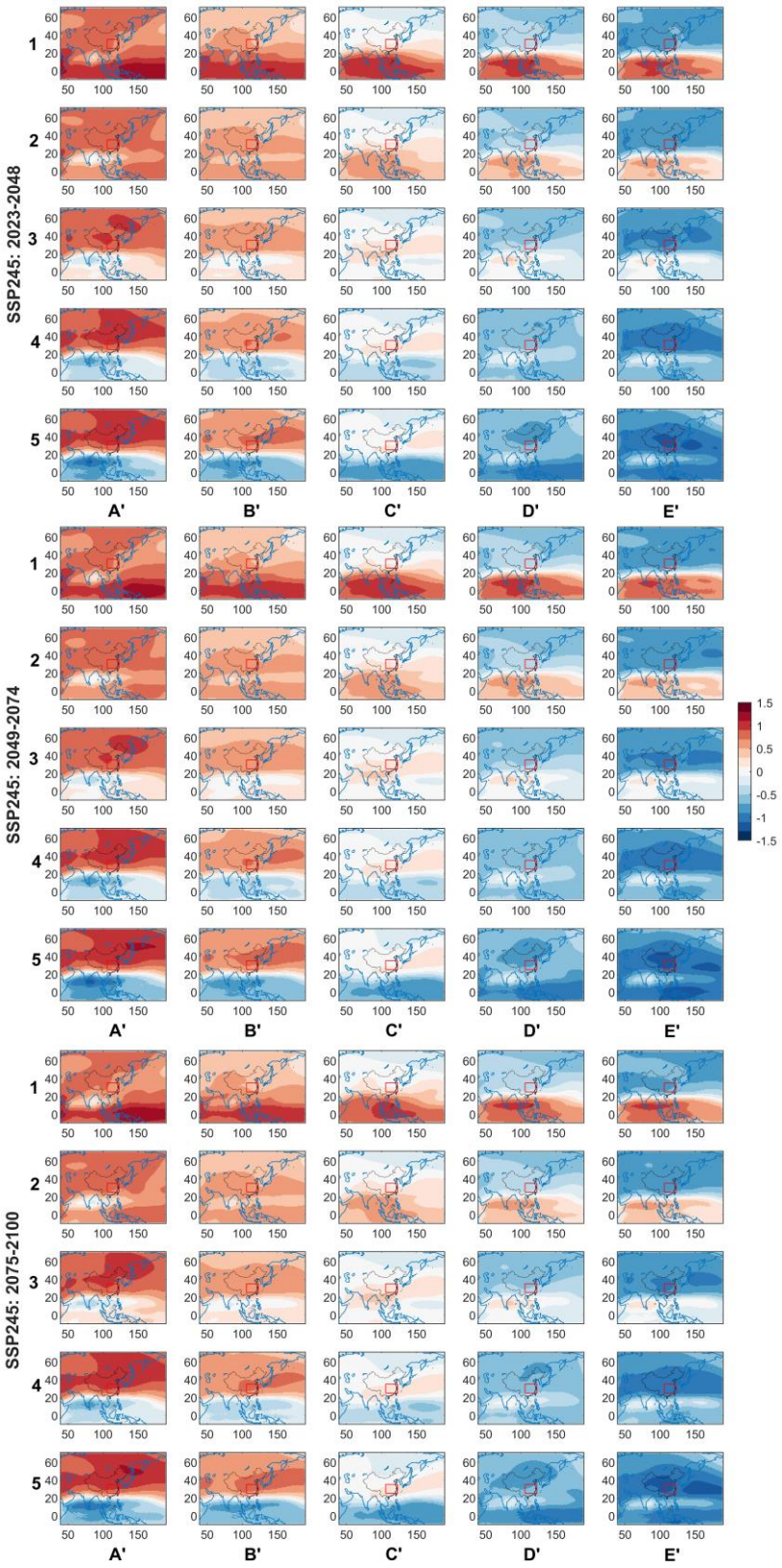

Figure S5-10. Same as Figure S5-9, but for the SSP245 scenario.

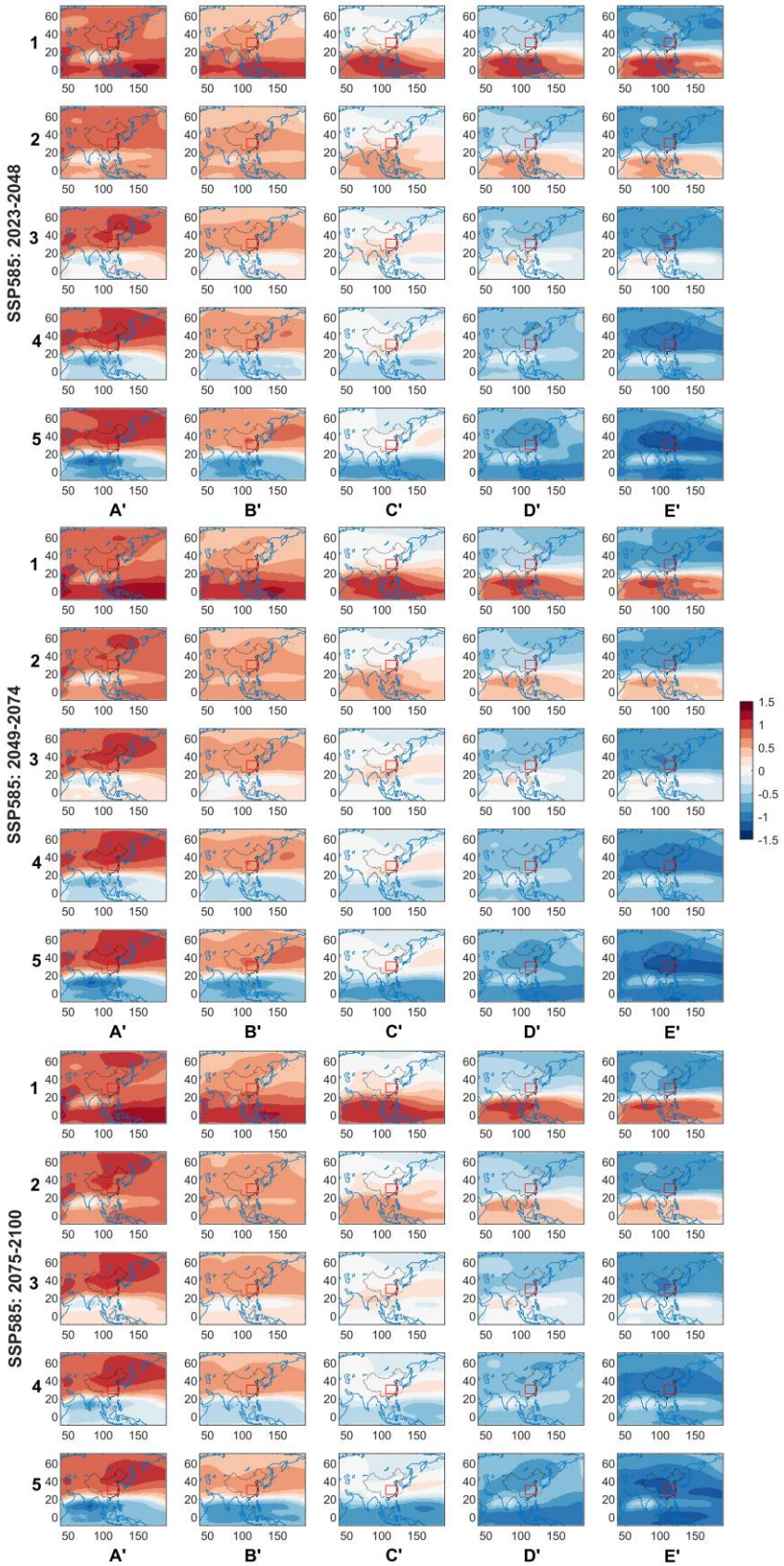

Figure S5-11. Same as Figure S5-9, but for the SSP585 scenario.

References

Abdelmoaty, H. M., Papalexiou, S. M., Rajulapati, C. R. & AghaKouchak, A. (2021), Biases Beyond the Mean in CMIP6 Extreme Precipitation: A Global Investigation. *Earth's Future*, 9(10), e2021EF002196.

Agel, L., Barlow, M., Feldstein, S. B. & Gutowski, W. J. (2018), Identification of large-scale meteorological patterns associated with extreme precipitation in the US northeast. *Climate Dynamics*, 50(5), 1819-1839.

Agel, L., Barlow, M., Colby, F., Binder, H., Catto, J. L., Hoell, A. & Cohen, J. (2019), Dynamical analysis of extreme precipitation in the US northeast based on large-scale meteorological patterns. *Climate Dynamics*, 52(3), 1739-1760.

Ahmed, A., Deo, R. C., Feng, Q., Ghahramani, A., Raj, N., Yin, Z. & Yang, L. (2022), Hybrid deep learning method for a week-ahead evapotranspiration forecasting. *Stochastic Environmental Research and Risk Assessment*, 36(3), 831-849.

Ahmed, K., Shahid, S., Nawaz, N. & Khan, N. (2019), Modeling climate change impacts on precipitation in arid regions of Pakistan: a non-local model output statistics downscaling approach. *Theoretical and Applied Climatology*, 137(1), 1347-1364.

Ahmed, K., Sachindra, D., Shahid, S., Iqbal, Z., Nawaz, N. & Khan, N. (2020), Multi-model ensemble predictions of precipitation and temperature using machine learning algorithms. *Atmospheric Research*, 236(104806.

Akinsanola, A. A., Ongoma, V. & Kooperman, G. J. (2021), Evaluation of CMIP6 models in simulating the statistics of extreme precipitation over Eastern Africa. *Atmospheric Research*, 254: 105509.

Albawi, S., Mohammed, T. A. & Al-Zawi, S. 2017. Understanding of a convolutional neural network. In *2017 international conference on engineering and technology (ICET)*, 1-6. IEEE.

Alexander, L. V., Bador, M., Roca, R., Contractor, S., Donat, M. G. & Nguyen, P. L. (2020), Intercomparison of annual precipitation indices and extremes over global land areas from in situ, space-based and reanalysis products. *Environmental Research Letters*, 15(5), 055002.

Allen, M. (2003), Liability for climate change. *Nature*, 421(6926), 891-892.

Anandh, P. C. & Vissa, N. K. (2022), Role of synoptic-scale circulations, mechanisms, and precursors during extreme rainfall events over the Southern Indian Peninsula. *Meteorology and Atmospheric Physics*, 134(2), 27.

Andrews, M. B., Ridley, J. K., Wood, R. A., Andrews, T., Blockley, E. W., Booth, B., Burke, E., Dittus, A. J., Florek, P., Gray, L. J., Haddad, S., Hardiman, S. C., Hermanson, L., Hodson, D., Hogan, E., Jones, G. S., Knight, J. R., Kuhlbrodt, T., Misios, S., Mizielinski, M. S., Ringer, M. A., Robson, J. & Sutton, R. T. (2020), Historical Simulations With HadGEM3-GC3.1 for CMIP6. *Journal of Advances in Modeling Earth Systems*, 12(6), e2019MS001995.

Angulo-Umana, P. & Kim, D. (2023), Mesoscale convective clustering enhances tropical precipitation. *Science Advances*, 9(2), eabo5317.

Araya-Osses, D., Casanueva, A., Román-Figueroa, C., Uribe, J. M. & Paneque, M. (2020), Climate change projections of temperature and precipitation in Chile based on statistical downscaling. *Climate Dynamics*, 54(9), 4309-4330.

Arulampalam, G. & Bouzerdoum, A. (2003), A generalized feedforward neural network architecture for classification and regression. *Neural networks*, 16(5-6), 561-568.

Ayantobo, O. O., Wei, J. H. & Wang, G. Q. (2022), Climatology of landfalling atmospheric rivers and its attribution to extreme precipitation events over Yangtze River Basin. *Atmospheric Research*, 270: 106077.

Ayugi, B., Zhihong, J., Zhu, H., Ngoma, H., Babaousmail, H., Rizwan, K. & Dike, V. (2021a), Comparison of CMIP6 and CMIP5 models in simulating mean and extreme precipitation over East Africa. *International Journal of Climatology*, 41(15), 6474-6496.

Ayugi, B., Jiang, Z. H., Zhu, H. H., Ngoma, H., Babaousmail, H., Rizwan, K. & Dike, V. (2021b), Comparison of

CMIP6 and CMIP5 models in simulating mean and extreme precipitation over East Africa. *International Journal of Climatology*, 41(15), 6474-6496.

Bacmeister, J. T., Reed, K. A., Hannay, C., Lawrence, P., Bates, S., Truesdale, J. E., Rosenbloom, N. & Levy, M. (2018), Projected changes in tropical cyclone activity under future warming scenarios using a high-resolution climate model. *Climatic Change*, 146(3), 547-560.

Baghanam, A. H., Eslahi, M., Sheikhbabaei, A. & Seifi, A. J. (2020), Assessing the impact of climate change over the northwest of Iran: an overview of statistical downscaling methods. *Theoretical and Applied Climatology*, 141(3), 1135-1150.

Banaji, S. (2022), Preventing the Deluge: Climate Change, the Four Spheres, Interactions, and Causalities. *Atmospheric and Climate Sciences*, 13(1), 1-9.

Bansal, A., Goldblum, M., Cherepanova, V., Schwarzschild, A., Bruss, C. B. & Goldstein, T. (2021), MetaBalance: High-Performance Neural Networks for Class-Imbalanced Data. *arXiv preprint arXiv:2106.09643*.

Barcikowska, M. J., Kapnick, S. B. & Feser, F. (2018), Impact of large-scale circulation changes in the North Atlantic sector on the current and future Mediterranean winter hydroclimate. *Climate Dynamics*, 50(5), 2039-2059.

Bardossy, A., Duckstein, L. & Bogardi, I. (1995), Fuzzy rule-based classification of atmospheric circulation patterns. *International Journal of Climatology*, 15(10), 1087-1097.

Barlow, M., Gutowski, W. J., Gyakum, J. R., Katz, R. W., Lim, Y.-K., Schumacher, R. S., Wehner, M. F., Agel, L., Bosilovich, M., Collow, A., Gershunov, A., Grotjahn, R., Leung, R., Milrad, S. & Min, S.-K. (2019), North American extreme precipitation events and related large-scale meteorological patterns: a review of statistical methods, dynamics, modeling, and trends. *Climate Dynamics*, 53(11), 6835-6875.

Barton, Y., Giannakaki, P., von Waldow, H., Chevalier, C., Pfahl, S. & Martius, O. (2016), Clustering of Regional-Scale Extreme Precipitation Events in Southern Switzerland. *Monthly Weather Review*, 144(1), 347-369.

Bates, B. C., Chandler, R. E., Charles, S. P. & Campbell, E. P. (2010), Assessment of apparent nonstationarity in time series of annual inflow, daily precipitation, and atmospheric circulation indices: A case study from southwest Western Australia. *Water Resources Research*, 46(3), W00H02.

Bates, B. C., Charles, S. P. & Hughes, J. P. (1998), Stochastic downscaling of numerical climate model simulations. *Environmental Modelling & Software*, 13(3), 325-331.

Ben Daoud, A., Sauquet, E., Lang, M., Bontron, G. & Obled, C. (2011), Precipitation forecasting through an analog sorting technique: a comparative study. *Advances in Geosciences*, 29: 103-107.

Bermúdez, M., Cea, L., Van Uytven, E., Willems, P., Farfán, J. F. & Puertas, J. (2020), A Robust Method to Update Local River Inundation Maps Using Global Climate Model Output and Weather Typing Based Statistical Downscaling. *Water Resources Management*, 34(14), 4345-4362.

Beyene, T. K., Jain, M. K., Yadav, B. K. & Agarwal, A. (2022), Multiscale investigation of precipitation extremes over Ethiopia and teleconnections to large-scale climate anomalies. *Stochastic Environmental Research and Risk Assessment*, 36(5), 1503-1519.

Bi, D., Dix, M., Marsland, S., O'Farrell, S., Sullivan, A., Bodman, R., Law, R., Harman, I., Srbinovsky, J., Rashid, H. A., Dobrohotoff, P., Mackallah, C., Yan, H., Hirst, A., Savita, A., Dias, F. B., Woodhouse, M., Fiedler, R. & Heerdegen, A. (2020), Configuration and spin-up of ACCESS-CM2, the new generation Australian Community Climate and Earth System Simulator Coupled Model. *Journal of Southern Hemisphere Earth Systems Science*, 70(1), 225-251.

Black, A. S., Monselesan, D. P., Risbey, J. S., Sloyan, B. M., Chapman, C. C., Hannachi, A., Richardson, D., Squire, D. T., Tozer, C. R. & Trendafilov, N. (2022), Archetypal Analysis of Geophysical Data Illustrated by Sea Surface Temperature. *Artificial Intelligence for the Earth Systems*, 1(3), e210007.

Blackport, R. & Screen, J. A. (2020), Insignificant effect of Arctic amplification on the amplitude of midlatitude

atmospheric waves. *Science Advances*, 6(8), eaay2880.

Blanc, A., Blanchet, J. & Creutin, J.-D. (2022), Characterizing large-scale circulations driving extreme precipitation in the Northern French Alps. *International Journal of Climatology*, 42(1), 465-480.

Blanchet, J., Blanc, A. & Creutin, J.-D. (2021), Explaining recent trends in extreme precipitation in the Southwestern Alps by changes in atmospheric influences. *Weather and Climate Extremes*, 33: 100356.

Bliefernicht, J., Rauch, M., Laux, P. & Kunstmann, H. (2022), Atmospheric circulation patterns that trigger heavy rainfall in West Africa. *International Journal of Climatology*, 42(12), 6515-6536.

Breiman, L. (1996), Bagging predictors. *Machine learning*, 24(2), 123-140.

Breiman, L. (2001), Random forests. *Machine learning*, 45(1), 5-32.

Cannon, F., Hecht, C. W., Cordeira, J. M. & Ralph, F. M. (2018), Synoptic and Mesoscale Forcing of Southern California Extreme Precipitation. *Journal of Geophysical Research: Atmospheres*, 123(24), 13,714-13,730.

Cassano, J. J., Uotila, P., Lynch, A. H. & Cassano, E. N. (2007), Predicted changes in synoptic forcing of net precipitation in large Arctic river basins during the 21st century. *Journal of Geophysical Research: Biogeosciences*, 112: G04S49.

Catto, J. L. & Pfahl, S. (2013), The importance of fronts for extreme precipitation. *Journal of Geophysical Research: Atmospheres*, 118(19), 10,791-10,801.

Catto, J. L., Madonna, E., Joos, H., Rudeva, I. & Simmonds, I. (2015), Global Relationship between Fronts and Warm Conveyor Belts and the Impact on Extreme Precipitation. *Journal of Climate*, 28(21), 8411-8429.

Catto, J. L., Nicholls, N., Jakob, C. & Shelton, K. L. (2014), Atmospheric fronts in current and future climates. *Geophysical Research Letters*, 41(21), 7642-7650.

Cavazos, T. (1997), Downscaling large-scale circulation to local winter rainfall in north–eastern Mexico. *International Journal of Climatology*, 17(10), 1069-1082.

Chakraborty, D. & Elzarka, H. (2018), Performance testing of energy models: are we using the right statistical metrics? *Journal of Building Performance Simulation*, 11(4), 433-448.

Chang, M. Y., Liu, B., Martinez-Villalobos, C., Ren, G. Y., Li, S. F. & Zhou, T. J. (2020), Changes in Extreme Precipitation Accumulations during the Warm Season over Continental China. *Journal of Climate*, 33(24), 10799-10811.

Chapman, W. E., Delle Monache, L., Alessandrini, S., Subramanian, A. C., Ralph, F. M., Xie, S.-P., Lerch, S. & Hayatbini, N. (2022), Probabilistic Predictions from Deterministic Atmospheric River Forecasts with Deep Learning. *Monthly Weather Review*, 150(1), 215-234.

Chattopadhyay, A., Nabizadeh, E. & Hassanzadeh, P. (2020), Analog Forecasting of Extreme-Causing Weather Patterns Using Deep Learning. *Journal of Advances in Modeling Earth Systems*, 12(2), e2019MS001958.

Chen, C.-A., Hsu, H.-H. & Liang, H.-C. (2021a), Evaluation and comparison of CMIP6 and CMIP5 model performance in simulating the seasonal extreme precipitation in the Western North Pacific and East Asia. *Weather and Climate Extremes*, 31: 100303.

Chen, H. P. (2013), Projected change in extreme rainfall events in China by the end of the 21st century using CMIP5 models. *Chinese Science Bulletin*, 58(12), 1462-1472.

Chen, J., Arsenault, R., Brissette, F. P. & Zhang, S. B. (2021b), Climate change impact studies: should we bias correct climate model outputs or post-process impact model outputs? *Water Resources Research*, 57(5), e2020WR028638.

Chen, J., Chen, H. & Guo, S. L. (2018a), Multi-site precipitation downscaling using a stochastic weather generator. *Climate Dynamics*, 50(5), 1975-1992.

Chen, J. & Zhang, X. J. (2021), Challenges and potential solutions in statistical downscaling of precipitation. *Climatic Change*, 165(3), 63.

Chen, L., Ma, Z. G., Li, Z. H., Wu, L., Flemke, J. & Li, Y. P. (2018b), Dynamical Downscaling of Temperature and

Precipitation Extremes in China under Current and Future Climates. *Atmosphere-Ocean*, 56(1), 55-70.

Chen, S. L., Liu, B. J., Tan, X. Z. & Huang, Z. Q. (2019), Characteristics and circulation background of extreme precipitation over East China. *Natural Hazards*, 99(1), 537-552.

Chen, T. Q. & Guestrin, C. 2016. XGBoost: A Scalable Tree Boosting System. In *Proceedings of the 22nd ACM SIGKDD International Conference on Knowledge Discovery and Data Mining*, 785–794. San Francisco, California, USA: Association for Computing Machinery.

Chen, Y. & Zhai, P. M. (2014), Two types of typical circulation pattern for persistent extreme precipitation in Central–Eastern China. *Quarterly Journal of the Royal Meteorological Society*, 140(682), 1467-1478.

Cheng, L. Y. & AghaKouchak, A. (2014), Nonstationary Precipitation Intensity-Duration-Frequency Curves for Infrastructure Design in a Changing Climate. *Scientific Reports*, 4(1), 7093.

Cheng, R., Novak, L. & Schneider, T. (2021), Predicting the Interannual Variability of California's Total Annual Precipitation. *Geophysical Research Letters*, 48(7), e2020GL091465.

Chikoore, H., Bopape, M.-J. M., Ndarana, T., Muofhe, T. P., Gijben, M., Munyai, R. B., Manyanya, T. C. & Maisha, R. (2021), Synoptic structure of a sub-daily extreme precipitation and flood event in Thohoyandou, north-eastern South Africa. *Weather and Climate Extremes*, 33: 100327.

Chou, C., Chen, C.-A., Tan, P.-H. & Chen, K. T. (2012), Mechanisms for Global Warming Impacts on Precipitation Frequency and Intensity. *Journal of Climate*, 25(9), 3291-3306.

Christensen, O. B. & Kjellström, E. (2020), Partitioning uncertainty components of mean climate and climate change in a large ensemble of European regional climate model projections. *Climate Dynamics*, 54(9), 4293-4308.

Cioffi, F., Conticello, F., Lall, U., Marotta, L. & Telesca, V. (2017), Large scale climate and rainfall seasonality in a Mediterranean Area: Insights from a non-homogeneous Markov model applied to the Agro-Pontino plain. *Hydrological Processes*, 31(3), 668-686.

Cioffi, F., Conticello, F. & Lall, U. (2016), Projecting changes in Tanzania rainfall for the 21st century. *International Journal of Climatology*, 36(13), 4297-4314.

Cioffi, F., Conticello, F. R. & Lall, U. (2020), Stochastic scenarios for 21st century rainfall seasonality, daily frequency, and intensity in South Florida. *Journal of Water Resources Planning and Management*, 146(8), 04020058.

Cioffi, F., Lall, U., Rus, E. & Krishnamurthy, C. K. B. (2015), Space-time structure of extreme precipitation in Europe over the last century. *International Journal of Climatology*, 35(8), 1749-1760.

Cipolla, G., Francipane, A. & Noto, L. V. (2020), Classification of extreme rainfall for a Mediterranean region by means of atmospheric circulation patterns and reanalysis data. *Water Resources Management*, 34(10), 3219-3235.

Collins, M., An, S.-I., Cai, W., Ganachaud, A., Guilyardi, E., Jin, F.-F., Jochum, M., Lengaigne, M., Power, S. & Timmermann, A. (2010), The impact of global warming on the tropical Pacific Ocean and El Niño. *Nature Geoscience*, 3(6), 391-397.

Collins, M., Minobe, S., Barreiro, M., Bordoni, S., Kaspi, Y., Kuwano-Yoshida, A., Keenlyside, N., Manzini, E., O'Reilly, C. H., Sutton, R., Xie, S.-P. & Zolina, O. (2018), Challenges and opportunities for improved understanding of regional climate dynamics. *Nature Climate Change*, 8(2), 101-108.

Conticello, F. R., Cioffi, F., Merz, B. & Lall, U. (2018), An event synchronization method to link heavy rainfall events and large-scale atmospheric circulation features. *International Journal of Climatology*, 38(3), 1421-1437.

Conticello, F. R., Cioffi, F., Lall, U. & Merz, B. (2020), Synchronization and Delay Between Circulation Patterns and High Streamflow Events in Germany. *Water Resources Research*, 56(4), e2019WR025598.

Coumou, D., Di Capua, G., Vavrus, S., Wang, L. & Wang, S. (2018), The influence of Arctic amplification on mid-

latitude summer circulation. *Nature Communications*, 9(1), 2959.

Cui, D. Y., Wang, C. H. & Santisirisomboon, J. (2019), Characteristics of extreme precipitation over eastern Asia and its possible connections with Asian summer monsoon activity. *International Journal of Climatology*, 39(2), 711-723.

Cui, T., Li, C. & Tian, F. (2021), Evaluation of Temperature and Precipitation Simulations in CMIP6 Models Over the Tibetan Plateau. *Earth and Space Science*, 8(7), e2020EA001620.

Dagon, K., Truesdale, J., Biard, J. C., Kunkel, K. E., Meehl, G. A. & Molina, M. J. (2022), Machine Learning-Based Detection of Weather Fronts and Associated Extreme Precipitation in Historical and Future Climates. *Journal of Geophysical Research: Atmospheres*, 127(21), e2022JD037038.

Davenport, F. V. & Diffenbaugh, N. S. (2021), Using Machine Learning to Analyze Physical Causes of Climate Change: A Case Study of U.S. Midwest Extreme Precipitation. *Geophysical Research Letters*, 48(15), e2021GL093787.

Deng, Y., Jiang, W. G., He, B., Chen, Z. & Jia, K. (2018), Change in Intensity and Frequency of Extreme Precipitation and its Possible Teleconnection With Large-Scale Climate Index Over the China From 1960 to 2015. *Journal of Geophysical Research: Atmospheres*, 123(4), 2068-2081.

Ding, Y. H., Liang, P., Liu, Y. J. & Zhang, Y. C. (2020), Multiscale variability of Meiyu and its prediction: A new review. *Journal of Geophysical Research: Atmospheres*, 125(7), e2019JD031496.

Donat, M. G., Lowry, A. L., Alexander, L. V., O'Gorman, P. A. & Maher, N. (2016), More extreme precipitation in the world's dry and wet regions. *Nature Climate Change*, 6(5), 508-513.

Dong, B., Sutton, R. T. & Scaife, A. A. (2006), Multidecadal modulation of El Niño–Southern Oscillation (ENSO) variance by Atlantic Ocean sea surface temperatures. *Geophysical Research Letters*, 33(8), L08705.

Dong, S. J., Yu, T. B., Farahmand, H. & Mostafavi, A. (2021), A hybrid deep learning model for predictive flood warning and situation awareness using channel network sensors data. *Computer-Aided Civil and Infrastructure Engineering*, 36(4), 402-420.

Du, H. B., Donat, M. G., Zong, S. W., Alexander, L. V., Manzanas, R., Kruger, A., Choi, G., Salinger, J., He, H. S., Li, M.-H., Fujibe, F., Nandintsetseg, B., Rehman, S., Abbas, F., Rusticucci, M., Srivastava, A., Zhai, P., Lippmann, T., Yabi, I., Stambaugh, M. C., Wang, S. Z., Batbold, A., Oliveira, P. T. d., Adrees, M., Hou, W., Silva, C. M. S. e., Lucio, P. S. & Wu, Z. F. (2022), Extreme Precipitation on Consecutive Days Occurs More Often in a Warming Climate. *Bulletin of the American Meteorological Society*, 103(4), 1130-1145.

Eiras-Barca, J., Ramos, A. M., Algarra, I., Vázquez, M., Dominguez, F., Miguez-Macho, G., Nieto, R., Gimeno, L., Taboada, J. & Ralph, F. M. (2021), European West Coast atmospheric rivers: A scale to characterize strength and impacts. *Weather and Climate Extremes*, 31: 100305.

Elison Timm, O., Takahashi, M., Giambelluca, T. W. & Diaz, H. F. (2013), On the relation between large-scale circulation pattern and heavy rain events over the Hawaiian Islands: Recent trends and future changes. *Journal of Geophysical Research: Atmospheres*, 118(10), 4129-4141.

Emori, S. & Brown, S. J. (2005), Dynamic and thermodynamic changes in mean and extreme precipitation under changed climate. *Geophysical Research Letters*, 32(17), L17706.

Enke, W., Schneider, F. & Deutschländer, T. (2005), A novel scheme to derive optimized circulation pattern classifications for downscaling and forecast purposes. *Theoretical and Applied Climatology*, 82(1), 51-63.

Espinoza, V., Waliser, D. E., Guan, B., Lavers, D. A. & Ralph, F. M. (2018), Global Analysis of Climate Change Projection Effects on Atmospheric Rivers. *Geophysical Research Letters*, 45(9), 4299-4308.

Fan, X. W., Jiang, L. & Gou, J. J. (2021), Statistical downscaling and projection of future temperatures across the Loess Plateau, China. *Weather and Climate Extremes*, 32: 100328.

Faye, A. & Akinsanola, A. A. (2022), Evaluation of extreme precipitation indices over West Africa in CMIP6 models. *Climate Dynamics*, 58(3), 925-939.

Feng, L. & Zhou, T. J. (2012), Water vapor transport for summer precipitation over the Tibetan Plateau: Multidata set analysis. *Journal of Geophysical Research: Atmospheres*, 117(D20), D20114.

Feng, Z., Leung, L. R., Hagos, S., Houze, R. A., Burleyson, C. D. & Balaguru, K. (2016), More frequent intense and long-lived storms dominate the springtime trend in central US rainfall. *Nature Communications*, 7(1), 13429.

Fernando, K. R. M. & Tsokos, C. P. (2021), Dynamically weighted balanced loss: class imbalanced learning and confidence calibration of deep neural networks. *IEEE Transactions on Neural Networks and Learning Systems*,

Forney, G. D. (1973), The viterbi algorithm. *Proceedings of the IEEE*, 61(3), 268-278.

Francis, J. A. & Vavrus, S. J. (2012), Evidence linking Arctic amplification to extreme weather in mid-latitudes. *Geophysical Research Letters*, 39(6), L06801.

Frost, A. J., Charles, S. P., Timbal, B., Chiew, F. H. S., Mehrotra, R., Nguyen, K. C., Chandler, R. E., McGregor, J. L., Fu, G., Kirono, D. G. C., Fernandez, E. & Kent, D. M. (2011), A comparison of multi-site daily rainfall downscaling techniques under Australian conditions. *Journal of Hydrology*, 408(1), 1-18.

Fu, G. B., Charles, S. P., Chiew, F. H. S., Ekström, M. & Potter, N. J. (2018), Uncertainties of statistical downscaling from predictor selection: Equifinality and transferability. *Atmospheric Research*, 203: 130-140.

Gao, X. & Mathur, S. (2021), Predictability of US regional extreme precipitation occurrence based on large-scale meteorological patterns (LSMPs). *Journal of Climate*, 34(17), 7181-7198.

Garbin, C., Zhu, X. & Marques, O. (2020), Dropout vs. batch normalization: an empirical study of their impact to deep learning. *Multimedia Tools and Applications*, 79(19), 12777-12815.

Gardner, M. W. & Dorling, S. (1998), Artificial neural networks (the multilayer perceptron)-a review of applications in the atmospheric sciences. *Atmospheric environment*, 32(14-15), 2627-2636.

Genuer, R., Poggi, J.-M., Tuleau-Malot, C. & Villa-Vialaneix, N. (2017), Random forests for big data. *Big Data Research*, 9: 28-46.

Ghamghami, M. & Bazrafshan, J. (2021), Relationships between Large-Scale Climate Signals and Winter Precipitation Amounts and Patterns over Iran. *Journal of Hydrologic Engineering*, 26(3), 05021001.

Ghamghami, M., Ghahreman, N., Olya, H. & Ghasdi, T. (2019), Comparison of three multi-site models in stochastic reconstruction of winter daily rainfall over Iran. *Modeling Earth Systems and Environment*, 5(4), 1319-1332.

Ghaseminezhad, M. H. & Karami, A. (2011), A novel self-organizing map (SOM) neural network for discrete groups of data clustering. *Applied Soft Computing*, 11(4), 3771-3778.

Giannakaki, P. & Martius, O. (2016), Synoptic-scale flow structures associated with extreme precipitation events in northern Switzerland. *International Journal of Climatology*, 36(6), 2497-2515.

Gibson, P. B., Uotila, P., Perkins-Kirkpatrick, S. E., Alexander, L. V. & Pitman, A. J. (2016), Evaluating synoptic systems in the CMIP5 climate models over the Australian region. *Climate Dynamics*, 47(7), 2235-2251.

Giorgi, F., Im, E.-S., Coppola, E., Diffenbaugh, N. S., Gao, X. J., Mariotti, L. & Shi, Y. (2011), Higher Hydroclimatic Intensity with Global Warming. *Journal of Climate*, 24(20), 5309-5324.

Girshick, R., Donahue, J., Darrell, T. & Malik, J. (2015), Region-based convolutional networks for accurate object detection and segmentation. *IEEE transactions on pattern analysis and machine intelligence*, 38(1), 142-158.

Goodfellow, I., Bengio, Y. & Courville, A. 2016. *Deep learning*. MIT press.

Gorman, P. A. & Schneider, T. (2009), The physical basis for increases in precipitation extremes in simulations of 21st-century climate change. *Proceedings of the National Academy of Sciences*, 106(35), 14773.

Griffin, S. M., Wimmers, A. & Velden, C. S. (2022), Predicting Rapid Intensification in North Atlantic and Eastern North Pacific Tropical Cyclones Using a Convolutional Neural Network. *Weather and Forecasting*, 37(8), 1333-1355.

Grose, M. R., Narsey, S., Delage, F., Dowdy, A. J., Bador, M., Boschat, G., Chung, C., Kajtar, J., Rauniyar, S. & Freund, M. (2020), Insights from CMIP6 for Australia's future climate. *Earth's Future*, 8(5), e2019EF001469.

Gründemann, G. J., van de Giesen, N., Brunner, L. & van der Ent, R. (2022), Rarest rainfall events will see the greatest relative increase in magnitude under future climate change. *Communications Earth & Environment*, 3(1), 235.

Gu, X. Z., Ye, L., Xin, Q., Zhang, C., Zeng, F. Z., Nerantzaki, S. D. & Papalexiou, S. M. (2022), Extreme precipitation in China: a review. *Advances in Water Resources*, 163: 104144.

Guan, P. Y., Chen, G. X., Zeng, W. X. & Liu, Q. (2020), Corridors of Mei-Yu-Season Rainfall over Eastern China. *Journal of Climate*, 33(7), 2603-2626.

Guo, L. Y., Jiang, Z. H., Li, L. & Wang, H. J. (2022), Increase of Future Summer Rainfall in the Middle and Lower Reach of the Yangtze River Basin Projected With a Nonhomogeneous Hidden Markov Model. *Geophysical Research Letters*, 49(7), e2021GL097325.

Hagos, S. M., Leung, L. R., Yoon, J.-H., Lu, J. & Gao, Y. (2016), A projection of changes in landfalling atmospheric river frequency and extreme precipitation over western North America from the Large Ensemble CESM simulations. *Geophysical Research Letters*, 43(3), 1357-1363.

Hamill, T. M., Scheuerer, M. & Bates, G. T. (2015), Analog Probabilistic Precipitation Forecasts Using GEFS Reforecasts and Climatology-Calibrated Precipitation Analyses. *Monthly Weather Review*, 143(8), 3300-3309.

Hamill, T. M. & Whitaker, J. S. (2006), Probabilistic Quantitative Precipitation Forecasts Based on Reforecast Analogs: Theory and Application. *Monthly Weather Review*, 134(11), 3209-3229.

Hand, D. J. & Till, R. J. (2001), A Simple Generalisation of the Area Under the ROC Curve for Multiple Class Classification Problems. *Machine Learning*, 45(2), 171-186.

Hartmann, D. L., Tank, A. M. K., Rusticucci, M., Alexander, L. V., Brönnimann, S., Charabi, Y. A. R., Dentener, F. J., Dlugokencky, E. J., Easterling, D. R. & Kaplan, A. 2013. Observations: atmosphere and surface. In *Climate change 2013 the physical science basis: Working group I contribution to the fifth assessment report of the intergovernmental panel on climate change*, 159-254. Cambridge University Press.

Hawcroft, M., Walsh, E., Hodges, K. & Zappa, G. (2018), Significantly increased extreme precipitation expected in Europe and North America from extratropical cyclones. *Environmental Research Letters*, 13(12), 124006.

He, X. G., Bryant, B. P., Moran, T., Mach, K. J., Wei, Z. W. & Freyberg, D. L. (2021), Climate-informed hydrologic modeling and policy typology to guide managed aquifer recharge. *Science Advances*, 7(17), eabe6025.

He, Y., Manful, D., Warren, R., Forstenhäusler, N., Osborn, T. J., Price, J., Jenkins, R., Wallace, C. & Yamazaki, D. (2022), Quantification of impacts between 1.5 and 4 C of global warming on flooding risks in six countries. *Climatic Change*, 170(1), 1-21.

Healy, D., Mohammed, Z., Kanwal, N., Asghar, M. N. & Ansari, M. S. 2022. Deep Learning Model for Thunderstorm Prediction with Class Imbalance Data. In *Proceedings of International Conference on Information Technology and Applications,* eds. A. Ullah, S. Anwar, Á. Rocha & S. Gill, 195-205. Singapore: Springer Nature Singapore.

Hertig, E. & Jacobeit, J. (2015), Considering observed and future nonstationarities in statistical downscaling of Mediterranean precipitation. *Theoretical and Applied Climatology*, 122(3), 667-683.

Hinton, G. E., Srivastava, N., Krizhevsky, A., Sutskever, I. & Salakhutdinov, R. R. (2012), Improving neural networks by preventing co-adaptation of feature detectors. *arXiv preprint arXiv:1207.0580*.

Ho, Y. & Wookey, S. (2020), The Real-World-Weight Cross-Entropy Loss Function: Modeling the Costs of Mislabeling. *IEEE Access*, 8: 4806-4813.

Hoffmann, P. & Spekat, A. (2021), Identification of possible dynamical drivers for long-term changes in temperature and rainfall patterns over Europe. *Theoretical and Applied Climatology*, 143(1), 177-191.

Holloway, C. E. & Neelin, J. D. (2009), Moisture Vertical Structure, Column Water Vapor, and Tropical Deep Convection. *Journal of the Atmospheric Sciences*, 66(6), 1665-1683.

Holsclaw, T., Greene, A. M., Robertson, A. W. & Smyth, P. (2017), Bayesian nonhomogeneous Markov models via

Pólya-Gamma data augmentation with applications to rainfall modeling. *The Annals of Applied Statistics*, 11(1), 393-426.

Hong, W. & Ren, X. J. (2013), Persistent heavy rainfall over South China during May–August: Subseasonal anomalies of circulation and sea surface temperature. *Acta Meteorologica Sinica*, 27(6), 769-787.

Horton, P., Jaboyedoff, M. & Obled, C. (2018), Using genetic algorithms to optimize the analogue method for precipitation prediction in the Swiss Alps. *Journal of Hydrology*, 556: 1220-1231.

Hu, Y., Deng, Y., Zhou, Z., Cui, C. & Dong, X. (2019), A statistical and dynamical characterization of large-scale circulation patterns associated with summer extreme precipitation over the middle reaches of Yangtze river. *Climate Dynamics*, 52(9), 6213-6228.

Huang, J. & Ling, C. X. (2005), Using AUC and accuracy in evaluating learning algorithms. *IEEE Transactions on knowledge and Data Engineering*, 17(3), 299-310.

Huang, S. H., Wen, Z. P., Chen, X. D., Guo, Y. Y. & Wang, Z. W. (2022), The Henan extreme rainfall in July 2021: Modulation of the northward-shift monsoon trough on the synoptic-scale wave train. *Advances in Climate Change Research*, 13(6), 819-825.

Huang, W. C. (2022), Extreme precipitation forecasting using attention augmented convolutions. *arXiv preprint arXiv:2201.13408*.

Huang, X. Y., Swain, D. L. & Hall, A. D. (2020a), Future precipitation increase from very high resolution ensemble downscaling of extreme atmospheric river storms in California. *Science advances*, 6(29), eaba1323.

Huang, X. Y. & Swain, D. L. (2022), Climate change is increasing the risk of a California megaflood. *Science Advances*, 8(32), eabq0995.

Huang, Z., Zhang, W., Geng, X. & Jin, F.-F. (2020b), Recent shift in the state of the western Pacific subtropical high due to ENSO change. *Journal of Climate*, 33(1), 229-241.

Hughes, J. P., Guttorp, P. & Charles, S. P. (1999), A non-homogeneous hidden Markov model for precipitation occurrence. *Journal of the Royal Statistical Society: Series C (Applied Statistics)*, 48(1), 15-30.

Hughes, J. P. & Guttorp, P. (1994), A class of stochastic models for relating synoptic atmospheric patterns to regional hydrologic phenomena. *Water Resources Research*, 30(5), 1535-1546.

Huth, R. & Beranová, R. (2021), How to Recognize a True Mode of Atmospheric Circulation Variability. *Earth and Space Science*, 8(3), e2020EA001275.

Ibebuchi, C. C. (2022), Patterns of atmospheric circulation in Western Europe linked to heavy rainfall in Germany: preliminary analysis into the 2021 heavy rainfall episode. *Theoretical and Applied Climatology*, 148(1), 269-283.

Imran, H. M., Kala, J., Uddin, S., Saiful Islam, A. K. M. & Acharya, N. (2023), Spatiotemporal analysis of temperature and precipitation extremes over Bangladesh using a novel gridded observational dataset. *Weather and Climate Extremes*, 39: 100544.

IPCC. 2021. Climate Change 2021: The Physical Science Basis. In *Contribution of Working Group I to the Sixth Assessment Report of the Intergovernment Panel on Climate Change* [V. Masson-Delmotte, P. Zhan, A. Pirani, S. L. Connors, C. Péan, S. Berger, N. Caud, Y. Chen, L. Goldfarb, M. I. Gomis, M. Huang, K. Leitzell, E. Lonnoy, J. B. R. Matthews, T. K. Maycock, T. Waterfield, O. Yelekçi, R. Yu & B. Zhou (eds.)]. Cambridge Univeristy Press, United Kingdom and New York, NY, USA, In Press.

Iturbide, M., Casanueva, A., Bedia, J., Herrera, S., Milovac, J. & Gutiérrez, J. M. (2022), On the need of bias adjustment for more plausible climate change projections of extreme heat. *Atmospheric Science Letters*, 23(2), e1072.

Jena, B., Saxena, S., Nayak, G. K., Saba, L., Sharma, N. & Suri, J. S. (2021), Artificial intelligence-based hybrid deep learning models for image classification: The first narrative review. *Computers in Biology and Medicine*, 137: 104803.

Jeong, D. I., St-Hilaire, A., Ouarda, T. B. & Gachon, P. (2012), Multisite statistical downscaling model for daily precipitation combined by multivariate multiple linear regression and stochastic weather generator. *Climatic Change*, 114(3), 567-591.

John, A., Douville, H., Ribes, A. & Yiou, P. (2022), Quantifying CMIP6 model uncertainties in extreme precipitation projections. *Weather and Climate Extremes*, 36: 100435.

Kadavi, P. R., Lee, C.-W. & Lee, S. (2018), Application of Ensemble-Based Machine Learning Models to Landslide Susceptibility Mapping. *Remote Sensing*, 10(8), 1252.

Kaesmacher, O. & Schneider, C. (2011), An objective circulation pattern classification for the region of Svalbard. *Geografiska Annaler: Series A, Physical Geography*, 93(4), 259-271.

Kamae, Y., Imada, Y., Kawase, H. & Mei, W. (2021), Atmospheric Rivers Bring More Frequent and Intense Extreme Rainfall Events Over East Asia Under Global Warming. *Geophysical Research Letters*, 48(24), e2021GL096030.

Kambalimath, S. & Deka, P. C. (2020), A basic review of fuzzy logic applications in hydrology and water resources. *Applied Water Science*, 10(8), 1-14.

Kao, S. C. & Ganguly, A. R. (2011), Intensity, duration, and frequency of precipitation extremes under 21st-century warming scenarios. *Journal of Geophysical Research: Atmospheres*, 116(D16), D16119.

Karl, T. R., Nicholls, N. & Ghazi, A. 1999. CLIVAR/GCOS/WMO Workshop on Indices and Indicators for Climate Extremes Workshop Summary. In *Weather and Climate Extremes: Changes, Variations and a Perspective from the Insurance Industry,* eds. T. R. Karl, N. Nicholls & A. Ghazi, 3-7. Dordrecht: Springer Netherlands.

Kautz, L. A., Martius, O., Pfahl, S., Pinto, J. G., Ramos, A. M., Sousa, P. M. & Woollings, T. (2022), Atmospheric blocking and weather extremes over the Euro-Atlantic sector – a review. *Weather and Climate Dynamics*, 3(1), 305-336.

Kebacho, L. L. (2021), Anomalous circulation patterns associated with 2011 heavy rainfall over northern Tanzania. *Natural Hazards*, 109(3), 2295-2312.

Kellenberger, B., Marcos, D. & Tuia, D. (2018), Detecting mammals in UAV images: Best practices to address a substantially imbalanced dataset with deep learning. *Remote Sensing of Environment*, 216: 139-153.

Khan, M., Nielsen, D., Tangkaratt, V., Lin, W., Gal, Y. & Srivastava, A. 2018. Fast and scalable bayesian deep learning by weight-perturbation in adam. In *International Conference on Machine Learning*, 2611-2620. PMLR.

Khan, M. I. & Maity, R. (2020), Hybrid Deep Learning Approach for Multi-Step-Ahead Daily Rainfall Prediction Using GCM Simulations. *IEEE Access*, 8: 52774-52784.

Kiang, M. Y. (2001), Extending the Kohonen self-organizing map networks for clustering analysis. *Computational Statistics & Data Analysis*, 38(2), 161-180.

Kim, H.-M., Zhou, Y. & Alexander, M. A. (2019), Changes in atmospheric rivers and moisture transport over the Northeast Pacific and western North America in response to ENSO diversity. *Climate Dynamics*, 52(12), 7375-7388.

Kim, Y.-H., Min, S.-K., Zhang, X., Sillmann, J. & Sandstad, M. (2020), Evaluation of the CMIP6 multi-model ensemble for climate extreme indices. *Weather and Climate Extremes*, 29: 100269.

Kirchmeier-Young, M. C. & Zhang, X. (2020), Human influence has intensified extreme precipitation in North America. *Proceedings of the National Academy of Sciences*, 117(24), 13308-13313.

Kitoh, A., Endo, H., Krishna Kumar, K., Cavalcanti, I. F. A., Goswami, P. & Zhou, T. (2013), Monsoons in a changing world: A regional perspective in a global context. *Journal of Geophysical Research: Atmospheres*, 118(8), 3053-3065.

Knighton, J., Pleiss, G., Carter, E., Lyon, S., Walter, M. T. & Steinschneider, S. (2019), Potential Predictability of Regional Precipitation and Discharge Extremes Using Synoptic-Scale Climate Information via Machine

Learning: An Evaluation for the Eastern Continental United States. *Journal of Hydrometeorology*, 20(5), 883-900.

Kohonen, T. (1998), The self-organizing map. *Neurocomputing*, 21(1), 1-6.

Kotsias, G., Lolis, C. J., Hatzianastassiou, N., Bakas, N., Lionello, P. & Bartzokas, A. (2023), Objective climatology and classification of the Mediterranean cyclones based on the ERA5 data set and the use of the results for the definition of seasons. *Theoretical and Applied Climatology*, 1-17.

Koutsoyiannis, D. (2012), Clausius–Clapeyron equation and saturation vapour pressure: simple theory reconciled with practice. *European Journal of Physics*, 33(2), 295-305.

Krishnan, R., Swapna, P., Vellore, R., Narayanasetti, S., Prajeesh, A. G., Choudhury, A. D., Singh, M., Sabin, T. P. & Sanjay, J. 2019. The IITM Earth System Model (ESM): Development and Future Roadmap. In *Current Trends in the Representation of Physical Processes in Weather and Climate Models,* eds. D. A. Randall, J. Srinivasan, R. S. Nanjundiah & P. Mukhopadhyay, 183-195. Singapore: Springer Singapore.

Ku, H.-Y., Noh, N., Jeong, J.-H., Koo, J.-H., Choi, W., Kim, B.-M., Lee, D. & Ban, S.-J. (2021), Classification of large-scale circulation patterns and their spatio-temporal variability during High-PM10 events over the Korean Peninsula. *Atmospheric Environment*, 262: 118632.

Kuma, P., McDonald, A. J., Morgenstern, O., Alexander, S. P., Cassano, J. J., Garrett, S., Halla, J., Hartery, S., Harvey, M. J., Parsons, S., Plank, G., Varma, V. & Williams, J. (2020), Evaluation of Southern Ocean cloud in the HadGEM3 general circulation model and MERRA-2 reanalysis using ship-based observations. *Atmos. Chem. Phys.*, 20(11), 6607-6630.

Lavers, D. A., Villarini, G., Allan, R. P., Wood, E. F. & Wade, A. J. (2012), The detection of atmospheric rivers in atmospheric reanalyses and their links to British winter floods and the large-scale climatic circulation. *Journal of Geophysical Research: Atmospheres*, 117: D20106.

Lavers, D. A., Ralph, F. M., Waliser, D. E., Gershunov, A. & Dettinger, M. D. (2015), Climate change intensification of horizontal water vapor transport in CMIP5. *Geophysical Research Letters*, 42(13), 5617-5625.

LeCun, Y., Bengio, Y. & Hinton, G. (2015), Deep learning. *nature*, 521(7553), 436-444.

Lee, D., Min, S.-K., Jin, J., Lee, J.-W., Cha, D.-H., Suh, M.-S., Ahn, J.-B., Hong, S.-Y., Kang, H.-S. & Joh, M. (2017a), Thermodynamic and dynamic contributions to future changes in summer precipitation over Northeast Asia and Korea: a multi-RCM study. *Climate Dynamics*, 49(11), 4121-4139.

Lee, S.-S., Moon, J.-Y., Wang, B. & Kim, H.-J. (2017b), Subseasonal Prediction of Extreme Precipitation over Asia: Boreal Summer Intraseasonal Oscillation Perspective. *Journal of Climate*, 30(8), 2849-2865.

Lehmann, J., Coumou, D. & Frieler, K. (2015), Increased record-breaking precipitation events under global warming. *Climatic Change*, 132(4), 501-515.

Lenderink, G., de Vries, H., Fowler, H. J., Barbero, R., van Ulft, B. & van Meijgaard, E. (2021), Scaling and responses of extreme hourly precipitation in three climate experiments with a convection-permitting model. *Philosophical Transactions of the Royal Society A: Mathematical, Physical and Engineering Sciences*, 379(2195), 20190544.

Lennard, C. & Hegerl, G. (2015), Relating changes in synoptic circulation to the surface rainfall response using self-organising maps. *Climate Dynamics*, 44(3), 861-879.

Li, C. F., Lu, R. Y., Dunstone, N., Scaife, A. A., Bett, P. E. & Zheng, F. (2021), The Seasonal Prediction of the Exceptional Yangtze River Rainfall in Summer 2020. *Advances in Atmospheric Sciences*, 38(12), 2055-2066.

Li, C. M., Tang, G. Q. & Hong, Y. (2018a), Cross-evaluation of ground-based, multi-satellite and reanalysis precipitation products: Applicability of the Triple Collocation method across Mainland China. *Journal of Hydrology*, 562: 71-83.

Li, J., Yu, R. C. & Sun, W. (2013), Duration and seasonality of hourly extreme rainfall in the central eastern China. *Acta Meteorologica Sinica*, 27(6), 799-807.

Li, L., Yu, Y., Tang, Y., Lin, P., Xie, J., Song, M., Dong, L., Zhou, T., Liu, L., Wang, L., Pu, Y., Chen, X., Chen, L., Xie, Z., Liu, H., Zhang, L., Huang, X., Feng, T., Zheng, W., Xia, K., Liu, H., Liu, J., Wang, Y., Wang, L., Jia, B., Xie, F., Wang, B., Zhao, S., Yu, Z., Zhao, B. & Wei, J. (2020), The Flexible Global Ocean-Atmosphere-Land System Model Grid-Point Version 3 (FGOALS-g3): Description and Evaluation. *Journal of Advances in Modeling Earth Systems*, 12(9), e2019MS002012.

Li, P. X., Guo, Z., Furtado, K., Chen, H. M., Li, J., Milton, S., Field, P. R. & Zhou, T. J. (2019), Prediction of heavy precipitation in the eastern China flooding events of 2016: Added value of convection-permitting simulations. *Quarterly Journal of the Royal Meteorological Society*, 145(724), 3300-3319.

Li, T. Y., Convertino, G., Wang, W. B., Most, H., Zajonc, T. & Tsai, Y.-H. 2018b. Hypertuner: Visual analytics for hyperparameter tuning by professionals. In *Proceedings of the Machine Learning from User Interaction for Visualization and Analytics Workshop at IEEE VIS*.

Li, W. D., Gao, X., Hao, Z. H. & Sun, R. (2022), Using deep learning for precipitation forecasting based on spatio-temporal information: a case study. *Climate Dynamics*, 58(1), 443-457.

Liang, S., Wang, D., Ziegler, A. D., Li, L. Z. X. & Zeng, Z. (2022), Madden–Julian Oscillation-induced extreme rainfalls constrained by global warming mitigation. *npj Climate and Atmospheric Science*, 5(1), 67.

Liashchynskyi, P. & Pavlo, L. (2019), Grid search, random search, genetic algorithm: a big comparison for NAS. *arXiv preprint arXiv:1912.06059*.

Lin, Y., Wang, D., Wang, G., Qiu, J., Long, K., Du, Y., Xie, H., Wei, Z., Shangguan, W. & Dai, Y. (2021), A hybrid deep learning algorithm and its application to streamflow prediction. *Journal of Hydrology*, 601: 126636.

Liu, B. J., Tan, X. Z., Gan, T. Y., Chen, X. H., Lin, K. R., Lu, M. Q. & Liu, Z. Y. (2020a), Global atmospheric moisture transport associated with precipitation extremes: Mechanisms and climate change impacts. *WIREs Water*, 7(2), e1412.

Liu, J., Wu, D., Xu, X., Ji, M., Chen, Q. & Wang, X. (2021a), Projection of extreme precipitation induced by Arctic amplification over the Northern Hemisphere. *Environmental Research Letters*, 16(7), 074012.

Liu, J., Zhang, J. R., Liu, F. & Yang, L. M. (2020b), Drivers of a sudden mesoscale rainstorm in arid and semi-arid regions at the edge of the western Pacific subtropical high. *Meteorological Applications*, 27(2), e1884.

Liu, W., Wen, Y., Yu, Z. & Yang, M. (2016), Large-margin softmax loss for convolutional neural networks. *arXiv preprint arXiv:1612.02295*.

Liu, Z., Huang, J., Xiao, X. & Tong, X. (2022), The capability of CMIP6 models on seasonal precipitation extremes over Central Asia. *Atmospheric Research*, 278: 106364.

Liu, Z., Bollasina, M. A., Wilcox, L. J., Rodríguez, J. M. & Regayre, L. A. (2021b), Contrasting the Role of Regional and Remote Circulation in Driving Asian Monsoon Biases in MetUM GA7.1. *Journal of Geophysical Research: Atmospheres*, 126(14), e2020JD034342.

Liu, Z. F., Xu, Z. X., Charles, S. P., Fu, G. B. & Liu, L. (2011), Evaluation of two statistical downscaling models for daily precipitation over an arid basin in China. *International Journal of Climatology*, 31(13), 2006-2020.

Loader, C. 2006. *Local regression and likelihood*. Springer Science & Business Media.

Loriaux, J. M., Lenderink, G. & Siebesma, A. P. (2017), Large-Scale Controls on Extreme Precipitation. *Journal of Climate*, 30(3), 955-968.

Lu, C., Kong, Y. & Guan, Z. (2020), A mask R-CNN model for reidentifying extratropical cyclones based on quasi-supervised thought. *Scientific Reports*, 10(1), 1-9.

Lu, K. D., Arshad, M., Ma, X. Y., Ullah, I., Wang, J. J. & Shao, W. (2022), Evaluating observed and future spatiotemporal changes in precipitation and temperature across China based on CMIP6-GCMs. *International Journal of Climatology*, 42(15), 7703-7729.

Ma, X. & Xie, F. (2020), Predicting April Precipitation in the Northwestern United States Based on Arctic Stratospheric Ozone and Local Circulation. *Frontiers in Earth Science*, 8: 1-12.

Ma, Y. Z., Hong, Y., Chen, Y., Yang, Y., Tang, G. Q., Yao, Y. J., Long, D., Li, C. M., Han, Z. Y. & Liu, R. H. (2018), Performance of Optimally Merged Multisatellite Precipitation Products Using the Dynamic Bayesian Model Averaging Scheme Over the Tibetan Plateau. *Journal of Geophysical Research: Atmospheres*, 123(2), 814-834.

Madakumbura, G. D., Thackeray, C. W., Norris, J., Goldenson, N. & Hall, A. (2021), Anthropogenic influence on extreme precipitation over global land areas seen in multiple observational datasets. *Nature Communications*, 12(1), 1-9.

Mairal, J., Koniusz, P., Harchaoui, Z. & Schmid, C. (2014), Convolutional kernel networks. *Advances in neural information processing systems*, 27.

Marquardt Collow, A. B., Bosilovich, M. G. & Koster, R. D. (2016), Large-Scale Influences on Summertime Extreme Precipitation in the Northeastern United States. *Journal of Hydrometeorology*, 17(12), 3045-3061.

Mastrantonas, N., Herrera-Lormendez, P., Magnusson, L., Pappenberger, F. & Matschullat, J. (2021), Extreme precipitation events in the Mediterranean: Spatiotemporal characteristics and connection to large-scale atmospheric flow patterns. *International Journal of Climatology*, 41(4), 2710-2728.

Mastrantonas, N., Magnusson, L., Pappenberger, F. & Matschullat, J. (2022), What do large-scale patterns teach us about extreme precipitation over the Mediterranean at medium-and extended-range forecasts? *Quarterly Journal of the Royal Meteorological Society*, 148(743), 875-890.

Matthews, H. D., Zickfeld, K., Knutti, R. & Allen, M. R. (2018), Focus on cumulative emissions, global carbon budgets and the implications for climate mitigation targets. *Environmental Research Letters*, 13(1), 010201.

McClenny, E. E., Ullrich, P. A. & Grotjahn, R. (2020), Sensitivity of Atmospheric River Vapor Transport and Precipitation to Uniform Sea Surface Temperature Increases. *Journal of Geophysical Research: Atmospheres*, 125(21), e2020JD033421.

Meher, J. K. & Das, L. (2022), Is the Western Himalayan region vulnerable with respect to downscaled precipitation? *Theoretical and Applied Climatology*, 149(1), 233-252.

Mehrotra, R., Sharma, A., Nagesh Kumar, D. & Reshmidevi, T. V. (2013), Assessing future rainfall projections using multiple GCMs and a multi-site stochastic downscaling model. *Journal of Hydrology*, 488: 84-100.

Meinshausen, M., Nicholls, Z. R. J., Lewis, J., Gidden, M. J., Vogel, E., Freund, M., Beyerle, U., Gessner, C., Nauels, A., Bauer, N., Canadell, J. G., Daniel, J. S., John, A., Krummel, P. B., Luderer, G., Meinshausen, N., Montzka, S. A., Rayner, P. J., Reimann, S., Smith, S. J., van den Berg, M., Velders, G. J. M., Vollmer, M. K. & Wang, R. H. J. (2020), The shared socio-economic pathway (SSP) greenhouse gas concentrations and their extensions to 2500. *Geoscientific Model Development*, 13(8), 3571-3605.

Mesbahzadeh, T., Miglietta, M. M., Mirakbari, M., Soleimani Sardoo, F. & Abdolhoseini, M. (2019), Joint Modeling of Precipitation and Temperature Using Copula Theory for Current and Future Prediction under Climate Change Scenarios in Arid Lands (Case Study, Kerman Province, Iran). *Advances in Meteorology*, 2019: 6848049.

Miller, D. E., Wang, Z., Li, B., Harnos, D. S. & Ford, T. (2021), Skillful Subseasonal Prediction of U.S. Extreme Warm Days and Standardized Precipitation Index in Boreal Summer. *Journal of Climate*, 34(14), 5887-5898.

Min, S.-K., Zhang, X. B., Zwiers, F. W. & Hegerl, G. C. (2011), Human contribution to more-intense precipitation extremes. *Nature*, 470(7334), 378-381.

Mindlin, J., Shepherd, T. G., Vera, C. & Osman, M. (2021), Combined effects of global warming and ozone depletion/recovery on Southern Hemisphere atmospheric circulation and regional precipitation. *Geophysical Research Letters*, 48(12), e2021GL092568.

Mohammadpour, K., Sciortino, M. & Kaskaoutis, D. G. (2021), Classification of weather clusters over the Middle East associated with high atmospheric dust-AODs in West Iran. *Atmospheric Research*, 259: 105682.

Moon, T. K. (1996), The expectation-maximization algorithm. *IEEE Signal processing magazine*, 13(6), 47-60.

Moustakis, Y., Onof, C. J. & Paschalis, A. (2020), Atmospheric convection, dynamics and topography shape the

scaling pattern of hourly rainfall extremes with temperature globally. *Communications Earth & Environment*, 1(1), 11.

Müller, W. A., Jungclaus, J. H., Mauritsen, T., Baehr, J., Bittner, M., Budich, R., Bunzel, F., Esch, M., Ghosh, R., Haak, H., Ilyina, T., Kleine, T., Kornblueh, L., Li, H., Modali, K., Notz, D., Pohlmann, H., Roeckner, E., Stemmler, I., Tian, F. & Marotzke, J. (2018), A Higher-resolution Version of the Max Planck Institute Earth System Model (MPI-ESM1.2-HR). *Journal of Advances in Modeling Earth Systems*, 10(7), 1383-1413.

Murakami, H. (2022), Substantial global influence of anthropogenic aerosols on tropical cyclones over the past 40 years. *Science Advances*, 8(19), eabn9493.

Murtagh, F. (1991), Multilayer perceptrons for classification and regression. *Neurocomputing*, 2(5-6), 183-197.

Nakamura, T. & Sato, T. (2022), A possible linkage of Eurasian heat wave and East Asian heavy rainfall in Relation to the Rapid Arctic warming. *Environmental Research*, 209(112881.

Neelin, J. D., Martinez-Villalobos, C., Stechmann, S. N., Ahmed, F., Chen, G., Norris, J. M., Kuo, Y.-H. & Lenderink, G. (2022), Precipitation Extremes and Water Vapor. *Current Climate Change Reports*, 8(1), 17-33.

Newman, M. E. J. (2004), Fast algorithm for detecting community structure in networks. *Physical Review E*, 69(6), 066133.

Newman, M. E. J. (2006), Modularity and community structure in networks. *Proceedings of the National Academy of Sciences*, 103(23), 8577-8582.

Nguyen-Le, D., Yamada, T. J. & Tran-Anh, D. (2017), Classification and forecast of heavy rainfall in northern Kyushu during Baiu season using weather pattern recognition. *Atmospheric Science Letters*, 18(8), 324-329.

Nguyen, P., Thorstensen, A., Sorooshian, S., Hsu, K., Aghakouchak, A., Ashouri, H., Tran, H. & Braithwaite, D. (2018), Global Precipitation Trends across Spatial Scales Using Satellite Observations. *Bulletin of the American Meteorological Society*, 99(4), 689-697.

Nie, J., Sobel, A. H., Shaevitz, D. A. & Wang, S. (2018), Dynamic amplification of extreme precipitation sensitivity. *Proceedings of the National Academy of Sciences*, 115(38), 9467-9472.

Nie, Y. B. & Sun, J. Q. (2022), Moisture Sources and Transport for Extreme Precipitation Over Henan in July 2021. *Geophysical Research Letters*, 49(4), e2021GL097446.

Ning, L., Liu, J. & Wang, B. (2017), How does the South Asian High influence extreme precipitation over eastern China? *Journal of Geophysical Research: Atmospheres*, 122(8), 4281-4298.

Nishant, N. & Sherwood, S. C. (2021), How strongly are mean and extreme precipitation coupled? *Geophysical Research Letters*, 48(10), e2020GL092075.

Nishant, N., Di Virgilio, G., Ji, F., Tam, E., Beyer, K. & Riley, M. L. (2022), Evaluation of Present-Day CMIP6 Model Simulations of Extreme Precipitation and Temperature over the Australian Continent. *Atmosphere*, 13(9), 1478.

Noble, W. S. (2006), What is a support vector machine? *Nature Biotechnology*, 24(12), 1565-1567.

Norris, J., Hall, A., Chen, D., Thackeray, C. W. & Madakumbura, G. D. (2021), Assessing the Representation of Synoptic Variability Associated With California Extreme Precipitation in CMIP6 Models. *Journal of Geophysical Research: Atmospheres*, 126(6), e2020JD033938.

Norris, J., Chen, G. & Neelin, J. D. (2019), Thermodynamic versus Dynamic Controls on Extreme Precipitation in a Warming Climate from the Community Earth System Model Large Ensemble. *Journal of Climate*, 32(4), 1025-1045.

O'Gorman, P. A. & Muller, C. J. (2010), How closely do changes in surface and column water vapor follow Clausius–Clapeyron scaling in climate change simulations? *Environmental Research Letters*, 5(2), 025207.

Ødemark, K., Müller, M., Palerme, C. & Tveito, O. E. (2023), Recent changes in circulation patterns and their opposing impact on extreme precipitation at the west coast of Norway. *Weather and Climate Extremes*, 39(100530.

Odoulami, R. C., Wolski, P. & New, M. (2021), A SOM-based analysis of the drivers of the 2015–2017 Western Cape drought in South Africa. *International Journal of Climatology*, 41(S1), E1518-E1530.

Olmo, M., Bettolli, M. L. & Rusticucci, M. (2020), Atmospheric circulation influence on temperature and precipitation individual and compound daily extreme events: Spatial variability and trends over southern South America. *Weather and Climate Extremes*, 29: 100267.

Olmo, M. E. & Bettolli, M. L. (2021), Extreme daily precipitation in southern South America: statistical characterization and circulation types using observational datasets and regional climate models. *Climate Dynamics*, 57(3), 895-916.

Osburn, L., Hope, P. & Dowdy, A. (2021), Changes in hourly extreme precipitation in Victoria, Australia, from the observational record. *Weather and Climate Extremes*, 31: 100294.

Oshima, N., Yukimoto, S., Deushi, M., Koshiro, T., Kawai, H., Tanaka, T. Y. & Yoshida, K. (2020), Global and Arctic effective radiative forcing of anthropogenic gases and aerosols in MRI-ESM2.0. *Progress in Earth and Planetary Science*, 7(1), 38.

Otto, F. E. L., Zachariah, M., Saeed, F., Siddiqi, A., Shahzad, K., Mushtaq, H., T, A., AchutaRao, K., S, T. C., Barnes, C., Philip, S., Kew, S., Vautard, R., Gerbrand, K., Pinto, I., Wolski, P., Vahlberg, M., Singh, R., Arrighi, J., Aalst, M. v., Thalheimer, L., Raju, E., Li, S. H., Yang, W. C., Harrington, L. J. & Clarke, B. 2022. Climate change likely increased extreme monsoon rainfall, flooding highly vulnerable communities in Pakistan. In *world weather attribution*.

Pahlavan, H. A., Zahraie, B., Nasseri, M. & Mahdipour Varnousfaderani, A. (2018), Improvement of multiple linear regression method for statistical downscaling of monthly precipitation. *International Journal of Environmental Science and Technology*, 15(9), 1897-1912.

Paik, S., Min, S.-K., Zhang, X., Donat, M. G., King, A. D. & Sun, Q. (2020), Determining the Anthropogenic Greenhouse Gas Contribution to the Observed Intensification of Extreme Precipitation. *Geophysical Research Letters*, 47(12), e2019GL086875.

Panda, K. C., Singh, R. M., Thakural, L. N. & Sahoo, D. P. (2022), Representative grid location-multivariate adaptive regression spline (RGL-MARS) algorithm for downscaling dry and wet season rainfall. *Journal of Hydrology*, 605: 127381.

Papalexiou, S. M. & Montanari, A. (2019), Global and regional increase of precipitation extremes under global warming. *Water Resources Research*, 55(6), 4901-4914.

Papalexiou, S. M., Rajulapati, C. R., Andreadis, K. M., Foufoula-Georgiou, E., Clark, M. P. & Trenberth, K. E. (2021), Probabilistic evaluation of drought in CMIP6 simulations. *Earth's future*, 9(10), e2021EF002150.

Park, J.-S., Kang, H.-S., Lee, Y. S. & Kim, M.-K. (2011), Changes in the extreme daily rainfall in South Korea. *International Journal of Climatology*, 31(15), 2290-2299.

Parsons, V. L. 2017. Stratified Sampling. In *Wiley StatsRef: Statistics Reference Online*, 1-11.

Patricola, C. M., Wehner, M. F., Bercos-Hickey, E., Maciel, F. V., May, C., Mak, M., Yip, O., Roche, A. M. & Leal, S. (2022), Future changes in extreme precipitation over the San Francisco Bay Area: Dependence on atmospheric river and extratropical cyclone events. *Weather and Climate Extremes*, 36: 100440.

Pendergrass, A. G. (2018), What precipitation is extreme? *Science*, 360(6393), 1072-1073.

Pendergrass, A. G., Knutti, R., Lehner, F., Deser, C. & Sanderson, B. M. (2017), Precipitation variability increases in a warmer climate. *Scientific Reports*, 7(1), 17966.

Pendergrass, A. G., Lehner, F., Sanderson, B. M. & Xu, Y. (2015), Does extreme precipitation intensity depend on the emissions scenario? *Geophysical Research Letters*, 42(20), 8767-8774.

Pendergrass, A. G. (2020), Changing Degree of Convective Organization as a Mechanism for Dynamic Changes in Extreme Precipitation. *Current Climate Change Reports*, 6(2), 47-54.

Pettitt, A. N. (1979), A non-parametric approach to the change-point problem. *Journal of the Royal Statistical*

Society: Series C (Applied Statistics), 28(2), 126-135.

Pfleiderer, P., Schleussner, C.-F., Kornhuber, K. & Coumou, D. (2019), Summer weather becomes more persistent in a 2 °C world. *Nature Climate Change*, 9(9), 666-671.

Phatak, A., Bates, B. C. & Charles, S. P. (2011), Statistical downscaling of rainfall data using sparse variable selection methods. *Environmental Modelling & Software*, 26(11), 1363-1371.

Philipp, A. (2009), Comparison of principal component and cluster analysis for classifying circulation pattern sequences for the European domain. *Theoretical and Applied Climatology*, 96(1), 31-41.

Pichuka, S. & Maity, R. (2018), Development of a time-varying downscaling model considering non-stationarity using a Bayesian approach. *International Journal of Climatology*, 38(7), 3157-3176.

Pimonsree, S., Kamworapan, S., Gheewala, S. H., Thongbhakdi, A. & Prueksakorn, K. (2023), Evaluation of CMIP6 GCMs performance to simulate precipitation over Southeast Asia. *Atmospheric Research*, 282: 106522.

Piotrowicz, K. & Ciaranek, D. (2020), A selection of weather type classification systems and examples of their application. *Theoretical and Applied Climatology*, 140(1), 719-730.

Pisso, I., Sollum, E., Grythe, H., Kristiansen, N. I., Cassiani, M., Eckhardt, S., Arnold, D., Morton, D., Thompson, R. L. & Groot Zwaaftink, C. D. (2019), The Lagrangian particle dispersion model FLEXPART version 10.4. *Geoscientific Model Development*, 12(12), 4955-4997.

Prince, H. D., Cullen, N. J., Gibson, P. B., Conway, J. & Kingston, D. G. (2021), A Climatology of Atmospheric Rivers in New Zealand. *Journal of Climate*, 34(11), 4383-4402.

Pringle, J., Stretch, D. D. & Bárdossy, A. (2015), On linking atmospheric circulation patterns to extreme wave events for coastal vulnerability assessments. *Natural Hazards*, 79(1), 45-59.

Qian, C., Ye, Y. B., Zhang, W. X. & Zhou, T. J. (2022), Heavy rainfall event in mid-August 2020 in southwestern China: Contribution of anthropogenic forcings and atmospheric circulation. *Bulletin of the American Meteorological Society*, 103: S111-S117.

Qin, H., Yuan, W., Wang, J., Chen, Y., Dai, P., Sobel, A. H., Meng, Z. & Nie, J. (2022), Climate change attribution of the 2021 Henan extreme precipitation: Impacts of convective organization. *Science China Earth Sciences*, 65(10), 1837-1846.

Quiroga, R. Q., Kreuz, T. & Grassberger, P. (2002), Event synchronization: a simple and fast method to measure synchronicity and time delay patterns. *Physical review E*, 66(4), 041904.

Rahman, M., Chen, N. S., Elbeltagi, A., Islam, M. M., Alam, M., Pourghasemi, H. R., Tao, W., Zhang, J., Shufeng, T., Faiz, H., Baig, M. A. & Dewan, A. (2021), Application of stacking hybrid machine learning algorithms in delineating multi-type flooding in Bangladesh. *Journal of Environmental Management*, 295: 113086.

Rajagopalan, B. & Lall, U. (1999), A k-nearest-neighbor simulator for daily precipitation and other weather variables. *Water Resources Research*, 35(10), 3089-3101.

Ralph, F. M., Rutz, J. J., Cordeira, J. M., Dettinger, M., Anderson, M., Reynolds, D., Schick, L. J. & Smallcomb, C. (2019), A Scale to Characterize the Strength and Impacts of Atmospheric Rivers. *Bulletin of the American Meteorological Society*, 100(2), 269-289.

Ramchoun, H., Ghanou, Y., Ettaouil, M. & Janati Idrissi, M. A. (2016), Multilayer perceptron: Architecture optimization and training. *International Journal of Interactive Multimedia and Artificial Intelligence*, 4(1), 26-30.

Reichstein, M., Camps-Valls, G., Stevens, B., Jung, M., Denzler, J., Carvalhais, N. & Prabhat. (2019), Deep learning and process understanding for data-driven Earth system science. *Nature*, 566(7743), 195-204.

Riahi, K., van Vuuren, D. P., Kriegler, E., Edmonds, J., O'Neill, B. C., Fujimori, S., Bauer, N., Calvin, K., Dellink, R., Fricko, O., Lutz, W., Popp, A., Cuaresma, J. C., Kc, S., Leimbach, M., Jiang, L., Kram, T., Rao, S., Emmerling, J., Ebi, K., Hasegawa, T., Havlik, P., Humpenöder, F., Da Silva, L. A., Smith, S., Stehfest, E., Bosetti, V., Eom, J., Gernaat, D., Masui, T., Rogelj, J., Strefler, J., Drouet, L., Krey, V., Luderer, G., Harmsen,

M., Takahashi, K., Baumstark, L., Doelman, J. C., Kainuma, M., Klimont, Z., Marangoni, G., Lotze-Campen, H., Obersteiner, M., Tabeau, A. & Tavoni, M. (2017), The Shared Socioeconomic Pathways and their energy, land use, and greenhouse gas emissions implications: An overview. *Global Environmental Change*, 42: 153-168.

Ribes, A., Qasmi, S. & Gillett, N. P. (2021), Making climate projections conditional on historical observations. *Science Advances*, 7(4), eabc0671.

Richardson, D., Neal, R., Dankers, R., Mylne, K., Cowling, R., Clements, H. & Millard, J. (2020), Linking weather patterns to regional extreme precipitation for highlighting potential flood events in medium- to long-range forecasts. *Meteorological Applications*, 27(4), e1931.

Rieger, N., Corral, Á., Olmedo, E. & Turiel, A. (2021), Lagged Teleconnections of Climate Variables Identified via Complex Rotated Maximum Covariance Analysis. *Journal of Climate*, 34(24), 9861-9878.

Rilling, G., Flandrin, P. & Goncalves, P. 2003. On empirical mode decomposition and its algorithms. In *IEEE-EURASIP workshop on nonlinear signal and image processing*, 8-11.

Ritzhaupt, N. & Maraun, D. (2023), Consistency of Seasonal Mean and Extreme Precipitation Projections Over Europe Across a Range of Climate Model Ensembles. *Journal of Geophysical Research: Atmospheres*, 128(1), e2022JD037845.

Rousi, E., Anagnostopoulou, C., Tolika, K. & Maheras, P. (2015), Representing teleconnection patterns over Europe: A comparison of SOM and PCA methods. *Atmospheric research*, 152: 123-137.

Rust, H. W., Vrac, M., Lengaigne, M. & Sultan, B. (2010), Quantifying Differences in Circulation Patterns Based on Probabilistic Models: IPCC AR4 Multimodel Comparison for the North Atlantic. *Journal of Climate*, 23(24), 6573-6589.

Ryberg, K. R., Hodgkins, G. A. & Dudley, R. W. (2020), Change points in annual peak streamflows: Method comparisons and historical change points in the United States. *Journal of Hydrology*, 583: 124307.

Salzmann, M. (2016), Global warming without global mean precipitation increase? *Science Advances*, 2(6), e1501572.

Sammen, S. S., Mohammed, T. A., Ghazali, A. H., Sidek, L. M., Shahid, S., Abba, S. I., Malik, A. & Al-Ansari, N. (2022), Assessment of climate change impact on probable maximum floods in a tropical catchment. *Theoretical and Applied Climatology*, 148(1), 15-31.

Scafetta, N. (2014), Multi-scale dynamical analysis (MSDA) of sea level records versus PDO, AMO, and NAO indexes. *Climate dynamics*, 43(1), 175-192.

Schiro, K. A., Neelin, J. D., Adams, D. K. & Lintner, B. R. (2016), Deep Convection and Column Water Vapor over Tropical Land versus Tropical Ocean: A Comparison between the Amazon and the Tropical Western Pacific. *Journal of the Atmospheric Sciences*, 73(10), 4043-4063.

Schroers, M. & Martin, E. (2022), Synoptic Connections and Impacts of 14-Day Extreme Precipitation Events in the United States. *Journal of Applied Meteorology and Climatology*, 61(7), 877-890.

Schwalm, C. R., Glendon, S. & Duffy, P. B. (2020), RCP8.5 tracks cumulative CO₂ emissions. *Proceedings of the National Academy of Sciences*, 117(33), 19656-19657.

Seland, Ø., Bentsen, M., Olivié, D., Toniazzo, T., Gjermundsen, A., Graff, L. S., Debernard, J. B., Gupta, A. K., He, Y. C., Kirkevåg, A., Schwinger, J., Tjiputra, J., Aas, K. S., Bethke, I., Fan, Y., Griesfeller, J., Grini, A., Guo, C., Ilicak, M., Karset, I. H. H., Landgren, O., Liakka, J., Moseid, K. O., Nummelin, A., Spensberger, C., Tang, H., Zhang, Z., Heinze, C., Iversen, T. & Schulz, M. (2020), Overview of the Norwegian Earth System Model (NorESM2) and key climate response of CMIP6 DECK, historical, and scenario simulations. *Geosci. Model Dev.*, 13(12), 6165-6200.

Sellar, A. A., Jones, C. G., Mulcahy, J. P., Tang, Y., Yool, A., Wiltshire, A., O'Connor, F. M., Stringer, M., Hill, R., Palmieri, J., Woodward, S., de Mora, L., Kuhlbrodt, T., Rumbold, S. T., Kelley, D. I., Ellis, R., Johnson, C. E.,

Walton, J., Abraham, N. L., Andrews, M. B., Andrews, T., Archibald, A. T., Berthou, S., Burke, E., Blockley, E., Carslaw, K., Dalvi, M., Edwards, J., Folberth, G. A., Gedney, N., Griffiths, P. T., Harper, A. B., Hendry, M. A., Hewitt, A. J., Johnson, B., Jones, A., Jones, C. D., Keeble, J., Liddicoat, S., Morgenstern, O., Parker, R. J., Predoi, V., Robertson, E., Siahaan, A., Smith, R. S., Swaminathan, R., Woodhouse, M. T., Zeng, G. & Zerroukat, M. (2019), UKESM1: Description and Evaluation of the U.K. Earth System Model. *Journal of Advances in Modeling Earth Systems*, 11(12), 4513-4558.

Senent-Aparicio, J., López-Ballesteros, A., Jimeno-Sáez, P. & Pérez-Sánchez, J. (2023), Recent precipitation trends in Peninsular Spain and implications for water infrastructure design. *Journal of Hydrology: Regional Studies*, 45: 101308.

Sha, Y. K., Gagne, D. J., West, G. & Stull, R. (2022), A Hybrid Analog-Ensemble–Convolutional-Neural-Network Method for Postprocessing Precipitation Forecasts. *Monthly Weather Review*, 150(6), 1495-1515.

Shahriar, S. A., Siddique, M. A. M. & Rahman, S. M. A. (2021), Climate change projection using statistical downscaling model over Chittagong Division, Bangladesh. *Meteorology and Atmospheric Physics*, 133(4), 1409-1427.

Sharifi, E., Saghafian, B. & Steinacker, R. (2019), Downscaling satellite precipitation estimates with multiple linear regression, artificial neural networks, and spline interpolation techniques. *Journal of Geophysical Research: Atmospheres*, 124(2), 789-805.

Sharma, S., Sharma, S. & Athaiya, A. (2017), Activation functions in neural networks. *towards data science*, 6(12), 310-316.

Shastri, H., Ghosh, S. & Karmakar, S. (2017), Improving Global Forecast System of extreme precipitation events with regional statistical model: Application of quantile-based probabilistic forecasts. *Journal of Geophysical Research: Atmospheres*, 122(3), 1617-1634.

Shen, Y. & Xiong, A. (2016), Validation and comparison of a new gauge-based precipitation analysis over mainland China. *International Journal of Climatology*, 36(1), 252-265.

Shibuya, R., Takayabu, Y. & Kamahori, H. (2021), Dynamics of Widespread Extreme Precipitation Events and the Associated Large-Scale Environment Using AMeDAS and JRA-55 Data. *Journal of Climate*, 34(22), 8955-8970.

Siabi, E. K., Kabobah, A. T., Akpoti, K., Anornu, G. K., Amo-Boateng, M. & Nyantakyi, E. K. (2021), Statistical downscaling of global circulation models to assess future climate changes in the Black Volta basin of Ghana. *Environmental Challenges*, 5: 100299.

Sivaramakrishna, S. S. V., Rao, B. R. S., Satyanarayana, G. C., Rao, N. N., Panda, R., Sai, S. M., Ramana, M. S. V. & Rao, D. V. B. (2022), Simulation of Regional Climate over the Indian subcontinent through dynamical downscaling using WRF-ARW model. *Theoretical and Applied Climatology*, 148(1), 391-413.

Sohn, K. T., Lee, J. H., Lee, S. H. & Ryu, C. S. (2005), Statistical prediction of heavy rain in South Korea. *Advances in Atmospheric Sciences*, 22(5), 703-710.

Song, F., Zhang, G. J., Ramanathan, V. & Leung, L. R. (2022), Trends in surface equivalent potential temperature: A more comprehensive metric for global warming and weather extremes. *Proceedings of the National Academy of Sciences*, 119(6), e2117832119.

Srivastava, A., Grotjahn, R. & Ullrich, P. A. (2020), Evaluation of historical CMIP6 model simulations of extreme precipitation over contiguous US regions. *Weather and Climate Extremes*, 29(100268.

Stein, A. F., Draxler, R. R., Rolph, G. D., Stunder, B. J. B., Cohen, M. D. & Ngan, F. (2015), NOAA's HYSPLIT Atmospheric Transport and Dispersion Modeling System. *Bulletin of the American Meteorological Society*, 96(12), 2059-2077.

Stott, P. A., Christidis, N., Otto, F. E., Sun, Y., Vanderlinden, J. P., van Oldenborgh, G. J., Vautard, R., von Storch, H., Walton, P. & Yiou, P. (2016), Attribution of extreme weather and climate-related events. *Wiley*

Interdisciplinary Reviews: Climate Change, 7(1), 23-41.

Stouffer, R. J., Eyring, V., Meehl, G. A., Bony, S., Senior, C., Stevens, B. & Taylor, K. E. (2017), CMIP5 Scientific Gaps and Recommendations for CMIP6. *Bulletin of the American Meteorological Society*, 98(1), 95-105.

Sun, Q. H., Zhang, X. B., Zwiers, F., Westra, S. & Alexander, L. V. (2021), A Global, Continental, and Regional Analysis of Changes in Extreme Precipitation. *Journal of Climate*, 34(1), 243-258.

Sun, Y. & Ding, Y. H. (2010), A projection of future changes in summer precipitation and monsoon in East Asia. *Science China Earth Sciences*, 53(2), 284-300.

Swain, D. L., Horton, D. E., Singh, D. & Diffenbaugh, N. S. (2016), Trends in atmospheric patterns conducive to seasonal precipitation and temperature extremes in California. *Science Advances*, 2(4), e1501344.

Swales, D., Alexander, M. & Hughes, M. (2016), Examining moisture pathways and extreme precipitation in the U.S. Intermountain West using self-organizing maps. *Geophysical Research Letters*, 43(4), 1727-1735.

Swart, N. C., Cole, J. N. S., Kharin, V. V., Lazare, M., Scinocca, J. F., Gillett, N. P., Anstey, J., Arora, V., Christian, J. R., Hanna, S., Jiao, Y., Lee, W. G., Majaess, F., Saenko, O. A., Seiler, C., Seinen, C., Shao, A., Sigmond, M., Solheim, L., von Salzen, K., Yang, D. & Winter, B. (2019), The Canadian Earth System Model version 5 (CanESM5.0.3). *Geosci. Model Dev.*, 12(11), 4823-4873.

Syarif, I., Prugel-Bennett, A. & Wills, G. (2016), SVM parameter optimization using grid search and genetic algorithm to improve classification performance. *TELKOMNIKA (Telecommunication Computing Electronics and Control)*, 14(4), 1502-1509.

Tabari, H. & Willems, P. (2018), Lagged influence of Atlantic and Pacific climate patterns on European extreme precipitation. *Scientific Reports*, 8(1), 5748.

Tabari, H. (2021), Extreme value analysis dilemma for climate change impact assessment on global flood and extreme precipitation. *Journal of Hydrology*, 593: 125932.

Takahashi, H. G. & Fujinami, H. (2021), Recent decadal enhancement of Meiyu–Baiu heavy rainfall over East Asia. *Scientific Reports*, 11(1), 13665.

Tandon, N. F., Zhang, X. B. & Sobel, A. H. (2018), Understanding the Dynamics of Future Changes in Extreme Precipitation Intensity. *Geophysical Research Letters*, 45(6), 2870-2878.

Tang, Y., Huang, A. N., Wu, P., Huang, D. Q., Xue, D. K. & Wu, Y. (2021), Drivers of Summer Extreme Precipitation Events Over East China. *Geophysical Research Letters*, 48(11), e2021GL093670.

Tang, Y. & Duan, A. (2021), Using deep learning to predict the East Asian summer monsoon. *Environmental Research Letters*, 16(12), 124006.

Tatebe, H., Ogura, T., Nitta, T., Komuro, Y., Ogochi, K., Takemura, T., Sudo, K., Sekiguchi, M., Abe, M., Saito, F., Chikira, M., Watanabe, S., Mori, M., Hirota, N., Kawatani, Y., Mochizuki, T., Yoshimura, K., Takata, K., O'Ishi, R., Yamazaki, D., Suzuki, T., Kurogi, M., Kataoka, T., Watanabe, M. & Kimoto, M. (2019), Description and basic evaluation of simulated mean state, internal variability, and climate sensitivity in MIROC6. *Geoscientific Model Development*, 12(7), 2727-2765.

Tebaldi, C., Debeire, K., Eyring, V., Fischer, E., Fyfe, J., Friedlingstein, P., Knutti, R., Lowe, J., O'Neill, B., Sanderson, B., van Vuuren, D., Riahi, K., Meinshausen, M., Nicholls, Z., Tokarska, K. B., Hurtt, G., Kriegler, E., Lamarque, J. F., Meehl, G., Moss, R., Bauer, S. E., Boucher, O., Brovkin, V., Byun, Y. H., Dix, M., Gualdi, S., Guo, H., John, J. G., Kharin, S., Kim, Y., Koshiro, T., Ma, L., Olivié, D., Panickal, S., Qiao, F., Rong, X., Rosenbloom, N., Schupfner, M., Séférian, R., Sellar, A., Semmler, T., Shi, X., Song, Z., Steger, C., Stouffer, R., Swart, N., Tachiiri, K., Tang, Q., Tatebe, H., Voldoire, A., Volodin, E., Wyser, K., Xin, X., Yang, S., Yu, Y. & Ziehn, T. (2021), Climate model projections from the Scenario Model Intercomparison Project (ScenarioMIP) of CMIP6. *Earth System Dynamics*, 12(1), 253-293.

Tebaldi, C. & Friedlingstein, P. (2013), Delayed detection of climate mitigation benefits due to climate inertia and variability. *Proceedings of the National Academy of Sciences*, 110(43), 17229-17234.

Teixeira, M. S. & Satyamurty, P. (2007), Dynamical and Synoptic Characteristics of Heavy Rainfall Episodes in Southern Brazil. *Monthly Weather Review*, 135(2), 598-617.

Thackeray, C. W., Hall, A., Norris, J. & Chen, D. (2022), Constraining the increased frequency of global precipitation extremes under warming. *Nature Climate Change*, 12(5), 441-448.

Toimil, A., Losada, I. J., Nicholls, R. J., Dalrymple, R. A. & Stive, M. J. F. (2020), Addressing the challenges of climate change risks and adaptation in coastal areas: A review. *Coastal Engineering*, 156: 103611.

Tomassetti, B., Verdecchia, M. & Giorgi, F. (2009), NN5: A neural network based approach for the downscaling of precipitation fields – Model description and preliminary results. *Journal of Hydrology*, 367(1), 14-26.

Toms, B. A., Kashinath, K., Prabhat & Yang, D. (2021), Testing the reliability of interpretable neural networks in geoscience using the Madden–Julian oscillation. *Geoscientific Model Development*, 14(7), 4495-4508.

Torralba, V., Gonzalez-Reviriego, N., Cortesi, N., Manrique-Suñén, A., Lledó, L., Marcos, R., Soret, A. & Doblas-Reyes, F. J. (2021), Challenges in the selection of atmospheric circulation patterns for the wind energy sector. *International Journal of Climatology*, 41(3), 1525-1541.

Tostes, J. O., Lyra, G. B., Oliveira- Júnior, J. F. & Francelino, M. R. (2017), Assessment of gridded precipitation and air temperature products for the State of Acre, southwestern Amazonia, Brazil. *Environmental Earth Sciences*, 76(4), 153.

Tsoumakas, G. & Katakis, I. (2007), Multi-label classification: An overview. *International Journal of Data Warehousing and Mining (IJDWM)*, 3(3), 1-13.

Ullah, W., Wang, G. J., Lou, D., Ullah, S., Bhatti, A. S., Ullah, S., Karim, A., Hagan, D. F. T. & Ali, G. (2021), Large-scale atmospheric circulation patterns associated with extreme monsoon precipitation in Pakistan during 1981–2018. *Atmospheric Research*, 253: 105489.

Uribe, A., Vial, J. & Mauritsen, T. (2021), Sensitivity of Tropical Extreme Precipitation to Surface Warming in Aquaplanet Experiments Using a Global Nonhydrostatic Model. *Geophysical Research Letters*, 48(9), e2020GL091371.

Valdés-Pineda, R., Cañón, J. & Valdés, J. B. (2018), Multi-decadal 40-to 60-year cycles of precipitation variability in Chile (South America) and their relationship to the AMO and PDO signals. *Journal of Hydrology*, 556: 1153-1170.

Vandal, T., Kodra, E. & Ganguly, A. R. (2019), Intercomparison of machine learning methods for statistical downscaling: the case of daily and extreme precipitation. *Theoretical and Applied Climatology*, 137(1), 557-570.

Varshney, M. & Singh, P. (2021), Optimizing nonlinear activation function for convolutional neural networks. *Signal, Image and Video Processing*, 15(6), 1323-1330.

Vavrus, S. J. (2018), The Influence of Arctic Amplification on Mid-latitude Weather and Climate. *Current Climate Change Reports*, 4(3), 238-249.

Vicente-Serrano, S. M., Beguería, S., López-Moreno, J. I., El Kenawy, A. M. & Angulo-Martínez, M. (2009), Daily atmospheric circulation events and extreme precipitation risk in northeast Spain: Role of the North Atlantic Oscillation, the Western Mediterranean Oscillation, and the Mediterranean Oscillation. *Journal of Geophysical Research: Atmospheres*, 114(D8), D08106.

Wang, H.-J., Zhang, R.-H., Cole, J. & Chavez, F. (1999), El Niño and the related phenomenon Southern Oscillation (ENSO): the largest signal in interannual climate variation. *Proceedings of the National Academy of Sciences*, 96(20), 11071-11072.

Wang, H.-M., Chen, J., Xu, C.-Y., Zhang, J. K. & Chen, H. (2020), A Framework to Quantify the Uncertainty Contribution of GCMs Over Multiple Sources in Hydrological Impacts of Climate Change. *Earth's Future*, 8(8), e2020EF001602.

Wang, J. & Kotamarthi, V. R. (2015), High-resolution dynamically downscaled projections of precipitation in the

mid and late 21st century over North America. *Earth's Future*, 3(7), 268-288.

Wang, L. C., Sun, X. G., Yang, X. Q., Tao, L. F. & Zhang, Z. Q. (2021), Contribution of Water Vapor to the Record-Breaking Extreme Meiyu Rainfall along the Yangtze River Valley in 2020. *Journal of Meteorological Research*, 35(4), 557-570.

Wang, T. J., Zhong, Z., Sun, Y. & Wang, J. (2019), Impacts of tropical cyclones on the meridional movement of the western Pacific subtropical high. *Atmospheric Science Letters*, 20(5), e893.

Wang, X. X., Jiang, D. B. & Lang, X. M. (2017), Future extreme climate changes linked to global warming intensity. *Science Bulletin*, 62(24), 1673-1680.

Wang, Z. Q., Fu, Z. H., Liu, B., Zheng, Z. Y., Zhang, W. C., Liu, Y. Y., Zhang, F. & Zhang, Q. (2022), Northward migration of the East Asian summer monsoon northern boundary during the twenty-first century. *Scientific Reports*, 12(1), 10066.

Warner, M. D., Mass, C. F. & Salathé, E. P. (2015), Changes in Winter Atmospheric Rivers along the North American West Coast in CMIP5 Climate Models. *Journal of Hydrometeorology*, 16(1), 118-128.

Warren, R. A., Jakob, C., Hitchcock, S. M. & White, B. A. (2021), Heavy versus extreme rainfall events in southeast Australia. *Quarterly Journal of the Royal Meteorological Society*, 147(739), 3201-3226.

Watterson, I. G., Keane, R. J., Dix, M., Ziehn, T., Andrews, T. & Tang, Y. (2021), Analysis of CMIP6 atmospheric moisture fluxes and the implications for projections of future change in mean and heavy rainfall. *International Journal of Climatology*, 41(S1), E1417-E1434.

Wehner, M., Gleckler, P. & Lee, J. (2020), Characterization of long period return values of extreme daily temperature and precipitation in the CMIP6 models: Part 1, model evaluation. *Weather and Climate Extremes*, 30: 100283.

Wentz Frank, J., Ricciardulli, L., Hilburn, K. & Mears, C. (2007), How Much More Rain Will Global Warming Bring? *Science*, 317(5835), 233-235.

Wilby, R. L. & Wigley, T. M. L. (1997), Downscaling general circulation model output: a review of methods and limitations. *Progress in Physical Geography: Earth and Environment*, 21(4), 530-548.

WMO. 2021. *WMO Atlas of Mortality and Economic Losses from Weather, Climate and Water Extremes (1970–2019)*.

Wu, H., Lei, H., Lu, W. & Liu, Z. (2022a), Future changes in precipitation over the upper Yangtze River basin based on bias correction spatial downscaling of models from CMIP6. *Environmental Research Communications*, 4(4), 045002.

Wu, H. B. & Gu, X. D. 2015. Max-pooling dropout for regularization of convolutional neural networks. In *International Conference on Neural Information Processing*, 46-54. Springer.

Wu, P., Liu, Y. J., Ding, Y. H., Li, X. C. & Wang, J. (2022b), Modulation of sea surface temperature over the North Atlantic and Indian-Pacific warm pool on interdecadal change of summer precipitation over northwest China. *International Journal of Climatology*, 42(16), 8526-8538.

Xin, X., Wu, T., Zhang, J., Yao, J. & Fang, Y. (2020), Comparison of CMIP6 and CMIP5 simulations of precipitation in China and the East Asian summer monsoon. *International Journal of Climatology*, 40(15), 6423-6440.

Xoplaki, E., González-Rouco, J. F., Luterbacher, J. & Wanner, H. (2004), Wet season Mediterranean precipitation variability: influence of large-scale dynamics and trends. *Climate Dynamics*, 23(1), 63-78.

Xu, M., Xu, H., Ma, J. & Deng, J. (2021), Impact of Atlantic multidecadal oscillation on interannual relationship between ENSO and East Asian early summer monsoon. *International Journal of Climatology*, 41(4), 2860-2877.

Yang, K., Cai, W. J., Huang, G., Hu, K. M., Ng, B. & Wang, G. J. (2022a), Increased variability of the western Pacific subtropical high under greenhouse warming. *Proceedings of the National Academy of Sciences*, 119(23), e2120335119.

Yang, M., Ma, H., Chen, B. & Dong, G. (2022b), Intensive Cold-Air Invasion Detection and Classification with

Deep Learning in Complicated Meteorological Systems. *Complexity*, 2022: 1-13.

Yang, X. L., Yu, X. H., Wang, Y. Q., He, X. G., Pan, M., Zhang, M. R., Liu, Y., Ren, L. L. & Sheffield, J. (2020), The Optimal Multimodel Ensemble of Bias-Corrected CMIP5 Climate Models over China. *Journal of Hydrometeorology*, 21(4), 845-863.

Ye, Y. B. & Qian, C. (2021), Conditional attribution of climate change and atmospheric circulation contributing to the record-breaking precipitation and temperature event of summer 2020 in southern China. *Environmental Research Letters*, 16(4), 044058.

You, Q. L., Cai, Z. Y., Wu, F. Y., Jiang, Z. H., Pepin, N. & Shen, S. S. (2021), Temperature dataset of CMIP6 models over China: evaluation, trend and uncertainty. *Climate Dynamics*, 57(1), 17-35.

Yu, B., Lin, H., Kharin, V. V. & Wang, X. L. (2020), Interannual variability of North American winter temperature extremes and its associated circulation anomalies in observations and CMIP5 simulations. *Journal of Climate*, 33(3), 847-865.

Yu, R. & Zhai, P. (2021), Changes in Summer Persistent Precipitation over the Middle-Lower Reaches of the Yangtze River and Associated Atmospheric Circulation Patterns. *Journal of Meteorological Research*, 35(3), 393-401.

Yu, Z. W., Montalto, F., Jacobson, S., Lall, U., Bader, D. & Horton, R. (2022), Stochastic Downscaling of Hourly Precipitation Series From Climate Change Projections. *Water Resources Research*, 58(10), e2022WR033140.

Yuan, Y., Gao, H. & Ding, T. (2020), The extremely north position of the western Pacific subtropical high in summer of 2018: Important role of the convective activities in the western Pacific. *International Journal of Climatology*, 40(3), 1361-1374.

Zamani, Y., Hashemi Monfared, S. A., Azhdari moghaddam, M. & Hamidianpour, M. (2020), A comparison of CMIP6 and CMIP5 projections for precipitation to observational data: the case of Northeastern Iran. *Theoretical and Applied Climatology*, 142(3), 1613-1623.

Zeder, J. & Fischer, E. M. (2020), Observed extreme precipitation trends and scaling in Central Europe. *Weather and Climate Extremes*, 29(100266.

Zeng, Z., Hsieh, W. W., Shabbar, A. & Burrows, W. R. (2011), Seasonal prediction of winter extreme precipitation over Canada by support vector regression. *Hydrol. Earth Syst. Sci.*, 15(1), 65-74.

Zha, X. N., Xiong, L. H., Chen, J., Kim, J.-S., Liu, D. D. & Wang, G. S. (2022), Estimating multisite precipitation by a stepwise NHMM-VAR model considering the spatiotemporal correlations of precipitation amounts. *Journal of Hydrology*, 612: 128065.

Zhan, W., He, X. G., Sheffield, J. & Wood, E. F. (2020), Projected Seasonal Changes in Large-Scale Global Precipitation and Temperature Extremes Based on the CMIP5 Ensemble. *Journal of Climate*, 33(13), 5651-5671.

Zhang, C., Brodeur, Z. P., Steinschneider, S. & Herman, J. D. (2022), Leveraging Spatial Patterns in Precipitation Forecasts Using Deep Learning to Support Regional Water Management. *Water Resources Research*, 58(9), e2021WR031910.

Zhang, J. P., Zhao, T. B., Dai, A. G. & Zhang, W. Y. (2019a), Detection and Attribution of Atmospheric Precipitable Water Changes since the 1970s over China. *Scientific Reports*, 9(1), 17609.

Zhang, L., Min, J., Zhuang, X. & Schumacher, R. S. (2019b), General Features of Extreme Rainfall Events Produced by MCSs over East China during 2016–17. *Monthly Weather Review*, 147(7), 2693-2714.

Zhang, L. P. & Delworth, T. L. (2016), Simulated Response of the Pacific Decadal Oscillation to Climate Change. *Journal of Climate*, 29(16), 5999-6018.

Zhang, W. X., Furtado, K., Wu, P. L., Zhou, T. J., Chadwick, R., Marzin, C., Rostron, J. & Sexton, D. (2021), Increasing precipitation variability on daily-to-multiyear time scales in a warmer world. *Science advances*, 7(31), eabf8021.

Zhong, S. Y., Yu, L. J., Heilman, W. E., Bian, X. D. & Fromm, H. (2020), Synoptic weather patterns for large wildfires in the northwestern United States—a climatological analysis using three classification methods. *Theoretical and Applied Climatology*, 141(3), 1057-1073.

Zhou, B. Q. & Zhai, P. M. (2016), A New Forecast Model Based on the Analog Method for Persistent Extreme Precipitation. *Weather and Forecasting*, 31(4), 1325-1341.

Zhou, B. Q., Zhai, P. M., Tett, S. F. & Lott, F. C. (2021a), Detectable anthropogenic changes in daily-scale circulations driving summer rainfall shifts over eastern China. *Environmental Research Letters*, 16(7), 074044.

Zhou, S., Yu, B. F. & Zhang, Y. (2023), Global concurrent climate extremes exacerbated by anthropogenic climate change. *Science Advances*, 9(10), eabo1638.

Zhou, Z. H. 2021. Ensemble Learning. In *Machine Learning,* ed. Z. H. Zhou, 181-210. Singapore: Springer Singapore.

Zhou, Z. Q., Xie, S. P. & Zhang, R. H. (2021b), Historic Yangtze flooding of 2020 tied to extreme Indian Ocean conditions. *Proceedings of the National Academy of Sciences*, 118(12), e2022255118.

Zhu, X., Wei, Z., Dong, W., Wen, X., Zheng, Z., Chen, G. & Liu, Y. (2019), Projected temperature and precipitation changes on the Tibetan Plateau: results from dynamical downscaling and CCSM4. *Theoretical and Applied Climatology*, 138(1), 861-875.

Zhu, Y.-Y. & Yang, S. (2020), Evaluation of CMIP6 for historical temperature and precipitation over the Tibetan Plateau and its comparison with CMIP5. *Advances in Climate Change Research*, 11(3), 239-251.

Zounemat-Kermani, M., Batelaan, O., Fadaee, M. & Hinkelmann, R. (2021), Ensemble machine learning paradigms in hydrology: A review. *Journal of Hydrology*, 598: 126266.

List of appended contributions

Published papers

Jiang Qin, Cioffi Francesco*, Giannini Mario, Wang Jun, Li Weiyue. Analysis of changes in large-scale circulation patterns driving extreme precipitation events over the Central-Eastern China. International Journal of Climatology. 2022, 43(1): 519-537.

Submitted papers

Jiang Qin, Cioffi Francesco*, Conticello, Rosario Federico, Giannini Mario, Wang Jun*. A Stacked Ensemble Learning and nonhomogeneous Hidden Markov Model for Daily Precipitation Downscaling and Projection. 2023, Hydrological Processes.

List of contributions not included in the thesis

Published papers

(1) **Jiang Qin**, Li Weiyue*, Fan Zedong, He Xiaogang, Sun Weiwei, Chen Sheng, Wen Jiahong, Gao Jun, Wang Jun*. Evaluation of the ERA5 reanalysis precipitation dataset over Chinese Mainland. Journal of Hydrology. 2021, 595:125660. ESI highly cited paper.

(2) **Jiang Qin**, He Xiaogang, Wang Jun*, Wen Jiahong, Mu Haizhen, Xu Ming. Spatiotemporal Analysis of Land Use and Land Cover (LULC) Changes and Precipitation Trends in Shanghai. Applied Sciences. 2020, 10(21):7897.

(3) Li Weiyue*, **Jiang Qin***, He Xiaogang, Sun Haiqing, Sun Weiwei, Scaioni Marco, Chen Sheng, Li Xin, Gao Jun, Hong Yang. Effective Multi-Satellite Precipitation Fusion Procedure Conditioned by Gauge Background Fields over the Chinese Mainland. Journal of Hydrology. 2022, 610:127783.

(4) Fan Zedong, Li Weiyue*, **Jiang Qin**, Sun Weiwei, Wen Jiahong, Gao Jun. A comparative study of four merging approaches for regional precipitation estimation. IEEE Access. 2021, 9:33625-33637.

ACKNOWLEDGEMENTS

In April 2019, I passed the final examination for doctoral admission and started the Ph.D. journey in September, this year. I treasure my memories of those joyous, grieved, ordinary, and untrammeled days over the past four years. I would like to thank all people who have contributed in his/her way and helped me.

For the first two years at East China Normal University, I meet many friends and learned a lot. On a walk together in the roads to the Hekou building, the canteen, and the postgraduate department, I felt the weather changes and desired to get more positive things in my life. I would like to thank all my friends and colleagues who have supported me during this period.

I would like to sincerely acknowledge the China Scholarship Council for supporting my living fees in Italy from 13 March, 2021 to 12 March, 2023. I would like to thank the Università degli Studi di ROMA "La Sapienza" for accepting me as the Joint-PhD student.

Foremost, I would like to express my gratitude to my supervisors Professor Jun Wang and Professor Francesco Cioffi for their insightful advice, continuous support and professional guidance. Without their wisdom, expertise, and encouragement, this thesis would not have been possible. Professor Jun Wang provided opportunities to pursue my academic goals. Professor Francesco Cioffi gave me the necessary resources and his experiences and perspectives have significantly enriched my knowledge.

I would like to thank Professor Weiyue Li at Shanghai Normal University who had useful suggestions and technical revises on my works. I would like to thank Professor Sun Xun who helped me to apply for the dual doctoral degree program. I would like to thank Dr. Federico Rosario Conticello and Mario Giannini, who shared the codes and gave the constructive feedback on this thesis. I would also like to express my gratitude to the professors and PhD students at DICEA, Sapienza who generously gave their time for helping me.

Last but not least, I would like to thank my family for their unwavering love throughout my academic pursuit.

Thank you all for your contributions to my doctoral journey.

This work was supported by the dual doctoral degree program in Geography and Environmental and Hydraulics Engineering between East China Normal University and Università degli Studi di ROMA "La Sapienza".